

Low-energy Electron Holography Microscope for Imaging of Single Molecules

Présentée le 12 mai 2022

Faculté des sciences de base
Laboratoire de science à l'échelle nanométrique
Programme doctoral en physique

pour l'obtention du grade de Docteur ès Sciences

par

Sven Alexander SZILAGYI

Acceptée sur proposition du jury

Prof. F. Courbin, président du jury
Prof. K. Kern, directeur de thèse
Prof. S. Rauschenbach, rapporteur
Prof. F. Forneris, rapporteur
Prof. G. Dietler, rapporteur

When you change the way you look at things,
the things you look at change.
— Max Planck

Abstract

Structure determination techniques are an essential tool to investigate and understand molecules, especially in biology, where functionality crucially depends on structure. The dominant high-resolution methods, such as transmission electron microscopy and X-ray diffraction, rely on ensemble averaging, making them unsuitable for evidencing structural variations of flexible molecules. Common single-molecule imaging techniques like scanning probe microscopy achieve high resolution but lack access to 3D objects. A possible way to overcome these limitations is offered by low-energy electron holography (LEEH). So far, LEEH achieved molecular imaging at resolutions in the range of 7–8 Å on the single-molecule level. A resolution in the range of a few Å, which would give access to atomic details of molecular structures, is in theory attainable. Obtaining a resolution near the theoretical limit requires a fully optimized LEEH setup and workflow, for which in particular sample and emitter preparation are crucial.

Here, I present a novel LEEH microscope with a unique experimental workflow, which is capable of resolving molecular substructures with an unprecedented resolution for LEEH experiments. The newly constructed LEEH microscope takes advantage of an efficient vibration isolation system and is remote-controlled to minimize external perturbations. The setup is capable of low-temperature (50 K) measurements, which enhances the stability of the system. A reliable way for preparing highly coherent electron emitters constituted by sharp tungsten tips is presented along with different methods for improving their performance via functionalization and UHV treatments. I show an optimized and reliable substrate preparation protocol resulting in ultra-clean free-standing single-layer graphene (SLG) samples. Native electrospray ion beam deposition (ES-IBD) allows for the transfer of non-volatile molecules from solution into gas phase and onto the substrate. By employing a quadrupole mass selection, highly pure molecular ion beams are obtained, which are soft-landed onto the SLG substrate in a controlled and reproducible manner while retaining an intact structure.

This versatile preparation method allows us to study a great variety of molecules by LEEH. Data on proteins with masses ranging from 12 – 820 kDa reveal molecular shapes consistent with model structures. Locally, structural details as small as 5 Å were identified, thus we are approaching our goal of a resolution in the range of a few Å. The application of our methodology to flexible proteins, exemplified by antibodies, allowed for the imaging of their conformational variability and for determining the influence of the sample preparation on their structure. This gave us the possibility to directly image gas-phase related conformations.

Abstract

Data of compact molecular systems with masses below 3 kDa reveal that our LEEH microscope is able to investigate small molecules, such as porphyrines, at high imaging contrast.

The presented results indicate that an optimized LEEH setup and workflow in combination with ES-IBD is a versatile microscopy method, which is filling the gap between high-resolution and single-molecule techniques by elucidating structural details of various molecular species.

Keywords: Low-energy electron holography (LEEH), Cryogenic LEEH, Structural biology, Ultra-sharp tungsten tips, Ultra-clean single-layer graphene, Electrospray ion beam deposition (ES-IBD), Native ESI, Protein imaging

Zusammenfassung

Strukturbestimmungsmethoden sind ein essentielles Werkzeug zur Untersuchung von Molekülen und spielen insbesondere in der Biologie eine wichtige Rolle, in der Funktion und Struktur zusammenhängen. Während hochauflösende Methoden wie Transmissionselektronenmikroskopie und Röntgenbeugung auf der Mittelung von Molekül-Ensembles basieren und damit ungeeignet zur Erfassung struktureller Unterschiede von flexiblen Molekülen sind, haben gängige Einzelmolekülmessmethoden wie die Rastersondenmikroskopie Probleme mit der Abbildung von 3D-Objekten. Niederenergetische Elektronenholographie (LEEH) kann diese Hürden überwinden und ermöglichte bisher das Abbilden von einzelnen Molekülen mit einer Auflösung von 7 – 8 Å. Theoretisch könnten mit einer Auflösung von wenigen Angström atomare Details in Molekülen sichtbar werden. Um diese Auflösungen zu erreichen, benötigt man ein optimiertes LEEH-Mikroskop mit passendem Workflow, bei dem besonders die Proben- und Emitterpräparation entscheidend sind.

Hier stelle ich ein neues LEEH-Mikroskop mit einem einzigartigen experimentellen Workflow vor, welches Molekülstrukturen mit einer bisher für LEEH-Experimente unübertroffenen Auflösung abbildet. Das neukonstruierte Mikroskop ist fernsteuerbar und nutzt eine effiziente Vibrationsisolation um externe Störfaktoren zu minimieren. Das Setup ermöglicht Messungen bei niedrigen Temperaturen (50 K), was die Stabilität des Systems erhöht. Scharfe Wolframspitzen werden mittels eines zuverlässigen Präparationsprotokolls zu kohärenten Elektronenquellen, deren Emissionseigenschaften durch Funktionalisierung und UHV-Verfahren weiter verbessert werden können. Die Herstellung des Probensubstrats erfolgt durch ein optimiertes Verfahren und liefert hochreines und freistehendes einlagiges Graphen. Mittels nativer Elektrospray-Ionenstrahld deposition (ES-IBD) werden nicht-volatile Moleküle aus der Lösung über die Gasphase zum Substrat transferiert. Die Nutzung einer Quadrupol-Massenselektion ergibt hochreine Ionenstrahlen der gewünschten Molekülspezies, welche kontrolliert, reproduzierbar und sanft auf dem Substrat deponiert werden, wobei die Molekülstruktur intakt bleibt.

Durch diese flexible Präparationsmethode kann eine Vielzahl an Molekülen durch LEEH abgebildet werden. Die molekularen Umrisse der untersuchten Proteine im Massenbereich von 12 – 820 kDa können durch Strukturmodelle bestätigt werden, wobei lokale Strukturdetails mit bis zu 5 Å identifiziert wurden, was einer Auflösung von wenigen Angström sehr nahe kommt. Durch unsere Methode abgebildete, flexible Proteine, wie beispielsweise Antikörper, zeigen verschiedene Adsorptionskonformationen, welche Hinweise auf den Einfluss der Pro-

Zusammenfassung

benpräparation auf deren Struktur geben. Dies ermöglicht uns das direkte Abbilden von aus der Gasphase stammenden Konformationen. Unser LEEH-Mikroskop ermöglicht außerdem das kontrastreiche Abbilden von kleinen, kompakten Molekülen mit Massen unter 3 kDa, z.B. Porphyrine.

Diese Ergebnisse zeigen, dass die Kombination aus ES-IBD und optimierter LEEH-Mikroskopie eine vielseitige Methode zur Untersuchung von Strukturdetails verschiedenster Molekülarten ergibt, welche hochauflösende und Einzelmolekülmessmethoden verknüpft.

Stichwörter: Niederenergetische Elektronenholographie (LEEh), kryogene LEEh, Strukturbiologie, scharfe Wolframspitzen, hochreines einlagiges Graphen, Elektrospray-Ionenstrahld deposition (ES-IBD), native Elektrospray-Ionisierung, Proteinabbildung

Contents

Abstract (English/Deutsch)	i
List of Figures	ix
List of Tables	xiii
List of Acronyms	xv
1 Introduction	1
2 Theoretical Background	7
2.1 Hologram Reconstruction	7
2.2 Electron Beam Coherence	11
2.3 Microscope Resolution	14
3 Experimental Setup	19
3.1 LEEH Microscope	19
3.1.1 Vacuum System	20
3.1.2 Microscope	20
3.1.3 External Damping System	22
3.1.4 Internal Damping System	24
3.1.5 Sample Transfer and Storage	26
3.2 Cryoholography	26
3.3 Data Acquisition, Reconstruction and Analysis	31
3.4 Remote Microscope Control Software	33
3.5 FIM Setup	35
3.5.1 Internal FIM	38
3.5.2 External FIM	39
3.6 LEEH Workflow	40
4 Emitter Preparation and Characterization	45
4.1 Electrochemical Etching	46
4.2 UHV Preparation and Characterization	50
4.2.1 Annealing	51
4.2.2 Field Emission	53

Contents

4.2.2.1	Field Emission at Room Temperature	55
4.2.2.2	Field Emission at Cryogenic Temperatures	59
4.2.3	Self-Sputtering	61
4.2.4	Field Ion Microscopy Investigation of Emitters	64
4.2.5	Emitter Functionalization	67
4.2.5.1	Reactive Nitrogen Etching	68
4.2.5.2	CNT Uptake	70
4.2.5.3	SLG Uptake	72
4.2.6	Characterization of Emitters via LEEH	75
4.2.6.1	Comparison of Different Emitters at Room Temperature	76
4.2.6.2	Emitter Performance at Cryogenic Temperatures	79
4.2.6.3	Ghost Image Artifacts	81
5	Substrate Preparation and Characterization	83
5.1	Grid Preparation	84
5.2	Graphene Preparation and Characterization	85
5.2.1	SLG Preparation	86
5.2.2	SLG Characterization	87
5.2.2.1	Grid Coverage and SLG Identification	88
5.2.2.2	SLG Contamination during Preparation	88
5.2.2.3	AFM Measurements of Prepared Substrates	89
5.2.2.4	Electron Transmission through SLG and MLG	90
5.2.2.5	Moiré-Patterns on BLG	92
5.2.2.6	Charges and Clusters on SLG	92
5.2.2.7	SLG Characterization before Deposition	94
5.2.2.8	SLG Imaging at Cryogenic Temperatures	95
6	Deposition methods	97
6.1	Electrospray Ion Beam Deposition	97
6.1.1	Protein Sample Preparation	97
6.1.2	Native ES-IBD for Protein Systems	98
6.2	Thermal Evaporation	105
6.3	Drop-casting	106
7	Measurements of Deposited Molecule Systems	107
7.1	Globular Proteins	108
7.1.1	Cytochrome <i>c</i>	108
7.1.2	Myoglobin	111
7.1.3	Hemoglobin	113
7.1.4	Discussion on Globular Proteins	116
7.2	Large Protein Complexes	117
7.2.1	Transferrin	117
7.2.2	Alcohol Dehydrogenase	119

7.2.3	Beta-Galactosidase	123
7.2.4	GroEL	125
7.2.5	Discussion on Large Protein Complexes	128
7.3	Flexible Protein Complexes	129
7.3.1	MAdCAM-Fc Complex	129
7.3.2	Native-like Herceptin Antibodies	132
7.3.3	Denatured Herceptin Antibodies	138
7.3.4	Discussion on Flexible Protein Complexes	141
7.4	Compact Molecules of Reduced Dimensions	142
7.4.1	Hemin	142
7.4.2	Phosphotungstic Acid	144
7.4.3	Platinum Phthalocyanine	146
7.4.4	Discussion on Compact Molecule Systems	147
7.5	Proteins Measured at Cryogenic Temperatures	148
8	Conclusion	151
9	Outlook	153
9.1	Cryoholography	153
9.2	Compensation of Stray Magnetic Fields	154
9.3	Novel ESI Source	156
9.4	Phase Retrieval	157
9.5	3D Imaging	158
9.6	Measurable systems	159
A	Appendix	161
	Bibliography	167
	Acknowledgements	191
	Curriculum Vitae	195

List of Figures

2.1	Working principle of in-line holography.	8
2.2	Apodization filter intensity distribution.	10
2.3	Temporal and spatial coherence of a plane wave.	12
3.1	Overview of the LEEH microscope.	21
3.2	External damping of the LEEH setup.	22
3.3	Improvement of the external damping performance.	24
3.4	Internal damping of the LEEH microscope head.	25
3.5	UHV storage and transport options.	26
3.6	Overview images of the Cryo-LEEH setup.	27
3.7	Cooling performance of the Cryo-LEEH microscope head.	28
3.8	Close-up view of the Cryo-LEEH microscope head.	29
3.9	Basic principle of a MCP detector.	31
3.10	Graphic user interface of the LEEH setup.	34
3.11	FEM and FIM images of a tungsten tip measured by Erwin Müller (1951).	36
3.12	General principle of field ion microscopy.	37
3.13	Images of the internal FIM setup.	38
3.14	Images of the external FIM setup.	39
3.15	Experimental LEEH workflow.	41
3.16	SEM images of crashed emitters and LEEH image of a crashed substrate.	42
4.1	Tipholder of the LEEH setup.	47
4.2	Electrochemical emitter etching procedure.	48
4.3	SEM images of two electrochemically etched tips.	49
4.4	Emitter annealing and sputtering procedure in UHV.	50
4.5	SEM images of two heavily annealed tips at high magnifications.	52
4.6	Influence of an applied electric field on an electron at a metal surface.	54
4.7	Field emission and Fowler-Nordheim plots of several emitters.	57
4.8	Tip radii of tip characterized by field emission.	58
4.9	Field emission voltage measured for a retracted emitter at RT and LT.	60
4.10	Field emission voltage measured for an extended emitter at RT and LT.	61
4.11	Sputtering results of emitters.	63
4.12	FIM characterization of two single-crystal emitters.	65

List of Figures

4.13 Emitter radius estimation via ring-counting in FIM images.	66
4.14 FIM images of the functionalization process of a sc tip via nitrogen etching. . .	69
4.15 LEEH image using a tilted, nitrogen etched sc emitter.	70
4.16 Functionalization of a pc tip via CNT uptake.	71
4.17 Functionalization of <i>pc</i> and <i>sc</i> tips via SLG uptake.	73
4.18 FIM and SEM images of SLG functionalized <i>pc</i> and <i>sc</i> tips.	74
4.19 FIM images of compared sc emitters.	76
4.20 Free-standing CNT imaged in LEEH via the compared sc emitters.	77
4.21 Antibody molecule measured in LEEH via the compared sc emitters.	79
4.22 Free-standing CNT molecule measured with an sc emitter via LEEH at RT and LT. .	80
4.23 Ghost image artifacts during LEEH measurements.	81
5.1 Images of the sample holder and support grid.	85
5.2 SLG preparation process.	86
5.3 LEEH images of SLG covered and empty holes.	88
5.4 LEEH images of different SLG samples.	89
5.5 AFM images of prepared SLG substrates.	90
5.6 Electron transmission through graphene layers.	91
5.7 Moiré pattern of bilayer graphene.	92
5.8 Individual charges on SLG imaged via LEEH.	94
5.9 Characterization of SLG before and after molecule deposition.	95
5.10 Sample contamination during cooling without cooling shields.	96
6.1 Native ES-IBD workflow and mass selection example.	99
6.2 Electrospray ionization principle for a positive ion beam.	100
6.3 Quadrupole mass selection schematic.	102
6.4 Ion beam energy measurement before deposition.	103
7.1 Mass spectra of <i>native-like</i> cytochrome <i>c</i> before and after mass selection. . . .	109
7.2 LEEH images of <i>native-like</i> cytochrome <i>c</i> deposited on SLG.	110
7.3 Mass spectra of <i>native-like</i> myoglobin before and after mass selection.	111
7.4 LEEH images of <i>native-like</i> myoglobin deposited on SLG.	112
7.5 Mass spectra of <i>native-like</i> hemoglobin before and after mass selection.	114
7.6 LEEH images of <i>native-like</i> hemoglobin deposited on SLG.	115
7.7 AFM images of <i>native-like</i> hemoglobin deposited on HOPG.	116
7.8 Mass spectra of <i>native-like</i> transferrin before and after mass selection.	118
7.9 LEEH images of <i>native-like</i> transferrin deposited on SLG.	119
7.10 Mass spectra of <i>native-like</i> alcohol dehydrogenase before and after mass selec- tion.	120
7.11 LEEH images of <i>native-like</i> alcohol dehydrogenase deposited on SLG.	121
7.12 AFM images of <i>native-like</i> alcohol dehydrogenase deposited on HOPG.	122
7.13 Mass spectra of <i>native-like</i> beta-galactosidase before and after mass selection. .	123
7.14 LEEH images of <i>native-like</i> beta-galactosidase deposited on SLG.	124

7.15	Mass spectra of <i>native-like</i> GroEL before and after mass selection.	126
7.16	LEEH images of <i>native-like</i> GroEL deposited on SLG.	127
7.17	AFM images of <i>native-like</i> GroEL deposited on HOPG.	128
7.18	Mass spectra of <i>native-like</i> MAdCAM-Fc complex before and after mass selection.	130
7.19	LEEH images of <i>native-like</i> MAdCAM-Fc complex deposited on SLG.	131
7.20	Mass spectra of <i>native-like</i> Herceptin antibodies before and after mass selection.	132
7.21	AB model structures showing possible adsorption geometries.	133
7.22	LEEH images of <i>native-like</i> antibodies deposited on SLG showing three lobes.	134
7.23	LEEH images of <i>native-like</i> antibodies deposited on SLG showing two lobes.	135
7.24	LEEH images of <i>native-like</i> antibodies deposited on SLG showing collapsed structures.	136
7.25	AFM images of <i>native-like</i> antibodies deposited on HOPG.	138
7.26	Mass spectra of denatured Herceptin antibodies before and after mass selection.	139
7.27	LEEH images of denatured antibodies deposited on SLG.	140
7.28	AFM images of denatured antibodies deposited on HOPG.	141
7.29	Molecular structures of hemin, PTA and PtPc.	142
7.30	Mass spectra of hemin before and after mass selection.	143
7.31	LEEH images of hemin clusters deposited on SLG.	144
7.32	Mass spectra of phosphotungstic acid before and after mass selection.	145
7.33	LEEH images of phosphotungstic acid clusters deposited on SLG.	145
7.34	LEEH images of platinum phthalocyanine clusters deposited on SLG.	147
7.35	LEEH images of <i>native-like</i> beta-galactosidase measured at 50 K.	148
7.36	LEEH images of <i>native-like</i> GroEL measured at 50 K.	149
9.1	Schematic showing the cooling shields for the Cryo-LEEH system.	154
9.2	Schematic showing the positions of the planned Helmholtz coils.	156
9.3	Schematic showing the planned mobile ESI connected to the LEEH setup.	157
9.4	Phase reconstructions of <i>native-like</i> hemoglobin imaged via LEEH.	158
9.5	Image of the rotational stage used for tomographic experiments.	159
A.1	Non-compressed image of the CNT measured via <i>sc1</i>	161
A.2	Non-compressed image of the CNT measured via <i>sc2</i>	162
A.3	Non-compressed image of the CNT measured via <i>sc3</i>	163
A.4	Non-compressed image of the CNT measured at RT.	164
A.5	Non-compressed image of the CNT measured at LT.	165

List of Tables

2.1	Theoretical resolution limits of our LEEH setup for different emission voltages.	15
4.1	Comparison of the emitter radii measured via field emission and SEM.	57
4.2	Voltage stability analysis of a sc emitter.	60
4.3	Measured and calculated properties of the compared sc emitters.	78
4.4	Measured and calculated properties of an sc emitter used at RT and LT.	79
5.1	Metal coating procedure of SiN grids via sputter coating.	84
5.2	Heating procedure for PMMA removal via platinum catalysis.	87
7.1	ESI parameters for a <i>native-like</i> cytochrome <i>c</i> ion beam.	109
7.2	ESI parameters for a <i>native-like</i> myoglobin ion beam.	111
7.3	ESI parameters for a <i>native-like</i> hemoglobin ion beam.	113
7.4	ESI parameters for a <i>native-like</i> transferrin ion beam.	117
7.5	ESI parameters for a <i>native-like</i> alcohol dehydrogenase ion beam.	120
7.6	ESI parameters for a <i>native-like</i> beta-galactosidase ion beam.	123
7.7	ESI parameters for a <i>native-like</i> GroEL ion beam.	125
7.8	ESI parameters for a MAdCAM-Fc ion beam.	129
7.9	ESI parameters for a <i>native-like</i> Herceptin antibody ion beam.	132
7.10	ESI parameters for a denatured Herceptin antibody ion beam.	139
7.11	ESI parameters for a hemin ion beam.	143
7.12	ESI parameters for a phosphotungstic acid ion beam.	144

List of Acronyms

2D	—	Two Dimensional
3D	—	Three Dimensional
AB	—	(Herceptin) Antibody
AC	—	Alternating Current
ADH	—	Alcohol Dehydrogenase
AFM	—	Atomic Force Microscope
AmAc	—	Ammonium Acetate
APS	—	Ammoniumpersulfate
bcc	—	Body-centred Cubic
BLG	—	Bilayer Graphene
β Gal	—	Beta-Galactosidase
CNT	—	Carbon Nanotube
CVD	—	Chemical Vapor Deposition
Cryo-LEEH	—	Cryogenic LEEH
Cryo-EM	—	Cryogenic Electron Microscopy
CVD	—	Chemical Vapour Deposition
CytC	—	Cytochrome <i>c</i>
DC	—	Direct Current
ESI	—	Electrospray Ionization
ES-IBD	—	Electrospray Ion-Beam Deposition
FEM	—	Field Emission Microscope
FIM	—	Field Ion Microscope
FTLL	—	Fast Transfer Load Lock
GUI	—	Graphic User Interface
Hb	—	Hemoglobin
HOPG	—	Highly Oriented Pyrolytic Graphite
IgG	—	Immunoglobulin G
IGP	—	Ion Getter Pump
LEEH	—	Low-Energy Electron Holography
LEEP	—	Low-Energy Electron Projection Microscopy
LT	—	Low Temperature (< 100 K)

List of Acronyms

MBE	—	Molecular Beam Epitaxy
MCP	—	Microchannel Plate
MLG	—	Multilayered Graphene
MS	—	Mass Spectrometry
Myo	—	Myoglobin
NMR	—	Nuclear Magnetic Resonance Spectroscopy
OMBE	—	Organic MBE
<i>pc</i>	—	Polycrystalline
PDB	—	Protein Data Bank
PMMA	—	Polymethylmethacrylate
PTA	—	Phosphotungstic Acid
PtPc	—	Platinum(II) Phthalocyanine
QMS	—	Quadrupole Mass Selection
RF	—	Radio Frequency
RT	—	Room Temperature ($\sim 294 - 300$ K)
<i>sc</i>	—	Single-crystal
SCLL	—	Suitcase Load Lock
SEM	—	Scanning Electron Microscope
SiN	—	Silicon Nitride
SLG	—	Single-layer Graphene
SNR	—	Signal-to-Noise Ratio
STED	—	Stimulated Emission Depletion Microscopy
STM	—	Scanning Tunneling Microscope
TEM	—	Transmission Electron Microscope
Tf	—	Transferrin
ToF	—	Time-of-Flight
UHV	—	Ultra-high Vacuum
XRD	—	X-ray Diffraction Crystallography

1 Introduction

Microscopy opens the door to our understanding of the microscopic, nanoscopic and atomic world as it gives us an intuitive image of the relation between structure and properties of molecules, materials and organisms [1]. The need to resolve an increasing amount of structural details drives the continuous development and improvement of microscopy techniques. This is demonstrated by the evolution of the basic optical microscope, which is still a standard tool for the investigation of objects in the micron range such as cells, towards super-resolution microscopy like spinning disc confocal microscopy [2][3][4] and stimulated emission depletion (STED) microscopy [5][6][7]. In STED, the positions and interactions of single molecules can be imaged by timed activation and repression of fluorescence signals from marker molecules, which was awarded with the Nobel Prize for S. Hell, E. Betzig and W. Moerner in 2014 [8]. However, since light-based microscopy techniques are ultimately limited in their performance due to the wavelengths of light and aberrations originating from the used lens systems, the necessary resolution for the structure determination of individual molecules has yet to be achieved by these methods.

Alternative techniques such as scanning probe microscopes, which were invented by G. Binnig, C. Gerber and H. Rohrer, offer approaches for the investigation of atomic layers on surfaces [9], while electron microscopy, which was initially developed by E. Ruska, enables non-contact imaging of structures at atomic resolution due to the small wavelengths of the used electrons [10]. The impact of these methods on the structure determination of materials, surfaces and molecules was awarded with a shared Nobel Prize in 1986 [11][12][13]. Furthermore, unraveling molecular structures of biologically relevant systems, such as protein complexes, by structural averaging via cryogenic electron microscopy (Cryo-EM) showed that high-resolution imaging of delicate biological molecules is achievable, which led to a shared Nobel Prize for J. Dubochet, J. Frank and R. Henderson in 2017 [14][15][16]. Another approach laying the foundation for lens-free transmission electron microscopy (TEM) is the point projection microscope developed by G. A. Morton in 1939. In these microscopes, an electron-emitting source is placed at a close distance in front of a sample constituted by partially transparent sections. The electrons transmitted through the object are collected by a detector, which is

placed behind the sample, and captures the image projected by the sample [17], whereby the achievable magnification of these microscopes is based on geometrical factors related to a spherical electron emission.

The discovery of electron waves via the Davisson-Germer experiment in 1927 led to the conclusion that electrons can interfere with each other [18]. Considering the wave nature of emitted electrons, D. Gabor invented in-line holography in 1948 by utilizing the principles of point projection microscopy to circumvent lens aberrations occurring in conventional TEMs, which were a crucial limiting factor for TEM resolution at that time [19][20]. The intensity of the interference patterns between the object wave, which is the wave that is scattered by the object to be investigated, and the reference wave, which is transmitted from the source through the sample and subsequently to the detector without being scattered, are known as holograms (see Sec. 2.1, Fig. 2.1) [19]. In this way, the structural information of the object is encoded in the complex field of the hologram, which contains both amplitude and phase signals, and can be recovered by an image reconstruction process [20][21].

Gabor himself experimentally proved the holography principle using light for both creating the hologram and its reconstruction. However, the diffuse background, which resulted from a phase ambiguity problem [19], already indicated the necessity to recover not only the amplitude but also the phase of the complex field, which generates the hologram intensity, for a clear view of the object. After this first proof of concept using light, it took several decades before electron holography, i.e. holograms acquired using coherent electron beams, would become available, because the emitting sources lacked emission brightness and coherence for the formation of high-quality holograms [21]. Furthermore, methods for accurate positioning of the emitter with respect to the sample in the nanometer range, which is a vital requirement for high magnification images, had yet to be introduced [22].

The development of ion emitters for the use in field ion projection microscopy significantly improved the quality of the electron sources [23][24]. This led to the development of low-energy electron projection microscopy (LEEP) by W. Stocker and H.-W. Fink, which was a fundamental step towards the low-energy electron holography (LEEH) method [25]. By using atomically sharp tungsten tip emitters showing high brightness and coherence, it was possible to obtain projection images and holograms of free-standing carbon fibers, which were suspended across the holes of perforated substrates (TEM grids) [26]. In these experiments, the relative tip-to-sample position was varied via piezoelectric actuators, following the design used for scanning probe microscopy [27]. The sample was imaged either in projection or holography mode depending on the emitter-to-sample distance [25][28]. Furthermore, the low emission energies of the emitted electrons in the range of 20 – 300 V yielded a high imaging contrast and no observable radiation damage of the sample, when compared to other techniques with higher energetic imaging beams [26].

Due to the advancements in computing power, in 1992 H. J. Kreuzer et al. introduced a numerical reconstruction method based on Fourier-like transforms, which overcame the

difficulties related to the optical reconstruction envisioned by Gabor [29]. Both theory and experimental design were further improved in the following years, which resulted in a detailed understanding of the imaging process [30][31][32] and led to the first imaging experiments of biomolecules [33][34][35]. Despite these developments, the method was still restricted to the investigation of freely suspended molecular structures and objects on support grids. This limitation is imposed by the small penetration depth of low-energy electrons, which hampers the use of traditional substrates such as TEM grids coated with lacey carbon [36]. The lack of a proper substrate acting as an equipotential plane results in the charging of the suspended molecules during measuring, which consequently exhibit an electric field and therefore act as a biprism [37]. Especially at closer emitter-to-sample distances below $5\text{ }\mu\text{m}$, the biprism effect dominates the holographic effect [38][39], thus leading to difficulties in properly interpreting the measured data, which diminished credibility and general interest in the technique for another decade.

After the discovery of graphene in 2004 by A. K. Geim and K. S. Novoselov [40], J. Y. Mutus et al. showed that it was possible to use this novel 2D material as a substrate for LEEP and holography experiments [41]. Indeed, graphene shows a high transmissibility for both high-energy [42] and low-energy electrons [41], acts as an equipotential plane preventing charging effects of the sample molecules during imaging [37][41], has a high mechanical stability [43], and shows inert behaviour towards most molecules [44][45]. All these properties are ideal for a LEEP substrate, and also graphene itself was an object of investigation by both LEEP and LEEH [36] [46]. The first deposited specimens, such as gold nanorods [47] and tobacco mosaic virions [45], were drop-casted, which provided an easy and fast deposition method, but at the cost of sample purity and control over the amount of deposited molecules. These issues could be resolved by using (native) electrospray ion beam deposition (ES-IBD) as preparative sample deposition method [48][49][50]. Combining ES-IBD and LEEH enables a full control over the deposition and imaging of various, even non-volatile molecule systems, such as proteins, which were investigated on the single-molecule level at maximum resolutions in the range of $7 - 8\text{ }\text{\AA}$ [51].

These experiments show that LEEH is a viable method for measuring single biological specimen when compared to conventional single-molecule measurement methods, such as scanning probe techniques. While atomic force microscopy (AFM) and scanning tunneling microscopy (STM) are precise methods for the investigation of rigid and flat molecules, the acquisition of high-resolution images of three-dimensional (3D) structures like proteins can be challenging. The 3D nature of these molecules leads to the observation of undesired tip-molecule interactions and effectively reduces the resolution of scanning probe methods [52][53][54]. AFM studies on large protein complexes, which can even take place in solution, are commonly used to investigate their shape, adsorption behaviour, (force) interactions, molecular reactivity, and dynamics [55][56][57][58][59], but rarely yield imaging resolutions below $10\text{ }\text{\AA}$.

On the other hand, high-resolution structure determination techniques, such as Cryo-EM

[14][60][61][62], X-ray diffraction crystallography (XRD) [63][64], and nuclear magnetic resonance spectroscopy (NMR) [65][66], which are capable of providing structural detail of large 3D molecules on the atomic scale, are ensemble averaging methods. This impedes the proper investigation of conformational variability of flexible structures [51], which is of relevance for many biomolecules. Furthermore, the high energies used in traditional TEM methods can lead to undesired alterations of the original molecular structure or even destroy the sample during the measurement [67][68][69]. For delicate and flexible molecule systems, where the application of these techniques is challenging, LEEH can act as an alternative non-destructive, single-molecule imaging technique with the potential to provide relevant structural information.

In the light of this, LEEH at resolutions below 3 Å would offer a completely new approach towards the investigation of large 3D molecules. Thus, the goal of this thesis is the construction, testing and establishing of a new LEEH microscope setup with a reliable experimental workflow routine, which is capable of imaging different types of proteins and other molecules, while aiming to approach the experimental resolution limit of the method. The idea of the approach is to use an in-line holography setup, where emitter, sample and detector are on the same optical axis, as originally envisioned by D. Gabor. To achieve this goal, several challenges have to be overcome. First, a noise-free instrument has to be constructed, which also enables measurements at ultra-high vacuum (UHV) conditions to prevent sample contamination and offers a sufficient sample magnification. Installing an additional cooling system is useful to reduce molecular vibrations of the sample [70][71] and can improve the emission properties of the emitters [72]. Second, the emitters have to be highly coherent low-energy electron sources to allow for the formation of high-quality holograms during imaging [28]. For this reason, we need to establish suitable preparation and characterization protocols, e.g. by using field ion microscopy (FIM). Third, regarding the sample preparation, a clean and stable substrate is necessary, which is also transparent for low-energy electrons. Free-standing single-layer graphene (SLG) has been shown to fulfill these criteria [41]. Especially for the investigation of proteins, a clean and delicate molecule deposition method is necessary to ensure imaging of the desired folded molecule species. ES-IBD serves as a non-destructive deposition technique for the controlled soft-landing of highly pure protein ions and other molecules on our substrate [51]. Finally, a reconstruction algorithm is needed to retrieve the image of the measured molecule from the acquired hologram [73].

The necessary theoretical basics are explained in chapter 2, focusing on the hologram reconstruction, electron coherence and achievable resolution limits. The experimental setup is presented in detail in chapter 3, containing information about the LEEH microscope, the experimental workflow and the newly added Cryo-LEE system, which allows for measurements at cryogenic temperatures. In chapter 4, the used emitter preparation, functionalization and characterization methods are presented, which yield ultra-sharp and highly coherent low-energy electron sources. A reliable and optimized substrate and SLG preparation protocol is shown in chapter 5. The prepared substrates contain ultra-clean free-standing SLG, which

is characterized in detail by LEEH. The used deposition methods are presented in chapter 6 and include native ES-IBD, which was the primarily used deposition technique, thermal evaporation and drop-casting. Chapter 7 contains the measured and analyzed results of various measured molecules, such as different types of protein complexes and small functional molecules, and first LEEH measurements of proteins at cryogenic temperatures. A short conclusion is presented in chapter 8 and future projects are shown in chapter 9.

The presented data shows that our novel LEEH microscope, in combination with the optimized emitter and substrate preparation protocols, and ES-IBD as a delicate and pure sample preparation method, enables measurements of diverse molecular systems including individual folded protein species. With the identification of molecular features as small as 5 Å [74], our unique technique offers the investigation of biologically relevant 3D molecules on a true single-molecule scale and with a resolution limit that can, in principle, reach the atomic scale [22][51], which closes the gap between high-resolution and single-molecule imaging.

2 Theoretical Background

This chapter contains the basic theoretical background on the formation and reconstruction of holograms (Sec. 2.1), the characteristics of coherent electron beams (Sec. 2.2), and the estimated resolution limits achievable by LEEH microscopy (Sec. 2.3).

2.1 Hologram Reconstruction

The original idea of Dennis Gabor was the development of a high-resolution transmission electron microscope using a lens-free imaging concept, called in-line holography, in order to circumvent the resolution-limiting factor of lens aberrations. For this original idea, Gabor was awarded with the Nobel Prize in 1971. The technique takes advantage of the wave nature of electron beams and relies on the interference of a primary reference wave ψ_{Ref} with a scattered object wave ψ_{Obj} [19]. Fig. 2.1 shows the basic principle for in-line electron holography. In in-line holography, the initial reference wavefront travels through a transparent substrate supporting the sample that partially diffracts the original reference wave and generates the so called object wave. The object wave propagates further beyond the sample and interacts with parts of the reference wave, which did not interact with the sample. This superposition of the two waves is called exit wave and contains amplitude and phase information of the imaged specimen [20]. The modulus squared of this complex wave field is called hologram and is experimentally recorded with a detector at a position far behind the sample. When utilizing a point source emitter, the reference wave is a spherical electron wave. For this reason, the hologram of the imaged object appears on the detector with a magnification factor that depends on the emitter-to-sample distance z and emitter-to-detector distance $z + Z$, without the auxiliary use of lenses [19][21]. Thus, the magnification factor can be tuned by varying z or Z . It is important to note that the captured hologram in itself does not yield an interpretable image, but has to be reconstructed to reveal information about the object. In Gabor's experiments, the images were reconstructed using an optical setup, while nowadays, the computational power at our disposal allows for image reconstruction via dedicated algorithms [75].

Chapter 2. Theoretical Background

The goal of the following theoretical description is to provide a mathematical expression for the hologram recorded at the detector plane and to define a reconstruction algorithm capable of retrieving the exit wave at the object plane and, as such, recovering the object image. This is accomplished by directly solving the Fresnel integral of the imaged hologram or, in order to make the process less computational demanding, by introducing a few approximations. An efficient way to write the reconstruction function was presented by T. Latychevskaia in 2015 [73] and is shortly summarized in the following.

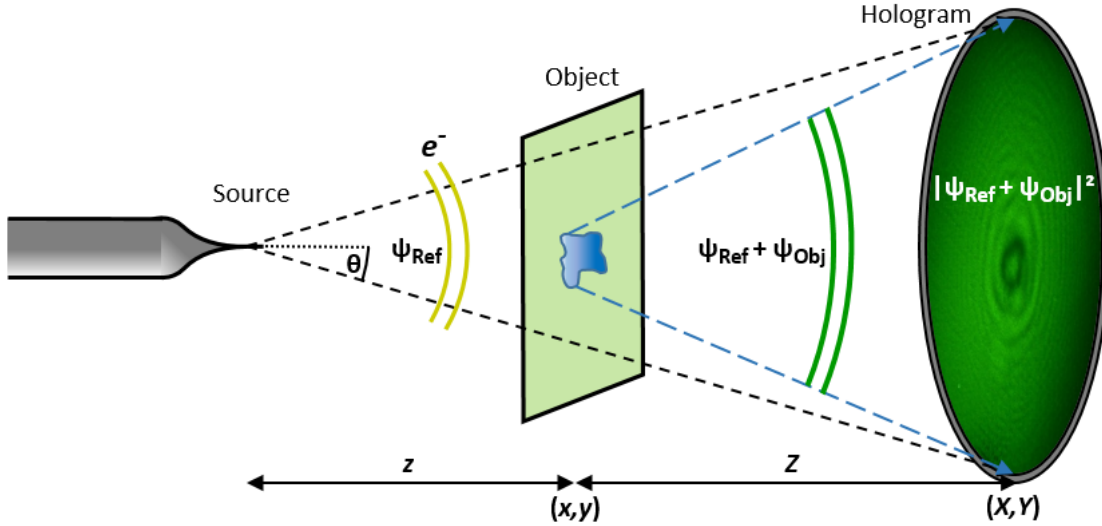


Figure 2.1: Scheme of the in-line holography working principle. The initial electron wave ψ_{Ref} , which has a beam opening angle of θ , propagates through the sample (x, y, z) towards the detector (X, Y, Z) creating a hologram due to the interference of reference wave ψ_{Ref} and object wave ψ_{Obj} .

The exit wave $U_{\text{Exit}}(x, y) = \psi_{\text{Ref}}(x, y) + \psi_{\text{Obj}}(x, y)$ can be described by using an incident wave $U_{\text{In}}(x, y)$ and a transmission function for the object $t(x, y) = \exp(-a(x, y)) \exp(i\phi(x, y))$, with the absorbance $a(x, y)$ and phase distribution $\phi(x, y)$ of the wave scattered by the object. With the transmission function being $t(x, y) = 1$ for full transmission (i.e. no object or $a = \phi = 0$), one can deduce $t(x, y) = 1 + \tilde{t}(x, y)$, with $\tilde{t}(x, y)$ being the perturbation of the reference wave upon scattering. This leads to equation 2.1, which describes the general exit wave front and separates the reference and object wave terms[73]:

$$U_{\text{Exit}}(x, y) = U_{\text{In}}(x, y) \cdot t(x, y) = U_{\text{In}}(x, y) \cdot (1 + \tilde{t}(x, y)) \quad (2.1)$$

For a spherical incident wave $U_{\text{In}}(x, y) = \frac{\exp(ikr)}{r}$ with $k = 2\pi/\lambda$ and small beam opening angles for the wave parts scattered by the object, the propagated exit wave reaching the detector at position (X, Y) can be approximated using the Fresnel-Kirchhoff diffraction formula. In this way, it is possible to use a propagator of the form $\frac{\exp(ik|\vec{r} - \vec{R}|)}{|\vec{r} - \vec{R}|}$, where $|\vec{r} - \vec{R}|$ is the distance between the object position $\vec{r} = (x, y, z)$ and detector position $\vec{R} = (X, Y, Z)$, as shown in equation 2.2 [76]:

$$U_{\text{Det}}(X, Y) = -\frac{i}{\lambda} \iint t(x, y) U_{\text{In}}(x, y) \frac{e^{(ik|\vec{r}-\vec{R}|)}}{|\vec{r}-\vec{R}|} dx dy = -\frac{i}{\lambda} \iint t(x, y) \frac{e^{ikr}}{r} \frac{e^{(ik|\vec{r}-\vec{R}|)}}{|\vec{r}-\vec{R}|} dx dy \quad (2.2)$$

For small beam opening angles θ (see Fig. 2.1), $|\vec{r}-\vec{R}| = \sqrt{(x-X)^2 + (y-Y)^2 + (z-Z)^2}$ can be simplified by the paraxial approximation as $r \approx z + (x^2 + y^2)/(2z)$ and $|\vec{r}-\vec{R}| \approx Z + ((x-X)^2 + (y-Y)^2)/(2Z)$. Since $z \ll Z$, the expression for U_{Det} can be further simplified to [76][73]:

$$U_{\text{Det}}(X, Y) = -\frac{i}{\lambda z Z} e^{\left(\frac{2\pi i}{\lambda}(Z+z)\right)} e^{\left(\frac{\pi i}{\lambda Z}(X^2+Y^2)\right)} \iint t(x, y) e^{\left(\frac{\pi i}{\lambda z}(x^2+y^2)\right)} e^{\left(-\frac{2\pi i}{\lambda Z}(xX+yY)\right)} dx dy \quad (2.3)$$

This expression has the form of a Fourier transform, which can be rewritten as a convolution to simplify the numerical reconstruction in the form $f * g(t) = \int_{-\infty}^{\infty} f(\tau) g(t-\tau) d\tau$ with $*$ being the convolution operator. Furthermore, the constant term $\frac{e^{\dots}}{\lambda z Z} = C$ can be neglected, and x and y can be separated leading to the final form of the convolution with the Fresnel function $s(x, y) = \exp\left(\frac{\pi i}{\lambda z}(x^2 + y^2)\right)$ [73]:

$$U_{\text{Det}}(X, Y) = -iC \iint t(x, y) e^{\left(\frac{\pi i}{\lambda z}\left(x+X\frac{z}{Z}\right)^2 + \left(y-Y\frac{z}{Z}\right)^2\right)} dx dy = t * s(X, Y) \quad (2.4)$$

Using equation 2.4, the hologram can be expressed as the squared modulus of the complex wave field at the detector:

$$H(X, Y) = |U_{\text{Det}}(X, Y)|^2 = |t * s(X, Y)|^2 \quad (2.5)$$

By propagating the wave backwards from the detector towards the object, one can integrate over the detector plane (X, Y) and replace the transmission function $t(x, y)$ with the hologram $H(X, Y)$ from equation 2.5, which yields the reconstructed exit wave [73]:

$$U_{\text{Exit}}(x, y) \approx -\frac{i}{\lambda} \iint H(X, Y) \frac{e^{ikr}}{r} \frac{e^{-(ik|\vec{r}-\vec{R}|)}}{|\vec{r}-\vec{R}|} dX dY \quad (2.6)$$

Since the hologram H is only real-valued while the transmission function t is complex, this expression for U_{Exit} is lacking the absolute phase information and therefore does not represent the complete reconstruction and is not fully accurate [77]. However, the reconstruction algorithm as described above is a good approximation for the object amplitude and can easily be implemented in an algorithm to numerically calculate the reconstructed object from the

Chapter 2. Theoretical Background

measured hologram [78][73].

The basic steps of an algorithm solving for the exit wave can be described with a series of (inverse) Fourier transforms (\mathfrak{F}), which can be applied to the hologram images (H) recorded on the detector, where $R(X, Y) = \exp(ikR)/R$ is the unscattered reference wave hitting the detector:

1. Calculate the Fourier transform of $(H \cdot R)$.
2. Calculate the Fourier transform of Fresnel function s .
3. Calculate the product of step 1 and 2.
4. Calculate the inverse Fourier transform of the product from step 3.

This can be summarized as: $U_{\text{Exit}} = \mathfrak{F}^{-1}(\mathfrak{F}(H \cdot R) \cdot \mathfrak{F}(s))$. Further possibilities to improve the quality of the reconstructed images include a background normalization, which can be simulated or measured, and an apodisation cosine filter $C(\rho)$ with $\rho = \sqrt{X^2 + Y^2}$, which removes image artifacts originating from the sharp detector edges, and is described via [73]:

$$C(\rho) = \begin{cases} \cos^2\left(\frac{\pi}{2\omega}(\rho - \eta)\right), & \eta < \rho < \eta + \omega \\ 1, & 0 < \rho < \eta \\ 0, & \rho > \eta + \omega \end{cases} \quad (2.7)$$

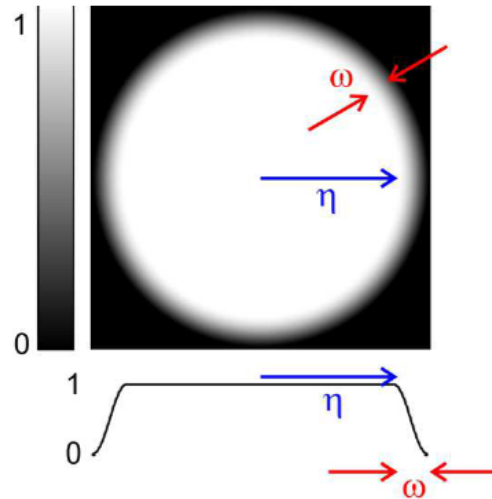


Figure 2.2: Intensity distribution for the apodization filter used in the reconstruction algorithm as shown in [73]. η is the region from the center of the detector screen almost up to the edge, ω is a short region bridging the end of η and the edge, smoothening the intensity distribution.

The respective regions for η and ω are shown in Fig. 2.2, which was illustrated by T. Latychevskaia [73]. The use of this filter smoothens the intensity drop at the detector edges allowing for an artifact reduced reconstruction of the object. With these elements, it is possible to program a reliable algorithm for the reconstruction of measured holograms, which is based on the work of T. Latychevskaia [73].

Here it is important to mention that the reconstruction algorithm used for our LEEH experiments was programmed, optimized and further developed in the course of the PhD thesis of my colleague Hannah Ochner (thesis title: *‘Amplitude and phase reconstruction for Low Energy Electron Holography of individual proteins’* [79]), who also reconstructed all the holograms shown in this work. Additionally, the currently utilized algorithm contains an effective background subtraction function, a noise filter for artifact signals generated by the detector, and a focus finder tool. Furthermore, we are working on an iterative phase reconstruction algorithm to recover the phase information of the imaged objects (see Sec. 9.4).

2.2 Electron Beam Coherence

The possibility for electromagnetic waves, such as light or electron beams, to interact with themselves leads to constructive and destructive interference depending on their relative phase. The extent of a well-defined phase relation is described by coherence, where a fully coherent beam leads to an interference signal of the waves $I_{\text{coherent}} = |\Psi_1 + \Psi_2|^2$, whereas an incoherent beam is only defined by the intensities of the waves $I_{\text{incoherent}} = |\Psi_1|^2 + |\Psi_2|^2$. If wavelength and phase relation are identical for two interfering waves, their superposition results in a coherent stationary wave, which is constant in energy dispersion ΔE (temporal coherence) and emission source position Δr (spatial coherence) [80][81]. In holography, interference and projection of the reference and scattered waves are important, thus a high or even full coherence is necessary [20]. However, in reality most waves show only partially coherent or even incoherent properties (see Fig. 2.3), which originates from several reasons affecting their temporal and/or spatial coherence and is explained in the following [82][81].

Full temporal coherence requires a monochromatic source, which is constant over time. However, the assumption of a perfectly monochromatic and point-like electron source can only be used in theory, since every emitter has a finite size and shows polychromatic emission over time [83]. If the wavelength changes, the coherence time τ_c must be finite and decreases proportionally to an increasing frequency spread Δf with $\tau_c = \Delta f^{-1}$ as shown for a plane wave in Fig. 2.3 **b** [84][81]. This frequency spread affects the coherence along the propagation direction \vec{k} and is related to the energy dispersion ΔE of the beam via the uncertainty relation $\tau_c = \frac{\hbar}{\Delta E}$ [85]. It implies that two waves, which have slightly varying wavelengths λ and $\lambda - \Delta\lambda$ and are simultaneously emitted from the same source, will be out of phase after a certain distance ℓ and again in phase after a distance of 2ℓ . With this, the temporal coherence can be expressed by the longitudinal coherence length $\ell_c = \frac{\lambda^2}{2\Delta\lambda}$, where λ is the wavelength and $\Delta\lambda$ is the wavelength spread [30][86]. This relation directly shows, that the longitudinal coherence

Chapter 2. Theoretical Background

length ℓ_c , and thus the coherence time τ_c , decreases for an increasing spread in wavelength (energy).

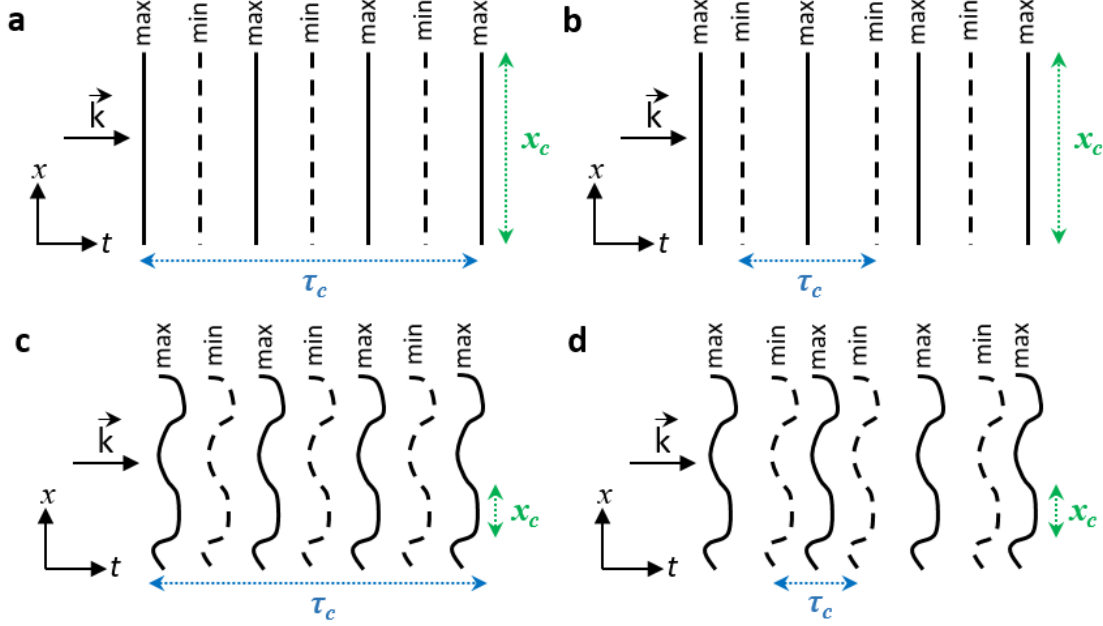


Figure 2.3: Sketch showing the temporal and spatial coherence of a plane wave. **a** Temporally and spatially coherent wave with long coherence time τ_c (labeled blue) and large transverse coherence length x_c (labeled green). **b** Spatially coherent and temporally incoherent wave with a short coherence time. **c** Temporally coherent and spatially incoherent wave with a small transverse coherence length. **d** Temporally and spatially incoherent wave with short transverse coherence length and time.

Full spatial coherence of a spherical wave would require a perfect point source ($\Delta r = 0$), which cannot be fulfilled in reality since each electron source has a finite size. The spatial coherence length x_c is defined by the transverse distance over which the wave front remains flat in respect to the source, as shown for a plane wave in Fig. 2.3 [83]. For a spherical source with a finite radius r , x_c decreases if two waves, which can have identical wavelengths, are expanding from different positions of the source. The varying emission angles affect the superposition of the waves leading to a reduced contrast of the interference pattern, which is comparable to the results found in a double slit experiment [80][81]. For small angles and a source-to-detector distance Z , the transverse coherence length is $x_c = \frac{\lambda Z}{r}$. By assuming a partially coherent Gaussian source, the effective source size can be derived from the van Cittert-Zernike theorem as $r_{\text{eff}} = \frac{\lambda Z}{\pi x_c}$ [30][87]. Furthermore, it is important to mention that the transverse coherence length is not restricted to one dimension, but can be defined as a coherence area [80][85]:

$$A_c = \pi r_{\text{eff}}^2 = \frac{\lambda^2 Z^2}{\pi x_c^2} \quad (2.8)$$

For a hologram, both r_{eff} and A_c can be calculated from the coherence angle $\theta_c = \tan^{-1} \left(\frac{w_{\text{Holo}}}{2Z} \right)$,

where w_{Holo} is the visible width of the hologram pattern on the detector. For small angles, this leads to $r_{\text{eff}} = \frac{2\lambda Z}{\pi w_{\text{Holo}}}$, which can also be used as an estimation for the obtainable resolution, and shows that the transverse coherence length x_c can be approximated with half the hologram width [30][39]. For a (partially) coherent emitter, $r_{\text{eff}} < r_{\text{geom}}$ applies, with r_{geom} being the geometric source size, and the effective source, also called virtual source, can be defined as the minimal area within the emitter, where the backpropagated electron trajectories would meet [72][88]. Even for emitters with a geometric source size of several nanometers, the virtual source size can be within the low angstrom range, especially if the hologram width is large, which indicates a high coherence [72][89]. Thus, the spatial coherence strongly depends on the effective source size r_{eff} of the emitter. Furthermore, mechanical vibrations acting on the emitter directly increase the effective source size, which results in an additional reduction of the spatial coherence [30][39].

The spatial coherence can be estimated via LEEH by imaging thin free-standing objects, such as suspended carbon nanotubes (CNTs) on a holey array [38][39][72][90]. Based on the biprism effect, where a charged object divides the incoming electron reference wave into two waves, this evaluation leads to the formation of a Fresnel diffraction pattern on the detector [39][91][92]. While these holograms cannot be reconstructed properly to yield structural features of the scattering CNTs due to the charging effects [93], the measured hologram width w_{Holo} can be used to calculate the effective source size r_{eff} . Another method for the quantification of degree of coherence is the calculation of the visibility contrast [72][90]:

$$C_{\text{vis}} = \frac{I_{\text{max}} - I_{\text{min}}}{I_{\text{max}} + I_{\text{min}}} \quad (2.9)$$

Here, the highest intensity signal I_{max} is compared to the lowest neighbouring intensity signal I_{min} . For the ideal case of a monochromatic wave with a uniform intensity distribution along the lateral direction, which can be defined as perfect coherence, $C_{\text{vis}} = 1$ would apply. However, the discussed energy spread of the source, finite source size, and mechanical vibrations reduce the obtainable visibility contrast. Additionally, inelastic scattering at the object and the rapid intensity decay of a Gaussian beam away from the beam center further decrease C_{vis} [90][94]. Common values are in the range of 0.5 – 0.7, but also higher values up to 0.78 are reported for specifically functionalized emitters [90]. A possibility to increase C_{vis} , and thus the coherence of the source, can be achieved by cooling the emitter to low temperatures of 80 K or below [72]. By reducing the temperature, phonon scattering effects within the emitter are reduced, leading to an increased inelastic mean free path of the conduction electrons. This results in a larger number of electrons being emitted from the tip, which can interfere with each other yielding an enhanced hologram pattern with increased contrast due to a higher beam brightness [72][83].

The degree of temporal and spatial coherence of the emitted electron waves plays a crucial role in the formation of the hologram and the obtainable resolution of any LEEH setup. In the

following section 2.3, the achievable resolution limits of the LEEH technique are discussed and approximated for our setup.

2.3 Microscope Resolution

The ability to resolve small-sized sample features beyond the capabilities of the human eye is the most important property of microscopes. In holography, the resolution of the reconstructed object depends on the finest distinguishable interference fringes of the hologram observable at the detector [20]. The lateral resolution limit obtainable via in-line holography is defined by the Abbe diffraction limit [95][96]:

$$R_{\text{Holo,lat}}^{\text{Abbe}} = \frac{\lambda}{2\text{NA}} = \frac{\lambda}{2n\sin\theta} = \frac{\lambda Z}{2\frac{w_{\text{Holo}}}{2}} = \frac{\lambda Z}{w_{\text{Holo}}} \quad (2.10)$$

Here, λ is the wavelength of the emitted electrons, NA is the numerical aperture, n is the refractive index of the medium, which can be set to $n = 1$ in vacuum, θ is half the beam opening angle, Z is the sample-to-detector distance, and w_{Holo} is the hologram width visible on the detector. Additionally, for small beam opening angles of $\theta < 10^\circ$, the numerical aperture can be replaced with [97][98]:

$$\text{NA} = n\sin\theta \approx n\tan\left(\frac{w_{\text{Holo}}}{2Z}\right) \approx n\frac{w_{\text{Holo}}}{2Z} \quad (2.11)$$

Even though the Abbe diffraction limit is a good approximation for the lateral achievable resolution of isolated individual features, Rayleigh defined a formula to distinguish several features in close distance to each other based on the overlap of two just resolvable point features, where the zero-order maximum of the diffraction pattern of one feature just intersects with the first minimum of the pattern of its neighbouring feature [99][98]:

$$R_{\text{Holo,lat}}^{\text{Rayleigh}} = \frac{1.22\lambda}{2\text{NA}} = \frac{0.61\lambda}{n\sin\theta} = \frac{0.61\lambda Z}{\frac{w_{\text{Holo}}}{2}} = \frac{1.22\lambda Z}{w_{\text{Holo}}} \quad (2.12)$$

This yields a slightly worse resolution limit by a factor of 1.22 compared to Abbe's formula. The additional factor originates from the calculated argument of the first zero of the Bessel function, which is used to fit the overlapping point features. Furthermore, for small angles of $\theta < 10^\circ$ the axial resolution along the z -axis, which constitutes the 3D image and affects the ability to find the image focus, is given by [98][100]:

$$R_{\text{Holo,ax}}^{\text{Rayleigh}} = \frac{2\lambda}{\text{NA}^2} = \frac{2\lambda}{n^2(\sin\theta)^2} = \frac{2\lambda Z^2}{\frac{w_{\text{Holo}}^2}{4}} = \frac{8\lambda Z^2}{w_{\text{Holo}}^2} \quad (2.13)$$

This shows that the limit of the lateral resolution is better than the axial resolution for $w_{\text{Holo}} < Z$, which is generally the case. In our system, we measure the emission voltages of the emitters (see Sec. 4.2.2), which can be used to calculate the wavelengths of the emitted electrons via [32][83]:

$$\lambda = \frac{h}{\sqrt{2m_e E}} \stackrel{E=e \cdot V}{=} \frac{6.626 \cdot 10^{-34}}{\sqrt{2 \cdot 9.109 \cdot 10^{-31} \cdot 1.602 \cdot 10^{-19} \cdot V}} [\text{m}] = \frac{1.227 \cdot 10^{-9}}{\sqrt{V}} [\text{m}] = \frac{12.27}{\sqrt{V}} [\text{\AA}] \quad (2.14)$$

Here, h is the Planck constant, m_e is the electron mass and $E = e \cdot V$ is the electron energy depending on the emission voltage V and the electron charge e . From these formulas, one can estimate the theoretical lateral and axial resolution limits for the respective setup geometries and emission energies. Tab. 2.1 summarizes the calculated resolution limits for different emission voltages and the given parameters of our LEEH microscope (see Sec. 3.1), where the emitter-to-detector distance Z during measurements is around 11.5 cm, and the electron wavelength is calculated from the emission voltage via equation 2.14. The maximum detectable opening angle is $\Theta_{\text{max}} = 36^\circ = 2\theta_{\text{max}}$, which is larger than the angle used for the prior simplifications. Thus $\theta_{\text{max}} = 18^\circ$ will be directly inserted as θ in the above mentioned equations.

Table 2.1: Theoretical resolution limits of our LEEH setup for different emission voltages.

Emission voltage (V)	Wavelength (Å)	$R_{\text{Holo,lat}}^{\text{Abbe}}$ (Å)	$R_{\text{Holo,lat}}^{\text{Rayleigh}}$ (Å)	$R_{\text{Holo,ax}}^{\text{Rayleigh}}$ (Å)
50	1.74	2.81	3.43	36.44
100	1.23	1.99	2.43	25.76
150	1.00	1.62	1.97	20.94
200	0.87	1.41	1.72	18.22

While the axial resolution is estimated to be in the range of several nanometers, the lateral resolution can be approximated to be twice the wavelength of the emitted electrons. To improve these resolution limits, a decrease in wavelength (via higher emission energies) and/or an increase of the hologram width (via a higher beam coherence and larger numerical aperture) would be necessary. However, these values can only be changed within a practical limitation range, which is addressed in the following.

Depending on the used emitter, typically achieved stable emission voltages are in a range of 150 V and below for close tip-to-sample distances and can only be further increased for higher emission currents. This can lead to instabilities of the emitter, since the higher emission currents increase field effects, e.g. by charging of the substrate, and can locally heat the apex region (as discussed in Sec. 4.2.2), which increases phonon scattering effects within the source resulting in a decreased coherence of the emitted beam (see Sec. 2.2). Furthermore, excessive emission currents are reported to induce radiation damage on the sample [35][51]. This

Chapter 2. Theoretical Background

indicates that wavelengths of less than 1 Å are usually not obtainable for LEEH imaging at high magnifications (i.e. for tip-to-sample distances below 1 μm).

Regarding the increase of the numerical aperture of the system, the detector size can be increased and/or the sample-to-detector distance decreased. A larger detector would only be useful, if the electron beam is already illuminating the whole detector area or, in case of a tilted beam, if the beam is cut off by the detector edge in one direction. Decreasing the sample-to-detector distance allows for larger beam opening angles, but yields lower magnifications, which can reduce the detectability of high-order fringes [83]. Furthermore, too large opening angles diminish the accuracy of the paraxial approximation used in the reconstruction algorithm (see Sec. 2.1). In general, a reasonable compromise has to be chosen concerning the numerical aperture and magnification of the system, which can in principle be estimated depending on the target resolution and used detector size by considering the sampling needed for reconstruction.

To correctly represent the finest resolvable fringes of a hologram on the detector screen, the fringes have to be sampled with a minimum of two pixels according to the Shannon sampling theorem [101][102]. The lateral achievable resolution depends on the amount of pixels used, the pixel size and the magnification factor of the microscope [98][102]. For a fixed pixel size at the detector, the required magnification for a target resolution can be calculated. Assuming the microchannel plate (MCP) detector has a channel size of 10 μm (see Sec. 3.3), and two pixels/channels are necessary to resolve a feature, the required magnification to be able to resolve a feature with a size of 1 Å can be calculated as:

$$M = \frac{2 \cdot 10 \mu\text{m}}{1 \text{ Å}} = \frac{20 \cdot 10^{-6} \text{ m}}{1 \cdot 10^{-10} \text{ m}} = 2 \cdot 10^5 \quad (2.15)$$

Therefore, the theoretically obtainable resolution is restricted by the diffraction limit for setups with high magnifications, where the detectable feature size is smaller than the actual resolution limit as shown above. For low magnifications however, the sampling is not large enough to resolve these features leading to a resolution limit above the diffraction limit. This issue can be overcome by a microscope design, where the detected signals are correctly sampled or even oversampled.

While the theoretical resolution limits can be calculated and approximated for the respective microscope system, the experimentally achievable resolution is difficult to determine exactly and depends on several factors, which have not yet been mentioned. These factors include emission instabilities during measuring, an extended emission source, mechanical vibrations acting on the emitter, sample and detector system, external electromagnetic stray fields affecting the electron beam, charging effects of the sample, and opaqueness of the imaged object [32].

Emission instabilities of the source usually correspond to an energy spread, thus decreasing the temporal coherence of the electron beam, whereas mechanical vibrations and a large emission source size reduce the degree of spatial coherence, as discussed in Sec. 2.2. In general, the coherence of the beam is essential for the obtainable resolution, since high-order fringes can only be formed for a high degree of temporal and spatial coherence. If the amount and contrast of the fringes is constrained intrinsically, the resolution and contrast of the reconstructed object image is also limited, even for higher resolutions. The temporal coherence can be increased by using an emitter with a high emission stability over time. For an increased spatial coherence, the emitter needs to have a small effective source size $r_{\text{eff}} = \frac{2\lambda Z}{\pi W_{\text{Holo}}}$ to restrict the possible emission area and thus minimize destructive interferences originating from waves being emitted at different source locations. Furthermore, an elaborate damping system can reduce mechanical vibrations in the setup, which also improves the spatial coherence, since even small vibrations can lead to an increased effective source size and smear out the detector signal, especially at high magnifications [30][39]. Effects of mechanical vibrations can be further reduced by using a detection system with short detection and acquisition times, which decreases the amount of averaged signal during the acquisition leading to a higher sharpness of the detected hologram [103].

Concerning external electromagnetic fields, proper shielding or a large distance to the field source are usually sufficient to reduce its effects on the electron beam. An additional possibility to actively remove external stray fields can be achieved via Helmholtz coils, which generate a controlled, constant, and uniform field within the affected area [104][105][106]. This possibility is further discussed in Sec. 9.2. Intrinsic electric fields originating from charging effects of the sample and/or substrate can be minimized by using a conductive substrate acting as an equipotential plane, which has to be transparent enough for low-energy electrons to prevent loss of signal. The optimal choice of substrate has been found to be single-layer graphene on a perforated and conductive TEM grid, which is discussed in detail in Chap. 5 [36][41].

The thickness and opaqueness of the imaged object or molecule plays an important role regarding the lateral and axial resolution along the optical axis. While the axial resolution is difficult to obtain in general, the imaged objects are usually three dimensional, which leads to overlapping scattering contributions from each molecular plane along the z direction [107]. The direct 3D reconstruction of these objects is difficult to implement and usually requires tomographic data and/or further improved algorithms [107][108]. The lateral obtainable amplitude signals varies in brightness and contrast depending on the molecular structure of the object [32]. For example, it has been shown for metal clusters [47] and also biological molecules [45] with sizes larger than 15 nm that the individual features close to the object center cannot be distinguished anymore, while features at the object edges are still visible. This opaqueness limits the achievable resolution within the molecule in both lateral and axial direction, since not enough low-energy electrons are transmitted towards the detector after hitting the object due to absorption and inelastic scattering. However, when measuring smaller objects this effect is reduced and the signal contrast within the reconstructed object

can indicate shape, orientation and/or even specific features of the imaged molecule [74].

In fact, the most reliable way to determine the actual resolution of the setup is to detect and identify reconstructed object features of known size and shape, which always depends on the respectively used emitter and sample. Even though the resolution for each acquired hologram is practically fixed, digital post-imaging processing can further improve the quality of the hologram and its reconstructed image. Applying an apodisation filter can reduce reconstruction artifacts originating from the detector edge, as discussed in Sec. 2.1 [32][73]. Averaging several images of the same object measured at identical emission voltages can increase the signal-to-noise ratio, thus improving the image contrast, which is especially useful for fine high-order fringes [103]. Furthermore, since the source is not an ideal point source, the beam intensity distribution will usually not be spherical. Thus, the application of a spatial high-frequency filter or a direct background subtraction can be performed prior to the reconstruction to correct for this issue by using [32]:

$$\Delta I = \frac{I - I_0}{\sqrt{I_0}} \quad (2.16)$$

Here, I_0 is the intensity distribution of a reference image recorded without the object, I is the intensity distribution of the object image and ΔI is the background-corrected intensity distribution, which can be used as input for the reconstruction.

These methods can help to approach the theoretical resolution limits mentioned above. However, surpassing these limits is not possible without additional sources of information. The following Chap. 3 contains a detailed description of the LEEH microscope system and data acquisition including the practical resolution limits defined by the setup. In Sec. 4.2.6 and Chap. 7, the results obtained from LEEH measurements are used to estimate the respective experimental resolutions and compare them with the theoretically suggested values to characterize the general performance of the setup.

3 Experimental Setup

In this chapter, I present our LEEH imaging system, which consists of a unique LEEH microscope setup (Sec. 3.1) with the respective data acquisition and analysis routine (Sec. 3.3), and a remote control software (Sec. 3.4). I introduce our field ion microscopes (Sec. 3.5) used for the emitter characterization and preparation in UHV, as well as the recently developed and installed cryo-holography microscope head (Sec. 3.2). Finally, I explain the general measurement workflow of our LEEH technique (Sec. 3.6).

3.1 LEEH Microscope

In this section, I present the experimental setup of our LEEH microscope. I explain the technical details and capabilities, as well as improvement steps over the course of this work.

In 1939, Morton et al. already presented a microscope with a very similar setup using a field emission source called point projector electron microscope [17]. Low-energy electron projection (LEEP) microscopy, which was introduced by H.-W. Fink and W. Stocker in 1989, follows the same construction principle [25]. The basic principle of our setup is inspired by D. Gabor's original idea for in-line holography, where the sample is placed on the optical axis in-between an emission source and a detector, as shown in Fig. 2.1 [19]. For the experimental realization and successful operation of a LEEH microscope, several requirements have to be fulfilled:

- Ultra-high vacuum (UHV) environment to avoid sample contamination and enable an unimpeded propagation of the emitted electrons from source to sample and/or detector (Sec. 3.1.1).
- Properly adjusted sample-to-detector distance allowing for high magnification factors $\geq 2 \cdot 10^5$ as deduced from Eq. 2.15 (Sec. 3.1.2).
- Effective vibration isolation for the UHV chamber, microscope head and detection

system (Sec. 3.1.3 and 3.1.4).

- Coherent, stable and robust electron source emitting low-energy electrons (Chap. 4).
- Precise and low-vibration 3D positioning stage for the emitter to move it relative to the sample (Sec. 3.1.2).
- Robust, conductive and inert sample substrate, which is free of adsorbates and defects, and transparent for low-energy electrons (Chap. 5).
- Controlled molecule deposition method, which is compatible with UHV conditions (Chap. 6).
- Electron detector with high sensitivity, resolution, and short acquisition times, and a sufficiently large detection area to allow for higher numerical apertures (Sec. 3.3).

3.1.1 Vacuum System

Our LEEH microscope is situated in a UHV chamber (see Fig. 3.1 **a**), which has a base pressure of $< 5 \cdot 10^{-10}$ mbar. This pressure is achieved via a pumping system including pre-pumps, turbomolecular pumps (MVP 070-3, HiPace 80 and 700TM, Pfeiffer) and ion getter pumps (IGPs) (SAES Getters D300-5 and D500-5, NexTorr). The system consists of two main chamber parts: a preparation (Prep) and a microscopy (LEEh) chamber, which is shown in Fig. 3.1 **b**. Both chamber parts can be separated via a gate valve, which is useful during field ion microscopy (FIM), sputtering and annealing procedures when the base pressure in the prep chamber can reach values up to $5 \cdot 10^{-4}$ mbar. Both chamber parts are equipped with an IGP, which can keep the respective chamber in a vacuum of $< 1 \cdot 10^{-9}$ mbar, e.g. when turning off the turbomolecular pumps during measurements (see Sec. 3.6). In this case, the main UHV valve (see Fig. 3.1 **a**, marked by the red arrow) is closed before the turbo pumps are turned off.

3.1.2 Microscope

The microscope head is mounted on a base flange containing a stage (Fig. 3.1 **c** marked green) and several electronic feedthroughs. The stage supports the microscope head (Fig. 3.1 **c** marked yellow) where a stack of piezoelectric motors allows for high-precision movement of our emitter towards the sample in the range of several angstroms up to microns. The stack consists of two horizontally moving piezos for the x and y direction (see Fig. 3.1 **e** and **f**, colored in green) (ANPx311/LT/UHV, Attocube) and a vertical moving piezo for the z direction (see Fig. 3.1 **e** and **f**, colored in blue) (ANPz101exT12/LT/UHV, Attocube). The tip holder is built onto the z -piezo, which is used to tune the tip-to-sample distance, and it is electrically insulated from the rest of the chamber allowing the application of a bias voltage required for field emission. The sample holder is placed in the top part of the head, just above the tip, and is always electrically grounded. The final component of the microscopic system is the electron detector (Fig. 3.1 **c** marked orange), which has a fixed distance of 11.5 cm to the sample. This

setup structure resembles the in-line holography principle, as shown by comparison with Fig. 3.1 **d**. Our microscope geometry allows for magnifications up to $1.15 \cdot 10^6$ for an emitter-to-sample distance of 100 nm. For a typical measurement distance between emitter and sample in the range of 250 – 500 nm, the obtainable magnification is above $2.3 \cdot 10^5$, which is sufficiently high compared to the theoretically necessary value of $2 \cdot 10^5$ for the observation of a feature with a size of 1 Å as calculated in Eq. 2.15. We use a high-resolution microchannel plate (MCP) electron detector with a sensor diameter of 7.5 cm, a channel diameter of 10 μm , an interchannel distance of 12.5 μm , and a bias angle of 6° (MCP-77-1-60-P43-CF160-HR, GIDS). More details on the MCP are given in Sec. 3.3.

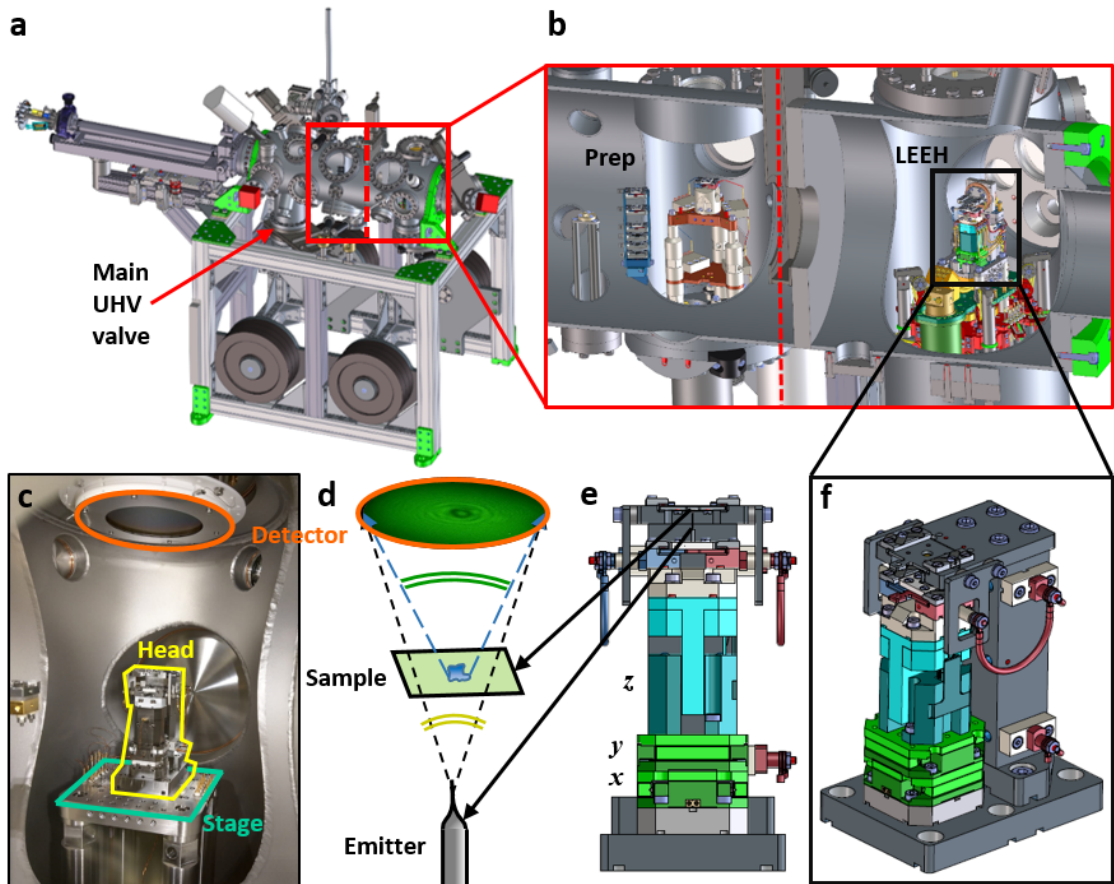


Figure 3.1: Overview of the LEEH microscope. **a** Drawing of the LEEH setup, where the preparation and microscopy chamber are marked in red. **b** Cut through the red marked area from **a**. The preparation chamber part (Prep) containing the internal FIM and microscope chamber part (LEE) containing the microscope head (upper part marked black) can be separated by an internal valve at the position of the red dashed line. **c** Photo of the microscope head (marked yellow) and detector (marked orange) within the chamber revealing the in-line construction principle when compared to the basic in-line holography schematic shown in **d**. **e** Front orientation drawing of the upper microscope head part from **f** showing the x - and y -piezo motors (colored in green), as well as the z -piezo motor (colored in blue). Tip and sample position are linked to the respective positions in **d**. **f** Close-up schematic of the upper microscope head shown in **b**.

3.1.3 External Damping System

The setup is situated in the *precision laboratory* of our institute providing an environment with a high level of vibrational stability [109]. Within the building each experiment has an individual measurement box as shown in Fig. 3.2 **a**, which contains a heavy concrete block, where the setup is built upon, and thick walls, which shield the box from external electromagnetic radiation and sound noise.

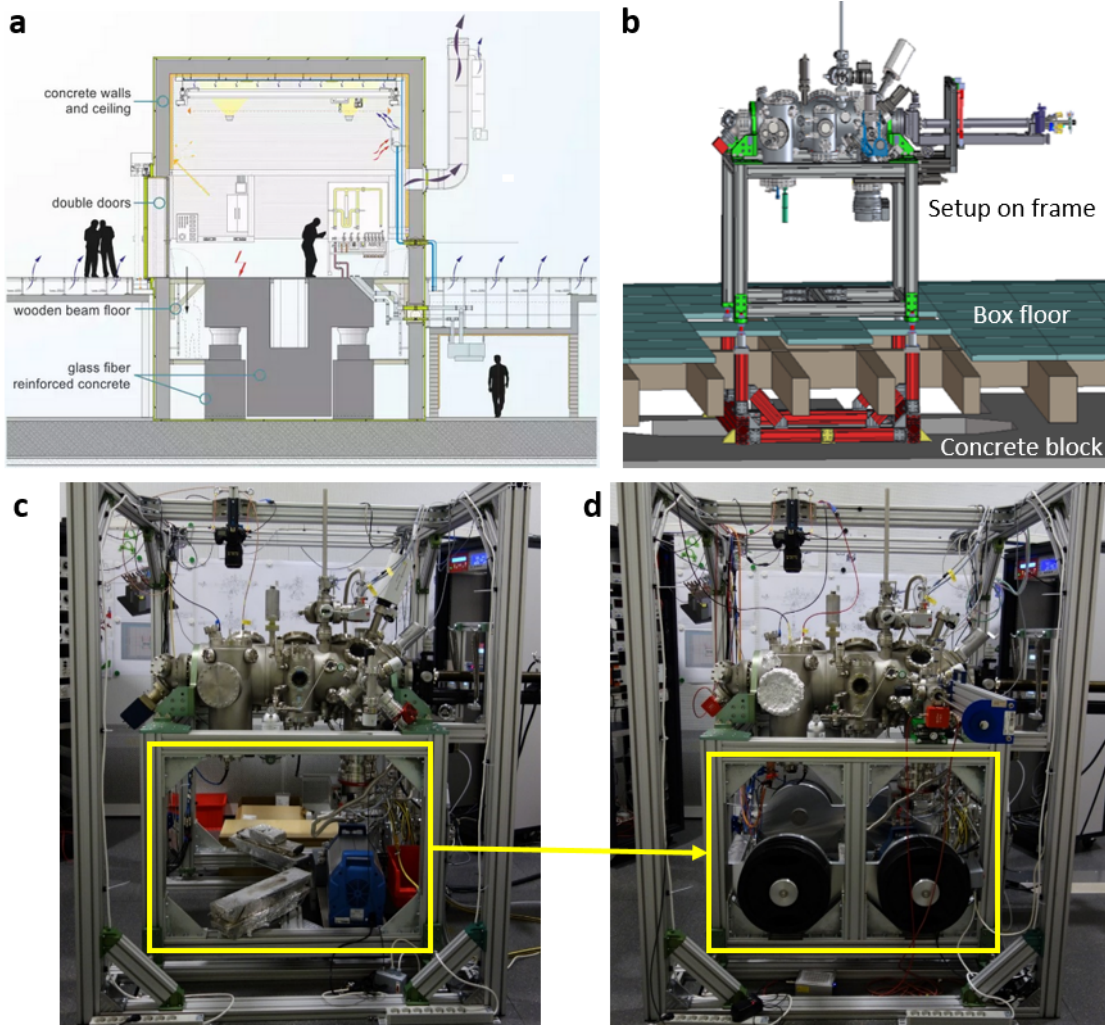


Figure 3.2: External damping of the LEEH setup. **a** Schematic of a measurement box in the precision laboratory showing the concrete block for mechanical vibration isolation and box walls, which provide additional electromagnetic shielding. Schematic taken from https://www.fkf.mpg.de/2489208/01_Precision_Laboratory, last accessed on 29.10.2021. **b** Drawing of the LEEH setup within the measurement box. The setup is constructed on a support frame, which is attached to the concrete block via a connecting frame (colored in red). There is no direct contact between the setup frame and the floor of the box. **c** Photo of the LEEH setup without additional frame support. **d** Photo of the LEEH setup after adding a frame support including additional weights (marked in yellow) to lower the cut-off frequency.

The concrete block has a mass of 120 metric tons and is actively damped by an air-damping system, which reduces low frequency mechanical noise originating from the building and its surroundings. The microscope chamber is constructed on a rigid metal frame, which is directly connected to the concrete block without contacting the decoupled box floor (see Fig. 3.2 **b**). In principle, this decoupling allows for the conduction of experiments in the box without the need for a remote control, since vibrations on the box floor, e.g. by people moving within the box, are not transferred to the setup. However, we found that a system mounted on a simple support frame as depicted in Fig. 3.2 **b** and **c** still transfers a lot of vibrational noise while measuring due to the chamber having an elevated center of mass compared to the frame, which acts like an oscillator when considering the relatively huge mass of the concrete block. For this reason, we added more weights (in total around 550 kg) and additional support connections to the frame as shown in Fig. 3.2 **d** (marked in yellow), which make the frame more rigid and lower the center of mass of the chamber. As shown in Fig. 3.3, these measures lower the frequencies and reduce the amplitude of mechanical vibrations acting on the system as indicated by the data.

We used a vibration measurement cube (Vibration Analyser VA-2C, The Table Stable LTD.), which was either positioned directly on the concrete block, for reference measurements (blue data in Fig. 3.3 **b** to **d**), or on the upper edge of the support frame next to the setup as shown by the blue cube in Fig. 3.3 **a** (black and red data in Fig. 3.3 **b** to **d**). The vibrations were measured in the range from 0 – 200 Hz in three directions: in the vertical axis **V** and in two horizontal axes **H1** and **H2**, which are orthogonal to each other. We chose 200 Hz as the upper limit for this measurement, since higher frequencies are not detectable in our LEEH system.

For each axis, we observed an omnipresent 50 Hz noise and its higher harmonics for the vertical axis. This vibration is originating from the intrinsic electric noise of the measurement device [110] and, as such, it will not be discussed further in the context of vibration isolation. In general, the additional weights and frame profiles resulted in a decrease or even vanishing of vibrational noise peaks in all three directions, which is indicated by the black arrows in Fig. 3.3 **b** to **d**. Few new modes were detected in the **V** and **H2** directions as indicated by the red arrows. These signals are most likely the result of frequency shifts of previous vibrational modes caused by the rise in weight [111]. This shift in frequency can be calculated using Eq. 3.1 with the frequency f , mass m and a fixed spring constant k . Considering that our initial system mass m_{before} is around 100 kg and the mass m_{after} after adding the weights is around 650 kg, this leads to a frequency shift of:

$$f = \frac{1}{2\pi} \sqrt{\frac{k}{m}} \Leftrightarrow \frac{f_{\text{after}}}{f_{\text{before}}} = \sqrt{\frac{m_{\text{before}}}{m_{\text{after}}}} \Leftrightarrow f_{\text{after}} \approx 0.39 \cdot f_{\text{before}} \quad (3.1)$$

Applying this factor on the measured peaks without the additional mass, one can get the newly observed peaks after the weights were added, which are marked by the red arrows in Fig. 3.3 **b** and **d**. For the **V** axis, the red peaks at 48 Hz and 66 Hz are thus correlated to the black peaks

Chapter 3. Experimental Setup

at 126 Hz and 168 Hz, respectively. For the **H2** axis, the red peak at 40 Hz roughly fits to one of the black peaks around 102 Hz. These values fit reasonably well considering that we have assumed a constant value for k , which is actually not the case due to the additional stiffness of the frame after adding the weights and interconnecting parts. It is important to note that in our LEEH system, the vibrational noise disturbing our measurements for frequencies below 20 Hz can easily be compensated by the much faster acquisition times of our detection system, which is explained in detail in Sec. 3.3.

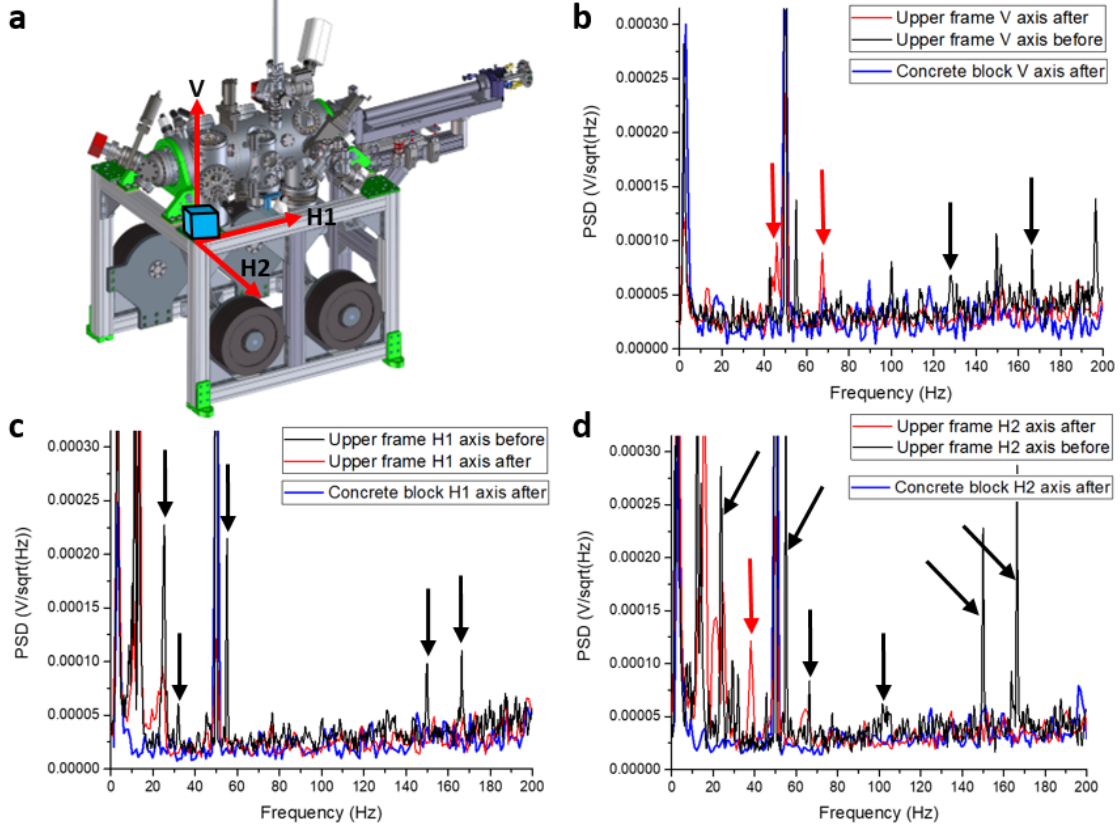


Figure 3.3: Improvement of the external damping performance. **a** LEEH setup drawing with the marked axes **V** (vertical), **H1** (horizontal 1) and **H2** (horizontal 2) used for the vibration measurements. The vibration sensor was placed on the indicated frame corner at the axis origin (blue cube). **b**, **c** and **d**: Vibration measurement results of the respective axes **V**, **H1** and **H2** before (black data) and after (red data) adding the additional weights, as well as a reference measurement on the concrete block (blue data). The added rigidity and mass reduced vibrational noise peaks, which are marked in black or shifted them to lower frequencies (marked in red). Noise peaks visible at 50 Hz and its multiples were identified as intrinsic noise known as electric hum [110].

3.1.4 Internal Damping System

An important adjustment of the LEEH system is the internal damping, which was installed later on. To reduce high-frequency vibrations acting on the microscope head, we decoupled the head from the rest of the UHV chamber via attaching it to soft Viton[®] O-rings. In this

way, the microscope head is free-hanging with a pair of Viton[®] O-rings connecting it to the microscope support at each corner, as shown in Fig. 3.4 **b** and **c** (marked in red). The internal damping improved the quality of measured holograms and the respective reconstructions, which is displayed for Herceptin antibody molecules from different samples measured via LEEH. Without the internal damping, the low signal-to-noise ratio and amount of resolvable fringes in Fig. 3.4 **d** leads to a poor reconstruction of the molecule (Fig. 3.4 **e**), even with all turbo pumps turned off for minimizing vibrations. With the internal damping installed, the hologram contains more fringes as shown in Fig. 3.4 **f** and yields a more detailed reconstruction of the molecule (Fig. 3.4 **g**) even for leaving the turbo pumps on while measuring. As already discussed in Sec. 2.2, a proper decoupling of the microscope system decreases the mechanical vibrations, thus increasing the spatial coherence of the emitted electron beam and improving the obtainable resolution.

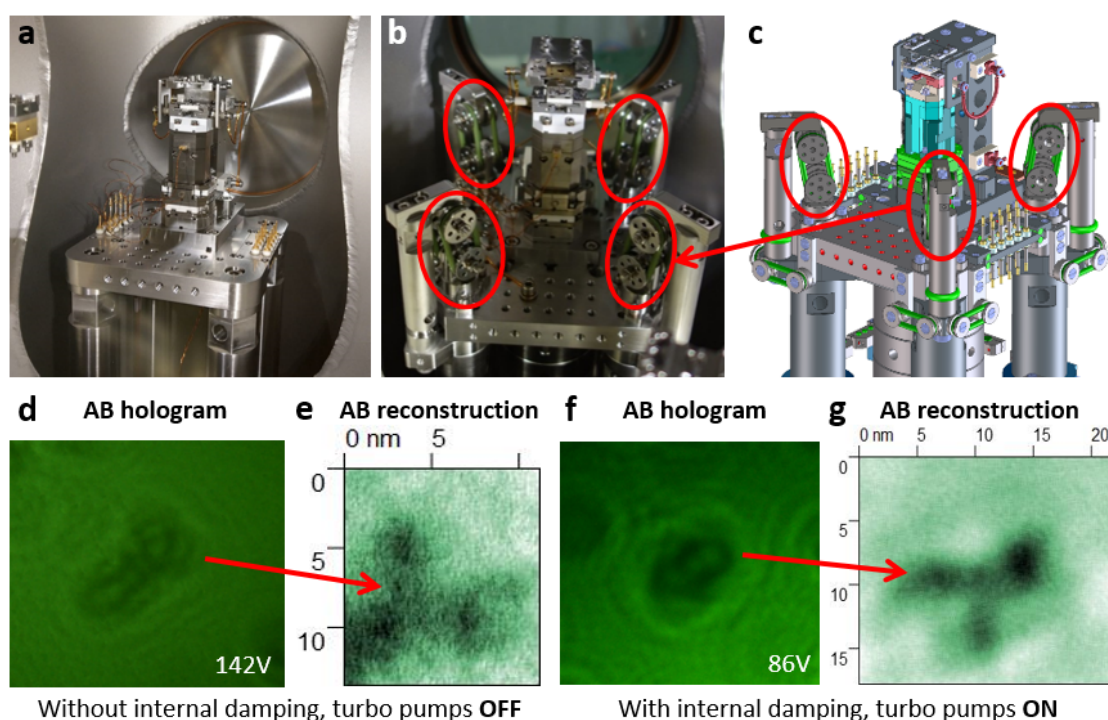


Figure 3.4: LEEH microscope head before **a** and after **b** adding of an internal damping (marked in red). **c** Drawing of the microscope head including the internal damping (marked in red). The damping consists of soft Viton[®] O-rings (colored in green) connecting the microscope base and head. **d** Hologram of a herceptin antibody molecule measured via LEEH and the respective reconstruction shown in **e** before addition of the internal damping. The image was acquired while all turbo pumps of the system were turned off. **f** Hologram of another herceptin antibody molecule measured via LEEH with its reconstruction shown in **g** after adding the internal damping. This image was acquired while all turbo pumps were still running, yet showing an improved signal in the hologram resulting in a clearer reconstructed image of the molecule when compared to **d** and **e**, respectively.

3.1.5 Sample Transfer and Storage

New tips and samples are transferred into the main UHV chamber via a fast transfer load lock (FTLL), which is vented to insert the respective sample and/or tip and subsequently pumped until a pressure of $< 2 \cdot 10^{-7}$ mbar is reached. Up to two samples/tips can be introduced to UHV this way and transferred into the prep chamber part. Here, they can be stored within a storage rack, which is marked in red in Fig. 3.5 **a** or directly transferred to the LEEH chamber, where another storage unit is present (see Fig. 3.5 **b**, marked in red). This allows for a reliable contamination-free storage of several samples and emitters in UHV conditions. Furthermore, we utilize a UHV suitcase for the sample and tip transfer between different setups, such as the external FIM and/or electrospray ion beam deposition (ES-IBD) setup. The suitcase has a base pressure of $< 1 \cdot 10^{-10}$ mbar and is connected to the respective setup via a suitcase load lock (SCLL), as shown for the LEEH setup in Fig. 3.5 **c**. The sample/tip transfer from the main chamber to the suitcase can be carried out, as soon as the SCLL pressure is $< 2 \cdot 10^{-8}$ mbar to prevent major pressure spikes and contamination during transfer. The suitcase allows for a simultaneous transfer of up to five samples or four samples and one emitter.

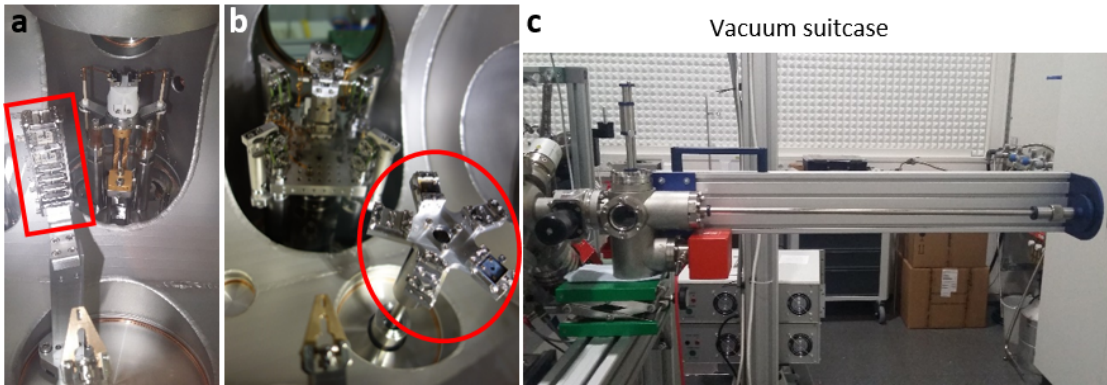


Figure 3.5: Photos of the UHV emitter and sample storage options in the preparation chamber (**a**) and microscopy chamber (**b**) of the LEEH setup (both marked in red). **c** Photo of the UHV suitcase used for the sample and emitter transfer between different setups.

3.2 Cryohology

In this section, I present the Cryo-LEEh microscope head, which allows for an efficient cooling of our emitters and samples during LEEh measurements. This latest feature added to our microscope is described in its construction and cooling performance, as well as how the cooling of our emitters affects their field emission properties. Measurement results of cooled emitters and samples are presented in Sec. 4.2.2.2 and 4.2.6.2, and 5.2.2.8, respectively. The possibility to measure at low temperatures has several advantages, such as:

- Higher spatial coherence of the emitted electron beam due to reduced phonon scattering effects within the emitter [72].

- Decreased atom diffusion on the tip, which leads to a higher emission stability [72].
- Reduced molecular diffusion on the sample, since $D \propto \exp\left(\frac{-E}{k_B T}\right)$, with E being the energy barrier for the molecular/atomic motion and k_B being the Boltzmann constant [112][113].
- Quenching of excited soft vibrational modes of the sample molecules relevant for large molecules, such as proteins [71], and the SLG substrate [70].
- Lower background pressure, since cold parts act as a cryotrap. However, this can also lead to tip and sample contamination if not handled with care.

For the construction of a coolable microscope head it is necessary to consider the following five technical key aspects:

1 Cryostat. We use a compact flow cryostat (He-Verdampferkryostat-40, VAb), which can be cooled via liquid nitrogen or helium. The cryostat has a helium consumption below $0.5 \frac{l}{h}$ for temperatures above 20 K and an almost linear cooling power of 3 – 80 W in the respective temperature range of 10 – 80 K. Since a tip and sample temperature of < 120 K for nitrogen cooling and < 60 K for helium cooling is sufficient for our system, these properties are adequate.

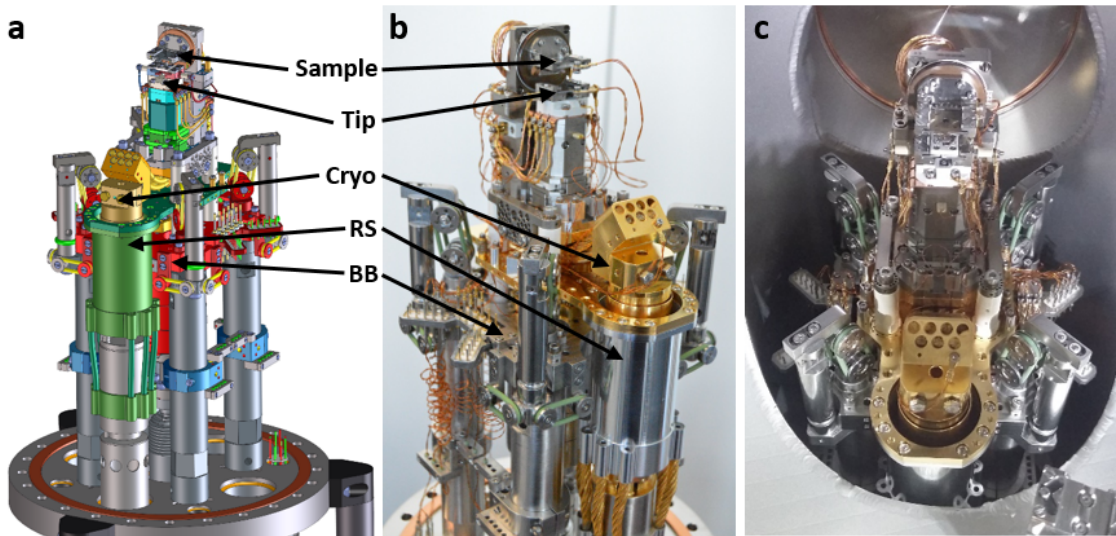


Figure 3.6: Overview images of the Cryo-LEEH microscope head: Schematic drawing (a), photo outside (b) and inside (c) the UHV chamber. Sample and tip position, as well as the cryostat (cryo) and recooling stage (RS, colored in green in the drawing) are marked in a and b. The temperature-isolated base block (BB, colored in red in the drawing) connects the microscope head with the internal damping system.

2 Temperature transfer from the cryostat to the system. The connection between the cryostat head and the microscope head has to be as short and/or direct as possible to ensure an efficient and fast cooling performance while minimizing cooling agent consumption.

Before going into the details of the cooling connection, it is important to mention that in order to reduce the amount of necessary cooling power, it is beneficial to cool down a minimum amount of material. For improving our LEEH microscope performance, this translates into the need of a low temperature operation of solely the top parts of the LEEH (see Fig. 3.6), i.e. the tip holder, sample holder and piezo motors. We use gold-plated copper connection pieces from the cryohead up to the microscope head (see Fig. 3.6 **b** and **c**), which allow an excellent heat conductance (additional details on this connection are provided below when discussing the vibration isolation aspects). For a faster cooling performance of the tip holder, which is positioned on top of the piezo motor stack, we added several thin copper braids connecting the top of the piezo stack with the efficiently cooled backside of the microscope head, as shown in Fig. 3.8 **b**. We also installed a recooling stage (see Fig. 3.6 **a**, colored in green) to reduce the needed amount of cooling agent by decreasing the temperature gradient between cold and warm setup parts. We separated the two stages using a material with poor heat conductivity, i.e. Vespel[®]. The top stage containing the piezo motors, tip holder and sample holder are thus directly connected to the cryostat head, whereas the second stage consists of the recooling stage. The bottom stage is a supporting base block (see Fig. 3.6 **a**, colored in red), which contains the internal damping of the system. Since soft Viton[®] O-rings, which can get stiff and brittle for temperatures below 250 K, are used for the internal damping, the temperature of the base block should not decrease below this value. This is ensured by the stage isolation and an additional silicon carbide heater, which is positioned in the center of the block.

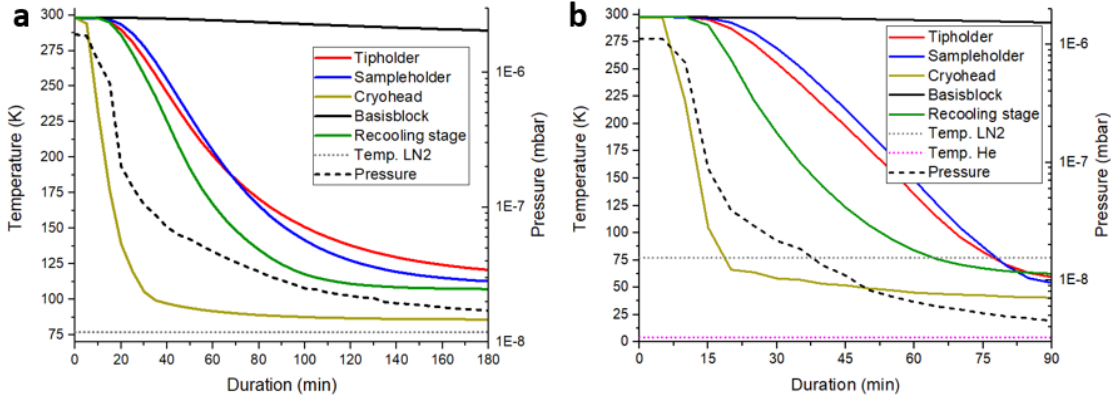


Figure 3.7: Cooling performance of the Cryo-LEEh microscope head for liquid nitrogen (LN₂, **a**) and helium (He, **b**). Temperatures were measured at the tip holder, sample holder, cryostat head, base block and recooling stage position. For liquid nitrogen and helium, the lowest achievable temperatures at the tip and sample position are around 100 K and 50 K, respectively. The temperature isolated base block stays at temperatures above 285 K for the respective cooling durations.

In order to test the performance of our setup, we installed several temperature sensors to track the temperature changes during cooling procedures. The sensors are positioned at the tip and sample holder, at the recooling stage, cryostat head and base block of the microscope head. Fig. 3.7 shows the cooling performance of the cryostat for liquid nitrogen and helium. In both cases, the base block temperature (black data) does not decrease below 285 K during the cooling

even without using the heater, which indicates an efficient temperature decoupling between the stages. However, for long time measurements or cooling of the system over several days, the heater is used to keep the base block at room temperature. The temperatures at the tip (red data) and sample (blue data) holder positions reach values of < 125 K when cooling with nitrogen for around 120 – 140 minutes and < 60 K when cooling with helium for around 80 – 90 minutes. These cooling performances are adequate for our purpose [72].

3 Vibration isolation of the coupled cryostat-microscope system. To ensure an efficient decoupling from mechanical vibrations acting on the microscope head via the UHV chamber, the Cryo-LEEH setup has an internal damping system consisting of bridging soft Viton[®] O-rings (see Sec. 3.1.4). Furthermore, the connection between the cryostat head and microscope head needs to be soft enough to prevent mechanical noise transfer induced by the cryostat. For this reason, we use several soft copper braids as bridging parts between cryostat and microscope, which allow for an efficient temperature transfer while also minimizing mechanical vibrations as shown in Fig. 3.8 **a**. These braids have to be cleaned and baked thoroughly to remove contaminants from their large surface, which can cause high background pressures in the UHV chamber if not handled properly.

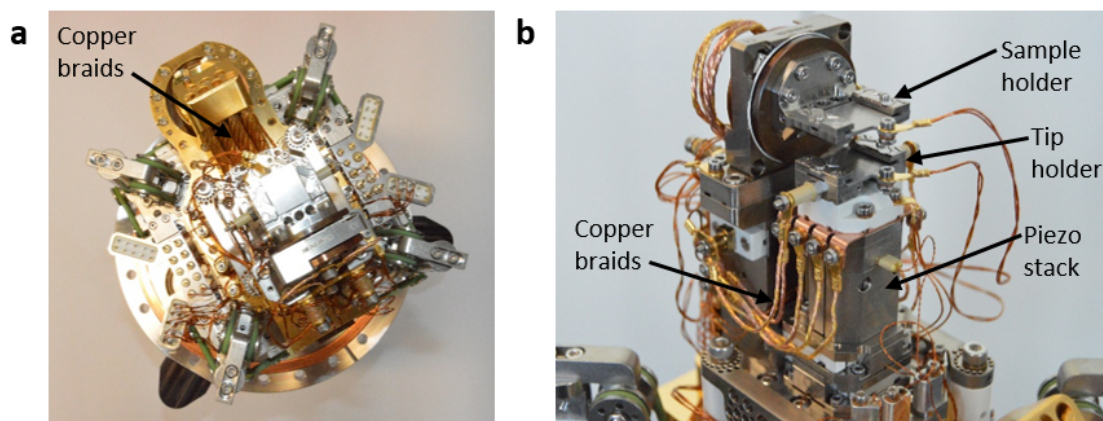


Figure 3.8: Close-up view of the Cryo-LEEH microscope showing the soft copper braids connecting the cryostat and microscope head (top view, **a**) and the thin copper braids connecting the backside of the head with the piezo stack for a more efficient cooling performance of the tip holder (**b**).

First measurements with the Cryo-LEEH microscope head at room temperature showed no additional mechanical vibrations acting on the system. While cooling, a background noise with a frequency of a few Hz is visible. However, the frequency range of the vibrations is below 20 Hz and thus its effect is negligible for fast acquisition imaging where images are acquired in less than 50 ms. These vibrations are predominantly observable when cooling with liquid nitrogen and are related to the cooling agent flow rate. When using low flow rates and/or helium as cooling agent, the vibrations are strongly reduced and have practically no effect on the measurements. This suggests that the internal damping and the copper braids provide enough vibration isolation for our LEEH system.

4 Sample and tip contamination at low temperature. The cooling of the system reduces the background pressure below $1 \cdot 10^{-10}$ mbar after the turbo pumps are turned off due to a cryopumping effect. Since both tip and sample are at low temperatures, contaminants will adsorb on their surfaces. This effect is detrimental to the quality of our investigation (additional details are provided in Sec. 5.2.2.8 Fig. 5.10). For this reason, we are currently constructing additional cooling shields for the top part of the LEEH microscope head with the goal of improving the cooling performance and minimizing the adsorption of particles on the sample and tip surfaces.

5 Thermal contraction of the materials. To prevent strain effects acting on the microscope parts during cooling, we used the same material for interconnecting parts along the optical axis. While the whole microscope head is cooled, the adjusting thermal compression lengths affect the tip-to-sample distance. As an example, the compression length of the tungsten emitter is determined in the following. With an initial tip length L_0 of 3 mm, a temperature difference of $\Delta T = 50 \text{ K} - 295 \text{ K} = -245 \text{ K}$, and the thermal expansion coefficient for tungsten of $\alpha = 4.5 \cdot 10^{-6} \text{ K}^{-1}$ at 293 K, the emitter length L at 50 K can be calculated as shown in Eq. 3.2.

$$L \approx L_0 \cdot (1 + \alpha \Delta T) = 3 \text{ mm} \cdot (1 - 4.5 \cdot 10^{-6} \text{ K}^{-1} \cdot 245 \text{ K}) = 2.9967 \text{ mm} \quad (3.2)$$

This yields a length difference of around $3.3 \mu\text{m}$, which can be crucial if the tip is in a close distance to the sample. While cooling down, the tip-to-sample distance increases and we observe additional drift effects in all three directions originating from the piezo motors, which can alter the sample position illuminated by the emitter. To avoid measuring while the drift is present, we cool the system for at least 120 minutes when using helium, where a thermal equilibrium of the cooled parts is reached and almost no further drift is visible. To track and compensate the drift and compression effects acting on the emitter, we usually image the sample during the cooling procedure and adjust the tip position if necessary using the piezo motors. While warming up, it is important to have a sufficiently large tip-to-sample distance, since the thermal expansion of the parts can lead to an uncontrolled crashing of the emitter into the substrate. For this reason, we usually completely retract the emitter before stopping the cooling procedure.

As shown in Sec. 4.2.2.2 and Sec. 4.2.6.2, emission stability and visibility contrast of emitters can be improved when measuring at low temperatures. These first experiments indicate that the Cryo-LEEH system with its efficient cooling performance and effective vibration isolation is a promising development for our LEEH microscope. A future implementation is the installation of cooling shields (see Sec. 9.1), which are the next step towards a contamination-free sample cooling. Furthermore, the shields can help to reduce the amount of necessary cooling agent, while improving the cooling performance.

3.3 Data Acquisition, Reconstruction and Analysis

Due to the vast amount of microscopy and spectroscopy techniques utilizing electrons as imaging source, their efficient, loss- and noise-free detection is a fairly developed field of research [114]. In particular, with the development of direct electron detectors, the detection quality in electron microscopy improved tremendously, specifically for samples with a low imaging contrast, such as carbon based molecules [115]. However, these detectors were designed to perform at best for high energy electrons (several keV), as used in TEM for example. For this reason, other detection systems, such as electron-multiplying charge-coupled devices [116][117] and microchannel plates (MCPs) [118][119], are used to enable an efficient detection of low-energy electrons in the range of several 100 eV. Their simple and robust design, fast acquisition times, high-resolution electron amplification, and high gain at low noise make MCP detectors a good choice for LEEH [28][41]. Furthermore, they can be utilized in FIM to detect emitted ions with a high efficiency, which makes them very flexible in terms of the imaging technique [120].

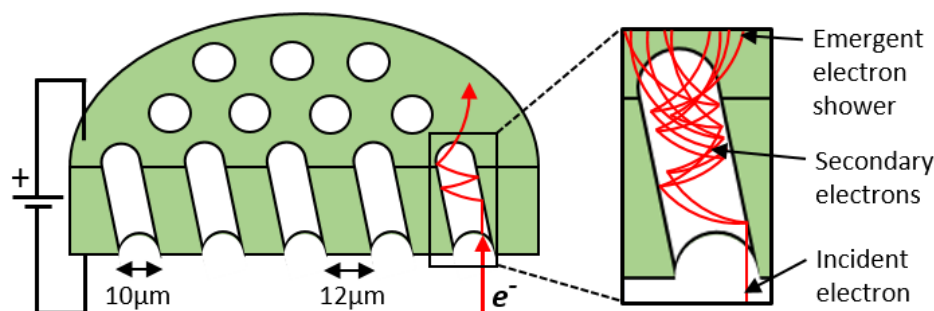


Figure 3.9: Basic principle of a MCP detector: incident electrons enter the tilted MCP channels and generate secondary electrons upon hitting the inner channel walls. The created secondary electrons travel through the channel generating more and more secondary electrons upon contact with the channel walls, called electron cascade. The emergent electron shower leaving the channels travels towards the screen, which usually consists of a phosphorescent layer converting the incoming electron signal into a visible signal.

The working principle of an MCP is shown in Fig. 3.9. After applying a high positive bias in the order of several hundred volts to the channel plates, electrons moving along the optical axis towards the detector are attracted and accelerated by the strong electric field. The MCP consists of a highly resistive slab (typically fabricated from lead glass) containing a large amount of small channels. The channels are tilted to ensure a contact between incident electrons and the channel walls. The channel size is around 10 – 12 μm and the pitch distance is in the range of 12 – 15 μm with tilting angles between 6 – 10° [118]. When entering the respective channel, the electrons are accelerated by the electric field within in the channel. Upon contact of the incident electrons with the channel walls, secondary electrons are released from the material leading to an electron cascade, which multiplies the signal along the channel axis [119]. The emergent electron shower leaving the MCP can be detected, e.g. via a phosphor screen, where an additional high positive voltage bias accelerates the electrons even further

Chapter 3. Experimental Setup

until they hit the screen [118][119]. On the phosphor screen, the electron impact is converted into a visible phosphorescence signal, which is distributed over the respective screen area. This signal can subsequently be captured, e.g. via a camera, and analyzed. Important parameters to ensure a high detection quality of the initial electron signal are [118][119]:

- High dynamic range, which is the quotient of the highest to lowest detectable intensity signal.
- High sensitivity, which is the quotient of the amount of detected to incident electrons.
- High gain, which defines the electron multiplying factor depending on the acceleration voltage.
- High spatial resolution, which is defined by the size and amount of MCP channels.
- High homogeneity of these properties across the complete active area of the MCP.

In our LEEH microscope, we use a high-resolution MCP detector (MCP-77-1-60-P43-CF160-HR, GIDS) with a screen diameter of 75 mm, a bias angle (channel tilt) of 6° , a channel diameter of $10\text{ }\mu\text{m}$, an interchannel distance of $12.5\text{ }\mu\text{m}$ and an aspect ratio of channel length to diameter of 60:1 resulting in a maximum gain at 1.2 kV of $> 2.5 \cdot 10^4$ secondary electrons per incident electron. The phosphor screen used is a P43 type screen consisting of $\text{Gd}_2\text{O}_2\text{S:Tb}$ with a green light emission at 545 nm and a signal decay time of 1 ms.

For our experiments, we apply a positive bias of 900 – 910 V to the MCP and 4.90 kV to the screen, which yields a sufficiently high signal for detected emission currents down to 1 nA depending on the emitter quality. Since we usually measure samples at emission currents in the range of 10 – 100 nA, these settings allow for high-contrast images. Due to the small channel diameter and our magnification factor of $> 2 \cdot 10^5$, a theoretical resolution of single features with a size below $1\text{ }\text{\AA}$ is in principle possible, but limited by the diffraction limit as discussed in Sec. 2.3. The signal decay time at the screen of 1 ms is short enough to acquire images of the screen with shutter times down to 1/1000 s.

To capture the images of projections or holograms displayed on the detector screen, we use a digital single-lens reflex camera (810D, Nikon), which is positioned on an external support frame around 38 cm above the chamber and directly focused onto the screen using an additional objective for a higher depth of focus. We use a remote control software (ControlMyNikon, version 5.4.98.99), which has a live-view feature and allows for the recording of single images, image series and videos. Typical camera settings for the photo acquisition are shutter times in the range of 1/20 s to 1/100 s, ISO values between 500 – 1000, a fixed aperture of f/8 and a focal length of 105 mm. The minimum necessary image size in pixels can be calculated from the amount of detector channels, which form an image on the screen:

$$N_{\text{Channel}} = \frac{d_{\text{Detector}}}{d_{\text{Pitch}}} = \frac{75 \text{ mm}}{22.5 \mu\text{m}} \approx 3333 \quad (3.3)$$

To avoid undersampling, the set image size of the camera should have at least N_{Channel} pixels. Therefore, we use a standard image size of 5520×3680 px, which is sufficiently large to resolve all channel signals of the detector. It is important to mention that the pixel geometries of screen and camera differ, which can lead to detection inaccuracies. Since the estimated detectable resolution limit is below the actual theoretically achievable diffraction limit, this effect can be neglected. Alternatively, a larger image size of up to 7360×4912 px can be chosen for our camera in case of a measured hologram with a very large amount of fringes. However, so far we did not observe a difference in quality for both image sizes even when imaging at high resolutions.

The acquired images are reconstructed using a modified reconstruction algorithm based on the theory presented in Sec. 2.1. The algorithm needs several parameters to numerically reconstruct the hologram: First, the measured field emission voltage of the tip while the image was recorded to calculate the respective electron energy and wavelength. Second, the sample-to-detector distance, which is fixed at 11.5 cm for our setup. Third, the exact emitter-to-sample distance, which is unknown before reconstruction. For this reason, the reconstruction is performed for a set of distances, usually ranging from 200 – 600 nm with 10 nm step sizes. This yields a stack of reconstructed images, which is screened to find the focus position of the imaged object, which indicates the emitter-to-sample distance for the respective measurement. Fourth, the detector screen size, which is 7.5 cm for our MCP detector. Finally, the apodization filter used requires two preset sizes for η and ω for the intensity smoothening near the detector edge (see Fig. 2.2). These values are typically chosen to be $\eta = 1400$ px and $\omega = 200$ px for a screen radius on the acquired image of around 1600 px.

With these parameters, the recorded holograms can be reconstructed and the resulting images can be further analyzed. For example, if the reconstructed objects are deposited molecules, we perform size measurements via the image analyzing software (Gwyddion 2.52, [121]) and compare the amplitude signal, which usually appears as a high-contrast dark shape, to models of the respective molecules. For proteins of known structure, we mainly use the RSCB protein data base (<http://www.rcsb.org/pdb/>, [122]). The results of measured molecules are presented in Chap. 7.

3.4 Remote Microscope Control Software

Another important feature of our setup is the remote controllability of LEEH measurements. To reduce noise caused by activities of the experimentators within the measurement box, I programmed a remote control software including a graphic user interface (GUI) for the complete control of the LEEH microscope head during measurements. The software is based

Chapter 3. Experimental Setup

on PyQt5, which is a python package for interactive handling of user interfaces. A screenshot of the interface is shown in Fig. 3.10, which displays the three main functions of the program.

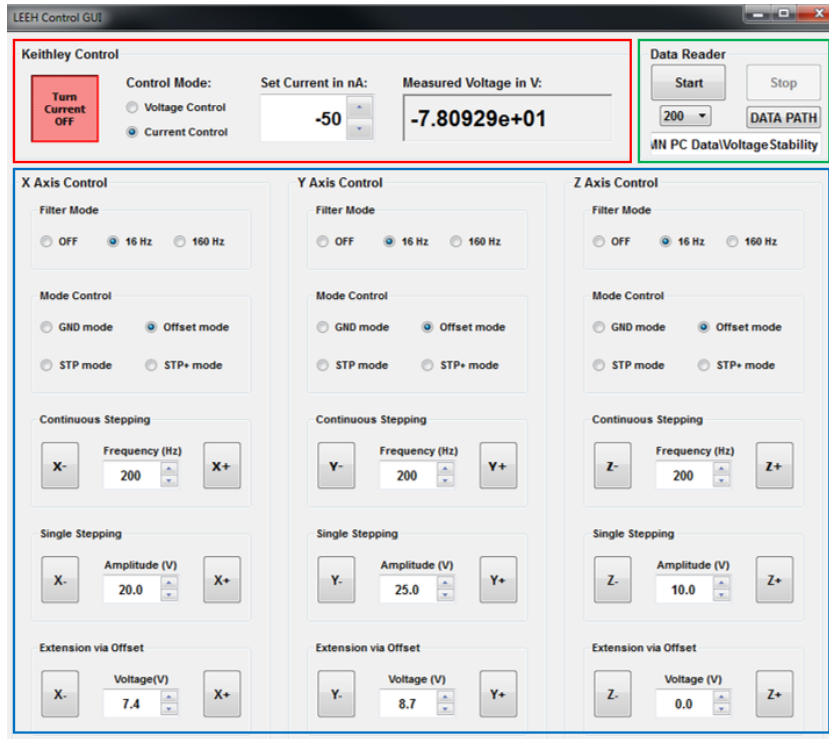


Figure 3.10: Screenshot of the graphic user interface used for the LEEH setup. The tip voltage and current control is marked in red, the emission voltage data recorder is marked in green, and the Piezo motor control enabling independent continuous, rough and fine stepping in x , y and z direction is marked in blue. In the case of this image, an applied tip voltage of -78 V was measured for a constant current emission of 50 nA while the emitter was close to the sample ($z < 1\text{ }\mu\text{m}$).

Within the red box (Fig. 3.10 top left), the voltage and current control of our emitter power supply (2657A, Keithley) is displayed. It allows for the electron emission operation at either constant current or constant voltage and shows the respectively measured emission voltage or current value. The green box (Fig. 3.10 top right) contains a voltage recording program, which enables long term measurements of the field emission voltage, for example to gain information about the emission stability of the respective emitter (see the data shown in Fig. 4.9 and 4.10). In the blue box (Fig. 3.10 bottom), the control system for the x -, y - and z -piezo motors is displayed. For each of the three movement directions, individual settings regarding the stepping mode, step size and frequency, and applied filter function can be chosen, which are executed by a piezo controller (ANC300, Attocube). While the stepping mode (**STP mode**) enables large single steps depending on the set amplitude, it can also be used for continuous stepping depending on the set frequency. For navigation of the emitter at close tip-to-sample distances, the fine positioning mode (**Offset mode**) is used, which allows for step sizes down to several angstroms. In this mode, we usually apply a 16 Hz filter (as indicated in the screenshot), which reduces vibrational noise artifacts influencing the piezo extension and yields smoother

movement of the emitter with respect to the sample, especially for a controlled approach and retracting. The **STP+ mode** combines the functionalities of rough and fine stepping, however, no filter can be applied during the use of this mode. The **GND mode** grounds the piezo motors, which is important when changing the emitter during measurements to avoid damaging of the sensitive piezo components. The GUI is thread-safe, which allows for the operation of different tasks simultaneously without blocking or interfering with each other. The upcoming version includes an additional rotation stage control unit to enable remotely controlled tomography experiments, which is discussed in Sec. 9.5.

3.5 FIM Setup

The fine control of the atomic structure of the emitter is crucial for the performance of the LEEH microscope. For this reason, we employ a field ion microscope (FIM) to investigate and characterize the tip apex of our emitters. To understand the working principle of FIM, it is worth to introduce its precursor technique, the field emission microscopy (FEM) invented by E. W. Müller in 1936 [123]. The experimental setup for FEM is reasonably simple: as for the LEEH setup (see Sec. 3.1.2), the emitter is placed in front of an electron detector, which serves as the counter electrode and is placed at a few centimeters distance. By applying a sufficiently high negative bias at the tip, electrons are extracted from the tip apex via field emission.

These electrons are emitted with low kinetic energies when leaving the potential barrier and follow the electric field lines close to the apex after emission. This results in almost radial emission trajectories from the tip towards the detector, where the electrons are collected and displayed on a screen [124]. Each electron collected this way generates a signal on the screen, usually in the form of a glowing spot, thus depicting the apex surface via electron point-projection. The signal width on the screen depends on the opening angle of the field lines at the apex during emission, which also influences the magnification of the image. Furthermore, the magnification also depends on the tip to detector distance and is usually in the range of $10^6 - 10^7$ [125].

During a FEM characterization, symmetrically arranged spots with different shapes and sizes are usually visible on the detector screen. This can be explained as follows: the emitter apex consists of facets with different crystallographic orientations, which have individual work functions leading to emission anisotropy during imaging [126]. The lower the work function of the respective emission position, the more current is emitted and the brighter the corresponding signal on the screen [127]. Furthermore, local variations of the electrostatic field can be imaged, which occur due to surface disorder and diffusion, grain boundaries and adsorbates [124][125].

Despite being able to provide very useful information about the structure of the tip apex, the lateral resolution of FEM is limited to 2 – 3 nm due to two main factors. Upon leaving the potential barrier, the electrons maintain a velocity component which is parallel to the surface

and leads to a statistical distribution of their momenta. This results in a spread of the electron trajectories, which can not be reduced, e.g. via cooling [126]. The second reason is the direct result of the Heisenberg uncertainty principle, where electrons, which are emitted from a distinctive location on the apex, show an uncertainty in their respective lateral momentum with a resulting resolution limit around 1 nm [124]. Therefore, FEM cannot resolve individual atoms (see Fig. 3.11).

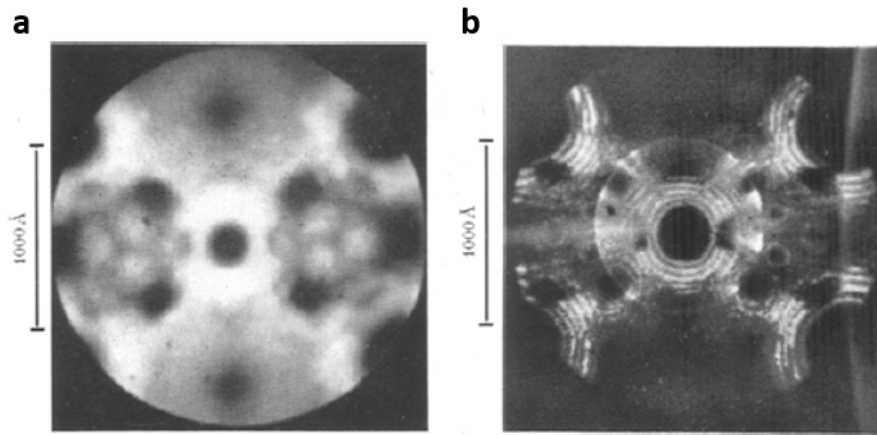


Figure 3.11: FEM (a) and FIM (b) images of a tungsten emitter, which was characterized by Erwin Müller in 1951. Hydrogen atoms were used for FIM. The difference in resolution of both techniques is clearly visible, the FIM image shows a much higher resolution revealing the facets of the emitter apex [128].

While experimenting with the adsorption of barium atoms on tip surfaces in 1941, Müller found a possibility to overcome the resolution issue described above. When applying a high bias at reversed polarity (positive bias at the tip), barium was desorbing from the emitter and Müller concluded, that the trajectories of the atoms would follow the field lines of the applied field towards the detector [128]. Due to the high mass of the atoms compared to electrons, the lateral velocity is much lower, leading to a magnified image on the detector screen with a higher resolution of the desorption sites [129].

For properly imaging the apex surface, a single adsorbed atomic layer is not sufficient. Therefore, a constant supply of non-reactive atoms is needed to maintain the process. Using noble gas atoms, which can be dosed into the chamber in a controlled manner, was found to be an ideal solution. For tungsten emitters, helium as well as neon are commonly used imaging gases [130]. As soon as the noble gas atoms are in the vicinity of the emitter apex, where a high positive electric field is applied, the atoms will be polarized and attracted towards the apex via dipole forces. Due to the increasing field gradient at the apex, the atoms are subsequently repelled towards the detector along the field lines [125]. To reduce the mobility of the atoms that adsorb on the tip surface, which is important for increasing the resolution of the method, the tip is usually cooled to cryogenic temperatures. This results in a thermal accommodation of the gas atoms. If the kinetic energy of the atoms is reduced sufficiently by this process, they are ionized within an ionization zone around the apex [131]. Usually, the

continuous ionization of helium or neon atoms takes place when the electric field is in the range of $\sim 4.4 \text{ V/\AA}$ or $\sim 3.75 \text{ V/\AA}$, respectively [132].

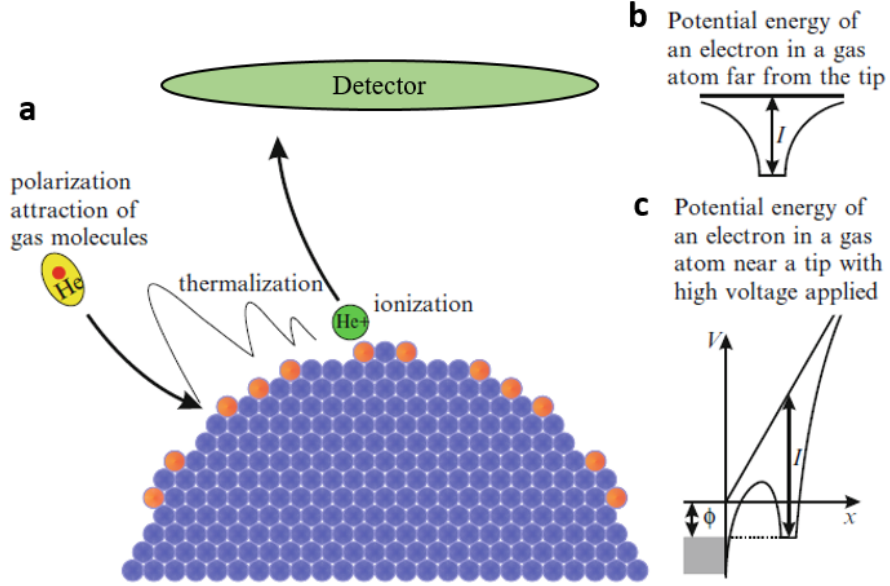


Figure 3.12: General principle of field ion microscopy. **a** Imaging gas atoms (helium) are attracted towards the emitter apex via dipole attraction. After thermal accommodation to the emitter, the atoms are ionized by a locally enhanced field at atomic edges (orange). Afterwards, the helium ions are accelerated towards the detector by the presence of the strong electric field. **b** Potential well of a valence electron in the imaging gas atom. **c** Potential energy diagram for an atom being within the tunneling distance of the emitter, which exerts a large electric field. Modified schematic taken from W. Paul et al. [132].

During ionization, one of the valence electrons of the gas atom tunnels from an electron state of the gas atom towards a free electron state of the metal. This changes the potential energy landscape from a potential well (Fig. 3.12 **b**) to an equilateral triangle potential well (Fig. 3.12 **c**), which enables tunneling with a barrier penetration probability D as shown in equation 3.4:

$$D(F) = \exp \left(-\frac{2}{3} \left(\frac{8m}{\hbar^2} \right)^{\frac{1}{2}} \left(I - 2\sqrt{e^3 F} \right)^{\frac{1}{2}} \frac{I - \Phi}{F} \right) \quad (3.4)$$

Here, m is the free electron mass, \hbar is the reduced Planck's constant, e is the elementary charge, I is the ionization energy of the gas atom, F is the applied electric field and Φ is the work function of the emitter [132][133]. This shows, that the tunneling probability is mainly dependent on the applied field F , as well as the ionization energy I and increases for a lower ionization energy, and a higher applied electric field. However, this only applies if the atoms are within the ionization zone, also called ionization disc, which has a width above the apex of $\sim 2.5 \text{ \AA}$ [132]. At sites where protruding atoms are present on the emitter apex, such as edges of crystallographic planes, the locally enhanced electric field leads to a positive ionization of the gas atom, which is directly repelled from the positively biased apex and accelerated towards

the counter electrode (detector) as shown in Fig. 3.12 **a** [124][131]. The image displayed on the detector, which usually is an MCP coupled to a phosphor screen, shows the gas atom ionization rate on the apex, which yields the position of single atoms depending on the emitter shape [132].

For the preparation and characterization of our emitters, we employ two separate FIM setups. The internal FIM (Sec. 3.5.1) is positioned within the preparation chamber of the LEEH setup and can be separated from the LEEH microscope chamber part via a gate valve. The external FIM (Sec. 3.5.2) is situated within another chamber and the UHV suitcase is used to transfer emitters from the LEEH setup to the external FIM and back. Both setups are described in detail in the following sections.

3.5.1 Internal FIM

The FIM in the preparation chamber of our LEEH setup (see Fig. 3.13 **a** and **b**) only contains a tip holder and an MCP detector with a sensor diameter of 4.0 cm, a channel diameter of 12 μm , an interchannel distance of 15 μm , and a bias angle of 6° (MCP-45-1-60-P43-CF100, GIDS).

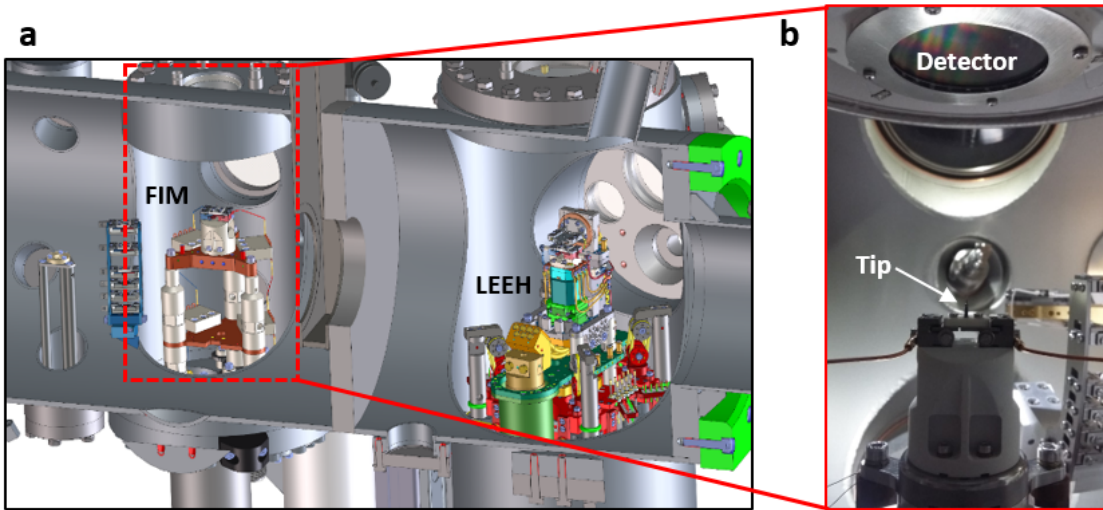


Figure 3.13: Images of the internal FIM setup: **a** Schematic of the LEEH setup. **b** Photo of the internal FIM acquired from the window on the back side showing the tip within the holder and the detector.

The distance between emitter and detector is around 6.2 cm depending on the tip length. Two needle valves (EULV075, MDC) with their respective gas lines are connected to this chamber part, allowing for simultaneous dosing of up to two different process gases. This setup enables field emission (Sec. 4.2.2), annealing (Sec. 4.2.1) and self-sputtering (Sec. 4.2.3) procedures, as well as FIM imaging (Sec. 4.2.4) of emitters. Since these processes are usually carried out at higher base pressures, the gate valve connecting the LEEH microscope chamber and prep chamber and the valve connecting the IGP to the prep chamber are closed before starting the respective procedure to prevent contamination of samples and saturation of the IGPs.

3.5.2 External FIM

In this section, I describe our external FIM setup, which allows for the annealing, field emission, self-sputtering, FIM characterization, and field-assisted nitrogen etching of our emitters (see Sec. 4.2).

While the possibility to perform FIM in the preparation chamber of our holography system is a very desirable option, it is not possible to measure LEEH while imaging or preparing emitters with it. For this reason, a separate FIM setup was developed. The FIM consists of a UHV chamber on a support frame with a standard background pressure of $2 \cdot 10^{-10}$ mbar, which is achieved via a pumping system including turbomolecular pumps (HiPace 300H and 80, Pfeiffer) and a pre-pump (MV 10 NT, Vacuubrand). The chamber contains a tip holder position (encircled in red in Fig. 3.14 **b** and **c**), a tip storage magazine for up to three emitters, a cryostat (He-Verdampferkryostat-40, VAb) enabling measurements at cryogenic temperatures, two gas inlets via needle valves (ULV150, MDC), which allow for simultaneous dosing of up to two different process gases, an MCP detector (MCP-45-1-60-P43-CF100-HR, GIDS) for the detection of FIM signals, and a load lock, which can be used to transfer emitters via a wobble stick inside the chamber or via a UHV suitcase to the LEEH setup.

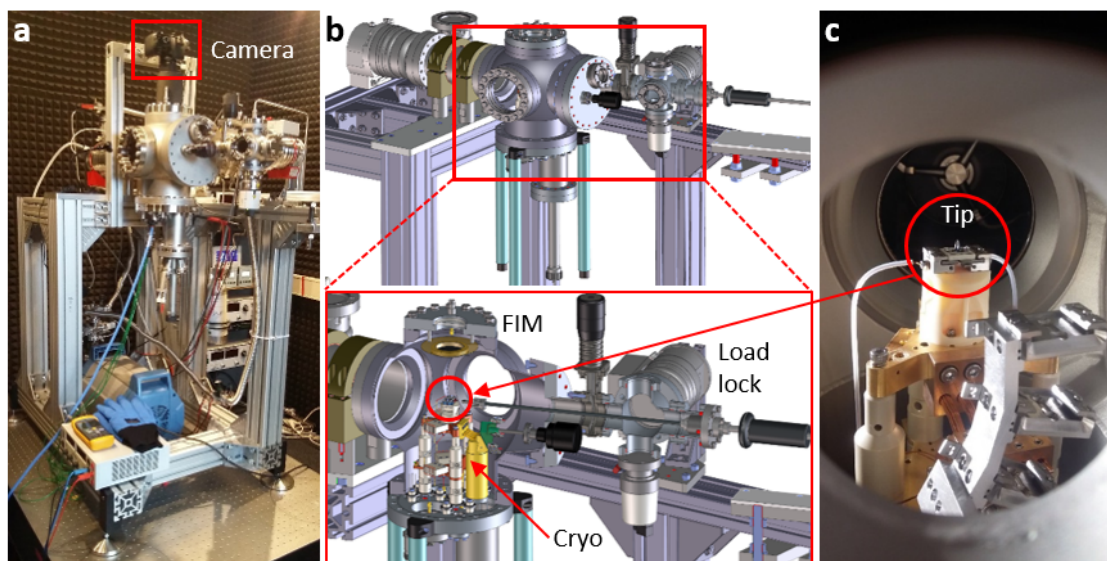


Figure 3.14: Images of the external FIM setup: **a** Photo of the setup. **b** Schematic drawing of the setup and its *in vacuo* parts. **c** Photo of the tip holder and storage magazine.

Fig. 3.14 shows the constructed FIM setup. The camera used for the image acquisition is a digital single-lens reflex camera (eos1100D, Canon), which is remote controlled using an open source software (digiCamControl). To apply high voltages to the emitter, a high voltage power supply (PNC 40000-1) is used, which allows for FIM imaging voltages up to 40 kV, if necessary. The cryostat is operated using liquid nitrogen, which enables FIM imaging and nitrogen functionalization at temperatures in the range of 100 K. This FIM setup is robust, flexible and perfectly suited for the preparation, characterization and improvement of our

emitters. The general FIM procedure is described in Sec. 4.2.4.

3.6 LEEH Workflow

After having discussed the details of our experimental setup, I provide an overview of the general workflow of our experiments that allows the investigation of molecular structures using our LEEH microscope. The workflow can be divided into several steps, as shown in Fig. 3.15. Before explaining these steps, it is worth to state that this part is not meant to be a comprehensive discussion, but rather introduces all the aspects, which will be further clarified in the following chapters.

At the beginning of each experiment, an emitter with high-quality emission properties is necessary. The emitter can be already characterized and stored within the LEEH setup or freshly prepared via electrochemical etching, as discussed in Sec. 4.1 (step [1]), and subsequently characterized and further prepared in UHV, as described in Sec. 4.2 (step [2]). As long as their emission quality is satisfactory, emitters are re-used to image different samples and, in case required, occasionally annealed and/or sputtered to restore their performance.

The next step is the substrate preparation, which is described in Chap. 5 (step [3]), and its subsequent characterization via LEEH (step [4]). Our substrate consists of a metal coated TEM grid covered by single-layer graphene (SLG) and is prepared at ambient conditions. As soon as the substrate is transferred into the UHV setup via the FTLL, it is characterized using the LEEH microscope and screened to confirm the quality of the surface. Several holes are imaged and their positions on the array are recorded. In this way, the same holes can be found and imaged again after deposition, revealing which signals on the SLG originate from freshly deposited molecules. During this first screening, holes in which the SLG is covered by contaminants, defects and/or not properly covered by SLG are also noted and will not be further investigated after the molecular deposition. For the deposition itself, the samples are transferred to the respective setup or deposition station (step [5]) and transferred back to the LEEH system afterwards. Usually, a vacuum suitcase is employed for the transfer, which is connected to the setup via the suitcase load lock (SCLL). The transfer is taking place after the SCLL reached a pressure below $2 \cdot 10^{-8}$ mbar to avoid contaminations on the sample during transfer. Each molecule deposition is carried out on an freshly prepared substrate to avoid ambiguous results due to a mixture of different deposited molecular species. Details about the different deposition methods used for the results presented in this thesis are discussed in Chap. 6.

The general measurement procedure consists of the following actions: In the beginning, the sample and emitter are placed in their respective holder positions in the LEEH microscope head, while a tunable voltage can be applied to the tip. Subsequently, the power supplies of the detector are set to the respective positive bias, which is around 900 – 910 V for the MCP out (via PNC 1500-40, Heinzinger) and 4.90 kV for the screen (via PNC 6000-19, Heinzinger).

It is important to mention that the voltage difference between MCP out and screen should never exceed 4 kV to avoid a spark-over, which can damage the sensitive MCP channels. Subsequently, the emitter power supply (2657A, Keithley) and piezo motor controller (ANC300, Attocube) are turned on. After their initialization, our custom-built remote control software handles the tip emission and positioning control (see Sec. 3.4). The camera is connected to its remote control software (ControlMyNikon version 5.4) and is used to record images of the detector screen.

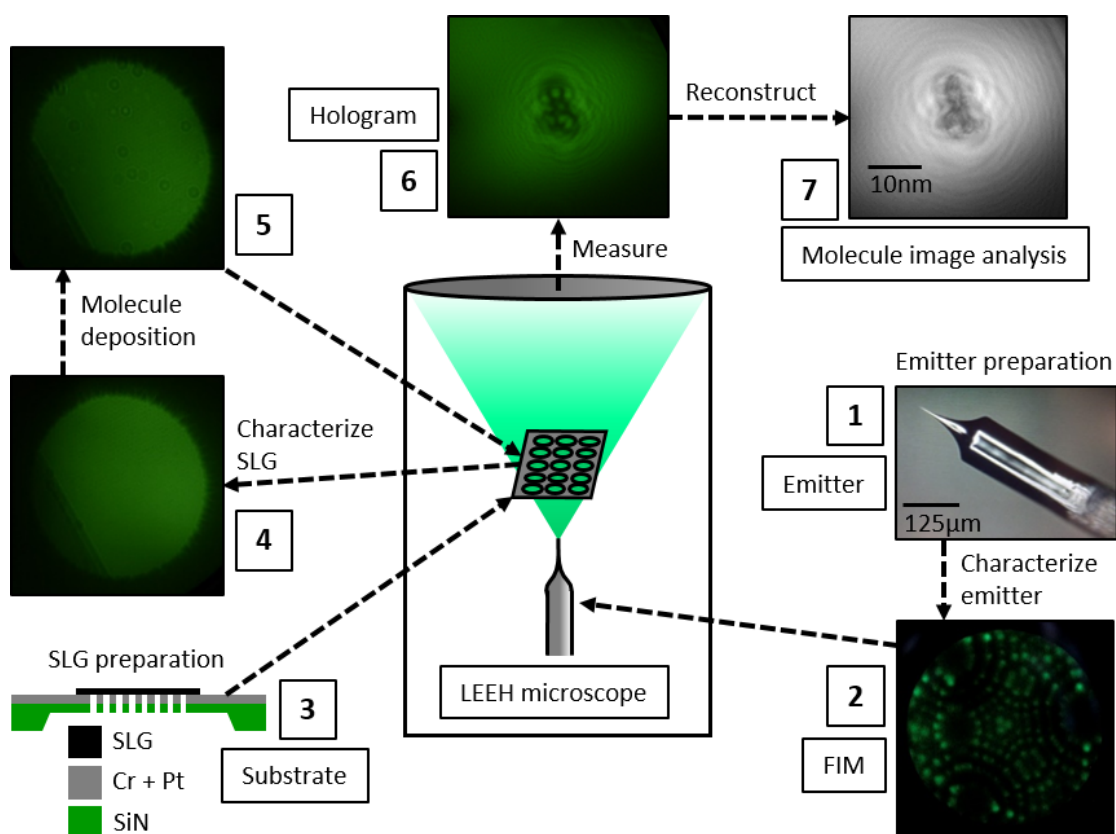


Figure 3.15: Experimental LEEH workflow steps: Electrochemical etching and UHV preparation of the emitter [1], emitter characterization (e.g. via FIM) [2], substrate preparation [3], SLG characterization via LEEH [4], sample transfer and molecule deposition (e.g. via ES-IBD) [5], molecule measurement via LEEH yielding hologram images [6], hologram reconstruction and data analysis [7].

Afterwards, an initial emission current in the range of 10 – 50 nA is set in the control software and the voltage applied to the emitter is regulated by the power supply to match the requested emission current. After the voltage stabilized at its field emission value, a signal, which is usually a projection of the holey array on the substrate membrane, appears on the detector and is visualized on the PC screen via the live-view of the camera. Moving the emitter laterally (in x and y) via the piezo motors allows the main illumination area of the tip, where the signal is brightest, to be found. Then, the emitter is moved towards the sample (z -direction) while checking the camera live-view until the desired tip-to-sample distance is reached. At far distances, the emitter is usually moved using the continuous mode of the piezo motors,

while at closer distances only single steps of approximately 300 nm are taken. For steps in a distance range of one micron and less (i.e. when only a single hole is visible during the approach), the fine positioning mode of the piezo motors with step sizes of about 8 nm is used for the further navigation in all three directions to avoid sudden movements, which can cause possible tip-sample crashes.

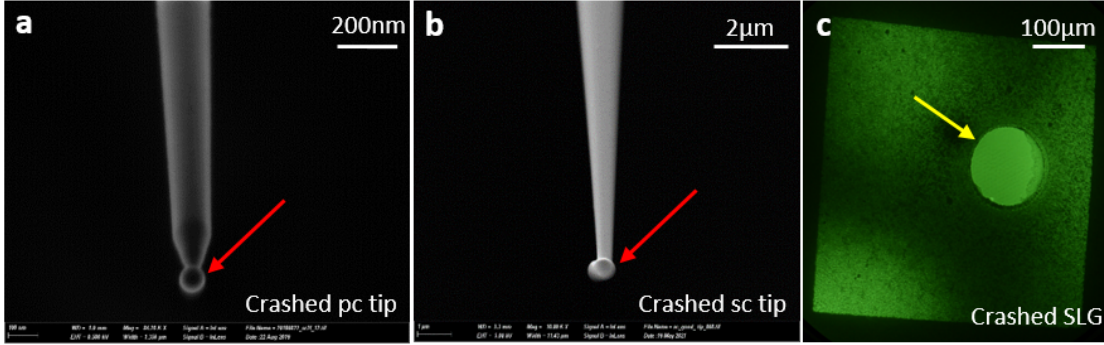


Figure 3.16: SEM images of a crashed pc emitter at 25.000 \times magnification (a) and sc emitter at 10.000 \times magnification (b) showing a ball-like apex indicated by the red arrows. Both tips did not emit after the substrate contact. c LEEH image of a crashed substrate membrane, where a hole with a diameter of around 130 nm was ripped into the substrate upon contact (marked by the yellow arrow).

Uncontrolled contact of the sample with the emitter is the highest risk during LEEH measurements, since it can lead to the damaging of the emitter apex and sample as shown in Fig. 3.16. Usually, a short spark-like signal is visible on the screen upon crashing, which is followed by an increase in field emission voltage up to the compliance limit of the power supply followed by the complete loss of signal at the detector, when measuring in the constant current mode. The spark-like signal originates from the short-circuit between the grounded sample and the tip. The emission properties of the emitters are generally compromised. This can be explained by the deformation of the tip apex upon crashing, which happens due to the mechanical stress and/or the melting of the apex due to a power discharge through a nanometric junction during contact. This effect appears to be similar to the deformation caused by annealing at too high temperatures [131][134][135]. As shown in Fig. 3.16 a and b, the ball-like apex after contact has diameters in the range of 50 nm up to several hundred nanometers, which would need high voltages, beyond the limit of the power supply used to establish any field emission, as discussed in Sec. 4.2.2. However, careful contacting can also lead to a tip functionalization via the uptake of CNTs or SLG depending on the used sample, see Sec. 4.2.5.2 and 4.2.5.3.

As soon as the tip-to-sample distance is in the holographic regime (i.e. around 500 nm and closer), the main valve of the chamber (see Fig. 3.1 a, marked by the red arrow) is closed and the turbo pumps are turned off to minimize vibrational noise acting on the sample. Meanwhile, the IGP's keep the chamber at UHV conditions during the measurement. Afterwards, the acquisition of hologram images can begin by capturing the fluorescence emitted from the detector screen with the camera, as described in Sec. 3.3 (step [6]). For SLG characterization, it is sufficient to acquire overview images showing the complete hole. In the case of

single-molecule measurements, the distance is adjusted until the target object is within the illumination area with as many fringes visible as possible.

Typical imaging currents are in the range of 10 – 50 nA and depend on the emitter performance. At close measuring distances (500 nm and less), this corresponds to a current density of 1 – 5 pA/nm² or 0.6 – 3.1 · 10⁷ electrons s⁻¹ nm⁻² for an illumination area of 100 × 100 nm². At these electron doses and low emission energies, molecules can be measured for long time periods in the order of hours to days without noticable contamination and/or taking observable damage [41][51][136]. Furthermore, since the molecules usually stay in their respective positions even for long measurement durations, the molecules can be revisited and imaged up to several weeks after the initial measurement.

The final step is the numerical hologram reconstruction via the algorithm presented in Sec. 2.1 and molecule analysis explained in Sec. 3.3 (step [7]). The reconstructed images show the amplitude signal of the respectively measured molecule species, as shown for different emitters in Sec. 4.2.6.1 and various molecular systems in Chap. 7.

4 Emitter Preparation and Characterization

The experimental detection of the free electron by J. J. Thompson in 1897 opened up several important branches of classical as well as modern physics leading to our current technology, many of which are based on the use of electrons and their properties for a broad variety of applications from computers to microscopes [137]. The extraction of electrons from materials can be achieved via different methods such as thermal-, photo-, and field emission. These methods are usually applied in vacuum to guarantee a longer mean free path of the electrons after leaving the material [138]. Thermionic emission utilizes the Edison effect where a metal filament is heated until the thermal energy overcomes the work function of the metal [139]. Photoemission is based on the irradiation of a metal or semiconductor surface using light to extract electrons [140]. For field emission, a strong electric field is applied to a metal antenna to overcome the potential barrier of the surface leading to the emission of electrons. The antenna is usually a sharp tip to reduce the required voltage at the emission source [138].

For microscopic imaging techniques such as transmission electron microscopy (TEM) [141] and scanning electron microscopy (SEM) [142], free electrons are typically generated via field emission. Electron beam methods offer the advantage to be capable of reaching very high resolutions due to short wave lengths, if compared to light-based optical microscopy. The resolution limits of transmission electron microscopes, which use beam energies in the range of tens to hundreds of keV, is indeed limited by spherical and chromatic aberrations occurring in the electron lenses [141]. In contrast, the resolution in a lens-free low-energy electron holography (LEEH) microscope is determined by various factors, as discussed in Sec. 2.3 [28]. Low emission energies of 50 – 150 eV correspond to larger de Broglie wavelengths of 1.7 – 1.0 Å compared to the high electron energies used in TEM, which confine the theoretical resolution limit of the beam. The emitted electrons need to be coherent to enable interference and hence the formation of fringes in the interference pattern of the hologram. The more coherent the beam is, the more detailed low- and high-order fringes are generated in the hologram, which affects the final resolution after reconstruction. Further necessary electron beam properties include emission stability and a large emission angle during the measurements [143].

All of the aforementioned properties are affected by the emitter quality. Therefore, the emitter preparation is a critical step in our workflow. The initial tip preparation from a thin precursor wire can be based on mechanical procedures including cutting [144] and machining [145], physicochemical processes such as ion milling [146], electrochemical etching [147], as well as electron beam deposition [148]. Mechanical preparation methods do not lead to uniform and sharp tip apices in general and both ion milling and deposition techniques are time consuming and challenging to obtain microscopically sharp emitters. On the contrary, electrochemical etching is a fast and reliable process for obtaining symmetrical and sharp field emitters [149]. Therefore, we employ the electrochemical etching technique for our emitters; the procedure is further discussed in Sec. 4.1.

Several metals such as tungsten, gold or platinum-iridium alloys qualify as material for the emitters. However, tungsten has been shown to be the material of choice for emitters to be used in LEEH. Tungsten has a high mechanical strength, which is preferable for the preparation of a thin and stable emitter. It can withstand high temperatures, which are commonly used during cleaning procedures via annealing. Furthermore, it can be prepared as an electron point source enabling the emission of a stable and highly coherent low-energy electron beam [26].

In the following sections, I present an emitter preparation protocol as well as characterization methods yielding sharp tungsten tips, which function as coherent low-energy electron sources in LEEH imaging. We use polycrystalline and single-crystal tungsten tips, which are electrochemically etched (Sec. 4.1) and further prepared and characterized in ultra-high vacuum (Sec. 4.2).

The resulting emitters work well for emission energies in the range of 50 to 150 eV with sufficiently high beam angles ranging from 7° up to 30° (maximum detectable angle of the microscope). Furthermore, I show that the emission stability, as well as the emission voltage range and imaging quality of the tips, can be improved by working at cryogenic temperatures. The presented ultra-sharp tungsten emitters enable reliable and non-destructive LEEH imaging of various single molecules at resolutions in the range of a few angstroms.

4.1 Electrochemical Etching

Here, I introduce the electrochemical etching technique used to obtain sharp electron emitters from blunt tungsten wire. I explain the electrochemical reaction steps, the etching parameters to be used and I focus on challenges, which have to be overcome for a reliable and efficient preparation process. The resulting tips have typical apex radii in the range of a few nanometers as shown via SEM and are further processed in UHV before usage in LEEH.

The electrochemical etching of tungsten tips is a well-known procedure mainly used in scanning probe and field ion microscopy, which can yield emitters with apex radii in the range of a

few nanometers to several microns. In general, a thin precursor wire, which is the anode, as well as a counter electrode, which is the cathode, are immersed in an alkaline caustic soda solution. A direct current (DC) voltage is applied to the electrodes. During the electrochemical process, the part of the wire close to the surface and next to the meniscus is etched most, which eventually leads to a break-off of the lower wire part resulting in two tip pieces [150].

We utilize both > 99.95% pure polycrystalline and single-crystal tungsten wires with a diameter of 0.125 mm (W005140 and W002130, Goodfellow), which is cut into pieces with lengths in the range of 3 – 5 mm. Each piece is spot welded on a respective arc-shaped tantalum wire with a diameter of 0.25 mm (TA005135, Goodfellow). The arc is fixed on a custom designed tip holder, which separates both wire parts of the arc to prevent short-circuits when applying a voltage to either side (see Fig. 4.1). The holder is attached to a tip etching station (Tip Etching Control Unit 058, Omicron Nanotechnology), which is positioned on the granite block of a vibration isolating table (Sartorius) and 20 wt% caustic soda solution is added to the reaction beaker. The counter electrode consists of a 3 mm wide, 0.5 mm thick ring-shaped tungsten sheet, which is partly immersed in the etching solution.

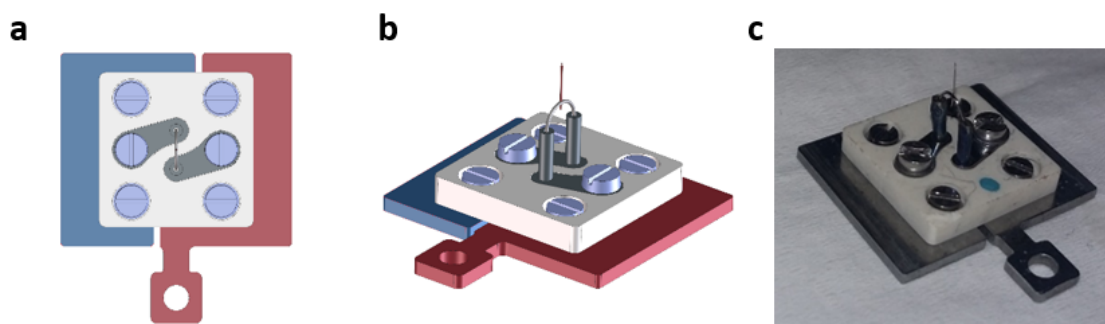
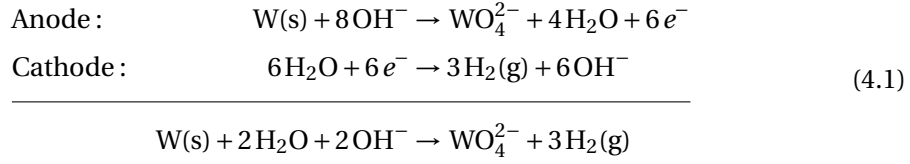


Figure 4.1: Schematic drawings **a** (top view), **b** (side view) and photo **c** of the tipholder used for our LEEH setup. The tantalum arc containing the spot welded tungsten wire piece is fixed on the holder via crimping. The respective attached connection plates (red and blue in the schematics) are isolated from each other, enabling current flow through the arc and hence the tungsten emitter. The width of the tip holder is 12 mm.

We use the differential etching mode, which tracks the current change during the process and contains an electronic cutoff circuit to immediately stop the process after a current breakdown. The etching voltage is set to +8.9 V, which we found to be working consistently well for our emitters. The differential sensitivity is set to an arbitrary value of 7.5 for a short pre-etching procedure. For pre-etching, the wire is immersed 1 mm into the solution and etched for 5 – 6 s to remove tungsten oxide and contaminants on the outer layer of the wire. Here, the measured current is usually in the range of 5 – 30 mA. Afterwards, the wire is cleaned using deionised water and re-immersed into the etching solution with an immersion depth of 0.4 – 0.6 mm. After increasing the differential sensitivity to an arbitrary value of 8.6, the etching process is started. Fig. 4.2 **c** shows the general etching process. The immersed wire forms a meniscus with the aqueous solution due to surface tension. Tungstate anions (WO_4^{2-}) are generated by the oxidation of tungsten at the anode as shown in the redox equation 4.1.



During the process, tungstate ions flow as an anodic film from the meniscus to the bottom part of the wire forming a viscous layer, which inhibits further etching of the lower anode [151]. While tungsten is continuously dissolved at the anode, hydroxide ions (OH^-) and gaseous hydrogen are formed at the cathode by the reduction of water molecules. The formed OH^- ions diffuse from the cathode towards the anode, where the highest OH^- concentration is in the immersed region of the anode below the meniscus. Due to both of these effects, the etching rate is highest just below the etchant surface resulting in a neck formation at the anode. Consequently, the neck becomes thinner during the etching process until the weight of the immersed bottom part surpasses the tensile strength of the wire and the breaking point is reached [152].

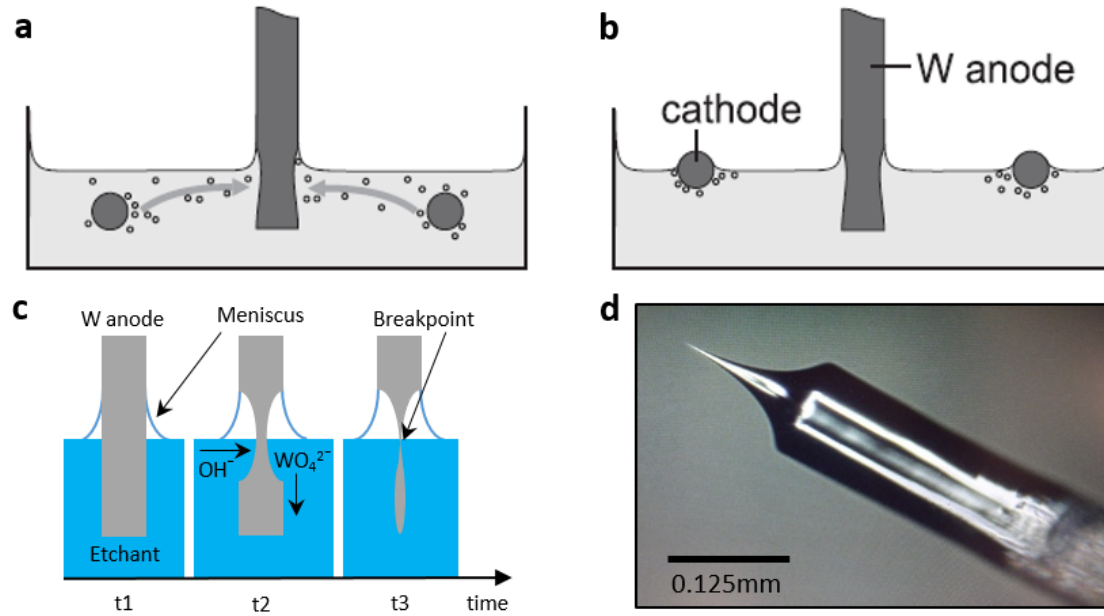


Figure 4.2: Overview of the electrochemical tip etching procedure. **a** Hydrogen diffusion towards the anode during etching for a fully immersed cathode. **b** In case of a partly immersed cathode, the formed hydrogen does not reach the anode during etching [134]. **c** Overview of the complete etching process over time. During etching, OH^- ions are diffusing towards the anode while WO_4^{2-} ions are flowing down along the anode (t2). Etching is stopped as soon as the lower wire part is severed from the upper one at the breakpoint (t3) [152]. **d** Optical microscopy image of a polycrystalline tungsten emitter after the etching procedure.

While the reaction is ongoing, the measured current at the etching control unit decreases linearly until the breaking point as the amount of tungsten at the anode is reduced [149]. The measured starting current is usually in the range of 4 – 6 mA and decreases to 0.5 – 2.0 mA

during the process. At the breakdown, the current shows a sudden non-linear decrease, which is detected by the etching station. The integrated electronic cutoff-circuit immediately stops the process to prevent further etching and thus blunting of the generated tip. A higher set differential sensitivity enables a faster detection of the current drop, resulting in a faster interruption time in the range of several nanoseconds and thus a sharper emitter. However, if the sensitivity is set too high, the slightest current change may stop the reaction, which is why the sensitivity has to be adapted for each process. For an immersion depth of 0.4 – 0.6 mm at an etching voltage of +8.9 V, we found that differential sensitivity values in the range between 8.3 and 8.6 work best. After the etching is finished, the upper etched emitter part, which is connected to the tip holder, is taken out of the etching solution and rinsed with deionised water to remove salt and ion residues. Subsequently, the tip is examined using an optical light microscope (VHX-2000, VHX) as shown in Fig. 4.2 d.

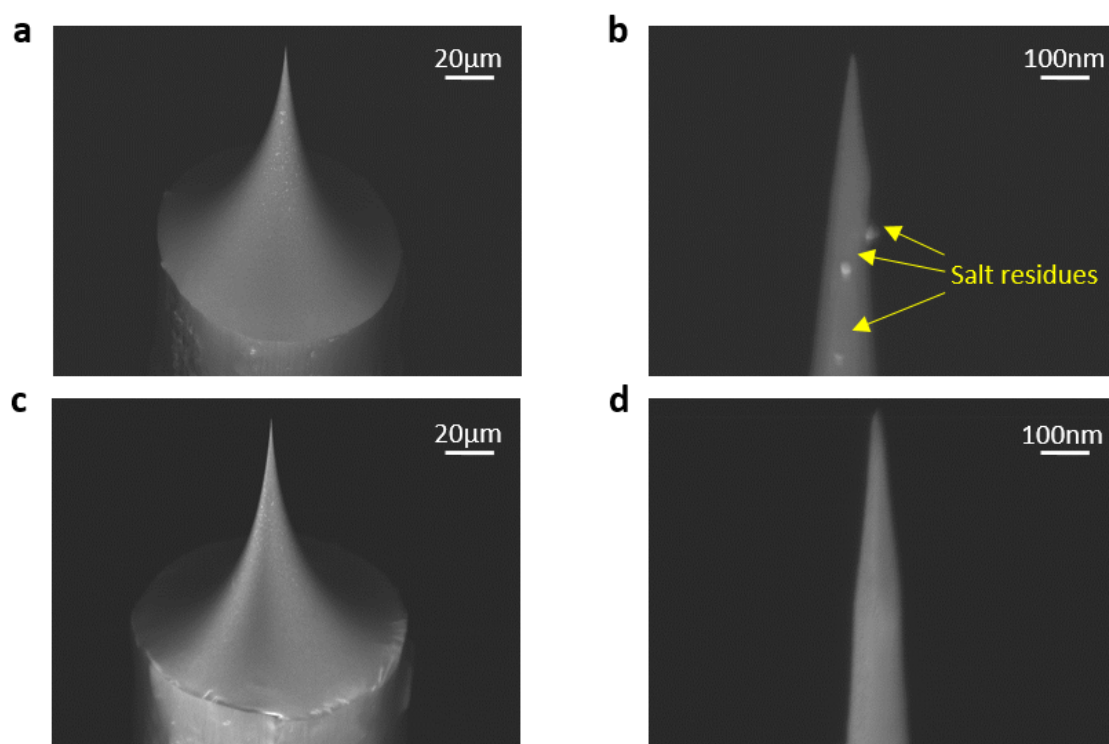


Figure 4.3: Overview of two different electrochemically etched tips imaged via SEM at different magnifications. The tip shown in **a** at 500 \times magnification and **b** at 115.000 \times magnification was not cleaned with deionised water after etching and salt residues close to the apex are visible. In contrast, the tip shown in **c** at 600 \times magnification and **d** at 111.000 \times magnification was thoroughly cleaned using deionised water resulting in a residue-free apex. Both tips show a good axial symmetry and have apex radii of 7 nm (**b**) and 10 nm (**d**) respectively. All SEM images were acquired *ex situ* using a Zeiss Gemini SEM 500 (Zeiss Merlin) microscope.

To get an uniformly etched tip shape, vibrations acting on the meniscus and etching solution have to be minimized. Two major factors disturbing the process are vibrations from the support table of the etching station and vibrations originating from the chemical reaction. We minimize mechanical noise by using a vibration-isolated support table containing a heavy

granite block upon which the etching setup is placed. The granite block itself is connected to the table via rubber pieces to damp high-frequency noise. Regarding the chemical reaction, hydrogen, which is formed at the cathode during the etching process, can diffuse towards the tungsten anode, disturbing the meniscus and solution surface, thus interfering with the process and leading to uncontrolled etching behaviour as shown in Fig. 4.2 **a**. This effect can be minimized in two ways: First, we use a circular, ring shaped counter electrode as cathode surrounding the tip, which is positioned in the center of the cathode. This leads to a more homogeneous reaction affecting the whole circumference of the anode equally. Second, the cathode ring is only partly immersed in the etchant, which limits the possible migration of formed hydrogen bubbles towards the anode wire as shown in Fig. 4.2 **b** [153][134].

With these adjustments, we observe no disruptions of the reaction process and are able to obtain symmetrically shaped, sharp emitters with tip apex diameters in the range of 10–20 nm as shown via SEM measurements, see Fig. 4.3 **a** to **d**. While most salt residues can be removed via cleaning the tips with deionised water post-etching (Fig. 4.3 **d**), the surface of the tungsten emitters oxidises and thus gets contaminated by a tungsten trioxide (WO_3) layer, which is insulating and can inhibit electron emission [135]. To minimize the formation of thick WO_3 layers, the tips are usually transferred to vacuum within a few minutes after etching. However, additional preparation steps in UHV are carried out to remove contaminants and improve the emission quality of the emitters before usage in LEEH, as explained in the following Sec. 4.2.

4.2 UHV Preparation and Characterization

After the electrochemical etching procedure, further tip improvement and characterization steps are carried out in UHV inside our LEEH microscopy chamber (Sec. 3.5.1). Additionally, we use a separate FIM setup in case the LEEH setup is in use for measuring (Sec. 3.5.2).

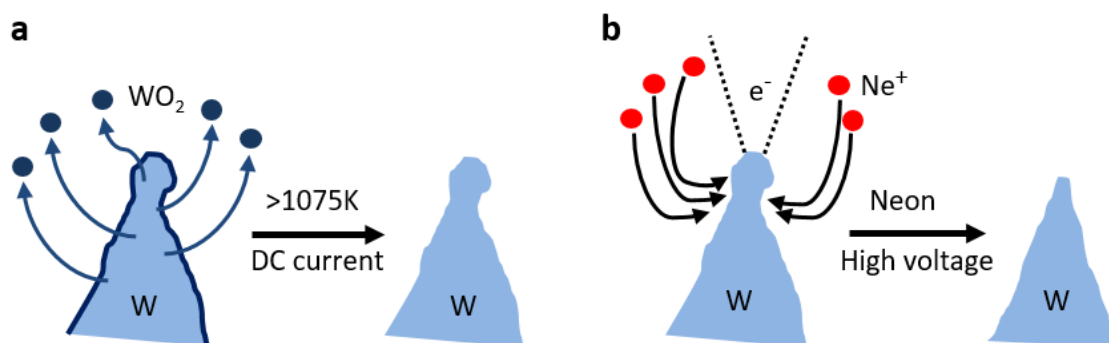


Figure 4.4: Schematic overview of the annealing (**a**) and sputtering (**b**) procedures of tips in UHV. Annealing is used to remove solvent residues and WO_3 layers from the tip surface, while sputtering with neon is used for additional emitter shaping and sharpening.

Both setups allow for the following preparation and characterization procedures: field emission to check for the emission voltage and stability; annealing to remove possible contaminations from the emitter surface and increase the emission voltage (see Fig. 4.4 **a**); self-sputtering

to reshape and reduce the emission voltage of the emitter apex (see Fig. 4.4 **b**); reactive nitrogen etching to further stabilize and protect the emitter apex; and field ion microscopy (FIM) to determine the atomic structure at the tip apex. On occasion, we use SEM to investigate the shape of selected emitters on the macroscopic to microscopic scale.

4.2.1 Annealing

The controlled heating of metal surfaces to remove contaminants or reshape the surface is called annealing. In this section, I explain the basics of tip annealing and why we use direct resistive annealing for our emitters in UHV. I give details about used parameters and processes happening during the procedure. Furthermore, I show the practical limits of this method (e.g. via SEM images) and how to avoid undesired detrimental effects.

As discussed in the previous section, the formation of tungsten trioxide layers during the electrochemical etching, as well as via oxidation of the tungsten tip in air, can inhibit the field emission of tips, since WO_3 acts as an isolating barrier. Furthermore, other contaminants such as residual etching solvent, salts and water from the cleaning process may contaminate the emitter surface, thus altering or corrupting the emission properties [154].

There are two main methods used in UHV to anneal electron emitters such as tungsten tips: heating by electron bombardment and direct resistive annealing. For electron bombardment annealing, a looped filament is positioned in close distance (usually a few millimeters) above the tip. The looped filament is resistively heated to induce thermal electron emission. Meanwhile, a positive high voltage is applied to the tip which generates an electric field accelerating the electrons from the filament towards the tip. When hitting the tip apex (where the field gradient is largest), the electrons are decelerated and the energy difference is released in the form of heat, which locally affects the tip apex [135].

For direct resistive annealing, a DC voltage is applied to the tip, which is connected to the closed circuit of a power supply. The resistance is highest when passing through the thinnest conductive circuit piece, which is the tip holder part connected to the emitter wire. In our case, the tantalum arc with the spot welded tungsten tip has the highest resistance leading to a gradual heating of the whole tip depending on the set current flow [155].

The disadvantage of electron bombardment is its local heating ability, which allows for residue diffusion from the non-heated shank part towards the apex during measurements which can generate emission instabilities [155]. For this reason, we chose to use the direct resistive heating as annealing technique. When thoroughly cleaned after etching, residues such as salt crystals can be removed from the tips as shown in SEM images (Fig. 4.3). We found that the main contaminant left on our emitters is a thin layer of tungsten trioxide, which forms during etching and could not be identified via SEM. When heating the emitter to temperatures above 1075 K, WO_3 is efficiently reduced to volatile WO_2 as shown in reaction 4.2 and Fig. 4.4 **a** [154]:



Resistive heating is conducted with a power supply (PS 2342-06B, Elektro-Automatik GmbH) in voltage control mode. Because of the material emission during the procedure, we close the valves connecting the ion getter pumps (IGPs) to the chamber to avoid saturation of the IGPs due to high background pressures of up to $2 \cdot 10^{-6}$ mbar. While ramping up the voltage, the current going through the circuit also increases until the tungsten tip and supporting tantalum arc start to glow due to blackbody radiation. We estimate the annealing temperature via the blackbody radiation color scheme: start of glowing at around 900 K with a dark red color, followed by orange color emission between 1170 to 1300 K and a yellow color emission at roughly 1370 K [156]. Since our power supply has a current limit of 6 A, temperatures above 1370 K, resulting in an emission of white light, were rarely reached. With a melting temperature of tungsten at 3695 K, melting of the tip should not happen at our applied annealing temperatures. However, diffusion of surface atoms already takes place at much lower temperatures and can lead to a smoothening of the tip surface which might blunt the tip (see Fig. 4.5) [157].

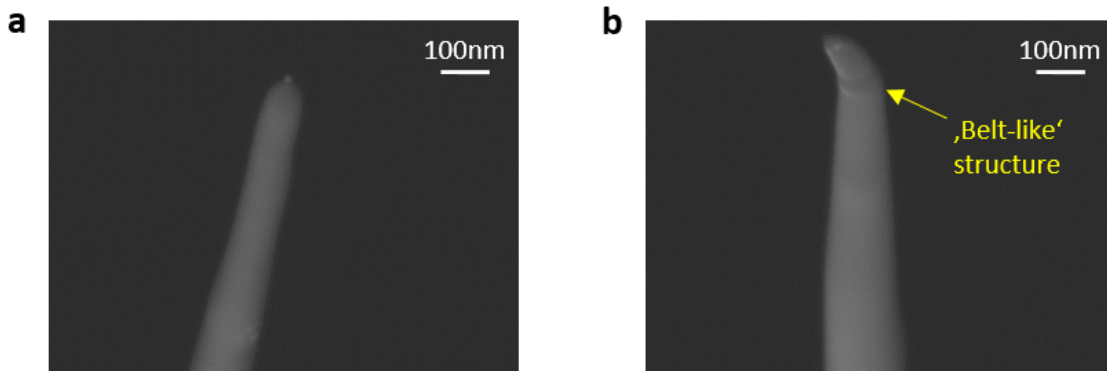


Figure 4.5: Overview of two different heavily annealed tips imaged via SEM at high magnifications. The tip shown in **a** at $116.000\times$ magnification was annealed at a high temperature above 1370 K (yellow-white color) for 5 s. The apex has a diameter of roughly 90 nm and is blunted as indicated by the round shape. The tip shown in **b** at $113.000\times$ magnification was annealed at a temperature in the range of 1200 to 1300 K (orange color) for 2 mins. The apex has a diameter of 50 – 60 nm and is blunted and deformed. The belt-like structure just below the apex indicates for an ongoing reshaping of the tip during annealing. Both tips were field emitting before the annealing procedure. After heating, neither of them was field emitting anymore, most probably due to the large apex diameters as well as the deformation of the tip shown in **b**.

By testing different temperatures and annealing durations, we established a reproducible protocol consisting of two annealing steps. First, the tip is annealed for 2 – 3 s at an orange to bright orange glow (around 1200 – 1300 K) to remove the WO_3 layer. The current values for this step are usually in the range of 4.5 – 5.5 A for applied voltages between 1.5 – 2.5 V depending on the individual tip. For the second step, the current is reduced to 3 – 4 A, leading to a dark red or even no color emission, and kept for 10 – 30 s. During this step at lower temperatures, remaining residues can degas without the risk of blunting the tip. When heating

the emitters at too high temperatures (above 1370 K) or for longer durations (i.e. several minutes) at temperatures with orange color emission, tip blunting occurs due to diffusion of tungsten atoms from the apex to the shank region. This results in misshaped apices with large radii above 20 nm as shown in SEM images in Fig. 4.5, which compromises the performance of the emitters.

We always anneal the emitters after electrochemical etching before testing the respective tip for its field emission properties. Furthermore, the more gentle heating procedure is also repeated for sputtered emitters and for emitters stored in UHV for several days before being used. The procedure helps to remove adsorbates and thus usually improves the emitter stability. After annealing, the field emission voltage of the annealed tip is checked to assure that no blunting or damaging occurred during the procedure, which is described in detail in the next section.

4.2.2 Field Emission

In our setups, we check the field emission voltage of newly etched tips. These values provide a first indication on the emitter quality. Additionally, they serve as reference for evaluating possible tip changes after the emitters are used for measurements. The field emission voltage and its stability are important parameters that can indicate the need for an annealing and/or sputtering procedure to improve the emitter quality. In the following, I briefly summarize the basics of field emission before describing our setup and how field emission could function as a fast screening test providing crucial information about the emitter quality.

Field emission describes a quantum mechanical phenomenon where electrons are emitted at a metal-vacuum interface by applying a strong electrostatic field to the metal. In general, metal electrons reside in a potential well, which is primarily explained by their attractive interaction with the positive metal nuclei. To escape the metal surface, the electron needs a minimum energy to overcome the potential barrier of the metal, namely the work function. The two main factors influencing the work function are the inner potential of the metal, which is a material property, and the electrostatic potential [124].

In contrast to thermionic and photoemission, where the electrons are provided with enough energy to overcome the potential barrier, field emission is based on the deformation of the potential barrier via an applied external field, which allows unexcited electrons to tunnel through. Since the work function is depending on the metal, as well as its crystallographic structure at the surface, the strength of the electrostatic potential necessary for electron emission also varies. Furthermore, the electron interacts with a mirror charge forming on the surface upon emission, which is based on coulomb interaction as soon as the electron left the surface [158].

Figure 4.6 shows the potential landscape of the metal-vacuum interface, where Φ is the work function of the metal surface, E_F is the Fermi energy and Φ_{eff} is the effective potential

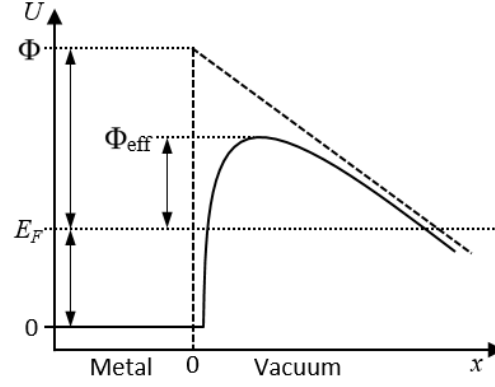


Figure 4.6: Schematic showing the influence of an electric field applied in x on an electron at a metal surface. The electron has to overcome the work function Φ of the metal. The effective potential Φ_{eff} is lower than the potential without accounting for the mirror charge effect (dashed line).

influenced by the mirror charge and an external electric field [159]. The total effective potential U_{eff} at the surface can be described via equation 4.3, where the $1/x$ term is the interaction of the electron with its mirror charge after leaving the metal and F is the applied electric field:

$$U_{\text{eff}}(x) = \Phi - \frac{e^2}{4x} - Fex \quad (4.3)$$

As equation 4.3 shows, the barrier width decreases for a stronger applied electric field, which increases the probability for an electron to tunnel through and leave the metal surface. In 1928, Fowler and Nordheim derived that the field emission current density j can be described as a function of the applied field F and the work function Φ [159][160]. Including the correction factor ξ , which accounts for the mirror charge interaction and has a value range between 0 and 1, the Fowler-Nordheim equation is given in Eq. 4.4 [161].

$$j = \frac{e^3}{2\pi h} \frac{(E_F/\Phi)^{\frac{1}{2}}}{\xi^2(E_F + \Phi)} F^2 \exp\left(-\frac{8\pi\sqrt{2m}}{3eh} \frac{\xi\Phi^{\frac{3}{2}}}{F}\right) \quad (4.4)$$

Equation 4.4 describes a low temperature scenario (0 K) where a high electrostatic field is applied on an infinite plane emitter. However, one can use the relation as an approximation for the emission of electrons from a metal tip at ambient temperatures (~ 300 K) when relating the tip geometry to the emission current. The electrostatic field at a tip-shaped object can be approximated with $F = \frac{V}{kr}$ where V is the applied voltage, r is the apex radius and k is a geometrical field reduction factor due to the tip shank below the apex. To get the field dependence of the total emission current, one can replace the constants of equation 4.4 with numerical values and use the above mentioned relation for F . This leads to the simplified expression 4.5 with V in volts, tip radius r in m and work function Φ in eV [134], which we apply to the measured values of our emitters.

$$I \propto \left(\frac{V}{kr} \right)^2 \exp \left(-6.8 \cdot 10^9 \Phi^{\frac{3}{2}} \frac{\xi kr}{V} \right) \quad (4.5)$$

In the following sections, I present field emission results of several example emitters, which were measured at room temperature (Sec. 4.2.2.1) and cryogenic temperatures (Sec. 4.2.2.2).

4.2.2.1 Field Emission at Room Temperature

To measure field emission in our LEEH setup (Sec. 3.1) we are able to use two high voltage power supplies. The power supply in our preparation chamber (Sec. 3.5.1) has a maximum output voltage of 20 kV (PNC 20000-3, Heinzinger). Our LEEH microscopy chamber (Sec. 3.1.2) utilizes a high precision power supply (Keithley 2657A, Keithley), which has a maximum output voltage of 1.5 kV. In our external FIM setup (Sec. 3.5.2) we utilize a high power supply with a maximum output voltage of 40 kV (PNC 40000-1, Heinzinger). For field emission, we connect the voltage supply to one side of our tip holder. When applying the voltage, the emission current measured at the power supply can be monitored. For the high voltage power supplies with maximum output values of 20 kV and 40 kV, the counter electrode (which is basically the MCP detector) is placed 6.2 cm and 7.2 cm away from the tip, respectively. In both cases a maximum threshold of 10 μ A is set for the emission current. For the voltage power supply in the LEEH microscope, the sample plate is used as counter electrode. The tip-to-sample distance at the most retracted position varies between 7.5 mm and 2.5 mm depending on the tip length. Here, the threshold current is usually set to 50 nA, but can also be increased up to 300 nA if necessary.

The voltage is ramped up, until the respective threshold current is reached and the emission stability is monitored for several seconds to minutes. If the voltage necessary for emission of the threshold current exceeds 4 kV when measured in the preparation or FIM chamber, or exceeds 1.2 kV when measured in the LEEH chamber, the tip is considered as too blunt for a reasonable emission. At this point, the emitter can be sputtered to reduce its emission voltage or can be electrochemically re-etched. However, some emitters show initial emission voltages of up to 9 kV (for a threshold current of 10 μ A), which slowly decrease during field emission. This process usually continues for a few minutes until a final emission voltage in the range of 2 – 4 kV is reached. This effect has been reported before and can be related to two specific reasons [162]. Firstly, an emission current of 10 μ A can lead to a local temperature increase at the apex. This local heating can remove leftover residues and oxide layers, which might not have been properly removed by the annealing procedure, thus cleaning the tip and reducing the voltage needed for the set emission current [131]. Secondly, heating the tip apex while a strong electric field is applied can result in the diffusion of atoms from the shank towards the apex. This effect is based on a surface field gradient forming along the tip surface while emitting. The diffusion flux at the surface is mainly directed from low field strength regions towards high field strength regions, thus surface atoms are moving from the tip shank to its

apex [157].

For emitters with emission voltages below 4 kV in the preparation or FIM chamber, the field emission behaviour in the LEEH microscope can be tested. In the LEEH microscope head, the tip is placed below a sample plate, with a final tip-to-sample distance in the range of 2.5 – 7.5 mm as stated before. The sample plate acts as counter electrode and the distance between emitter and sample is significantly shorter when compared to the setups in the preparation and FIM chamber. Since the electric field depends on the emitter-to-sample distance, lower voltages are necessary for constant current emission if the distance is reduced [163]. We can use the Fowler-Nordheim equation 4.5 to estimate the tip radius. Therefore, we measured the emission currents of several tips while changing the applied voltage, which is displayed in Fig. 4.7

Here, we measured field emission for a single-crystal (sc) emitter (*tip 1*, black square marker in the plot), as well as two polycrystalline (pc) emitters (*tip 2*, red circle marker and *tip 3*, blue triangle marker in the plot). The respective voltage values for an emission of 10 μA in the preparation chamber were 1.6 kV for *tip 1*, 1.4 kV for *tip 2* and 3.0 kV for *tip 3*. As shown in Fig. 4.7 **a**, the emitters also have different emission voltages for the same current values when measured in the LEEH microscope. For an emission of 100 nA, the voltage values were around 400 V for *tip 1*, 355 V for *tip 2* and 625 V for *tip 3*, which is in agreement with the voltage trend measured in the preparation chamber. For each tip, the current does increase non-linearly with raising voltage, according to equation 4.5. By transforming equation 4.5 into equation 4.6 via dividing both sides by V^2 and applying the natural logarithm, one can describe the relation between the measured $I - V$ values and the radius r approximated via the Fowler-Nordheim equation [134]:

$$\ln\left(\frac{I}{V^2}\right) = -6.8 \cdot 10^9 \xi k r \Phi^{\frac{3}{2}} \cdot \frac{1}{V} + \text{const.} \quad (4.6)$$

The resulting Fowler-Nordheim plots are shown in Fig. 4.7 **b**. With $\ln(I/V^2)$ being a linear function of $1/V$, one can apply linear fit functions to the data. The resulting slope contains several constants as well as the apex radius r and the geometrical field reduction factor k . The average work function Φ can be approximated with a value of 4.5 eV for tungsten [164]. The correction factor ξ can be set to 1, since the effect of the mirror charge can be neglected for relatively large distances between the electrodes [124]. The value of k is estimated via the structure of the tip, which can also be derived from modeled simulations [165]. The value can range from 3 for tips with a bulbous apex shape [130] to 35 for very sharp tips with a very high aspect ratio [162]. For tips with a slender shank, k can be estimated to be in the range between 5 – 8 [131]. For most geometries, $k \sim 5$ is regarded as a sufficient approximation [124][158].

With these values, one can calculate the respective radius from the slope of the Fowler-Nordheim plot. The general trend can already be seen in the plots: the smaller the slope

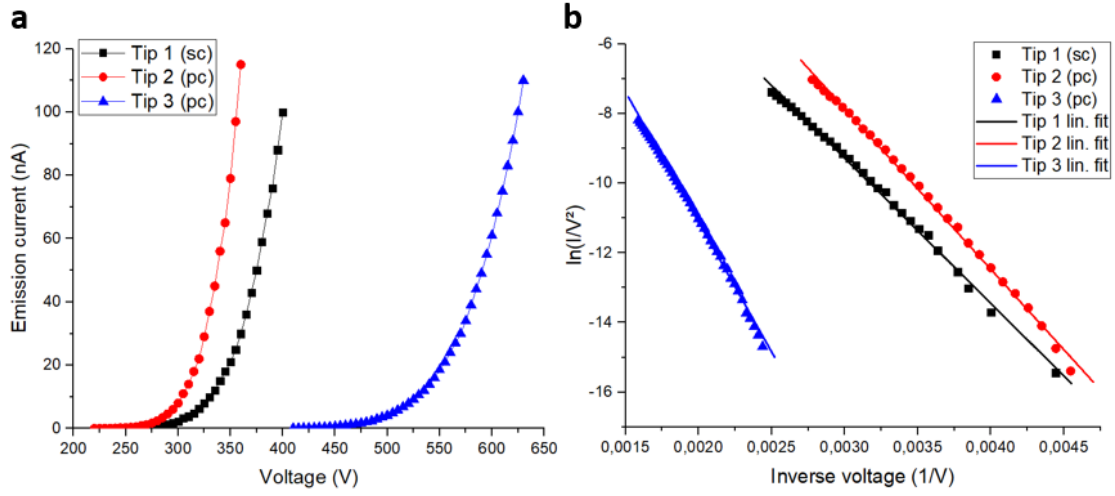


Figure 4.7: Field emission test of emitters in the LEEH microscope. **a** Emission currents of three tips measured for different voltages. The data of *tip 1*, a sc W(111) emitter, is plotted in black, while *tip 2* and *tip 3*, which were pc emitters, are plotted in red and blue, respectively. **b** Fowler-Nordheim plot of the three tips with the respective linear fits.

of the fit, the smaller the approximated tip radius. The estimated radii for the emitters shown in Fig. 4.7 are 12.85 ± 0.13 nm for *tip 1*, 14.22 ± 0.14 nm for *tip 2* and 23.01 ± 0.20 nm for *tip 3* with respective fit deviations in the range of 1% (see Tab. 4.1). From this, one can conclude that emitters with a smaller apex radius emit higher currents if the voltage is fixed [131]. To check how reliable this method is for determining the emitter radii, we measured the apices of these emitters via SEM, as shown in Fig. 4.8 **a** to **c**. The measured values for both methods are summarized and compared in Tab. 4.1.

Table 4.1: Comparison of the emitter radii measured via field emission and SEM.

Emitter	Emission (kV)	Field emission radius (nm)	SEM radius (nm)	$ \Delta $ (nm)
<i>Tip 1</i> (sc)	1.6	12.85 ± 0.13	11.9 ± 0.50	0.95 ± 0.63
<i>Tip 2</i> (pc)	1.4	14.22 ± 0.14	11.4 ± 0.50	2.82 ± 0.64
<i>Tip 3</i> (pc)	3.0	23.01 ± 0.20	31.2 ± 0.50	8.19 ± 0.70

The data shows that the radii approximated via the Fowler-Nordheim equation vary from the real radii measured via SEM. For the single-crystal *tip 1*, the difference is smallest with less than 1 nm which corresponds to less than 10% of the real radius. For the polycrystalline *tips 2* and *3*, a difference of roughly 3 nm and 8 nm is calculated respectively, which corresponds to a deviation of $\sim 25\%$ from the real radius.

These values indicate, that the Fowler-Nordheim plots can yield radii within the range of the real apex dimensions. However, because of the assumptions and approximations used, small to significant differences can be observed when comparing the data. For example, when looking at the apex shape of *tip 3* in Fig. 4.8 **c**, one can realize that the apex shape is close to a sphere. This would lead to an adjusted geometrical field reduction factor k . When using $k = 4$

instead of 5, the estimated emitter radius would be around 28.8 nm, which is much closer to the value of 31.2 nm. By analyzing this data, we were able to conclude, that field emission can be utilized to guess the range of the measured emitter radius. The direct relation of radius to emission voltage when measuring the tips in the preparation chamber is visualized in Fig. 4.8 **d**. The SEM data confirms, that emitters with a larger apex radius need higher emission voltages for a fixed threshold current, which fits the expected trend shown above [131].

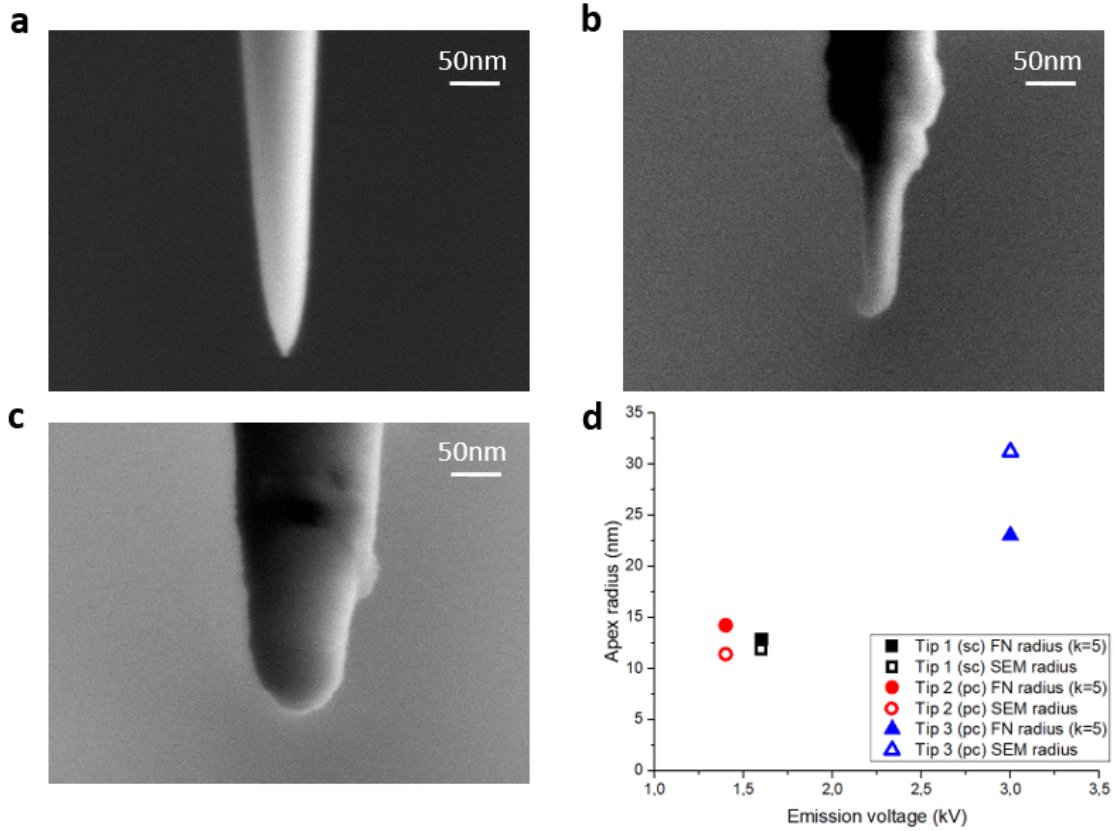


Figure 4.8: SEM images of tips characterized by field emission at 200.000 \times magnification. **a** *Tip 1* has a measured tip radius of 11.9 nm. **b** *Tip 2* has a measured tip radius of 11.4 nm. **c** *Tip 3* has a measured tip radius of 31.2 nm. In **d** the respective emission voltages measured in the preparation chamber are plotted against the SEM measured and Fowler-Nordheim derived tip radii.

It is important to mention, that we checked all three of the above shown emitters for their imaging quality in LEEH. Only *tip 1* could be used to image samples and showed very low emission energies of less than 50 eV when measuring close to the sample. *Tip 2* did not show any signal on our detector even though it was emitting. A reasonable explanation could be the tilt of its apex, which enables emission in general, but the electrons are emitted at a largely skewed angle relative to sample and thus might not reach the detector. *Tip 3* showed a very weak and unstable signal indicating leftover tungsten oxide residues on the apex. Another reason could be its tip shape, which is relatively large and spherical, which can enable emission from different positions on the apex. These findings imply that tips which are able to field emit within our set voltage range can still be unemployable for LEEH without further preparation

steps. Besides annealing, which is smoothening and cleaning while also blunting the emitter apex, sputtering can be used to further sharpen the emitter apex in UHV. Because coherence plays an important role in the formation of the holograms during LEEH [26] and it is reported that the coherence of emitters is improving the sharper the emitters are [39], we employ self-sputtering to reduce the apex radii of emitters, which is described in Sec. 4.2.3.

4.2.2.2 Field Emission at Cryogenic Temperatures

An interesting effect is the improved field emission voltage stability at cryogenic temperatures when compared to the performance at room temperature [72], which we observed for several cooled emitters. Fig. 4.9 and 4.10 show recorded field emission voltage data of an example single-crystal tip, which was measured for 120 s at room and low temperatures both at a fully retracted and close tip-to-sample distance, respectively. Independently of temperature and emitter-to-sample distance, we encountered two types of noise, which influence the voltage stability during emission.

First, there is telegraphic noise, where the field emission voltage changes from a certain mean value to another. These voltage jumps can be referred to as different emission states on the emitter apex and depend on the apex position of the emission source. For example, if the tip emits from the W(111) plane, its mean field emission voltage is different compared to the field emission voltages necessary at the W(211) or W(110) plane to emit the same electron current, since the crystallographic planes provide different work functions and source sizes (see Sec. 4.2.4) [126][127]. Telegraphic noise affects the temporal and spatial coherence of the emitted electron beam, since varying field emission voltages lead to varying electron energies and changes in the emission source position lead to a larger effective source size (see Sec. 2.2). In the recorded data, at least three species of different field emission states were identified and used as basis for the respective Gaussian fits shown in Fig. 4.9 and 4.10.

Second, we observe a thermally induced background noise, which consists of voltage fluctuations within an emission state. This noise can originate from several sources, such as atom diffusion on the emitter apex, external electromagnetic fields leading to emission instabilities, position changes of the emission source within a crystallographic plane, and/or phonon scattering effects within the emitter [72]. These effects also influence both temporal and spatial coherence of the electron beam, due to the fast voltage changes in emission energy and source position. The measured data suggests that this noise is partly temperature-dependent and can vary in the range from several millivolts to volts. The distribution width (full width half maximum) within each observed emission state yields the thermal noise range of the respective emitter, as shown in the respective graphs on the right in Fig. 4.9 and 4.10. The Gaussian fits for all the recorded data sets are summarized in Tab. 4.2. The analysis shows a reduced voltage spread $|\Delta V|$ and distribution width w at low temperatures indicating a higher emission stability for both emitter-to-sample distances.

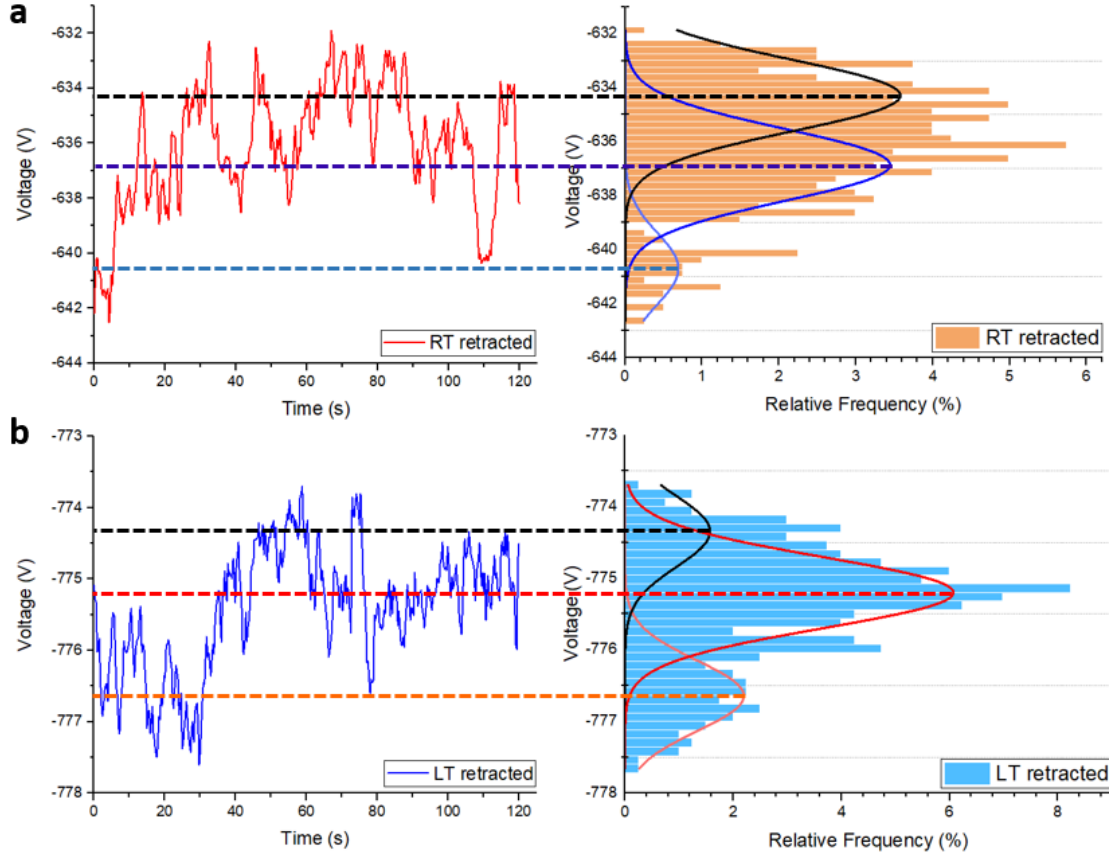


Figure 4.9: Field emission voltage measurement of a retracted sc tip in the LEEH setup at room temperature (RT = 295 K, **a**) and low temperature (LT = 50 K, **b**). The respective graphs on the left show the recorded emission voltage over a duration of 120 s, the histograms on the right show the binned voltage distribution. Several emission states can be identified by the telegraphic noise and individually fit using a Gaussian. The full width half maxima w for both temperature ranges are $w_{\text{RT}} = 2.650 \pm 0.364$ V and $w_{\text{LT}} = 0.989 \pm 0.152$ V implying a higher emission stability for a cooled emitter.

Table 4.2: Voltage stability analysis of a *sc* emitter at RT and LT for two different emitter-to-sample distances.

Distance	Retracted		Close	
Temperature (K)	295	50	295	50
Peak 1 (V)	-634.291 ± 0.256	-774.348 ± 0.469	-76.602 ± 0.007	-83.076 ± 0.015
Peak 2 (V)	-636.860 ± 0.294	-775.203 ± 0.151	-77.012 ± 0.071	-83.168 ± 0.004
Peak 3 (V)	-640.699 ± 0.948	-776.644 ± 0.127	-77.535 ± 0.098	-83.285 ± 0.001
$ \Delta V $ (V)	6.408 ± 1.204	2.296 ± 0.596	0.933 ± 0.105	0.209 ± 0.016
Width w (V)	2.650 ± 0.364	0.989 ± 0.152	0.316 ± 0.015	0.058 ± 0.003

The increase in emission stability at low temperatures allows for higher temporal and spatial coherence [72], which we also tested by imaging free-standing carbon nanotubes (CNTs) via LEEH. As shown in Fig. 4.22 (Sec. 4.2.6.2), a cooled emitter can yield a higher visibility contrast and larger hologram width on the detector when compared to its performance

at room temperature. Since more fringes can be resolved for field emission at cryogenic temperatures, this enables measurements with a resolution closer to the theoretical resolution limit depending on the properties of the respectively used emitter.

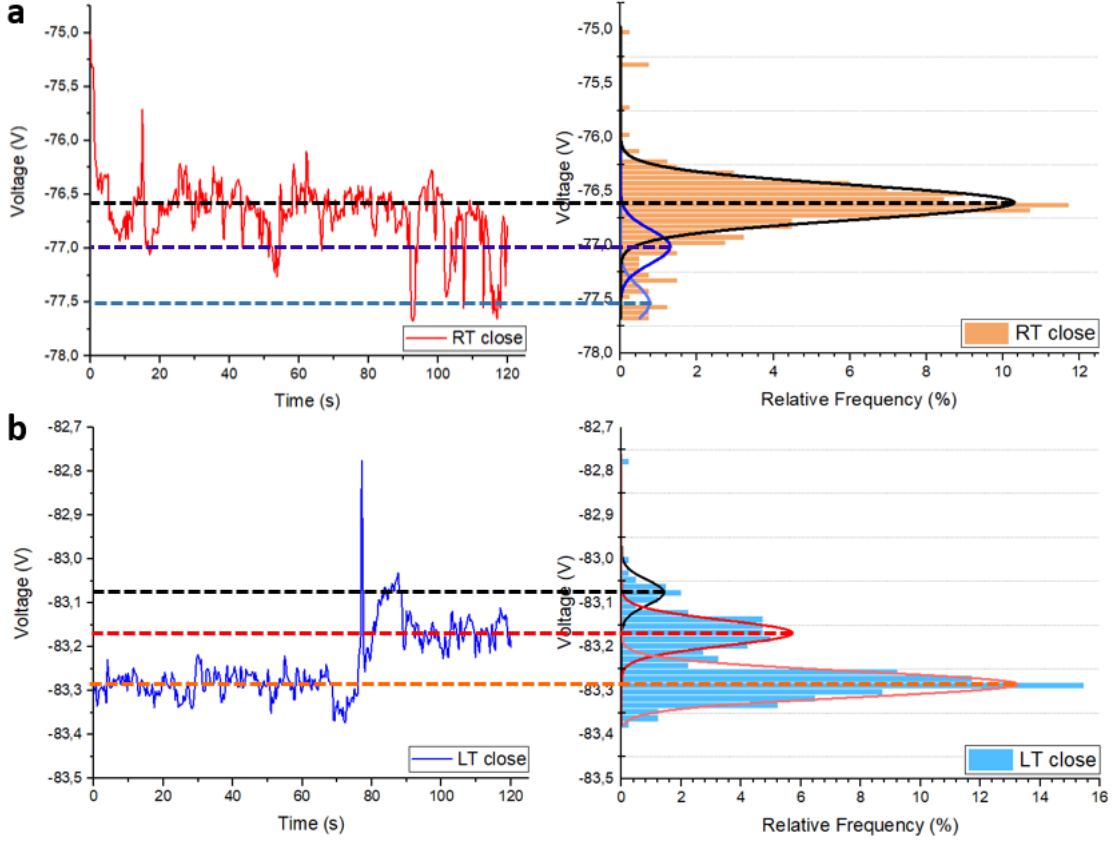


Figure 4.10: Field emission voltage measurement of a sc tip, which is in close distance to the sample ($z < 2 \mu\text{m}$) in the LEEM setup, at room temperature (RT = 295 K, **a**) and low temperature (LT = 50 K, **b**). The respective graphs on the left show the recorded emission voltage over a duration of 120 s, the histograms on the right show the binned voltage distribution. Several emission voltage states can be identified by the telegraphic noise and individually fit using a Gaussian. The respective full width half maxima w for the two temperature ranges are $w_{\text{RT}} = 0.316 \pm 0.015 \text{ V}$ and $w_{\text{LT}} = 0.058 \pm 0.003 \text{ V}$ implying a higher emission stability when the emitter is cooled. The data matches the results shown in Fig. 4.9.

4.2.3 Self-Sputtering

Here, I describe how we use self-sputtering to reduce the emission voltages and thereby the apex radii of our emitters in UHV. I show that this method can be employed to improve the emitter quality for LEEM imaging.

Originally applied in field ion microscopy [158], sputtering of emitters is a common practice for the removal of material and contaminants with the general goal of sharpening the tip apex [135][166]. Sputtering processes are based on the bombardment of a target surface with energetic ions, which leads to an ejection of secondary ions, atoms and even clusters

from the affected region. Noble gas ions are generally used as projectiles in order to prevent possible chemical reactions between the reactive ions and the atoms of the target material [158]. Contrary to traditional sputtering procedures used for surface preparation, the self-sputtering procedure of the emitters does not involve the use of an ion gun for generating the noble gas ion. By applying a high negative bias at the tip in the presence of a noble gas, field emitted electrons ionize the noble gas atoms. Due to the high electric field, the positively charged noble gas ions are subsequently accelerated towards the emitter as shown in Fig. 4.4 b [167].

It is important to note that the sputtering process involves mainly the shank region of the tip, just behind the tip apex, causing the formation of a neck. When interrupting the process after a short sputter time, the formed neck can be imaged via SEM as shown in Fig. 4.11 a, where the tip was only sputtered for a minute. This can be explained by the following reasons: since the produced ions have a different energy than the emitted electrons, their trajectories are deviant, leading to a higher number of ion impacts behind the apex [168]. A second reason is related to the sputtering efficiency, which is higher for a sputtering angle of about 60° between the surface normal and the ion trajectories. This angle is achieved behind the tip apex for geometrical reasons, increasing the speed of the sputtering process [167]. While the material at the tip is reduced, the required voltage for maintaining a constant emission current is decreasing simultaneously. When the neck diameter is too thin to further support the apex part above, it breaks off and a sudden voltage drop is detected. This process is known as Schiller-decapitation and can yield very sharp emitter apices with radii of a few nanometers if sputtering is stopped immediately after the event [169].

Among the different noble gases, we use neon. Helium is too light to provide efficient sputtering [158], while argon has been proven to be less reliable by having a too high sputtering rate [167]. The gas pressure can vary from $1 \cdot 10^{-5}$ mbar to $5 \cdot 10^{-4}$ mbar [168]. In general, the sputter rate is proportional to the partial pressure P_{Neon} , because more noble gas atoms are present to participate in the process, which can be expressed by a voltage reduction rate $-\frac{dV}{dt} \propto K \cdot P_{\text{Neon}}$ with K being the reduction factor in $\text{V min}^{-1} \text{mbar}^{-1}$ [158].

In our experimental setup, the sputtering procedure can be performed in two different UHV chambers: in the FIM (see Sec. 3.5.2) and in the preparation chamber of the LEEH system (see Sec. 3.5.1). For both setups, we use the same process parameters. Neon gas is let into the chamber using a needle valve (FIM: ULV150, LEEH: EULV075, both from MDC) until a partial pressure of $5 \cdot 10^{-4}$ mbar is reached. Subsequently, a negative high voltage bias between tip and counter electrode is applied with a high voltage power supply (LEE: PNC 20000-3, FIM: PNC 40000-1, both from Heinzinger) until an emission current of $0.5 \mu\text{A}$ is drawn from the emitter. We use the constant current mode to monitor the emission voltage during the procedure. The process duration usually varies in the range of 3 – 10 minutes depending on the emission voltage of the respective emitter. For a neon partial pressure of $5 \cdot 10^{-4}$ mbar, the reduction factor K was determined to be in the range of 4.0 to $6.8 \cdot 10^5 \text{V min}^{-1} \text{mbar}^{-1}$ for our emitters, which is comparable to values reported in literature [158].

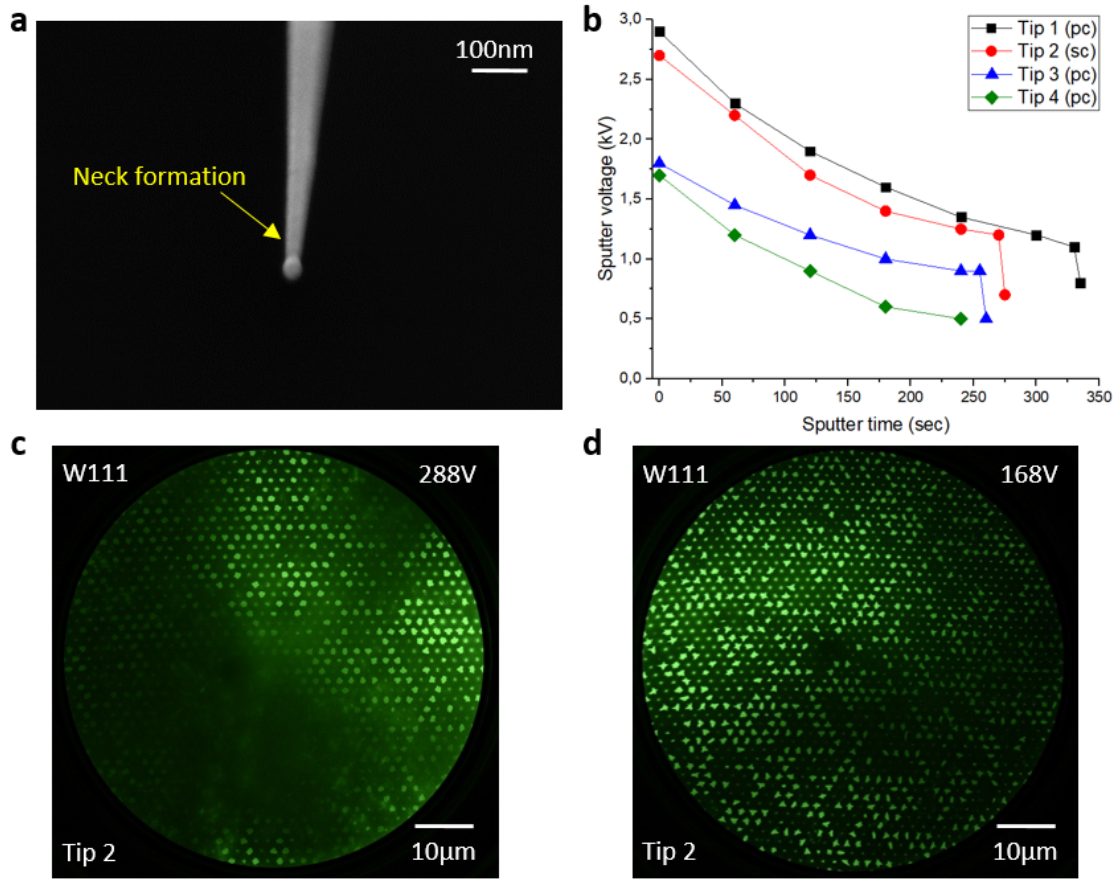


Figure 4.11: Results from emitter self-sputtering with neon at a partial pressure of $5 \cdot 10^{-4}$ mbar. **a** SEM image at $119.000\times$ magnification of a tip, which was sputtered for only one minute at a constant current of $5 \mu\text{A}$ and a starting voltage of 3.1 kV. Sputtering was stopped before the occurrence of the Schiller decapitation. The neck formation during the process is clearly visible. **b** Emission voltage reduction of four individual emitters (pc and sc) during sputtering at a constant emission current of $5 \mu\text{A}$. Schiller decapitation was detected as a sudden voltage drop for the tips 1, 2 and 3. For tip 4, sputtering was stopped before a decapitation took place since the emission voltage value was already at 0.5 kV, which is a low emission value for our system. **c** and **d** show LEIS images of an SLG covered SiN grid which was imaged by the sc tip 2 from **b** before and after sputtering respectively. The emission voltage during imaging was 288 V before (**c**) and 168 V after sputtering (**d**). The imaging quality of the tip was improved by the procedure as indicated by the removal of disturbing signal (dark shroud in **c**).

We frequently observe the Schiller-decapitation process while sputtering, as shown in Fig. 4.11 **b**. While the emission voltage of tip 4 does decrease continuously until reaching a low voltage value, tips 1, 2 and 3 show an abrupt voltage drop, which indicates the breaking off of the apex part above the neck. After the drop, we immediately stop the sputtering to avoid blunting of the newly generated apex. To stop the sputtering procedure, the applied voltage is turned off first. Afterwards, the sputter gas flow is stopped. As soon as the pressure is in the UHV range, a short annealing step is applied to remove neon residues from the tip [166].

Fig. 4.11 **c** and **d** show the results of an effective sputtering procedure for the sc tip 2 from Fig.

4.11 **b** measured via LEEH. The emission voltage was reduced from 288 V to 168 V and artifacts appearing during imaging were removed after the procedure. Our main application of this technique is the modification of the tip apex to remove disturbing signals and artifacts, which can occur during LEEH measurements. We found that these signals might originate from a misshaped apex and/or contaminant residues on or near the apex region, since they can be altered or even eliminated after annealing and sputtering procedures. This further confirms that the structure of the emitter apex is crucial for the emission properties and it is necessary to analyse it in a more precise manner. For this purpose, we use field ion microscopy (FIM), which is described in the following section. This technique enables the investigation of emitter apices on the single-atom level.

4.2.4 Field Ion Microscopy Investigation of Emitters

In this section, I describe how to take advantage of FIM to characterize our emitters on the atomic scale. I show how to detect the crystallographic structure of the apex, evidence emitters showing atomic disorders and show how this information correlates with the emission properties of the respective emitters when using them for LEEH imaging, which is presented in Sec. 4.2.6.1.

We mainly conduct FIM experiments in our external FIM setup (see Sec. 3.5.2) and use a vacuum suitcase (Ferrovac) to transfer tips between the LEEH and the FIM setup. This enables a transfer in UHV conditions (below $1 \cdot 10^{-10}$ mbar), preventing the contamination of the emitter. In order to check that no major alterations of the tip apex occur during the transfer, the field emission voltage of the emitter is always measured before and after the procedure. Only a short, low temperature annealing procedure is carried out to remove possible adsorbates after the procedure.

In our experiments, the FIM head is cooled via liquid nitrogen using a flow cryostat (He-Verdampferkryostat-40, VAb). As soon as the temperature at the emitter is below 100 K, we ramp up the voltages of the MCP detector (MCP-45-1-60-P43-CF100-HR, GIDS) via two high voltage power supplies (PNC 6000-10 and PNC 1500-40, Heinzinger). While we keep the MCP-in, which can be used to remove low-energy ions, grounded, we set the voltages for the screen and MCP-out to 4.6 kV and 860 V, respectively. These values can be adjusted during the measurement to regulate the brightness of the image.

We use helium gas as imaging gas at a partial pressure of $5 \cdot 10^{-4}$ mbar (base pressure of the chamber: $2 \cdot 10^{-10}$ mbar) using a needle valve (ULV150, MDC). Afterwards, a positive bias is applied to the tip via a high voltage supply (PNC 40000-1, Heinzinger) until a signal is visible on the screen. The voltage values are adjusted to get a stable signal on the detector, which is subsequently captured using a digital single-lens reflex camera (eos1100D, Canon), which is remote controlled using an open source software (digiCamControl). Fig. 4.12 shows FIM images of two *sc* emitters (*tip 1* and *tip 2* in this example) at two different imaging voltages.

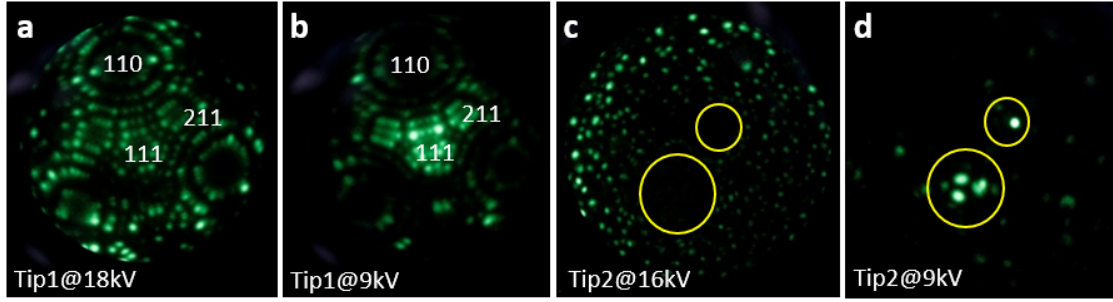


Figure 4.12: FIM characterization of two sc emitters at different applied voltages. *Tip 1* was imaged at 18 kV (a) and 9 kV (b) and shows the expected crystallographic planes for a single-crystal W(111) apex. The W(111), W(211) and W(110) planes can be identified for both applied voltages. At lower voltages (b), the signal is stronger at the apex termination. *Tip 2* was imaged at 16 kV (c), as well as 9 kV (d) and does not reveal crystallographic planes. At higher voltages (c), a random pattern is visible with two dark, circular areas near the center of the apex, which are marked by yellow circles. When reducing the imaging voltage (d), the outer signal vanishes, while both dark areas show bright spots indicating atomically sharp apex termination locations.

For *tip 1*, the crystallographic planes on the emitter apex are W(111), W(211) and W(110) (Fig. 4.12 a and b) [170][132]. At high voltages, the field strength is similar on a larger apex area, which leads to an overall bright image (Fig. 4.12 a). When lowering the applied voltage and thereby decreasing the electric field, the overall signal is reduced while the visibility of the apex termination is increased (Fig. 4.12 b). This effect is due to the higher electric field in the proximity of the apex, which attracts the gas atoms and favors their ionization, while in other tip regions, the electric field is not strong enough to promote this process [131].

For *tip 2*, no crystallographic planes could be identified. Instead, two dark circular areas are visible at a higher applied voltage (Fig. 4.12 c), which are enclosed by a seemingly non-ordered structure. When reducing the applied voltage, the outer signal disappears and the previously dark areas show few individual spots (Fig. 4.12 d). This suggests an apex termination consisting of only a few individual atoms [26][171][172]. Since we observe two separate bright signals, the lower one showing three distinct bright spots and the upper one only a single bright spot, we assume the presence of two distinct apex termination spots, also known as double-tip.

When the crystallographic planes are visible, such as in Fig. 4.12 a, the apex radius of the emitter can be estimated. Assuming a spherical shape of the apex, the amount of atomic steps between the crystallographic planes can be counted. Since these edges appear as rings in the FIM image, the procedure is known as *ring counting* method, which is shown for the single-crystal *tip 1* in Fig. 4.13 [132][170].

The geometrical distances for single atomic steps can be derived from the interlayer spacing s , which is normal to the direction (hkl) , and the angle Θ between the (hkl) and $(h'k'l')$ poles of an atomic layer in a distance $n \times s$ below the origin plane, where n is the amount of edges (rings) counted between the planes (see Fig. 4.13 a) [170]. The resulting radius can be calculated as $R = ns_{hkl} / (1 - \cos\Theta)$. For a bcc crystal, such as W(111), the (110) planes are

easiest to distinguish, since they have the largest step heights, thus representing the ideal choice for the ring counting method [132].

In Fig. 4.13 **b**, the FIM image of *tip 1* is analyzed and the amount of rings between the (110) axis and the (211) (red), as well as the (111) (blue) axes are counted. The number of distinguishable rings is about 5.5 for the (110)–(211) plane and about 7.5 for the (110)–(111) plane, respectively. The respective spacing factors $s_{(110)}/(1 - \cos\Theta)$ are 1.66 for the (110)–(211) plane and 1.21 for the (110)–(111) plane [173]. By multiplying the spacing factors with the number of rings, we obtain two separate radius estimations for our emitter that are 9.13 nm ((110)–(211)) and 9.07 nm ((110)–(111)). These values are in good agreement with the respective SEM image of *tip 1* shown in Fig. 4.13 **c**, where a tip radius of 9.0 – 9.5 nm was measured.

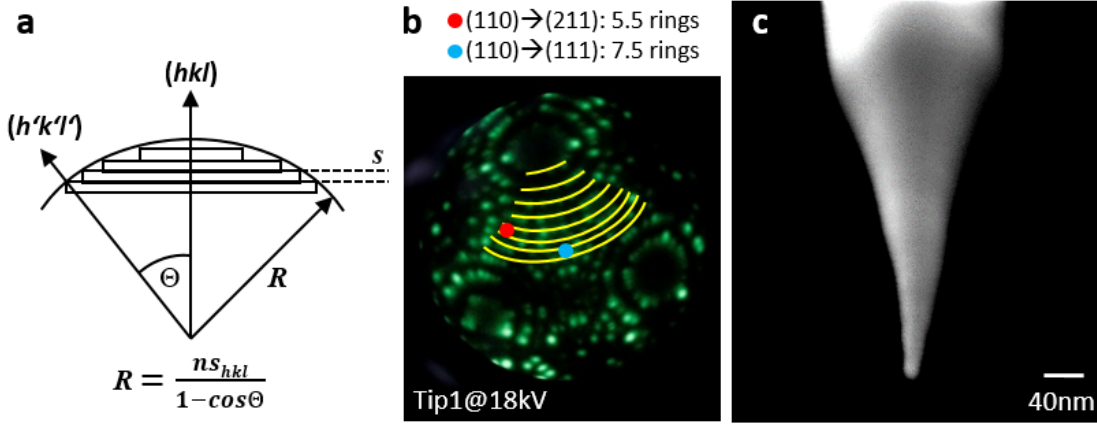


Figure 4.13: Emitter radius estimation via the ring counting method in FIM images. **a** Geometry of a spherical apex with tip radius R , interlayer spacing between planes s , amount of rings n counted between planes and angle Θ between the poles hkl and $h'k'l'$ [132]. **b** Ring counting method in the FIM image of the *sc tip 1* yielding an estimated tip radius of ~ 9.1 nm. The rings are marked in yellow and the red and blue spots indicate the position of the (211) and (111) poles, respectively. **c** SEM image of the *sc tip 1* with a measured radius of $\sim 9.0 - 9.5$ nm at $200,000\times$ magnification.

These results show that FIM is a unique method for imaging the apex structure of our emitters on an atomic scale. The radius estimation via ring counting is a viable method for emitters, which show crystallographic planes at their termination sites. Concerning the apex radius of *tip 2*: since the emitter was crashed during LEEH measurements, which were conducted after the characterization via FIM, it was not possible to get SEM images of its undamaged apex. It is important to mention that FIM imaging usually did not affect the tip performance. On the other hand, tips imaged via SEM are contaminated due to the well-known deposition of non-conductive hydrocarbon layers on the tip apex during the SEM process, which compromises their electron emission properties [174].

After FIM imaging is finished, we ramp down the voltages applied to tip and detector, close the helium gas flow and stop the cooling of the emitter. As soon as the tip has warmed up to room temperature, we conduct a short and gentle annealing step to remove helium gas residues from the emitter, before (re-)using the emitters in LEEH. In general, FIM is helping

us to understand the apex structure of our emitters in relation to their performance in LEEH. Furthermore, it can be used to track tip apex changes, for example after the occurrence of major emission value changes during LEEH measurements or after performing tip enhancing procedures, such as functionalization processes of the emitter apex, which is presented in the following Sec. 4.2.5.

4.2.5 Emitter Functionalization

The controlled addition of functional groups to surfaces, particles and/or molecules is known as functionalization. The general goal of tip functionalization is to improve the emission properties of the emitter apex, such as emission voltage, stability, beam divergence angle and coherence. In this section, I discuss several possible functionalization methods for tungsten tips used for field emission and LEEH imaging. I show the procedures explored by us, as well as the results on the emission behaviour of the functionalized tips. Some of the investigated methods show promising results, however, further efforts are required to fully control the complex task of tip functionalization.

To increase the coherence of the emitted electron beam, it is suggested that the apex termination size has to be reduced down to atomic dimensions [39][175][176]. There are several possibilities to manipulate the apex of the emitter that can lead to an atomically sharp apex termination. The use of high electric fields at the emitter apex can lead to field evaporation of tungsten atoms, which can yield emitters with three terminating tungsten atoms [177]. Depositing a single tungsten atom from the gas phase onto the trimer structure of the apex leads to a monoatomic apex termination, which can be identified as a single bright spot via FIM at cryogenic temperatures. This suggests that field emitted electrons mainly originate from the terminating atom, which behaves as an electron point source [178]. These point sources have been shown to yield bright electron beams with small divergence angles and high coherence [26]. Due to the atomically small curvature of the apex termination, very low voltages in the range of 20 – 300 V can be applied for electron emission, resulting in low-energy electrons being emitted [33].

Another approach to obtain highly coherent nano or single-atom emitters is the deposition of noble metal atoms, such as platinum, palladium or iridium, onto the tip apex [90]. The deposition can either be done in an electrochemical cell [179] or by thermal evaporation of the noble metal in UHV [180]. Subsequent thermal annealing in UHV at temperatures up to 1000 K leads to the formation of faceted nanopylramids via thermodynamic processes, which can terminate with a single noble metal atom [180][181]. These emitters have been shown to yield highly coherent electron beams with divergence angles up to 3° [90].

However, both of the above mentioned techniques yield emitter apices, which are sensitive to diffusion and evaporation of apex atoms at ambient or high temperatures. Pure tungsten point sources are difficult to generate and are usually only stable at cryogenic temperatures,

while the terminating atom can easily diffuse or evaporate during field emission even at room temperature [180]. It was possible to get point source-like emitters having a trimetric apex structure, which could be identified via FIM (see Fig. 4.12 **d**), but for most prepared tips, field evaporation did not yield these kind of emitters in our system. Noble metal coated emitters are sensitive to annealing temperatures above 1000 K [181], which we usually use to remove contaminants and adsorbants. Furthermore, it is reported, that these emitters usually yield small beam divergence angles, which limits the obtainable field of view during LEEH and can restrict the amount of visible hologram fringes leading to a lower resolution [22][39].

In the following, I present three different functionalization techniques, which we investigated to improve the emission qualities of our emitters.

4.2.5.1 Reactive Nitrogen Etching

Instead of depositing atoms on the tip apex to form an atomically sharp emitter, controlled material removal from the shank towards the apex can also be used to reduce the amount of terminating atoms. Field-assisted etching of tungsten tips with nitrogen at low temperatures in UHV can be used to obtain atomically sharp emitters, which also possess a protective layer against atom diffusion and evaporation even for temperatures above 1000 K [171]. Furthermore, it is reported, that the resulting emitters can have fully coherent divergence angles up to 14° [39].

This process is based on the formation of a strong-bond state during the nitrogen adsorption on the tungsten surface. Nitrogen molecules dissociate on the tungsten surface when a sufficiently high positive electric field is applied and diffuse into the atomic layers of the tungsten [182]. The reaction only takes place at lower field regions, which are usually below the apex, where the ionization barrier is low enough to be penetrated by single nitrogen atoms. The nitrogen atoms diffusing into the tip material form tungsten protrusions on the surface, yielding an enhanced electric field, which can cause atom ionization and evaporation [171]. This leads to the removal of protruding tungsten atoms from certain planes along the emitter shank, especially on the (111) and (001) planes [183]. At a constant supply of nitrogen, the corrosive reaction is continuously etching the emitter surface from the shank towards the apex, effectively sharpening the tip. Additionally, the strong-bonded nitrogen atoms, which diffused into the tungsten surface, form a protective tungsten nitride layer which is lowering the electric field, preventing further nitrogen adsorption at the etched locations [172]. The procedure can be coupled to FIM imaging and thus monitored in real-time.

We tried this functionalization method in our external FIM setup (see Sec. 3.5.2) on several sc emitters. The etching process could be observed for a few tips so far, an example is shown in Fig. 4.14. While conducting FIM imaging with helium at a partial pressure of $5 \cdot 10^{-4}$ mbar at a low emitter temperature of less than 100 K (see Sec. 4.2.4), additional nitrogen gas is added to the chamber using a needle valve (ULV150, MDC) up to a partial pressure of $5 \cdot 10^{-6}$ mbar. The

applied positive voltage for imaging is reduced to start the process and will be further reduced during the procedure to prevent uncontrolled field evaporation, which can occur due to the increasing local electric field at the apex upon sharpening, as described in [172]. Fig. 4.14 **a** to **d** shows the emitter apex change during the procedure.

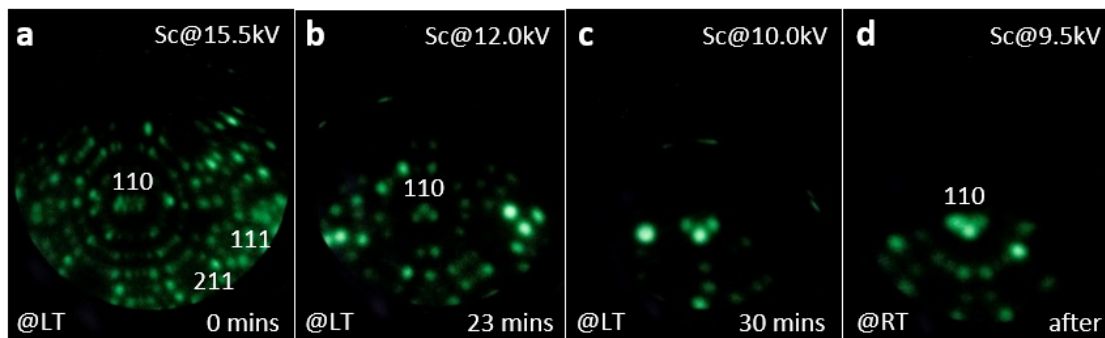


Figure 4.14: FIM imaging of the reactive nitrogen etching functionalization process of a pc tip at low temperatures (LT = 95 K). **a** The process is carried out with an initial applied voltage of 15.5 kV. Crystallographic facets of the apex are visible. The applied voltage is lowered during the process to maintain a stable signal. **b** Intermediate state of the process (applied voltage of 12.0 kV). The area from which the ions are generated decreased during the procedure, but some facets can still be identified. **c** End of process after 30 minutes (applied voltage of 10.0 kV). The crystallographic facets almost vanished and only a few distinct spots are clearly visible. **d** Room temperature FIM image of the same tip: the apex retained the low temperature structure and a few facets are visible again.

While the etching proceeds and the applied voltage at the tip is lowered, the outer signal of the apex becomes darker, while the signal in the center becomes brighter. This effect is similar to the observation discussed in Sec. 4.2.4, however the signal of the outer locations cannot be recovered by increasing the voltage again. This development of an etching band implies the formation of the tungsten nitride layer, which exerts a lower electric field compared to the unetched tungsten surface above [172]. During the process, the crystallographic facets close to the etching band become more unstructured, which is due to the increasing amount of nitrogen absorbed by the emitter. The process was stopped after 30 minutes (Fig. 4.14 **c**), showing four bright spots on the emitter apex, as well as some darker spots below them.

In order to verify the stability of the apex created via nitrogen sputtering, we let the tip warm up to room temperature before re-imaging it via FIM (Fig. 4.14 **d**). This investigation shows that the atomic structure of the apex is mostly retained, confirming the stability of the process to room temperature annealing. It is also important to mention that the procedure resulted in a reduction of the field emission voltage of the emitter from 3.0 kV to 2.5 kV at a constant emission current of $5 \mu\text{A}$. However, the used tip was not symmetric, most likely due to a tilted apex and the etching was stopped before reaching an atomically sharp emitter. After a short annealing step to remove nitrogen and helium residues from the tip, we tested the emitter for LEEH, which confirmed a tilted apex. As shown in Fig. 4.15, the field of view is shifted towards the edge of the detector, which still enables imaging. However, the detection of high-order fringes can be compromised by the limited illumination area. In general, the field-assisted

nitrogen etching is a promising technique, which we want to further explore and test.

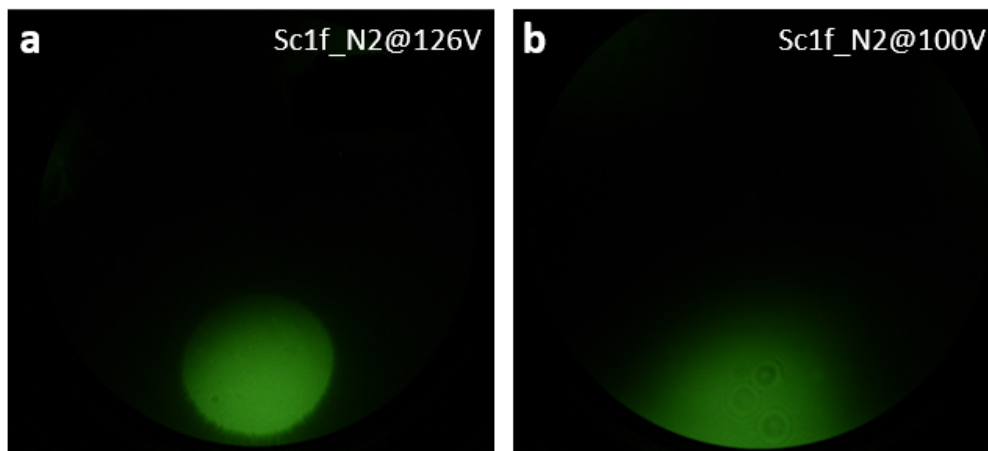


Figure 4.15: LEEH imaging of a SGL covered hole (diameter of 500 nm) using the nitrogen etched sc emitter presented in Fig. 4.14. The images were acquired at different distances with the respective emission voltages of 126 V (**a**) and 100 V (**b**). The illumination area of the beam is shifted towards the detector edge, indicating a tilted emitter apex.

4.2.5.2 CNT Uptake

An alternative possibility to get emitters with a highly coherent electron emission is the termination of the tip apex with a carbon nanotube (CNT) [184]. This yields a well-defined emitter with a small radius in the order of a few nanometers and a very high aspect ratio due to the curvature of the CNT [185]. It is reported that the field emission properties of CNTs include a low energy spread [186], high emission current stability [187], high brightness [188][189], and long lifetimes [190]. The preparation of CNT-functionalized tip apices can be achieved in several ways. CNTs can be directly grown on the emitter apex via chemical vapor deposition (CVD) [191] or hydrocarbon pyrolysis[192], which can lead to an uncontrolled amount of CNTs on the apex [193]. Another method is to use the tip to directly contact individual free-standing CNTs, which are deposited on a holey grid [184] or grown on a sample surface [194][195]. In both cases, the CNT is connected to the emitter apex via Van der Waals forces [185][191].

We tried the direct contacting method of CNTs for our emitters. Therefore, we used single-walled CNTs (ap-grade with diameter 1.2 – 1.5 nm, CarboLex) diluted in 1,2-dichlorobenzene (Sigma-Aldrich), which were drop-casted on a metal coated holey silicon nitride (SiN) grid without SLG. The general grid preparation for our substrates is described in Sec. 5.1). The CNT covered grid was heated to 200°C for 15 minutes to remove the solvent and subsequently brought into UHV via the fast transfer loadlock of our LEEH setup. The sample is imaged via LEEH at an emission current of 50 nA and holes containing single free-standing CNTs are identified.

The target CNT is carefully approached with the imaging tip and the emission current is

reduced stepwise down to 1 nA during the approach. Just before reaching the CNT, the emission voltage is turned off to avoid field effects during contact. The final steps are carried out blind and the tip is further moved towards the sample in very small steps, until a small, short-time current flow is measured, which indicates for the contact. At this point, the emission voltage can be turned on again, with a constant current emission of 1 – 4 nA. The tip is slowly retracted stepwise and the emission current is increased. After retracting to a safe distance (several microns away from the hole), the emission current can be set to 50 nA again and the sample is checked to verify whether the CNT has been removed. As shown in Fig. 4.16, it is possible to remove the CNT, which leads to a substantial modification of the emitter performance.

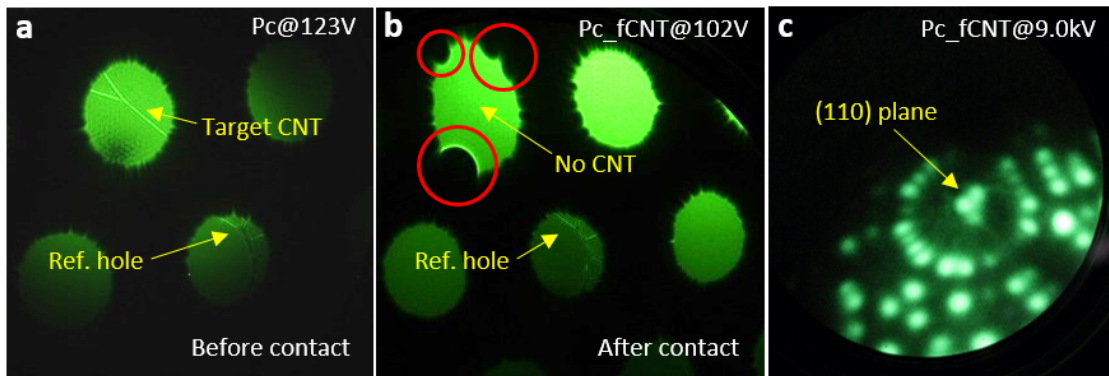


Figure 4.16: Emitter functionalization of a pc tip via contacting a free-standing CNT. Hole diameters are 1 μm . **a** LEEH image of a CNT sample acquired with a *pc* tip at an emission voltage of 123 V. The tip is approached to the Y-shaped CNTs in the top left hole until a contact between tip and CNT is established. The hole at the bottom of the image (Ref. hole) containing another CNT bundle is used as a position reference. **b** LEEH image of the same sample location after the CNT contacting took place. The upper left hole is empty and the emission voltage, as well as the illumination area of the emitter changed. This suggests a change of the emitter apex possibly due to a successful uptake of the CNT. The edges of the empty hole show dark, circular distortions (marked in red), which change in size depending on the emitter-to-sample distance. **c** FIM image of the pc tip after the CNT uptake experiment. The FIM signal shows a crystallographic structure with an identified (110) plane. There is no clear evidence for a CNT on the apex.

After the contact with the targeted CNT, which led to a removal of the CNT from the hole in Fig. 4.16 **a**, the emission voltage and illumination area of the emitter changed. The brightness was increased by around 60% and the field of view shifted from the upper left of the detector towards the upper right. Furthermore, some dark and circular distortions are visible in the hole after CNT removal (Fig. 4.16 **b**, encircled in red), which seemed to originate from a local charging of the hole edges.

To verify the emitter termination, we transferred the tip to our FIM chamber. The FIM characterization, however, shows the crystallographic planes of the tungsten with a clearly visible (110) plane (Fig. 4.16 **c**). No indication of a CNT functionalization is thus visible [196], which can have several possible explanations. The first possibility is that the CNT was not contacted directly via the apex termination of the emitter, but instead by a region close to the termination,

which caused the emission property changes upon uptake. Depending on the position of CNT, the field emission would still take place via the apex termination instead of the CNT. The second explanation involves the loss of the CNT functionalization during the LEEH-to-FIM transfer. However, this explanation is very remote, since there is no reason suggesting that the transfer could reshape the apex. A third possibility is that the contacting itself did not work properly and the presence of the applied electric field right after the short current flow removed the CNT from the hole without a stable contact taking place. The measured short current spike could have altered the apex structure leading to the observed changes in emission.

The process was repeated several times without being able to create a functionalized CNT tip. As such, the procedure revealed to be very erratic and a significant revision is required. Due to these difficulties, we have decided to explore a novel method inspired by the CNT functionalization, which is the uptake of SLG sheets via controlled crashing of the tips into the SLG substrate.

4.2.5.3 SLG Uptake

Graphene sheets are used as films to improve the emission performance of flat electrode material by yielding high field enhancement factors and providing high current stability during emission [197][198]. Concerning tip-shaped emitters, CVD-grown SLG covering the emitter apex was reported for nickel tips [199], while amorphous carbon layers were evaporated onto tungsten emitter apices [89]. In both of these studies, the carbon coating reduced the virtual source size during field emission and increased the emission current stability. Furthermore, in the case of an SLG covered tip, the work function of the emitter was found to be lowered [199].

We found that direct contacting of free-standing SLG substrate with the emitter apex can improve its emission properties. During this process, SLG flakes or pieces are removed from the substrate and cover the emitter apex upon contact. The procedure is similar to the CNT uptake protocol. While imaging an SLG-covered sample in LEEH (see Sec. 5.2.2), the emitter is brought into close distance towards the free-standing SLG substrate. For a controlled contact, the emission current is typically reduced to 5 – 10 nA and kept constant during the approach. Upon contact, the detector usually shows a short flashing signal on the screen, followed by a recovery of the field of view after a few seconds. After contact, the tip has to be retracted very carefully to avoid additional crashing or contact with the surrounding substrate. In Fig. 4.17, the SLG uptake is shown for three different emitters. Fig. 4.17 **a**, **b** and **c** show the target SLG covered holes measured at an emission current of 50 nA before contact, while 4.17 **d**, **e** and **f** show the same holes after contact.

From a direct comparison between the images obtained before and after the SLG functionalization, a few conclusions can be drawn. For all three emitters, the emission voltages increased by a factor of three or more for a fixed emission of 50 nA and a comparable tip-to-sample

distance. Additionally, the illumination area is larger and more centered. For *sc1* and *pc1*, an increase in brightness is also observed. These modifications indicate an improvement of the emission properties. The dimension of the SLG flakes, removed from the substrate and covering the emitter apex, can be estimated by knowing the dimension of the TEM grid hole (500 nm). This yields SLG surfaces of about $38 \cdot 10^3 \text{ nm}^2$ for *sc1*, $25 \cdot 10^3 \text{ nm}^2$ for *pc1* and an area larger than $200 \cdot 10^3 \text{ nm}^2$ for *pc2*. Our investigations suggest that the field emission voltage increases with an increasing area of the SLG flake taken up during the functionalization. Furthermore, the field emission voltage could depend on the SLG configuration on the emitter apex. It is reasonable to suppose that an emitter with a crumpled-up SLG flake at its apex emits differently than an emitter with an SLG flake that adheres well to its overall surface.

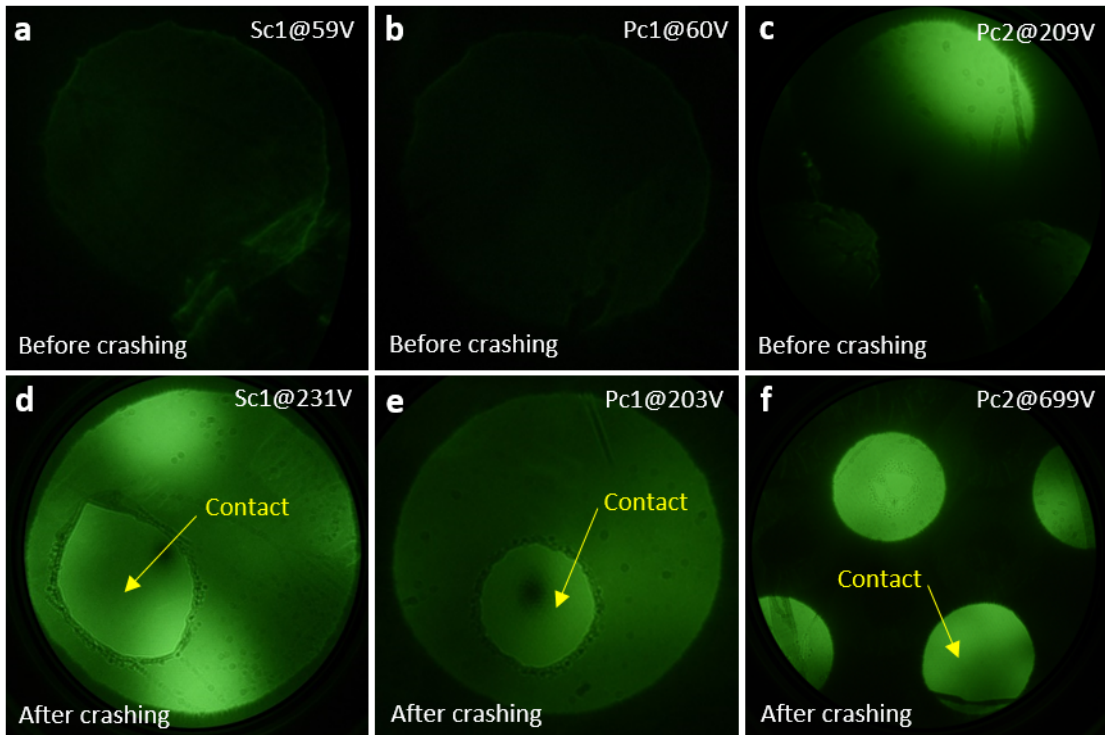


Figure 4.17: Emitter functionalization of one *sc* and two *pc* tips via SLG contacting during LEEH leading to SLG removal from the substrate. Tip *sc1* before (a) and after (d) SLG contacting. The emission voltage increased from 59 V to 231 V during the SLG uptake. Tip *pc1* before (b) and after (e) contacting SLG. For this tip, the emission voltage increased from 60 V to 203 V during the SLG uptake. Tip *pc2* before (c) and after (f) SLG contacting. The emission voltage increased from 209 V to 699 V during the SLG uptake. After functionalization, the contact sites could be identified for each tip, as indicated in the images. The tips *sc1* and *pc1* show a similar increase in voltage during the procedure. Tip *pc2* shows much higher emission voltages and a larger piece of SLG was taken up during the procedure. Hole diameters are 500 nm.

In order to gain further details about the SLG position on the emitter apices, we investigated them using FIM. For example, in Fig. 4.18 a to d, FIM images of the functionalized *pc1* tip from Fig. 4.17 e are shown for different applied field voltages in a range of 14 – 20 kV at low temperatures (< 100 K). FIM imaging was conducted as described in Sec. 4.2.4. The FIM image

shows a few bright spots at low energy (see Fig. 4.18 **a**) that are not correlated to any specific crystallographic feature. Interestingly, by increasing the applied voltage, new spots appear along with novel stripe-like features, which are bend outwards (Fig. 4.18 **b** to **d**). The impinging helium atoms seem to ionize both at the apex surface and along the SLG edges, which could lead to the stripe signals. We observed this signals for several SLG-functionalized tips, which suggests the successful SLG uptake by the respective emitter apices. Similar streak-like signals have been reported for FIM images of CNTs [196], folded graphene sheets on platinum emitters [200] and multilayered graphene edges on tungsten emitters [201]. However, it is not yet clear, how these signals are correlated to the positioning of the SLG on the tip apex.

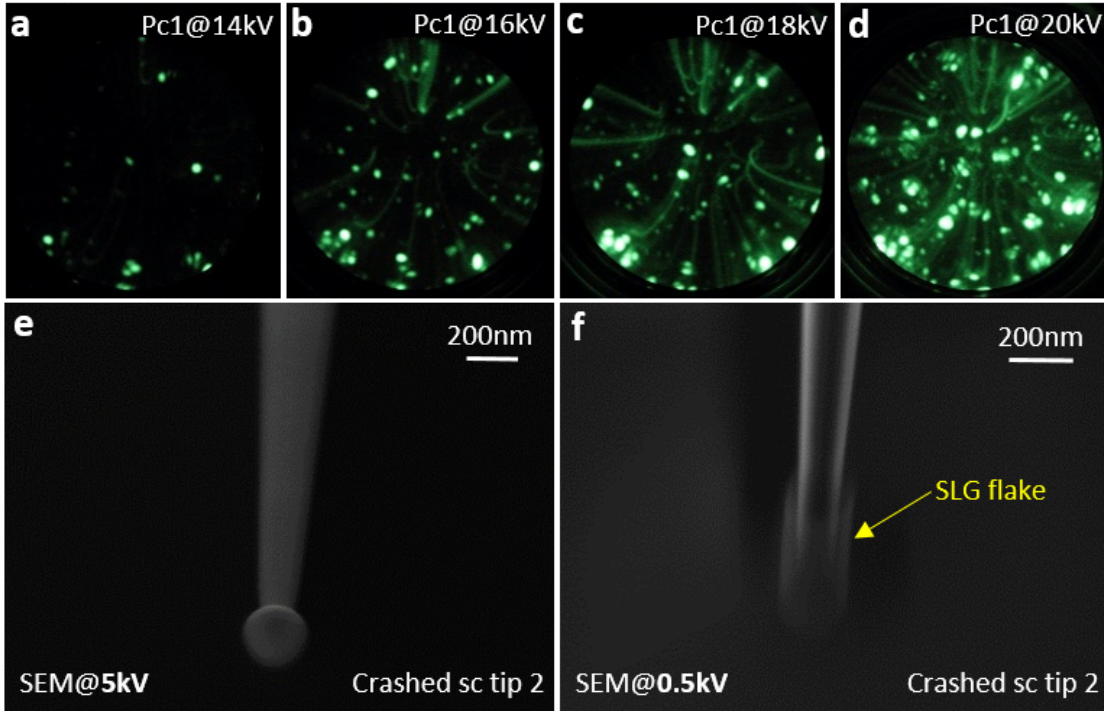


Figure 4.18: FIM images of the SLG functionalized *pc* tip 1 shown in Fig. 4.17 **e** at low temperatures: By increasing the applied emitter voltage during FIM imaging from 14 kV (**a**) over 16 kV (**b**) and 18 kV (**c**) up to 20 kV (**d**), stripe-like signals and bright unstructured spots become visible. No crystallographic planes are identified. The amount of spots and stripes and their brightness increases by increasing the applied voltages. SEM images of a *sc* tip, whose emission properties were totally compromised after the SLG functionalization procedure: When imaging the tip using 5 kV imaging voltage at 51.000× magnification (**e**), a bulb-like apex is observed, which indicates a strong contacting of tip and substrate during LEEH imaging. At lower imaging voltages (0.5 kV at 64.000× magnification) (**f**), an unresolved feature enveloping the apex and shank is visible, which can be identified as an SLG flake.

Even though this technique can lead to the improvement of the emission properties, it can also result in unusable emitters and it is difficult to predict its outcome for several reasons. First, the emitter apex varies in size and shape for each tip, thus the contacting area and electric field at the apex termination also differs. Second, the target SLG piece is usually not a perfectly even plane on the grid, but can be bent and/or have folds, which also influences the contacting area and the interaction upon contact. Third, the procedure used so far does not allow for the

control of the area of graphene removed during the process. This could depend on the apex size and shape, the applied emission voltage and current, how the graphene is attached to the supporting grid, the step size during approach, and perhaps additional unknown factors. Fourth, we do not have control over the folding of the graphene on the emitter apex. The graphene can lay flat, layered or crumpled on the apex. Different graphene folding influences the work function of the emitter and thus the electric field and electron emission.

The reliability of the technique in terms of a stable field emission after substrate contact depends strongly on a controlled step size upon contact, i.e. how far the tip is moved into the substrate. Tips, which contacted the SLG in an uncontrolled manner or with a too large step size, usually lose their ability to field-emit. These emitters are considered to be crashed and have to be electrochemically re-etched. Fig. 4.18 e shows the apex of a crashed *sc* tip imaged via SEM, which field-emitted only for a few seconds after the substrate contact before stopping to emit. This SEM image of the tip was acquired using 5 kV as imaging voltage. The tip shows a ball-like structure with a radius of around 125 nm. The ball-like apex structure results from the melting of the tip due to the high power applied to it during the contact, as explained in more detail in Sec. 3.6. By lowering the SEM imaging voltage to 0.5 kV, a shadow-like structure around the tip apex is visible, see Fig. 4.18 f. This unresolved feature probably originates from the presence of the SLG flake, which is covering the apex. This interpretation is supported by the fact that this unresolved feature is only visible for low imaging voltages. In fact, an SLG flake would be imaged only at low voltages for the following reasons: Firstly, the electron permeability of SLG increases for higher electron energies [202] and secondly, the amount of secondary electrons emitted by the substrate decreases at lower imaging voltages, which increases the intensity ratio of secondary electrons originating from the graphene [203]. The large size of the SLG sheet on the tip and the large apex radius indicate for an intense tip-sample contact (crash), which explains why the tip was not capable of maintaining a suitable electron emission.

Nevertheless, if carried out in a controlled way, the apex functionalization via direct contacting of free-standing SLG is a novel approach for the improvement of low-quality emitters. For these reasons, we are currently working on the development of reliable preparation protocols for the field-assisted etching of tungsten tips with nitrogen and the SLG-contacting method.

4.2.6 Characterization of Emitters via LEEH

In this section, the results of several example emitters characterized via LEEH are presented. In Sec. 4.2.6.1, three emitters are compared with each other at room temperature in terms of their apex structure (via FIM), the visible amount of fringes by measuring free-standing CNTs and their imaging quality after reconstruction by investigating an individual antibody molecule. In Sec. 4.2.6.2, results of a CNT measurement are displayed, which were imaged using the same emitter being at room and cryogenic temperatures. In Sec. 4.2.6.3, imaging effects from emitters with multiple emission sources are discussed.

4.2.6.1 Comparison of Different Emitters at Room Temperature

To show the importance of the emitter quality for LEEH imaging, I compare the performance of three individual single-crystal emitters *sc1*, *sc2* and *sc3* by investigating them via FIM and LEEH measurements. The apex structures of the emitters were first characterized via FIM, as shown in Fig. 4.19.

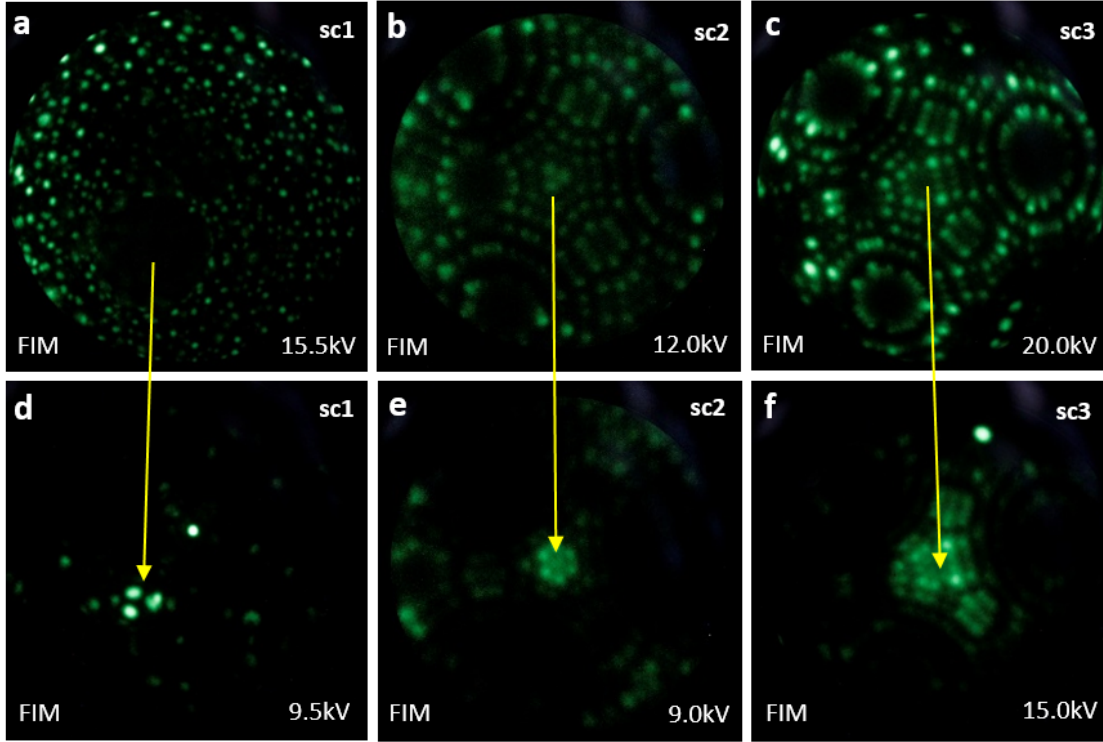


Figure 4.19: FIM images of compared sc emitters at different imaging voltages. **a** and **d**: *sc1* has an apex termination of three atoms (three signals in **d**). **b** and **e**: *sc2* has a crystallographically ordered apex termination between three and seven atoms. **c** and **f**: *sc3* also has a crystallographically ordered apex with several atom locations on the W(111) plane as possible termination sites. The apex sharpness decreases from *sc1* to *sc3*.

While *sc1* is terminated by only three atoms, as indicated by the three bright spots in Fig. 4.19 **d**, no crystallographic planes are visible in the FIM signal of this tip. *Sc2* and *sc3* show crystallographic planes, where *sc2* is terminated by a few atoms in the range of three to seven (Fig. 4.19 **e**) and the apex structure of *sc3* contains a blunt W(111) plane as termination site (Fig. 4.19 **f**). This indicates, that *sc1* has the sharpest apex, followed by *sc2* and finally *sc3*. After the characterization via FIM, the respective emitter performances in LEEH are characterized, which can be done in two ways: via the imaging of free-standing CNTs and the measuring of deposited molecules on free-standing SLG.

As discussed in Sec. 2.2, LEEH imaging of CNTs leads to a biprism effect. The system is commonly used to estimate the virtual source size and contrast visibility of the emitter, which indicates the coherence of the emitted electron beam [38][39][72][90]. Fig. 4.20 displays the

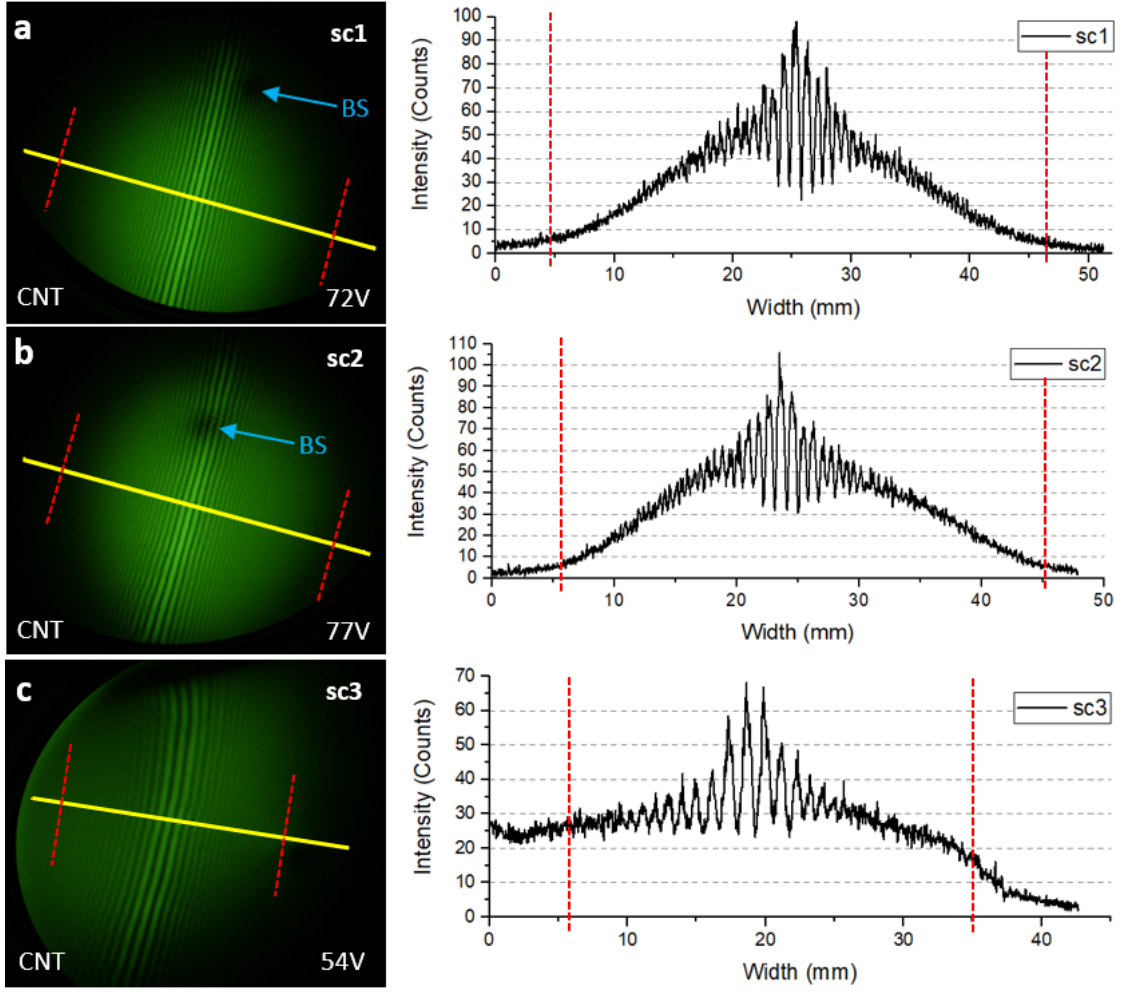


Figure 4.20: Free-standing CNT imaged via the compared emitters *sc1* (a), *sc2* (b) and *sc3* (c) and the respective intensity profiles (yellow line profiles in the images). The dashed red lines indicate the positions of the outermost fringes still visible in the original image, which are difficult to see in the presented images due to the image compression upon figure preparation. The distance between the dashed red lines is used to estimate the hologram width w_{Holo} on the screen, which is around 42.5 mm for *sc1*, 40.0 mm for *sc2* and 29.0 mm for *sc3*. The detector blind spots (BS), visible in **a** and **b**, are marked with blue arrows.

results of the respective free-standing CNT measurements. In Fig. 4.20 **a** and **b**, a periodic dark pattern is visible on the screen, which is the blind spot (BS) of the detector (respectively marked with blue arrows). The size and position of these spots depend on the channel tilt and emitted electron beam trajectories, which vary for different emitters. These patterns are usually visible for large illumination areas and can be ignored in the hologram reconstruction, if not overlapping with hologram fringes of the target molecule.

For each emitter, the same CNT molecule was measured to directly compare the contrast visibility C_{vis} via Eq. 2.9 and detectable hologram width w_{Holo} on the screen. The effective source size $r_{\text{eff}} = \frac{2\lambda Z}{\pi w_{\text{Holo}}}$ and coherence angle $\theta_c = \tan^{-1}\left(\frac{w_{\text{Holo}}}{2Z}\right)$ can both be deduced from the

Chapter 4. Emitter Preparation and Characterization

hologram width using the respective emission wavelengths λ and $Z = 11.5$ cm (see Sec. 2.2). Furthermore, the lateral Abbe and Rayleigh resolution limits can be calculated from λ and θ_c via Eq. 2.10 and 2.12. The respective measured and calculated values for each emitter are summarized in Tab. 4.3:

Table 4.3: Measured and calculated properties of the compared sc emitters.

Tip	λ (Å)	w_{Holo} (cm)	r_{eff} (Å)	θ_c (°)	$R_{\text{Holo,lat}}^{\text{Abbe}}$ (Å)	$R_{\text{Holo,lat}}^{\text{Rayleigh}}$ (Å)	C_{vis}
<i>sc1</i>	1.45	4.25 ± 0.05	2.49 ± 0.03	10.47 ± 0.12	3.99 ± 0.04	4.87 ± 0.05	0.623
<i>sc2</i>	1.40	4.00 ± 0.05	2.56 ± 0.03	9.87 ± 0.12	4.08 ± 0.05	4.98 ± 0.06	0.540
<i>sc3</i>	1.67	2.90 ± 0.05	4.22 ± 0.07	7.19 ± 0.13	6.67 ± 0.12	8.05 ± 0.15	0.492

It is important to mention that the images shown in Fig. 4.20 were compressed in size and amount of pixels during the figure preparation, which compromises the actual visibility of fringes in the displayed figure. The non-compressed raw image versions are displayed in the Appendix as Fig. A.1, A.2 and A.3, where the finest outer fringes for *sc1* and *sc2* are still visible. The resulting hologram widths and intensity profiles indicate the highest coherence, resolution and contrast visibility values for *sc1* and the lowest values for *sc3*. With a contrast visibility of > 0.60 , an effective source size of around 2.5 Å and a coherence angle of around 10.5° , the measured properties of *sc1* match the performance of reported values of other tungsten point sources, indicating a high-quality performance in LEEH measurements [39][72][90].

To confirm the respective imaging performances of the tips, a three-lobe Herceptin antibody molecule deposited on SLG via ES-IBD (see also Sec. 7.3.2 for more details) was measured with all three emitters via LEEH. The acquired holograms and their amplitude reconstructions are shown in Fig. 4.21. While the focus distance for *sc1* and *sc2* can be determined with high certainty when analyzing the amplitude reconstruction stack (290 nm and 270 nm, respectively), it is difficult to determine the focus for *sc3*. For *sc1* and *sc2*, more high-order fringes are visible in the hologram and the reconstructed three-lobe structure of the antibody is clearly recognizable with the subunits fitting the respective shape and sizes in the range of 4 – 6 nm of known model structures, e.g. if compared to the antibody model *IIGY* shown in the RCSB protein data bank (see <https://www.rcsb.org/structure/IIGY> and Sec. 7.3.2). When imaged with the *sc3* emitter, less fringes of less contrast are observable and the amplitude reconstruction shows a more fuzzy, less well-defined antibody shape and an exact size measurement is difficult. The estimated local resolution, which is approximated via the identification of visible molecular features, ranges from less than one nanometer for *sc1* and *sc2*, where the individual lobes of the three antibody subunits can be identified, to several nanometers for *sc3*.

These results emphasize the importance of the emitter quality in relation to the image quality. A sharper and more defined apex termination leads to a smaller effective source size and higher spatial coherence, which consequently increases the amount and contrast of visible fringes in the hologram, resulting in a higher resolved image of the molecule after reconstruction.

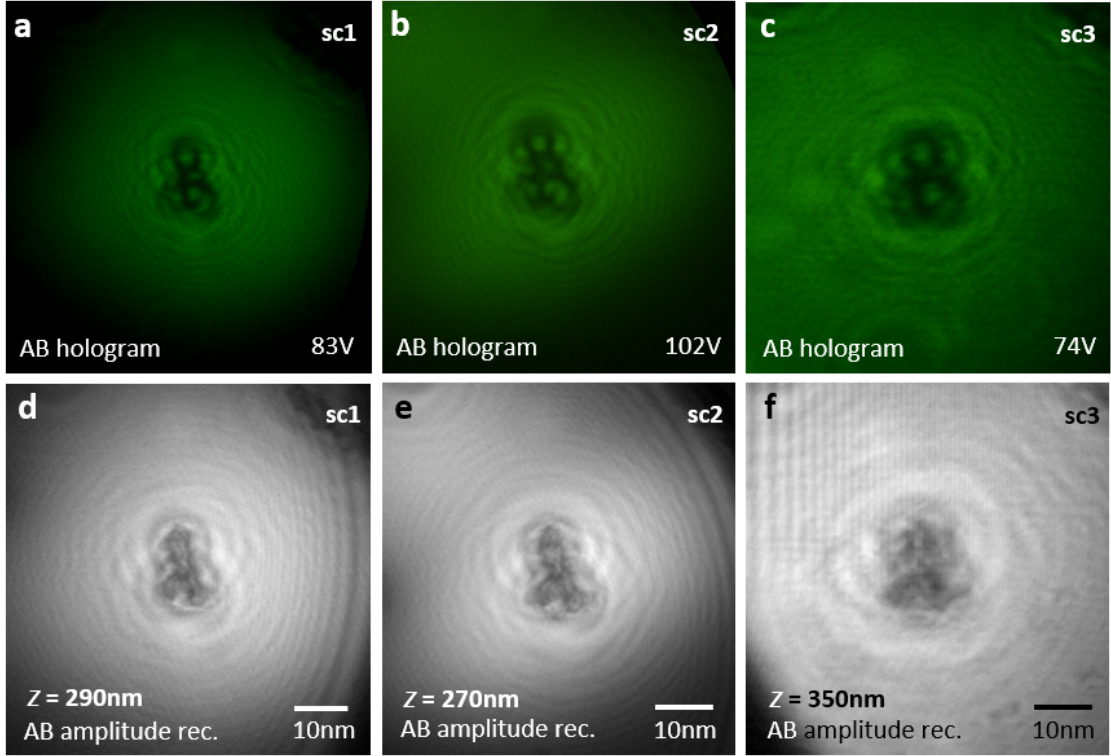


Figure 4.21: Holograms of a three-lobe Herceptin antibody molecule measured in LEEH via the compared sc emitters *sc1* (a), *sc2* (b) and *sc3* (c), as well as the respective reconstructions shown in d, e and f. While images measured with *sc1* and *sc2* show a similar, high-quality in the acquired hologram and a reconstruction with a sharp focus, the imaging quality of *sc3* is much lower and does not yield a distinct focus distance.

4.2.6.2 Emitter Performance at Cryogenic Temperatures

A way to improve the field emission properties of the tip is measuring at cryogenic temperatures [72], which we demonstrate for the field emission stability and noise reduction in Sec. 4.2.2.2. To test the influence of cryogenic emitter temperature on the LEEH imaging performance, we measured free-standing CNTs with an individual emitter at room temperature (RT, 295 K) and cryogenic temperatures (LT, 50 K). Fig. 4.22 shows the results measured with a single-crystal (sc) emitter at both temperature ranges.

Table 4.4: Measured and calculated properties of an sc emitter used at RT and LT.

Temp. (K)	λ (Å)	w_{Holo} (cm)	r_{eff} (Å)	θ_c (°)	$R_{\text{Holo,lat}}^{\text{Abbe}}$ (Å)	$R_{\text{Holo,lat}}^{\text{Rayleigh}}$ (Å)	C_{vis}
295 (RT)	1.28	2.90 ± 0.05	3.23 ± 0.05	7.19 ± 0.13	5.11 ± 0.09	6.23 ± 0.06	0.564
50 (LT)	1.44	3.80 ± 0.05	2.78 ± 0.04	9.38 ± 0.12	4.42 ± 0.06	5.39 ± 0.07	0.648

As already discussed for Fig. 4.20, the images shown in Fig. 4.22 also had to be compressed during the figure preparation, which reduces the visibility of fringes in the figure. Non-compressed raw image versions are displayed in the Appendix as Fig. A.4 and A.5 for the

RT and LT measurements, respectively. The measurement results are summarized in Tab. 4.4.

Even though the emitter had a lower emission energy, and thus a larger electron wavelength λ while cooled to around 50 K, all other measured and calculated emitter values show improved values compared to the measurement at RT. The hologram width w_{Holo} , coherence angle θ_c , and visibility contrast C_{vis} increased, while the calculated effective source radius r_{eff} , and resolution limits $R_{\text{Holo,lat}}^{\text{Abbe}}$ and $R_{\text{Holo,lat}}^{\text{Rayleigh}}$ decreased by a factor of around 16%. Similar emission property improvements for measurements of CNTs with emitters at cryogenic temperatures were reported by B. Cho, et al. [72], where the increased image resolution and contrast are resulting from a higher spatial and temporal coherence of the cooled emitter, as explained in the sections 2.2 and 4.2.2.2. The results obtained from the Cryo-LEEH tests are promising and suggest higher achievable resolutions for molecules measured at LT when compared to measurements at RT. Combined with very defined and sharp emitters, the Cryo-LEEH system could yield local resolutions very close to the theoretical limits described in Sec. 2.3.

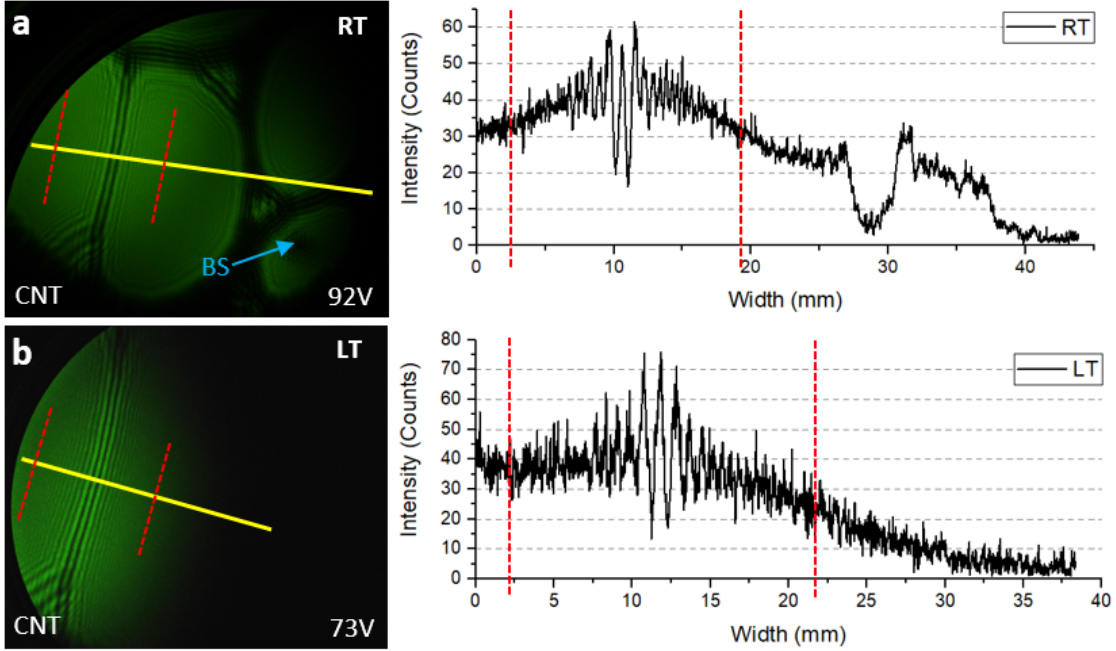


Figure 4.22: LEEH measurements of a free-standing CNT using an sc emitter at room temperature (RT = 295 K, **a**) and low temperature (LT = 50 K, **b**) with the intensity profiles (yellow line profiles in the images) plotted to the right of the respective measurement. The dashed red lines indicate the regions within the images, where fringes are still distinguishable, which does not hold for the displayed images due to the image compression upon figure preparation. The visibility contrast and hologram width are improved when the emitter is cooled to cryogenic temperatures. The measured hologram widths for the used emitter are 2.90 mm at RT and 3.80 mm at LT. In **a**, the blind spot of the detector (BS, marked by a blue arrow) is visible due to the larger illumination area when compared to **b**.

4.2.6.3 Ghost Image Artifacts

We found that even high-quality emitters can have two or more very defined emission sources, such as double tips, which for example could have been the case for *sc1* when analyzing the FIM image, where a separated single bright spot is visible next to the three spots at the apex (see Fig. 4.19 **d** and 4.12 **d**). These separated emission spots can lead to the formation of ghost image artifacts, where the signals of neighboring holes overlap with the signal of the imaged target hole. As shown in Fig. 4.23 (marked by yellow arrows), these artifacts have a lower intensity compared to the target hole and usually appear at the detector edges.

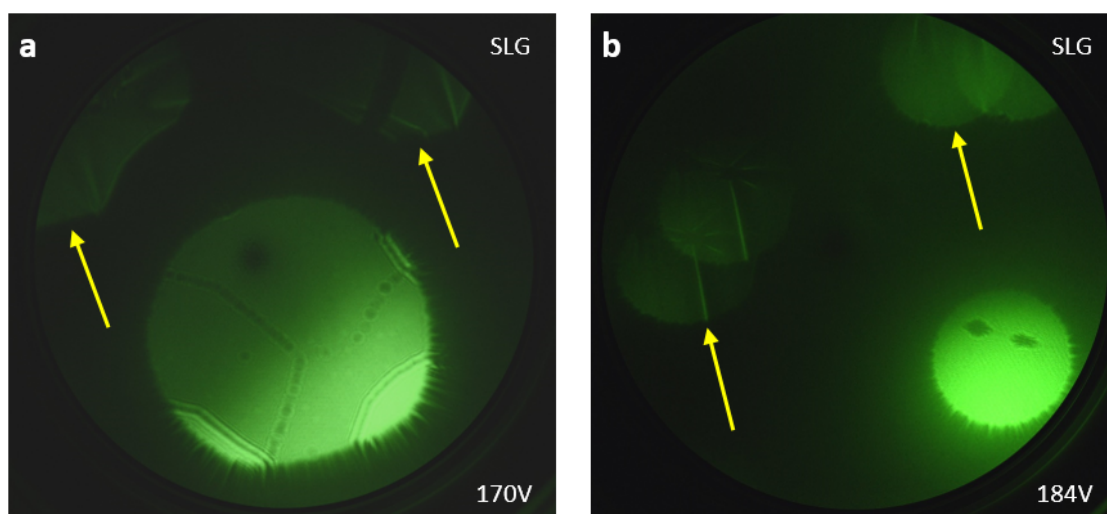


Figure 4.23: Two images of characterized SLG holes with holes sizes of 1 μm (**a**) and 500 nm (**b**) showing ghost image artifacts due to a double tip emission. The artifacts mainly occur for tips with several effective source positions on the apex and are visible on sample grids with short pitch sizes between the holes, where $d_{\text{pitch}} < 2.5 \cdot d_{\text{hole}}$.

In principle, molecules on these image artifacts can be reconstructed if fringes are visible. However, the intensity, contrast and amount of fringes is usually too low to yield a high-quality image and it is difficult to find a distinct focus position. This can be explained by the formation process of the ghost images, where the electron beam emitted from a second defined source position is hitting the sample with a different angle and the projection of the neighboring hole is diffracted towards the detector leading to a distorted image signal. The effect can be minimized by using grids with larger pitch sizes $d_{\text{pitch}} \gtrsim 2.5 \cdot d_{\text{hole}}$, since the electrons emitted from the additional source position cannot be transmitted through the grid, if no neighboring hole is in close proximity to the target hole. Other possibilities to prevent this kind of artifacts are additional sputtering and annealing procedures to remove the interfering emission source position, and/or the centering of the illumination area, which is determined by the field emission angle of the electron beam. For example, repositioning can be achieved by the use of Helmholtz coils, which is further discussed in Sec. 9.2.

5 Substrate Preparation and Characterization

Surface science is a fundamental field in physics, chemistry, biology and medicine. The reactivity and properties at the surface of most materials differ vastly from the bulk, which offers tremendous possibilities for research and application [204][205][206]. This is even more stringent for our experiments that deal with specific requirements dictated by our LEEH microscope and the fragile nature of biological samples. In particular, the reduced penetration depth of low-energy electrons suggests the use of an atomically thin substrate (2D material).

One of the most important 2D materials is graphene, which consists of a single layer of sp^2 -hybridized carbon forming a honeycomb lattice [40][207]. It was first isolated from graphite in 2004 by Geim and Novoselov, both of whom were awarded with the Nobel Prize in Physics in 2010 for this discovery [208]. Single graphene sheets can be produced via various methods [209], such as exfoliation [210] or controlled chemical vapor deposition (CVD) of carbohydrates [211].

Single-layer graphene (SLG) sheets have ideal properties for the use as a substrate in electron microscopy techniques [212][213]. SLG shows a high transparency in the range from 74% for low- [36][41] and up to 98% for high-energy electrons [42][214]. Furthermore, it acts as an equipotential plane, which can prevent charging of the sample and thus, decreases distortions via electrostatic fields caused by the imaged objects [37][41]. It possesses a very high mechanical stability [43], which is necessary for the deposition of larger samples onto it, and is thermally stable up to 450°C in air, when oxidation starts to take place [215], and up to 800°C in inert conditions [216]. Since its main interaction with sample materials is caused by Van der Waals forces [43], it has been shown by several studies to be mostly non-reactive towards biological molecules during imaging [44][45][51].

These properties fulfill the criteria for LEEH imaging, therefore, we use SLG as support substrate for the deposition of molecules and their investigation via LEEH. However, the quality of the SLG in terms of its purity and cleanliness is crucial for our technique. For this reason, we adapted the SLG preparation technique reported by J.-N. Longchamp et al. [217] and further

optimized it for our purpose. In the following sections, I describe the substrate preparation procedure in detail and also mention crucial steps, which strongly affect the quality of the substrate. With the illustrated technique, we are able to produce ultra-clean free-standing SLG samples in a reproducible manner, which can be used for the deposition of molecules and subsequent high-quality imaging via LEEH.

5.1 Grid Preparation

Here, I describe the preparation of the supporting grids, on which the graphene is suspended. The requirements for these grids are a high cleanliness, full conductivity to avoid charging effects during LEEH measurements, and one or more holey arrays containing holes with a defined size within a thin membrane. The reduced thickness of the membrane is important to avoid a cutoff of the diverging electron beam.

The basic support grids are silicon nitride (SiN) grids containing a 200 nm thin membrane window with holey arrays and hole diameters of 500 nm (NH050D050, Norcada) or 1 μm (21581-10, Ted Pella), which are commonly used for TEM applications. SiN has a high thermal stability, which is necessary for heating procedures, and the thin membrane window is robust enough for the SLG uptake, as described in Sec. 5.2.1. However, since SiN is an insulating material, an additional conductive layer is needed to prevent charging of the grid due to the electron emission during LEEH experiments. For this reason, we employed a metal coating procedure to ensure a clean and uniform coverage of the grid, which is shown in Tab. 5.1.

Table 5.1: Metal coating procedure of SiN grids via sputter coating.

Step (side)	Process	Material	Layer thickness
1 (bottom)	<i>Plasma clean</i>		
2 (bottom)	Sputter coat	Chromium	5 nm
3 (bottom)	Sputter coat	Platinum	10 nm
4 (top)	<i>Plasma clean</i>		
5 (top)	Sputter coat	Chromium	5 nm
6 (top)	Sputter coat	Platinum	10 nm
7 (top)	<i>Plasma clean</i>		
8 (top)	Fish SLG		

To remove carbohydrates and other contaminants before and during the process, we plasma clean (Atto QL-PCEE, Diener) the grids at a partial air pressure of 0.5 mbar with a power of 0.2 kW for four minutes. We found that the plasma cleaning steps before sputtering and fishing of the SLG helped to reduce the amount of contaminations on the sample. We use a sputter coater (EM ACE600, Leica) to cover the grids with chromium and platinum metal layers. In total, 15 nm of metal are sputter coated on each side of the grid making it conductive. We sputter at an angle of 20° while the grids are rotating, as well as both grid sides to ensure, that the inside of the holes are also covered with metal. This prevents charging effects during

LEEH imaging for almost all measured holes with very rare exceptions. We use 5 nm of chromium as first metal layer to roughen the grid surface, which increases the surface area of the subsequently added platinum for the contact with the SLG upon uptake. The 10 nm of platinum are added as a catalyst layer to support the removal of PMMA, which is covering the SLG during the preparation process (see Sec. 5.2.1). The sputter coated and plasma cleaned support grids are finally used to ‘fish’ the prepared SLG-PMMA flakes with their top side.

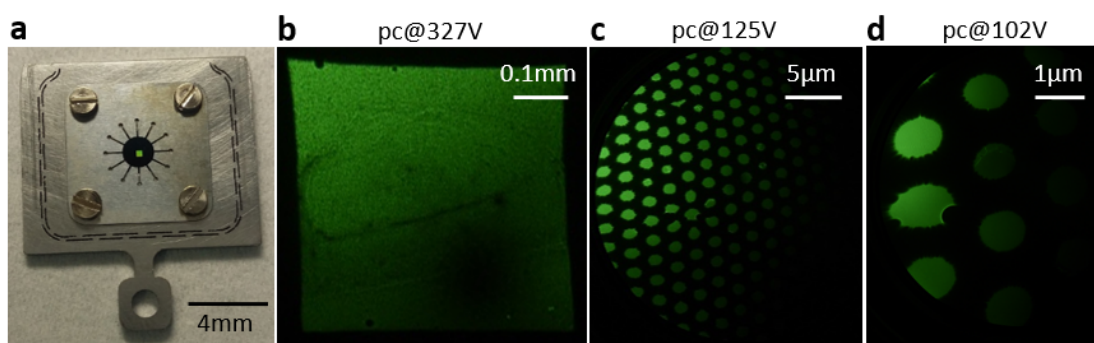


Figure 5.1: **a** Photo of a sample holder with an inserted support grid (Ted Pella, hole size $1\ \mu\text{m}$). The width of the sample holder plate is 12 mm. **b** LEEH image of the holey array within the 200 nm thin membrane window. **c** Zoom in on **b**, where single holes within the array are visible. **d** Zoom in on **c**, where the hole diameter of $1\ \mu\text{m}$ is visible.

Fig. 5.1 shows overview images of the sample holder and a holey SiN support grid with hole sizes of $1\ \mu\text{m}$ at different imaging distances in LEEH. This sample did not contain SLG, but CNTs were drop-casted on it (see Fig. 4.16 **b**). The metal coated SiN grid is fixed via a spring plate on the sample holder (Fig. 5.1 **a**), which prevents slipping or vibrating of the grid during transport and measurements.

5.2 Graphene Preparation and Characterization

In this section, the SLG preparation for the use as substrate in LEEH imaging is discussed (Sec. 5.2.1). I point out critical preparation steps, which can lead to contaminations of the SLG. Furthermore, I show AFM data of our SLG covered holey grids and overview images of contaminated and ultra-clean free-standing SLG characterized via LEEH (Sec. 5.2.2).

5.2.1 SLG Preparation

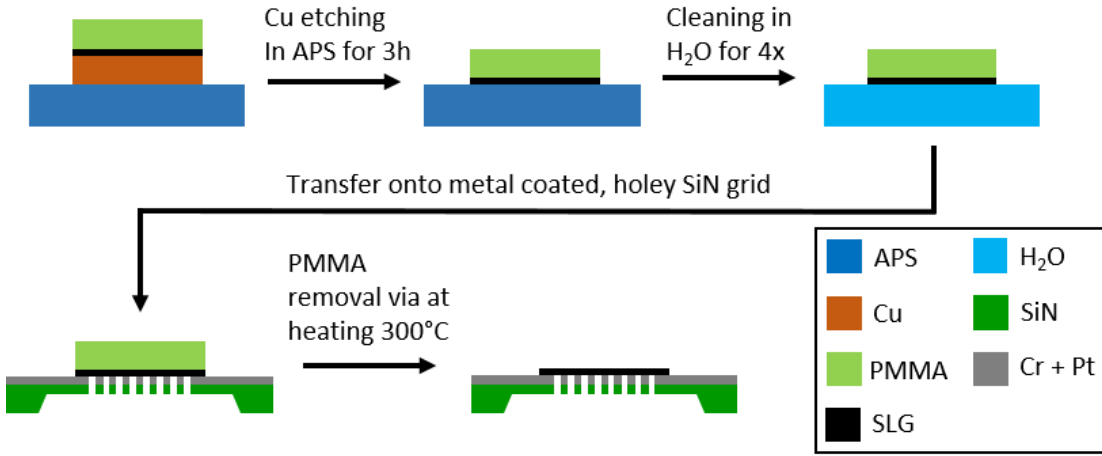
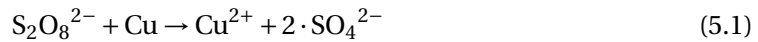


Figure 5.2: SLG preparation process for LEEH imaging as reported by J.-N. Longchamp [217].

Fig. 5.2 shows the different steps required for the preparation of the SLG substrate. We use SLG grown via chemical vapour deposition (CVD) on a copper substrate (Graphenea) as precursor material and spin coat polymethyl methacrylate (PMMA) on the SLG side with a layer thickness of 100 nm. The PMMA serves as a protective layer to prevent contamination or folding of the SLG during the upcoming steps of the procedure and has to be removed again in the final step [211]. Rectangular flakes with a side length of 2 – 3 mm are cut from the precursor Cu-SLG-PMMA sheet using a razor blade. Subsequently, the flakes are suspended on an ammonium persulfate (APS, Serva) solution, which has a concentration of $0.33 \frac{\text{mol}}{\text{l}}$ in deionized water with the copper side facing the APS. The flakes are kept on the etchant for around 3 hours. During this time, the APS solution dissolves the copper layer completely (see equation 5.1) and the remaining and transparent SLG-PMMA flakes can be identified on the solution by their light reflecting properties when illuminated with a lamp [218].



After the etching is finished, the flakes are transferred to fresh and clean deionized water and left floating on the surface for around 1 hour. Afterwards, the flakes are transferred to another beaker with fresh and clean deionized water for another hour. These cleaning steps are repeated for another 2 – 3 times leading to the complete removal of metal and etchant residues. Finally, each flake is fished via a respectively prepared SiN grid (see Sec. 5.1) and are used for an individual experiment. During the fishing, it is important to place the flake above the membrane part of the SiN grid containing the holey array. With the PMMA layer still on the SLG, the substrates can be stored for months in a dry and closed container.

Before usage, the PMMA layer has to be removed from the SLG, which is commonly achieved by adding acetone to the PMMA surface. However, this technique has been shown to leave

high amounts of PMMA residues on the SLG surface, which act as a contaminant [219]. For this reason we employ the platinum catalysis method for the PMMA removal, which consists of a controlled, stepwise heating procedure of the platinum covered grids in air [217]. For this process, the grid is put into one of our sample holders (as shown in Fig. 5.1 a) and placed on a programmable heating plate (HP40A, Torrey Pines Scientific). The exact heating process is shown in Tab. 5.2 and has a total duration of around 3 hours:

Table 5.2: Heating procedure for PMMA removal via platinum catalysis.

Step	Final temperature	Gradient	Incubation time
1	50°C	—	10 min
2	100°C	120°C/h	5 min
3	240°C	240°C/h	5 min
4	270°C	120°C/h	5 min
5	300°C	60°C/h	0 min
6	300°C	—	45 min
7	<i>Fast transfer of hot sample into UHV.</i>		

During this process, which is performed at temperatures below the oxidation temperature of SLG, platinum acts as a catalyst for the removal of PMMA layers via different possible decomposition mechanisms such as depolymerization, depropagation, random-chain scission and end-chain initiation [220]. Hereby, the platinum metal layer decreases the temperature necessary for an efficient hydrogenation of the PMMA, which can initiate the polymer decomposition even at non-coated substrate locations within the vicinity of the platinum, such as the free-standing SLG [217]. Without the catalyst, the process would require temperatures of at least 400°C, which could also lead to an oxidation of the SLG [215].

After PMMA removal, the sample holder containing the SiN grids with SLG have to be transferred into UHV as fast as possible and while still hot, for which we use the fast transfer load lock (FTLL) of our LEEH setup. As soon as the substrate is evacuated to a FTLL pressure of $< 2 \cdot 10^{-7}$ mbar, it can be transferred into the LEEH chamber and characterized via LEEH.

5.2.2 SLG Characterization

Here, I present the characterization of SLG via AFM (Sec. 5.2.2.3) and LEEH. Different aspects are discussed, such as grid coverage (Sec. 5.2.2.1), contamination (Sec. 5.2.2.2), transmission of SLG and graphene multilayers (Sec. 5.2.2.4), observed Moiré patterns (Sec. 5.2.2.5), visible charges and clusters prior to any deposition (Sec. 5.2.2.6), and imaging at cryogenic temperatures (Sec. 5.2.2.8).

5.2.2.1 Grid Coverage and SLG Identification

The presented preparation procedure yields a general SLG coverage of the SiN grids of 70–95%, which is more than sufficient for LEEH experiments. An interesting effect can be seen for holes, which do not contain free-standing SLG: their shape appears larger and edged when compared to SLG covered holes. This distortion is due to charging effects occurring on the inside of the SiN membrane [221]. This effect can be useful, since it enables us to easily distinguish holes covered with ultra-clean SLG from empty ones, as shown in Fig. 5.3. Another possibility to identify holes, which are empty or contain suspended SLG or even multiple layers of graphene (MLG), is via measuring the electron signal intensities for different regions of the imaged hole, which is further explained and discussed in Sec. 5.2.2.4.

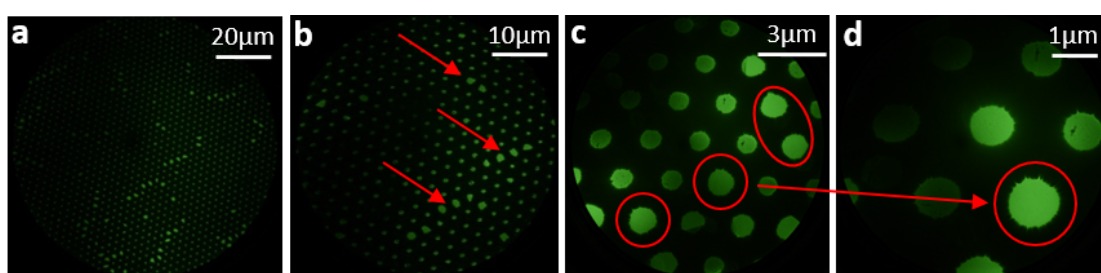


Figure 5.3: LEEH images of SLG covered and empty holes. In **a** and **b**, overview images are indicating a high SLG coverage of the SiN grid membrane. Covered holes appear smaller than empty holes, which usually show an edged shape during imaging. Some empty holes are marked by red arrows in **b**, and are encircled in red in **c** and **d**, which were measured at closer distances.

5.2.2.2 SLG Contamination during Preparation

We found that several factors during the preparation procedure can lead to contaminated free-standing SLG samples, which is illustrated in Fig. 5.4. If the heating procedure is stopped at lower temperatures or carried out too fast, e.g. with incubation times of less than 30 minutes for the final step at 300°C, PMMA residues can remain on the graphene, which massively compromise the imaging capabilities of LEEH as shown in Fig. 5.4 **a**. If the sample transfer into UHV is not carried out fast enough and/or after the sample has already cooled down, the SLG can get contaminated by the adsorption of molecules such as hydrocarbons, which also reduces the imaging quality as shown in Fig. 5.4 **b**, where the sample was cooled down to room temperature before transfer into the FTLL.

Further contamination sources are SiN grids, which were not plasma cleaned and can lead to hydrocarbon contaminations, as well as the use of impure water during the cleaning steps after the APS etching. Moreover, copper residues can remain on the sample if the etching procedure is interrupted too early and copper sulfate residues can be found on the sample, if the cleaning process is not carried out properly. Fig. 5.4 **c** shows a hole covered by ultra-clean SLG, where no contaminations are visible, demonstrating the final result obtained following our procedure. However, holes showing folded graphene multilayers or ripped SLG parts with empty areas

cannot be avoided, even after a careful preparation procedure. An example image of a hole containing ultra-clean SLG, an empty part and MLG can be seen in Fig. 5.4 **d**. However, each grid contains a large number of SLG-covered holes, which still qualify for characterization prior to the deposition.

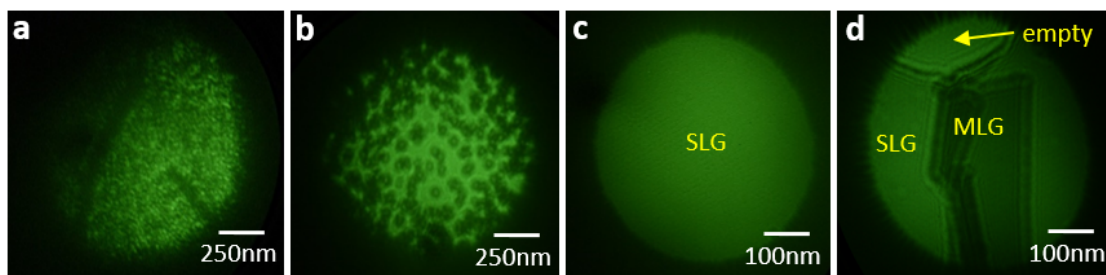


Figure 5.4: LEEH images of different SLG samples. **a**, **b** and **c** show images of different SLG-covered holes at various stages of cleanliness. The sample is highly contaminated in **a**, where the heating process was stopped only 5 minutes after reaching 300°C, and **b**. **c** shows an ultra-clean SLG hole. **d** displays a hole containing SLG, an empty space at the top and graphene multilayers (MLG). Hole diameters are 1 μm for all samples except **c** and **d**, where the hole diameters are 500 nm.

5.2.2.3 AFM Measurements of Prepared Substrates

We also investigated some prepared SLG samples via AFM, which is shown in Fig. 5.5. We used the tapping mode in air with a microcantilever (OMCL-AC200TS-R3, Olympus) at ambient conditions for AFM measurements (Dimension Icon, Bruker) and acquired images via a remote control software (Nanoscope v.8.15, Bruker). The images were analyzed with an open source software, which is optimized for scanning probe microscopy (WSxM v5.0 develop 9.0 by [222]).

As displayed in Fig. 5.5 **a**, empty and SLG-covered holes can be easily identified by the height profiles. While SLG-covered holes show a height difference of about 15 nm between the free-standing SLG and the metal covered SiN support grid (see Fig. 5.5 **d**, **e** and **f**), the height profiles of empty holes show a height difference of 150 – 200 nm between hole and grid, which is within the SiN membrane thickness range. The close-up images in Fig. 5.5 **b** and **c** show a rough surface texture on the support grid, which suggests the formation of metal nanoclusters during sputter coating [223]. Furthermore, contaminated (Fig. 5.5 **b**) and ultra-clean SLG (Fig. 5.5 **b**) can be distinguished from each other, where the contaminated sample shows some PMMA residues due to an interrupted heating procedure, which was stopped before 30 minutes at 300°C.

The presented AFM results confirm that the used preparation protocol can yield ultra-clean free-standing SLG substrates in a reproducible manner, which can be characterized via different methods and used for the deposition of other molecules for the investigation via LEEH.

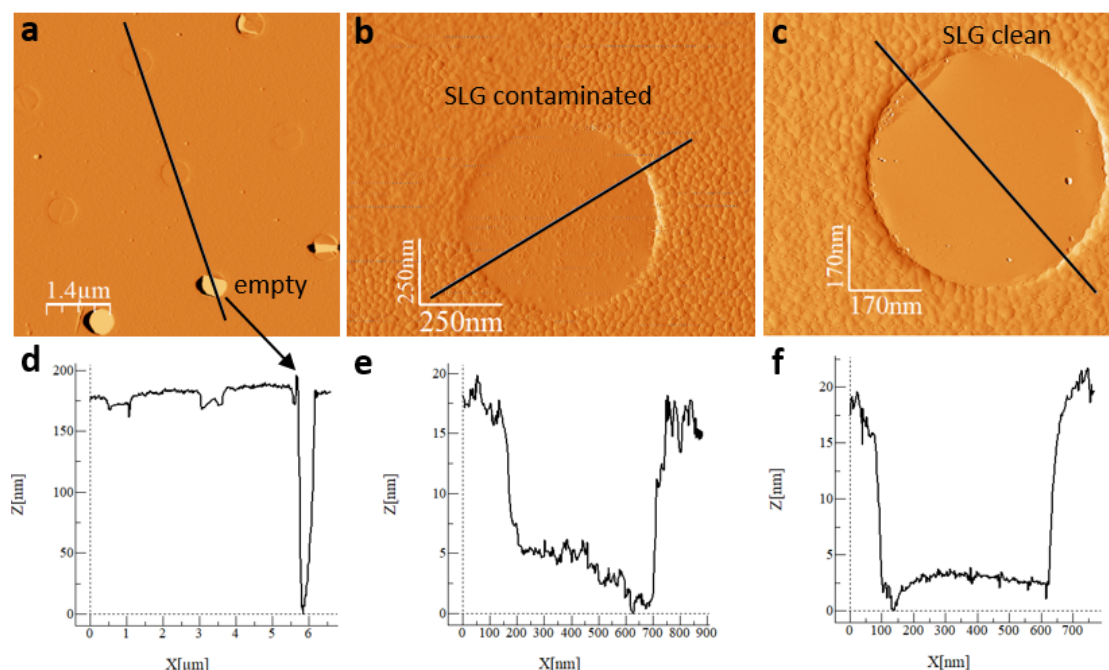


Figure 5.5: **a** Overview image of a SiN grid containing SLG covered and empty holes. **b** Close-up image of a hole with contaminated SLG. **c** Close-up image of a hole with ultra-clean SLG. **d**, **e** and **f** are the respective line profiles measuring the height of the substrates. The empty holes can be clearly distinguished in the images and by the height profile. The close-up image profiles show a substrate to free-standing SLG height difference of 12 – 20 nm, which fits the amount of deposited chromium and platinum metal on the SiN grid. The contaminated SLG shows PMMA residues on its surface, which originate from an interrupted heating procedure. Hole diameters are 500 nm.

5.2.2.4 Electron Transmission through SLG and MLG

The characterization of individual holes covered by free-standing SLG via LEEH is of great importance for a controlled deposition of molecules (see Sec. 5.2.2.7). While the determination of the SLG cleanliness after preparation has already been discussed in Sec. 5.2.2.2, the characterization of bilayer graphene (BLG) and multilayer graphene (MLG) is discussed in the following.

In contrast to its very high transparency for visible light, where the opacity of SLG is around 2.3% per molecular layer [202], it has already been shown by J.-N. Longchamp et al. that the SLG opacity is at least an order of magnitude larger for low-energy electrons [36]. We measured and analyzed this property for 150 individual holes containing SLG, BLG, MLG and/or empty areas and averaged the respective transmission intensities, which is shown in Fig. 5.6 **b**. It is important to mention, that the data was normalized by setting the transmission through an empty area to 100%, while the transmission through the grid substrate parts was used as a background offset and subtracted from the data.

The resulting transmission values (black data in Fig. 5.6 **b**) are $75.7 \pm 9.1\%$, $46.7 \pm 9.5\%$ and

$30.0 \pm 7.3\%$ for the respective graphene layer numbers of $n_{\text{SLG}} = 1, 2, 3$, which are in good agreement with the values reported by [36]. Since the transmissibility function T depends on the amount of carbon layers, it is possible to fit the data with an exponential function $T(x) = \exp(-t \cdot x)$ (red fit function in Fig. 5.6b) [224], where x can be interpreted as layer thickness or layer amount n_{SLG} and the transmission coefficient is determined from the fit as $t = 0.40$. The relatively large errors of 7.3 – 9.5% in the graph originate from noise and the fact that the electron beam has a Gaussian shape, which is difficult to subtract from the images. The effect is illustrated in the intensity profile plots of the two regions in Fig. 5.6c and d, which are marked with the respective colored arrows in Fig. 5.6a. The normalized and averaged transmission values vary for SLG from around 69% (red profile) to around 61% (blue profile) and for MLG from around 30% (red profile) to around 24% (blue profile), which roughly fits the expected deviations observed in Fig. 5.6b.

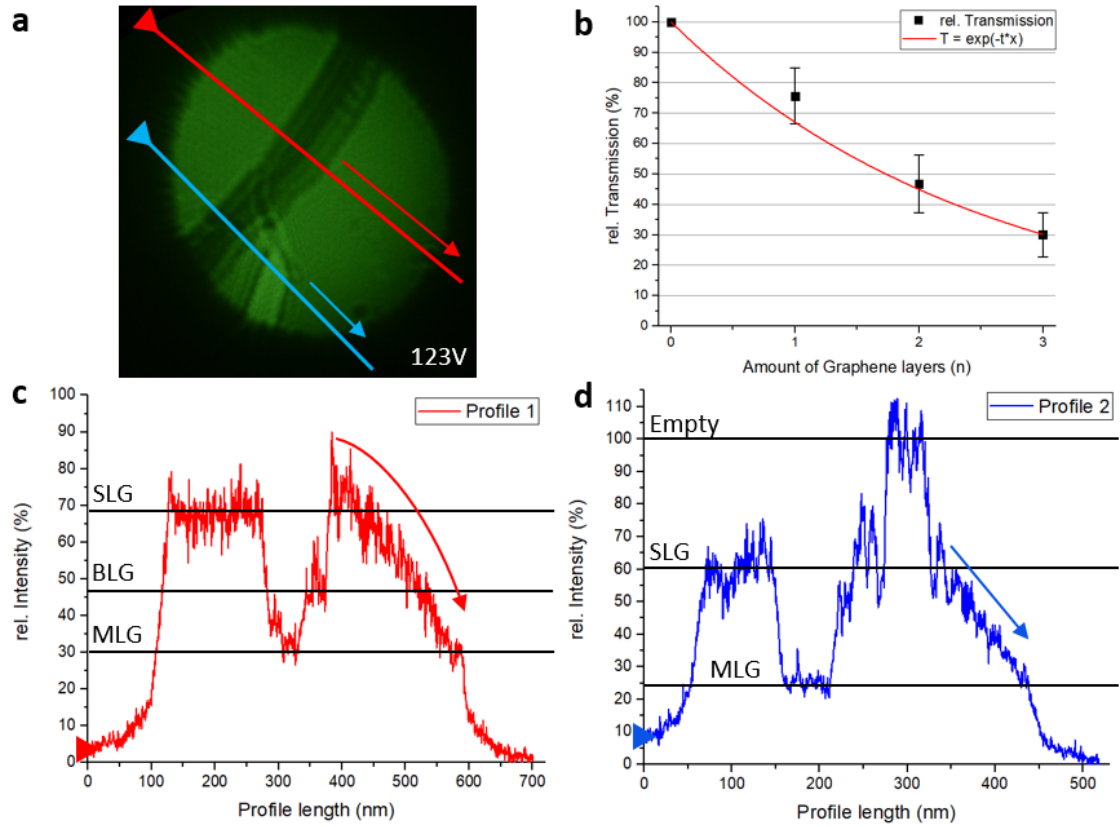


Figure 5.6: Electron transmission through graphene layers. **a** A hole containing SLG, BLG, MLG and an empty area. The red and blue colored line profiles are shown after normalization and background subtraction in **c** and **d**, respectively. **b** Transmission data (black squares) in relation to the amount of graphene layers averaged for 150 holes with an exponential fit (red line fit: $T = \exp(-t \cdot x)$) leading to a transmission coefficient $t = 0.40$. **c** Red line profile from **a** showing relative averaged intensity values for SLG (around 69%), BLG (around 46%) and MLG (around 30%). **d** Blue line profile from **a** showing the relative averaged intensity values for SLG (around 61%), MLG (around 24%) and the empty area (set to 100%). The overall intensity decrease compared to the red profile depends on the illumination area of the electron beam, which decays rapidly away from its center.

5.2.2.5 Moiré-Patterns on BLG

An interesting feature, which can occasionally be observed on BLG, is the formation of Moiré patterns. These patterns originate from the large-scale interference of two stacked, periodic structures, which are rotated with respect to each other. Moiré patterns have been reported for graphene sheets by measurements via TEM [225] and LEEH [36].

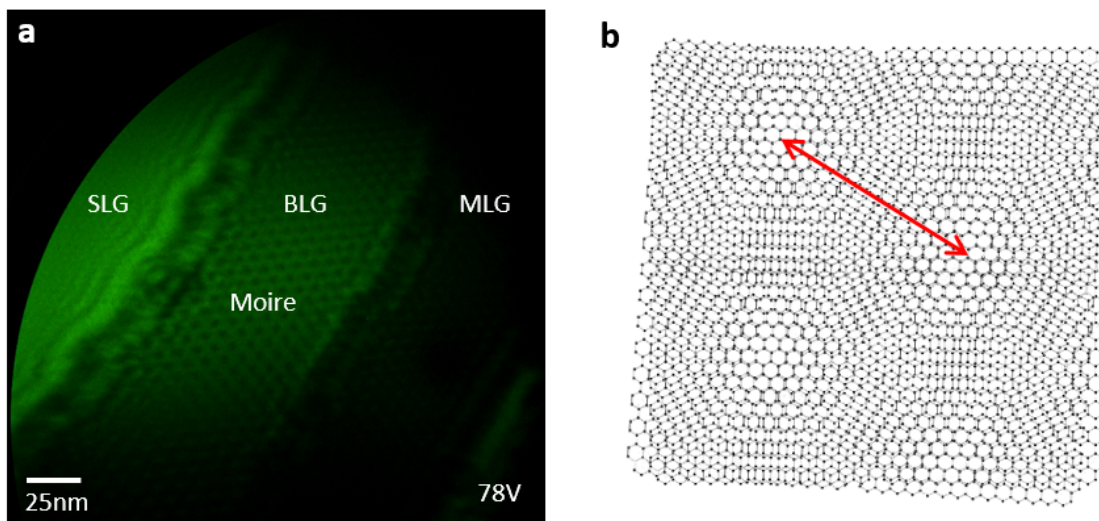


Figure 5.7: Moiré pattern of BLG visible during LEEH imaging. **a** Image of a hole containing SLG, BLG and MLG, where the BLG stripe shows a Moiré pattern with distinct periodic dark and bright signal width of the stripe is about 58 nm. A single dark feature contains around 19 carbon atoms, when using the bond length of graphene of 0.142 nm. **b** The estimated twisting angle of the graphene layers forming the Moiré pattern shown in **a** is around 4° , where the amount of carbon atoms between two feature centers is 37-38 (red line).

Fig. 5.7 **a** shows an example image of a BLG stripe displaying a Moiré pattern, which was measured in our LEEH setup. The BLG width is measured to be around 58 nm, which allows for a rough estimation of the amount of carbon atoms N_C within the Moiré pattern stripe width. For a C–C bond length of 0.142 nm in graphene, $N_C \approx 408$. With around 10 – 11 dark periodic features along the stripe, which are separated by bright ribbons, this results in 37 – 38 carbon atoms separating the respective centers of two neighboring dark features. By overlaying two graphene model layers and rotating them against each other, it is possible to find a configuration with a fitting amount of carbon atoms between two feature centers as indicated in Fig. 5.7 **b** (red marked distance). This model yields a rotation angle of around 4° for the formation of this specific Moiré pattern on the BLG stripe.

5.2.2.6 Charges and Clusters on SLG

Apart from the observation of SLG, BLG, and MLG areas on the graphene substrate, various other features can be observed on the clean SLG surface. Fig. 5.8 shows overview images of freshly prepared SLG samples (**a** and **b**) and SLG samples containing deposited cytochrome c

(CytC, marked by yellow arrows) molecules (**c** and **d**). In Fig. 5.8 **a** and **b**, several features with a strong dark contrast are visible close to the substrate grid (marked by red arrows). These features have been observed before by J.-N. Longchamp et al. [36][217] and are most likely metal clusters originating from the SiN substrate, which is metal covered. During the heating steps of the SLG preparation, metal atoms and clusters can diffuse into the free-standing SLG regions, where they show a strong absorbance of low-energy electrons during imaging. Thus, they appear with a opaque dark contrast as indicated in [47].

Furthermore, the diffusion of small platinum clusters on graphene surfaces has been shown to take place even at room temperature, which affirms our observations [226][227]. During LEEH measurements, large clusters usually do not move anymore on the SLG surface, while small clusters rarely show mobile behaviour and typically diffuse within milliseconds from free-standing SLG towards the grid. In general, mobility of imaged molecules must be prevented or reduced to a minimum before and during measurements, since it lowers the spatial resolution of fringes in the hologram. By cooling the sample using the Cryo-LEEh microscope head, molecular mobility and diffusion should be reduced, which can in principle improve the obtainable amount of visible fringes and thus the image resolution.

Another visible feature on the SLG substrate are charges and charged defects. These signals have been reported by Latychevskaia et al. and mainly consist of slightly and strongly positively charged impurities and/or vacancies within the graphene structure [46][228]. Partially charged signals appear as white spots without any fringes, as indicated by white arrows for some example spots in Fig. 5.8. During LEEH measurements, these signals usually have faint bright signals, which can blink, move, or even reverse their charge, where the signal becomes dark indicating a partial negative charge [46].

Charged signals with stronger contrast (marked by pink arrows in Fig. 5.8) are usually stationary. They show a dark contrast for larger emitter-to-sample distances (Fig. 5.8 **a** and **b**) and get brighter in the signal center, the closer one approaches the sample with the tip (Fig. 5.8 **c** and **d**). Measurements and simulations of these charged objects by Latychevskaia et al. suggest different charge states from $-e$ up to $+2e$ depending on the observed contrast [46][228]. While charged features in general can yield holograms if fringes are visible, we found that it is difficult to find proper focus positions for the reconstructed images, which typically also show angular distortions due to the high local electric field generated by the charges. This effect compromises the reference wave around the respective charged object similar to the biprism effect, which was discussed for measurements of free-standing CNTs, and does not yield a distinct reconstructed object.

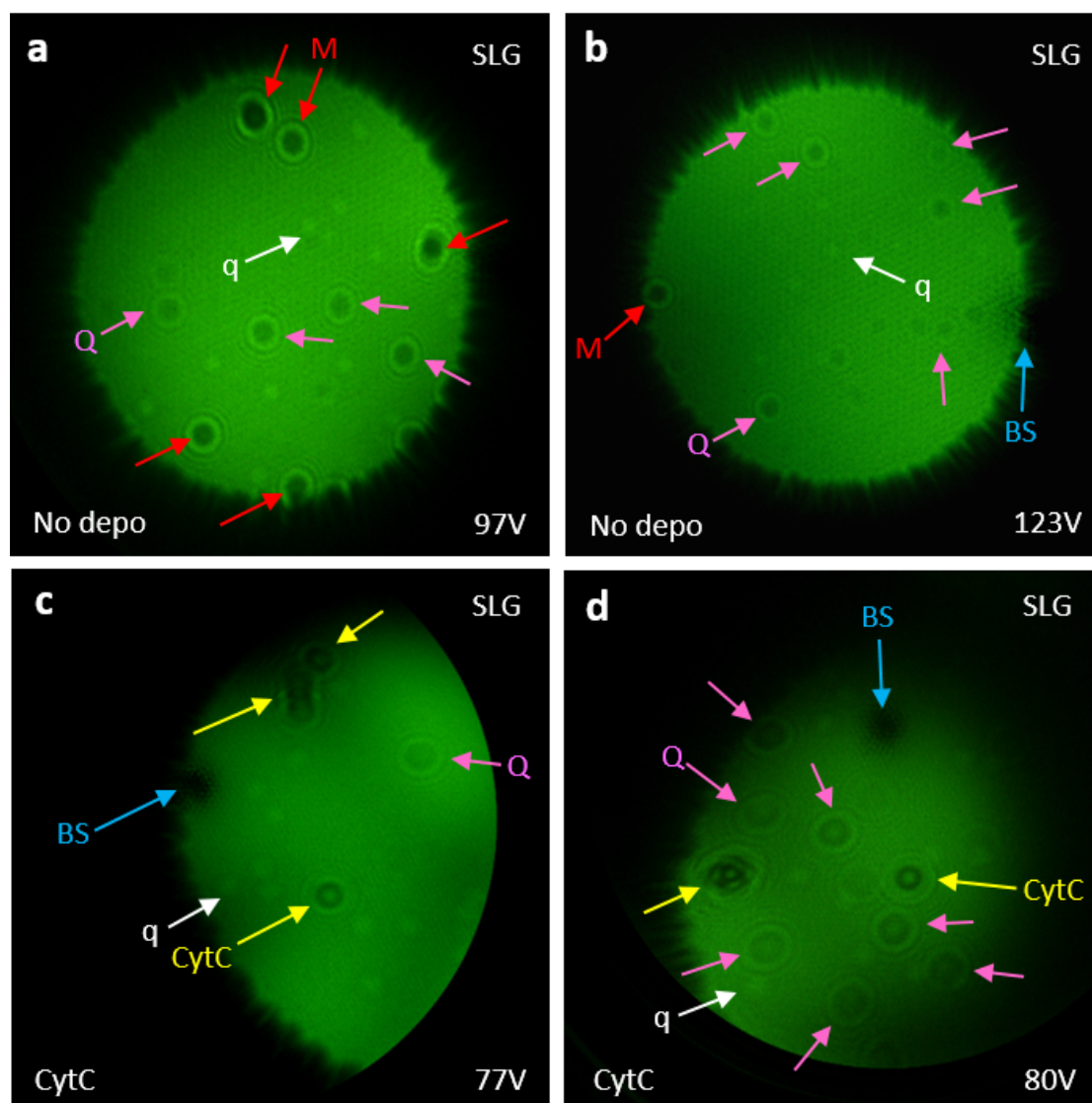


Figure 5.8: LEEH images of free-standing SLG samples containing individual charged defects. **a** and **b** show images of freshly prepared SLG (no molecule deposition). Diffused metal clusters with a high dark contrast (M, marked red), slightly positively charged defects (q, marked white), which are observed as small, mobile white spots on the surface, and strongly positively charged defects (Q, marked pink), which show a higher contrast compared to the slightly charged defects, are visible on both samples. **c** and **d** show images of two SLG holes containing deposited cytochrome *c* molecules (CytC, marked in yellow). Slightly and strongly positively charged defects are indicated on the samples by white and pink arrows, respectively. The detector blind spot (BS, marked in blue) is visible in **b** to **d**.

5.2.2.7 SLG Characterization before Deposition

Due to the features described above, the characterization of ultra-clean SLG is an important step prior to the molecule deposition and imaging. Whenever a freshly prepared SLG sample is transferred into our LEEH setup, we systematically screen its holey membrane to identify holes containing large areas of free-standing ultra-clean SLG, which are imaged and their position

in the array is noted to image them again after deposition. In this way, we are able to identify features and molecules, which appeared after the deposition process and allow for a reliable measurement of target molecular species via LEEH. In Fig. 5.9, an example of a hole containing an ultra-clean SLG area and an MLG stripe is shown before (Fig. 5.9 **a**) and after deposition (Fig. 5.9 **b**). The deposited molecules can be easily recognized as circular features on the previously clean SLG area. As stated in the figure, the deposition can be accomplished via different methods, which are discussed in detail in Chap. 6. After deposition, the characterized holes containing free-standing SLG are systematically re-checked for new features, which usually correspond to the deposited molecule species, see Fig. 5.9 **b**.

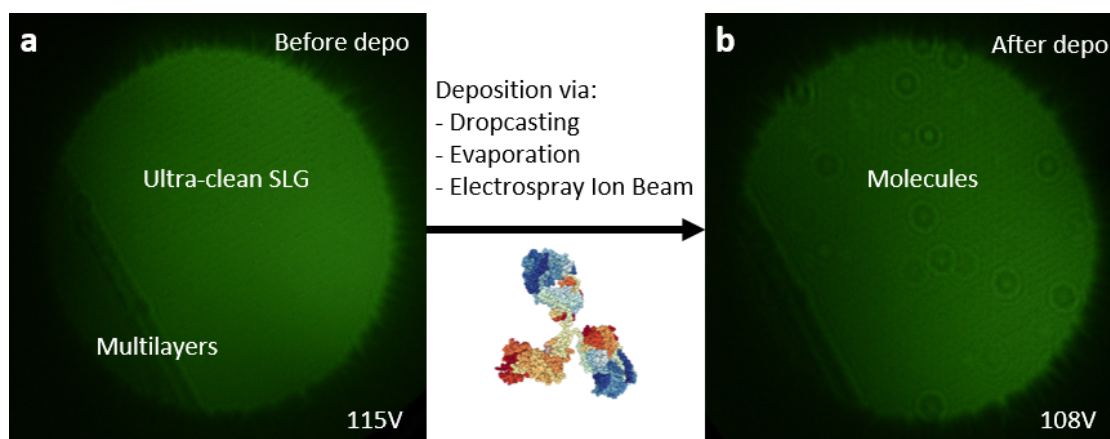


Figure 5.9: SLG characterization before (**a**) and after (**b**) molecule deposition, where the new, circular features on the SLG indicate deposited proteins. Each feature resembles either a single protein or a cluster of several proteins, which usually differ in feature contrast and size.

5.2.2.8 SLG Imaging at Cryogenic Temperatures

When operating the LEEH setup at cryogenic temperatures (see Sec. 3.2), the cooled parts of the microscope head act as a cryo-trap, which immobilizes adsorbates upon contact. We observed the occasional adsorption of molecules and charged particles on the cooled emitter and sample surface, which is shown in Fig. 5.10 **a** to **c**. These additional features visible in Fig. 5.10 **b** arose during cooling and measuring of the sample via LEEH, where the previously identified molecules are marked by red circles. The other signals most probably arise from adsorbed carbohydrates, gas molecules and atoms, and/or other charged and uncharged particles. It is also interesting to note that many of the newly appearing contaminants adsorb onto previously charged features on the SLG, which could indicate a higher reactivity of these locations.

The adsorbed contamination objects act as additional scatterers and can lead to an overlapping of the visible fringes if positioned too close to the target molecule (in this case beta-galactosidase). Furthermore, imaging isolated molecules yields a better interference between the reference wave and object wave, while further electron absorbing objects near the target

molecule reduce the amount of transmitted electrons, and thus the signal intensity and coherence. Both effects compromise the hologram formation and consequently the resolution of the reconstructed images [97][228]. As shown in Fig. 5.10 **c**, the adsorbants stay on the sample even after rewarming it to room temperature, which can permanently compromise the imaging quality of deposited single molecules on the affected sample. The addition of cooling shields to the microscope head could solve or reduce the contamination issue, since the large surface of the shields is able to trap molecules emitted from the warm chamber walls before they reach the sample, which leaves less molecules to adsorb on the emitter and sample. Furthermore, the shields should be able to reduce heat radiation from non-cooled chamber parts, which allows for lower LEEH measurement temperatures and a reduced cooling agent consumption. A more detailed description of the cooling shields, which are currently under construction, is shown in the outlook (Sec. 9.1). However, depending on the cleanliness of the tip and SLG substrate, it is possible to acquire images of good quality even without cooling shields, as shown in Sec. 7.5.

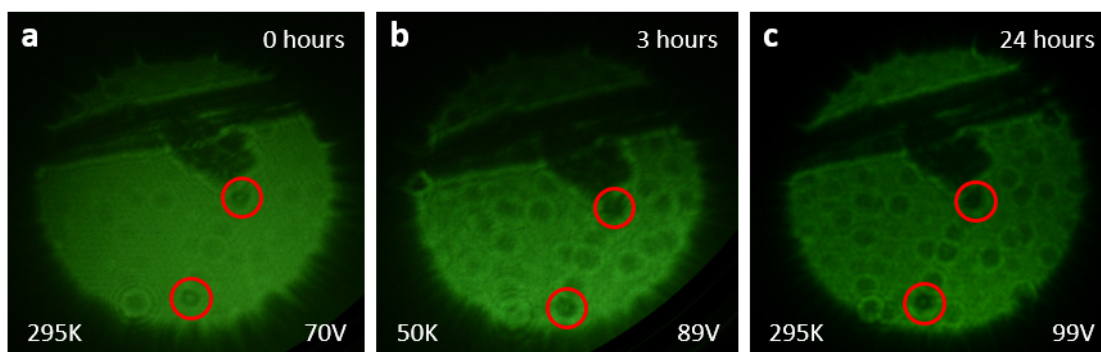


Figure 5.10: Sample contamination during cooling without cooling shields. The sample already contained 5 pAh of deposited beta-galactosidase protein (marked in red), which was measured via LEEH at 295 K before cooling (**a**), while cooling at 50 K (**b**) and after rewarming the sample to 295 K (**c**). Signals from charges and defects on the SLG show a stronger contrast during (**b**) and after (**c**) the cooling process and additional signals are visible indicating the adsorption of molecules or charged particles on the substrate.

6 Deposition methods

In this section, I discuss the methods used for the molecular deposition on the SLG surface. The principal deposition method used in this work is native electrospray ion beam deposition (ES-IBD), which allows even large and fragile biomolecules to be transferred from solution to surface while retaining a folded configuration (see Sec. 6.1). Different methods were used for molecular systems that cannot be deposited via ES-IBD, such as drop-casting (Sec. 6.3) for carbon nanotubes (CNTs), or thermal evaporation (Sec. 6.2), which is more convenient in the case of platinum phthalocyanine (PtPc). In the following sections, these methods are explained, discussing their basic principles, experimental implementations and performances.

6.1 Electrospray Ion Beam Deposition

The development of the electrospray ionization (ESI) technique for the use in mass spectrometry (MS) in the 1980s enabled the gentle transfer of non-volatile, large molecules from the liquid into the gas phase without fragmentation. The method was first established by J. B. Fenn et al., who was awarded with the Nobel Prize in chemistry in 2002 for his pioneering work in this field [229][230]. Nowadays, ESI is a common method for transferring complex, fragile and intricate molecular systems, such as membrane proteins [231][232] or even whole viruses [233], into the gas-phase, yielding chemically intact specimens, which can be investigated, for example by ion mobility measurements and mass spectroscopy [234][235][236]. In the upcoming sections, the protein solution preparation (Sec. 6.1.1), as well as our native ES-IBD routine (Sec. 6.1.2) are explained.

6.1.1 Protein Sample Preparation

To be able to spray and investigate folded protein species, the biomolecules first have to be dissolved in a buffer solution that can be used for the ESI process [237]. To satisfy native solution conditions, a water-based and pH buffering solution is usually used, such as the commonly chosen ammonium acetate (AmAc) [238]. We use 200 mM AmAc (pH = 7.6) in ultra-pure

deionized water as buffer solution to dissolve proteins that are stored as lyophilized powder. In case the proteins are stored in a different buffer solution, a solvent exchange procedure is carried out. To this end, a biospinning procedure consisting of several centrifugation steps is used to remove salts and contaminants with molecular weights below 6 kDa via size exclusion chromatography [239][240].

First, the spin columns (Bio-Spin P-6 Gel Columns with Tris Buffer, Biorad) containing a silica polymer in Tris Buffer (pH = 7.6) are drained via centrifugation for four minutes at 1000 rcf leading to the formation of a filtering column structure. Second, the columns are cleaned and saturated with 200 mM AmAc buffer in four to five consecutive centrifugation steps, where each step takes one minute at 1000 rcf while around 500 μ l of fresh AmAc is flushed through the columns. Finally, 50 – 100 μ l of protein stock solution are added to the spin column and centrifuged for four minutes at 1000 rcf, which is afterwards repeated an additional time with another clean and AmAc flushed column. To ensure the protein stability before the ESI process, the protein solutions are kept in ice or in cooled devices during the purification process. For this reason, we also use a coolable microcentrifuge (5418R, Eppendorf), which is cooled to 4°C and kept at this temperature during the whole procedure. The resulting solution contains mostly purified, native protein molecules in AmAc buffer.

Independently of the initial protein conditions, i.e. lyophilized or in buffer solution, the final solution to employ in the ESI process has a protein concentration in the range of 0.1 – 2 mg/ml in 200 mM AmAc buffer. In case an unfolded protein sample shall be investigated, the spray solution is diluted after the purification procedure using a respective amount of ethanol with a final ratio of 1:1. Furthermore, an amount of 0.1 – 0.5% vol. of formic acid is added to the diluted sample solution and incubated for several minutes before the solution is ready for use in the ES-IBD process (see Sec. 6.1.2) [241][242].

6.1.2 Native ES-IBD for Protein Systems

For our LEEH experiments, we are mainly interested in the observation of folded or even *native-like* protein systems (see Chap. 7), which have to be deposited on the SLG substrate in a highly pure and non-destructive manner. This can be accomplished by the combination of native ESI-MS and a controlled ion beam deposition technique in UHV. This approach was introduced by Z. Ouyang et al. in 2003 [243] and was further developed and optimized by several other groups [48][50]. The combination of ESI, mass selection, and controlled soft-landing deposition is referred to as electrospray ion beam deposition (ES-IBD) [244]. In Fig. 6.1 a, the experimental workflow of the native ES-IBD technique is displayed, which yields SLG substrates containing pure, soft-landed and folded proteins, that can be investigated via LEEH [51][74].

Before starting the process, a characterized SLG substrate is transferred from the LEEH setup to the ES-IBD setup via a UHV suitcase. Furthermore, ESI nanoemitters are prepared, which are

thin glass capillaries (30-0044 GC120F-10, Harvard Apparatus) that are thinned even further via melting with a needle puller device (P-1000, Sutter Instruments). Afterwards, the glass capillaries are made conductive by covering them with a layer of 10 nm of platinum using a sputter coater (EM ACE600, Leica). Finally, the melted capillary side is carefully clipped open to generate a nanoemitter with an orifice diameter of less than 1 μm .

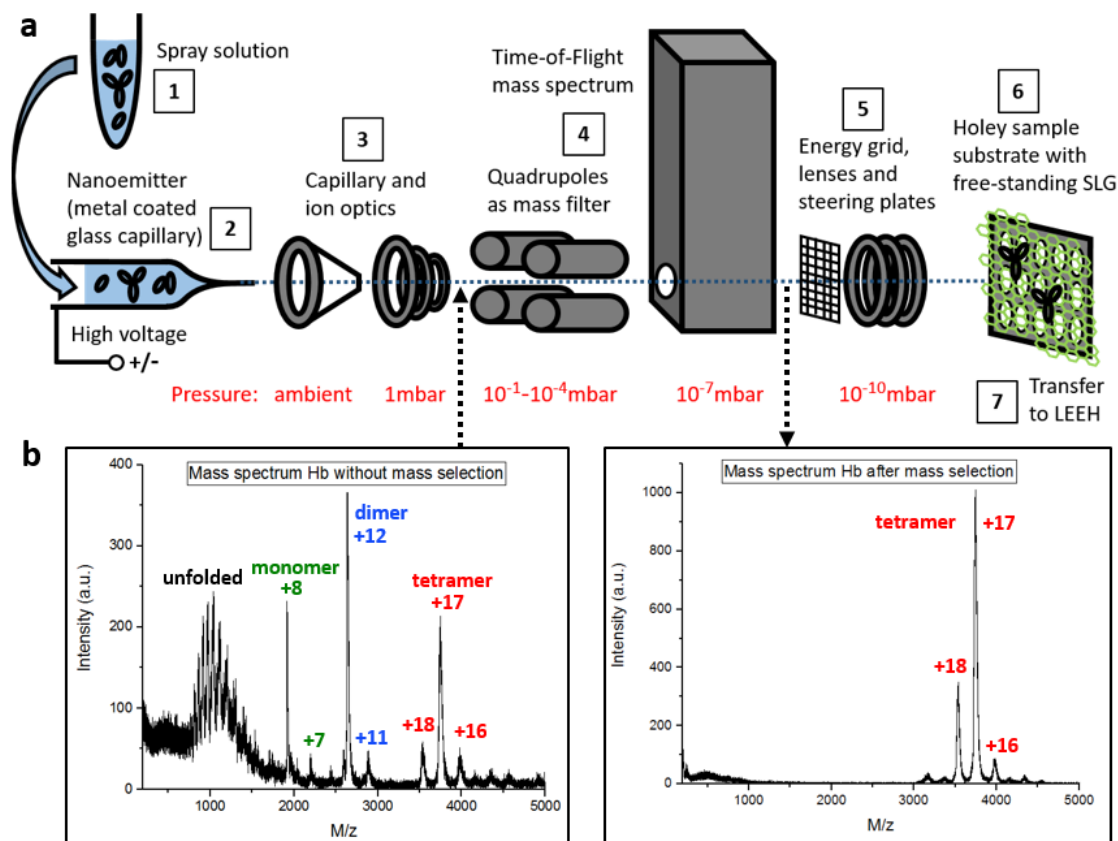


Figure 6.1: **a** Schematic of the native ES-IBD workflow steps: **1** Protein spray solution preparation via biospinning. **2** ESI with a nanoemitter at native conditions. **3** Ion beam transfer into vacuum and focusing via the ion funnel. **4** Mass selection of the target molecule species via quadrupoles and ToF-MS. **5** Determination of the kinetic beam energy via the retarding grid and transfer of the ion beam towards the sample via lenses and steering plates. **6** Controlled soft-landing of the molecule ions onto a characterized SLG substrate (green). **7** Transfer of the deposited sample to the LEEH setup via the UHV suitcase. **b** Two mass spectra of a hemoglobin (Hb) ion beam showing the respective M/z states before and after mass selection. For this sample beam, only the tetramer (red) species with the respective charge states from +17 to +15 was mass selected via the quadrupoles, while unfolded (black), monomer (green) and dimer (blue) species were cut off.

The first step of the procedure involves the protein spray solution preparation, which is explained in Sec. 6.1.1 (Fig. 6.1 **a** step **1**). Around 3–5 μl of solution are filled into a nanoemitter while avoiding the formation of air bubbles. The emitter is subsequently connected to the emitter-holder of the ES-IBD setup and brought in a relatively close distance to the aperture (capillary) of the first vacuum stage of the machine.

The next step is the transfer of the protein species from the solution into the gas phase via ESI (Fig. 6.1 a step [2]). ESI is a well-studied process, where a solvent containing the target molecule is pushed through an emitter with a small nozzle while applying a high positive or negative bias to the emitter (see Fig. 6.2 a). Due to the strong applied electric field at the orifice, particles within the solution are getting charged at the liquid-air interface [230]. The emitter usually consists of a metal capillary with an orifice diameter of less than $20\text{ }\mu\text{m}$. However, for delicate molecules such as proteins, metal coated glass capillaries with orifice diameters of less than $1\text{ }\mu\text{m}$ are used as described above, which decreases the applied voltage necessary for the ionization of solvent and molecule particles at the nozzle due to a smaller meniscus surface [245][233].

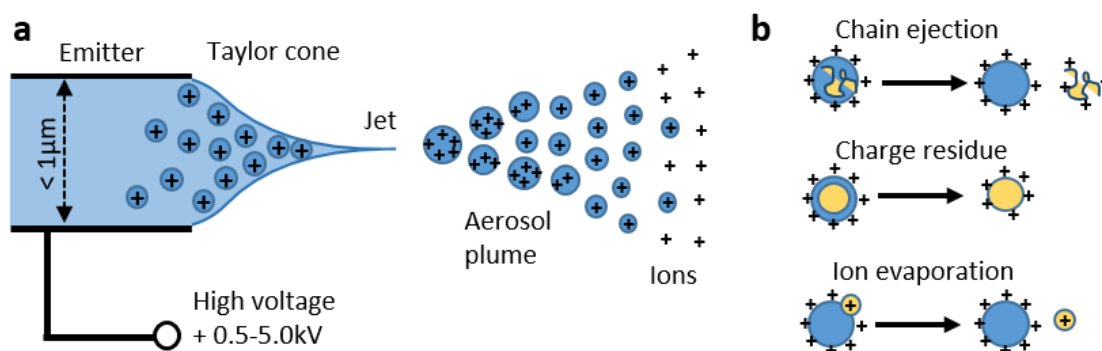


Figure 6.2: Electrospray ionization principle for a positive ion beam: **a** Schematic of ESI showing the formation of a Taylor cone at the emitter nozzle upon applying a high positive bias. The cone transitions into a Rayleigh jet of charged solvent droplets containing the target molecule, which first forms an aerosol plume and finally a spray of isolated molecule ions. **b** Overview of different models showing the separation of solvent and target analyte ions via the chain ejection, charge residue, and ion evaporation process.

Upon charge separation in the solution caused by the applied electric field, the meniscus transforms into a cone, which is called Taylor cone [246]. At the end of the Taylor cone, the electric field is locally enhanced, leading to the formation of a liquid jet, called Rayleigh jet [247], where a stable cone-jet flow is established. While getting further accelerated by the electric field, the jet finally extends into an aerosol plume carrying highly charged solvent droplets, which also contain the charged target molecules [248]. At this stage, solvent evaporates from the droplets, increasing their charge density until the Rayleigh limit is reached, where the surface tension γ of the droplet is exceeded by Coulomb repulsion of the charged particles within. The limit is defined as $Q = 8\pi\sqrt{\epsilon\gamma r^3}$, with Q being the amount of charges, ϵ being the electric permittivity in the medium and r being the droplet radius [247]. As shown for a positive ion beam in Fig. 6.2 a, this process reduces the droplet size by disintegration and fission, finally yielding solvent-free molecular ions, which are expanding from the cone-jet [249].

The ion formation process can be described by different models, depending on the target molecule properties [250][251][252]. Fig. 6.2 b displays the three main models: First, the chain ejection model, where charged long polymer chains are consecutively ejected in a

linear manner from the droplet [253]. Second, the charge residue model, where the solvent completely evaporates yielding isolated molecule ions, which is usually assumed for large globular shaped molecules, such as folded proteins [254]. Third, the ion evaporation model, where the ion is ejected from the charged droplet, which is commonly used for small, low-weight molecules [255][256]. The whole process takes place in atmosphere and the resulting ion beam is accelerated towards a heated transfer capillary, which bridges the ion beam path into vacuum and helps to completely evaporate remaining solvent particles [257].

Depending on the desired protein species, the ESI voltage and capillary temperature have to be adjusted. In general we use positive voltages for protein beams. For unfolded proteins, voltages up to 3.5 kV can be applied at the emitter and the capillary can be heated up to 130°C. For folded or *native-like* proteins, the ESI voltages are usually in the range of 1.1 kV to 1.5 kV with capillary temperatures between 70 – 80°C. The lower ionization voltages and capillary temperatures allow for a molecule beam containing intact folded protein ions [236]. While applying the ionization voltage to the nanoemitter, nitrogen gas is pushed into the emitter backside with a pressure of 0.02 – 0.1 bar to establish a continuous and stable ESI process. The ES-IBD setup consists of several differentially pumped vacuum stages. The first stage contains the heated capillary, where the ESI generated molecule ion spray is transferred from ambient pressure into a vacuum of 1 mbar. The spray is focused by an ion funnel, where several metal rings with alternating positive and negative applied voltages and decreasing radii are forming an ion beam (Fig. 6.1 a step [3]). Typical ion funnel voltages are in the range of 9 – 12 V for protein samples. It is important to mention that, except for the ion funnel, all applied voltages and current readouts are remote controlled by a custom-programmed LabView software.

After being focused, the ion beam, consisting of different molecular species, is guided via several ion optics through quadrupoles, where usually preset voltages of 80 – 110 V are applied at a background pressure of around $2 \cdot 10^{-4}$ mbar, and is consecutively transferred into a movable Time-of-Flight (ToF) mass spectrometer, which allows for the investigation of the different molecule species within the ion beam at a background pressure of $< 5 \cdot 10^{-7}$ mbar. The quadrupoles are used as a bandpass filter, allowing only selected species to pass depending on the set voltage regimes [258] (Fig. 6.1 a step [4]). The ions within the electric field of a quadrupole experience an electric force, which can be described as $E(u) = \frac{\partial \Phi(x,y,z)}{\partial u} = -\frac{2u}{r^2}(U - V \cos(\omega t))$ with u being the direction in x or y towards a quadrupole [259]. Here, U is the applied DC bias between poles and ground, while V is the applied AC voltage between two opposite poles with a frequency ω , and r is the distance towards the center of the field. A general solution simulating the ion path through the quadrupoles is given by the Mathieu's equation, which can be further simplified using the parameters $a_u = \frac{8zeU}{Mr^2\omega^2}$ and $q_u = \frac{4zeV}{Mr^2\omega^2}$, and $\tau = 2\omega t$, where e is the electron charge and z is the charge number of the ion [259]:

$$\frac{d^2u}{d\tau^2} + (a_u - 2q_u \cos(2\tau))u = 0 \quad (6.1)$$

With Eq. 6.1, two solutions can be found for the $a - q$ space, which is shown in the first region plot of the Mathieu's equation in Fig. 6.3. The stable solution part (colored in green) allows ions to pass through the quadrupole filter, while the unstable solution part (colored in red) gets filtered out and collides with the respective quadrupole electrodes. With a and q being proportional to z/M , molecules with lower mass-to-charge ratios M/z are present in the upper right part of the plot and molecules with high M/z can be found in the lower left part. By using a constant ratio between U and V , the quadrupoles can be operated with a mass selection line, which has a characteristic slope of $2U/V$ determining the bandwidth of the filter and thus the amount as well as the M/z states of the selected species [258]. In general, different voltages are applied for a fixed U/V ratio, while the ion beam composition is tracked with a mass spectrometer positioned behind the quadrupole mass filters. This allows for a simultaneous monitoring of the filtered species and the resulting selected ion beam exclusively contains the target molecule ions.

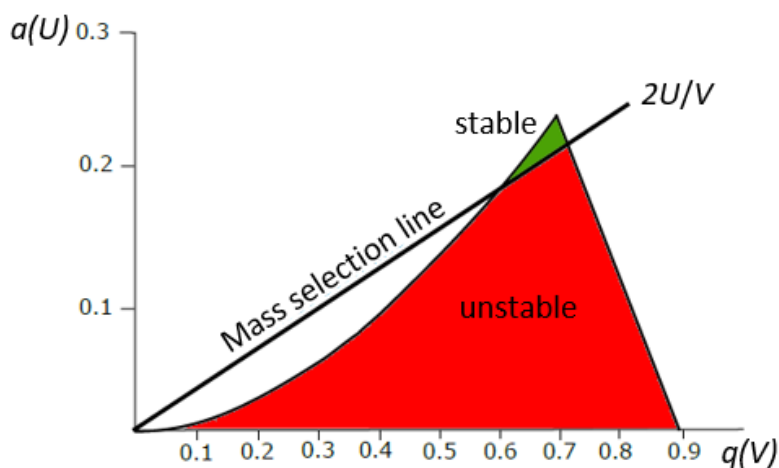


Figure 6.3: Quadrupole mass selection schematic showing the first stability region for the $a - q$ space using the Mathieu's equation. The mass selection line separating the stable and unstable M/z species is defined by the slope $2U/V$. While ions in the red (unstable) area are removed from the passing beam, ion species in the green (stable) region can pass the quadrupole mass filter.

Depending on the desired species, the quadrupole voltages as well as the U/V ratio are adjusted to select for the respective target molecule ions, as shown for an example beam of hemoglobin (Hb) in Fig. 6.1 **b**, where the tetramer species has higher M/z states due to the larger surface compared to the monomer and dimer species. Typical applied voltages are in the range of 230 – 450 V with U/V ratios between 0.5 – 5%. This ensures an effective filtering of small molecule ions, while also cutting off protein clusters with large M/z states. Further examples of this filtering procedure are shown for the various molecule ion beams presented in Chap. 7.

After the mass selection process, the kinetic energy E_{kin} of the filtered ion beam has to be determined to enable the soft-landing of the molecular ions on the substrate by applying a retarding voltage at the sample during deposition (Fig. 6.1 **a** step 5). This can be accomplished

via an energy detector consisting of a front plate with an opening covered by a fine metal grid and a separated contact (energy contact) behind the grid. When the ion beam is hitting both the front plate and energy contact, the respective currents flowing through the parts can be measured and tracked. For example, by applying a positive voltage bias at the front plate and thus simultaneously at the grid, positively charged ions with a lower kinetic energy than the applied voltage are repelled.

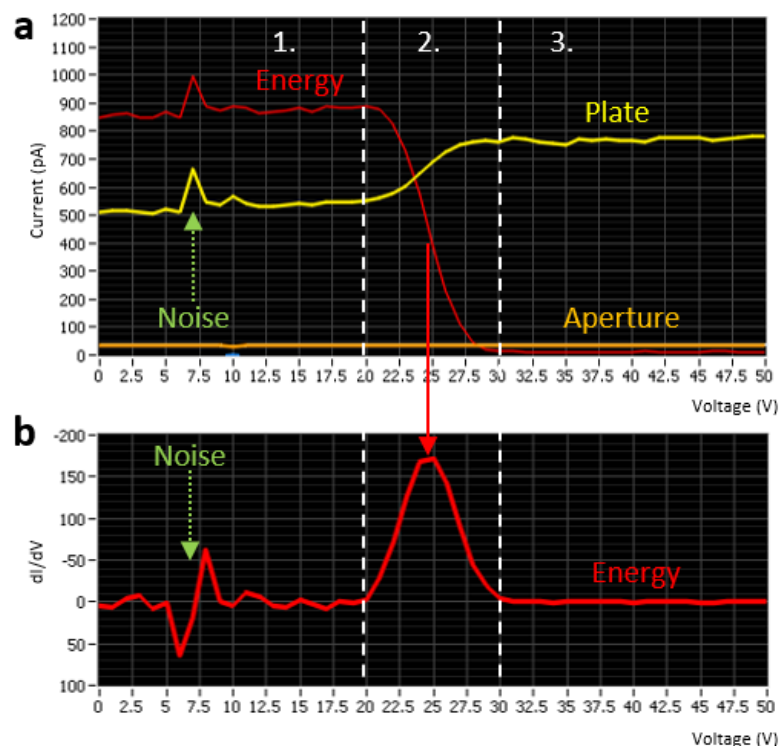


Figure 6.4: Ion beam energy measurement of a cytochrome *c* beam before deposition: **a** Voltage sweep from 0 V to 50 V applied to the plate grid in front of the energy contact. Between 21 V and 28 V, the current measured on the energy contact (red current data) drops from around 860 pA to 0 pA, while the current measured on the front plate (yellow current data) simultaneously rises from around 500 pA to 780 pA. The current measured on an aperture in front of the energy detector plate (orange current data) stays stable at around 30 pA during the sweep. **b** Derivative dI/dV of the measured current on the energy contact during the sweep showing the short pickup at around 7 V (marked with a green arrow) and a maximum at around 24.5 V (marked with a red arrow), which indicates an average ion beam energy of around 24.5 ± 2.5 eV. The three voltage regimes are marked by **1**, **2** and **3** and separated by the white, dashed lines. The noise visible at around 7 V is marked green.

By sweeping through different voltage values, the measured current can be plotted resulting in three voltage regimes, as shown for a positive cytochrome *c* ion beam in Fig. 6.4 **a**: **1.** For low voltages, the current measured at the energy contact shows a stable signal, which is usually higher than the current measured at the plate. **2.** For voltages within the range of the kinetic beam energy, the current measured at the energy contact drops, while the current measured at the plate increases. **3.** For high voltages the current measured at the energy contact is around 0 pA, while the current measured at the plate is maximized. This indicates a total repulsion of

the ion beam by the retarding grid. A noise peak at around 7 V is also detected (see Fig. 6.4, marked green) and is not relevant for the analysis of the beam energy.

The derivative dI/dV of the plot yields a Gaussian-shaped curve with a maximum at the steepest current drop of the energy contact and a respective energy width, as shown in Fig. 6.4 **b**. The landing energy $E_{\text{land}} = E_{\text{kin}} - E_{\text{applied}}$ of the molecules can thus be influenced depending on the positive or negative charge of the ion beam by applying a respective voltage bias at the sample. For most ion beams, the measured kinetic energy is within a range of 40 – 55 eV, and a respective voltage is applied to the sample holder position depending on the desired landing mode. For soft-landing of the target molecules, the applied voltage should match or be slightly lower than the measured kinetic beam energy [48][260]. To increase the chance of breaking or fragmenting molecules upon landing, which is commonly tried for reactivity and/or stability experiments, the molecules can also be hard-landed by applying a high opposite voltage bias at the sample [49][261].

After the energy measurement, the beam is transferred via electron lenses and steering plates through the following UHV stages, where the pressure is below $2 \cdot 10^{-10}$ mbar. Upon deposition in the final pumping stage, a retarding voltage is applied to the sample: In case of a soft-landed protein sample, the voltage is set to a repulsive value, which typically yields a landing energy of $E_{\text{land}} \approx 0 - 3$ eV per charge. While depositing, the ion beam current measured on the sample can be tracked over time to control the amount of deposited molecules on the sample, which enables us to deposit molecules in a reliable and reproducible manner (Fig. 6.1 **a** step [6]). By knowing the number of charges per molecule and measuring the deposited charge, we can estimate the number of molecules. Experience values, which usually depend on the molecule type, size and M/z ratio, are used to determine the respective deposition time. Typical deposition amounts to get samples with isolated single protein molecules are in the range of 3 – 10 pAh for proteins with high and low M/z states, respectively, which corresponds to large and small protein molecules.

After a successful deposition onto the SLG substrate, the sample is transferred through a load lock into the UHV suitcase and subsequently transferred back to the LEEH setup (Fig. 6.1 **a** step [7]). This deposition and transfer routine ensures the preparation of pure protein samples, which can be investigated via LEEH.

6.2 Thermal Evaporation

The directed thermal evaporation of molecules onto a substrate was first established by K. G. Günther in 1958 [262] and was further developed for the use in vacuum by J. E. Davey and T. Pankey [263]. Also known as molecular beam epitaxy (MBE), the target molecule species is heated within a Knudsen cell until sublimation takes place. The evaporated molecules are subsequently emitted towards the sample substrate, where they condensate on the surface [264]. Depending on the deposition rate of the molecule, clusters, islands and films can be epitaxially grown on the substrate. This method is commonly used for the deposition of thin semiconductor layers, but can also be utilized for organic compounds, where it is called organic MBE (OMBE) [265]. Since the evaporation takes place in UHV (background pressure $< 1 \cdot 10^{-10}$ mbar) and can be performed with highly pure sample material, it is an alternative deposition method for organic complexes, which can be sublimated without decomposition.

We use this technique exclusively for the deposition of organic molecule complexes, where the thermal evaporation process is more convenient than the ESI process, such as platinum phthalocyanine (PtPc) [266]. The procedure takes place in an external UHV chamber, which can be accessed via the UHV suitcase. The evaporation is carried out by an OMBE source (4x OMBE evaporator, Dodecon), which is filled with the target molecule powder. As a preparative step to increase the pureness of the respective molecule by evaporating contaminants, the evaporator is annealed for around 36 hours at a temperature below the sublimation point of the target molecule. After the sample characterization and transfer to the deposition chamber, the Knudsen cell containing the target molecule is heated to its sublimation temperature. As soon as the required temperature is stabilized, the shutter towards the sample is opened and the deposition can take place. Depending on the molecule deposition rate, the process is continued for a certain time (usually in the range of 1 – 2 hours) and stopped before molecular islands are formed on the substrate, since we aim for single molecules and/or small molecule clusters. After deposition, the sample is transferred back to the LEEH setup via the UHV suitcase and imaged via LEEH. We used this procedure only for the deposition and subsequent investigation of PtPc molecules on SLG, as shown in Sec. 7.4.3.

6.3 Drop-casting

Drop-casting is one of the easiest and fastest deposition methods, requiring a highly pure solution preparation to prevent contaminations. While commonly used in optical microscopy, where a droplet of solution containing the sample is dispersed on a microscope slide or substrate, we utilize the drop-casting method only for species that cannot be deposited via ES-IBD or evaporation, such as CNTs. Drop-casting of solutions onto SLG covered samples most likely leads to contaminations and detaching of the SLG layer, as experimentally observed on several occasions. For this reason, we exclusively prepare samples containing free-standing CNTs with this technique. The drop-casting procedure for samples imaged in our LEEH setup consists of several steps:

1. Prepare a metal covered substrate grid as described in Sec. 5.1 without SLG.
2. Mount the grid in a sample holder plate, transfer it into the LEEH chamber via the FTLL and check the perforated grid membrane for defects and fissures. Proceed, if the membrane is intact and the holey array is visible via LEEH.
3. Transfer the grid outside the LEEH chamber via the FTLL and carefully suspend $2 - 3 \mu\text{l}$ of sample solution onto the membrane part of the substrate.
4. Let the solution incubate for 30 – 60 s, then remove excess of solution with a paper tissue.
5. Put the sample holder containing the grid and sample onto a hot plate, which is pre-heated to 100°C to remove solvent residues, cover the grid with a beaker to prevent contaminations from dust particles, and let it heat for 15 mins.
6. Transfer the hot sample holder into the FTLL, pump down and transfer it into the LEEH chamber to investigate the sample.

For CNTs, we use 1,2-dichlorobenzene as solvent, with a final CNT concentration of around $1 \mu\text{g/ml}$. Before CNT suspension, the solution is centrifuged for 10 mins at 1000 rcf to separate large CNT clusters from the solution. After transferring the sample into the LEEH microscope, individual holes are checked for free-standing CNTs, which can be subsequently imaged via LEEH to characterize emitter properties, see Sec. 4.2.6.1 and 4.2.6.2, or are used for functionalization as described in Sec. 4.2.5.2. This technique can in principle be used for other large, stretched molecules and systems by adjusting the heating temperature, such as nanowires [267], polymer fibers [22], and even DNA [33][34]. However, for most protein systems, this method is not applicable due to the heat treatment, lack of protein species selection and the large molecule size necessary to be properly suspended over the membrane holes. Furthermore, the imaging of these systems without an equipotential plane leads to charging effects and thus to a biprism effect, which does not allow for a proper reconstruction of structural features, as discussed in Sec. 2.2 [93].

7 Measurements of Deposited Molecule Systems

In this chapter, I present the results of the room and low temperature LEEH investigations of a variety of molecular systems deposited on SLG. Furthermore, I compare the measured LEEH-data of selected molecules with respective AFM measurements. The AFM characterizations were carried out on samples using highly oriented pyrolytic graphite (HOPG) as substrate, which grants a chemical environment similar to graphene, while also providing a rigid surface for the investigation in AFM. If the molecular systems were deposited via ES-IBD, the respective mass spectra before and after mass selection are displayed. In general, the mass selection for most of the presented protein systems was applied to filter out unfolded and/or denatured molecular species, resulting in the deposition of chemically intact proteins retaining a tertiary structure close to the native conformation, which I refer to as *native-like* in this work [234][236].

LEEH measurements were performed as described in Sec. 3.6 and the acquired data was reconstructed and analyzed as discussed in the sections 2.1 and 3.3. AFM (Dimension Icon, Bruker) measurements were conducted in our institute at ambient conditions and in air using the tapping mode with a microcantilever (OMCL-AC200TS-R3, Olympus). The AFM image analysis was conducted via an open source software for scanning probe microscopy (WSxM v5.0 develop 9.0 [222]). In general, the data measured via LEEH is compared to model structures, which for most protein systems were obtained from the RCSB protein data bank (PDB) [122].

Different classes of molecular systems were investigated:

1. Globular protein systems including cytochrome *c*, myoglobin, and hemoglobin, which usually have simple structures with well-defined sizes, were used to test the performance of the native ES-IBD procedure and its effects on the molecular structure upon landing. Their approximately spherical shape is easy to identify by LEEH and their size can be used as a rough calibration to verify our reconstruction procedure (Sec. 7.1).

2. By using large protein complexes including transferrin, alcohol dehydrogenase, beta-galactosidase, and GroEL, which all are constituted of several subunits, we aimed to explore the upper mass boundary of our ES-IBD setup. These experiments give us the opportunity to attempt to distinguish the different subunits in our LEEH microscope (Sec. 7.2).

3. Measurements on flexible protein species including MAdCAM-Fc, as well as *native-like* and denatured Herceptin antibodies, show the capability of LEEH to image the manifold conformations that such systems can adopt, while retaining an intact tertiary structure. It is important to note that the identification of such a conformation variety is only possible because LEEH is capable of imaging individual molecules (Sec. 7.3).

4. Small, functional molecules including hemin, phosphotungstic acid and platinum phthalocyanine, which tend to form clusters on the substrate, were measured to test the lower intensity signal detection and resolution limits of our LEEH setup (Sec. 7.4).

After showing the imaging capabilities of our investigation method on a large variety of molecular systems, I briefly report on first results of measurements using the Cryo-LEEH system. I present two different molecular species, which were measured at cryogenic temperatures (Sec. 7.5).

The comparison of our measured data to model structures of the respective molecules reveals that we are capable of imaging folded proteins via LEEH in UHV with resolutions of less than 1 nm without the need for averaging. Furthermore, we are able to resolve features of single molecules at a local resolution of up to 5 Å, which is close to the theoretical resolution limit for the given measurement parameters (see Sec. 2.3 and Tab. 2.1).

7.1 Globular Proteins

To test the general performance of our LEEH microscope, we measured *native-like*, globular proteins, which offer a relatively simple molecular structure. Some of these systems had already been investigated by J.-N. Longchamp et al. using a different LEEH instrument [51]. Reproducing this data enables us to validate our methodology. Mass spectra and LEEH images of cytochrome *c* (CytC), myoglobin (Myo) and hemoglobin (Hb) are shown. Furthermore, AFM data of Hb deposited on HOPG is presented.

7.1.1 Cytochrome *c*

Cytochrome *c* (CytC) is a relatively small protein monomer consisting of 104 amino acids and a heme *c* group [268]. Located in the mitochondria of cells, CytC plays an important role as a component within the electron transport chain [269]. Furthermore, it is also an initiating factor for cell apoptosis, if released from the mitochondria into the cytoplasm [270][271].

For our experiments, cytochrome *c* from horse heart (*Equus caballus*, 9007-43-6, Fluka) was used; it has a molecular mass of around 12.4 kDa and its molecular size is in the range of 2.5 – 3.5 nm. The spray solution was prepared as described in Sec. 6.1.1 and typically used parameters for the native ESI process of cytochrome *c* are:

Table 7.1: ESI parameters for a *native-like* cytochrome *c* ion beam.

c_{Spray}	$T_{\text{capillary}}$	V_{Emitter}	$V_{\text{IonFunnel}}$	$V_{\text{QMS}}^{\text{RF}}$	U/V	Depo charge
1 mg/ml	80°C	+1350 to +1400 V	10 V	200 to 230 V	1.05	8 pAh

Fig. 7.1 shows the mass spectra of the ion beam before (a) and after (b) the quadrupole mass selection (QMS). The filtered mass spectrum of this ion beam (Fig. 7.1 b) shows peaks at M/z values of around 1546, 1768 and 2064, which corresponds to charge states of +8, +7 and +6 for *native-like* protein ions [272]. These values are used to estimate the molecular mass of the sprayed protein yielding a mass of 12369 ± 9 Da, which is in good agreement with the nominal molecular mass of 12384 Da given for horse heart CytC. Already the unfiltered ion beam was mainly constituted by native CytC species and the mass selection did not significantly improve the visible beam quality. However, this step is important to remove contaminant ions of low abundance in the lower and higher M/z -range. The relative abundance of the peak at 2064 M/z , corresponding to the +6 charge state, was increased after applying the filter. This shows that the QMS altered the initial beam composition, allowing preferably higher M/z species to pass through.

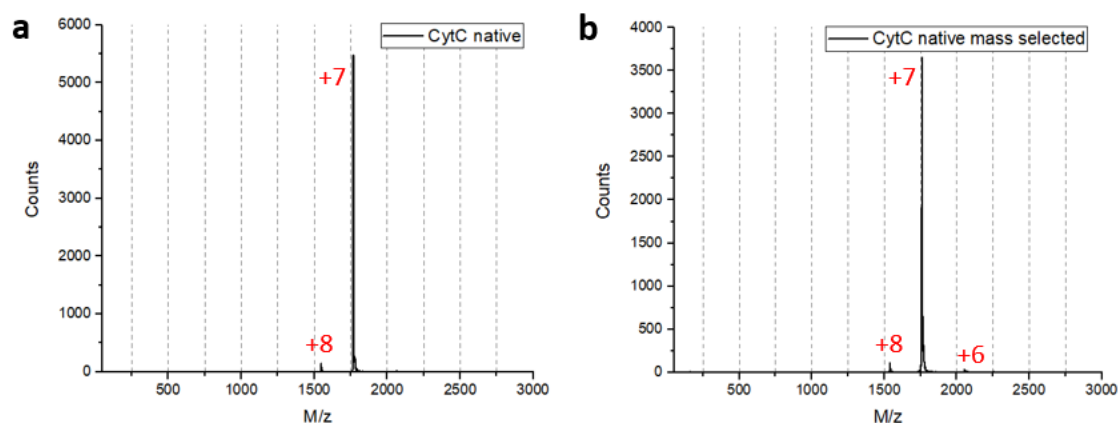


Figure 7.1: Mass spectra of *native-like* cytochrome *c* (CytC) before (a) and after mass selection (b). The peaks indicating a *native-like* species are visible at 1546 (+8), 1768 (+7), and 2064 (+6) M/z (with their respective charge states) and yield a molecule mass of 12369 ± 9 Da.

The selected cytochrome *c* species was soft-landed onto SLG with an energy of 2 eV/charge and subsequently transferred to the LEEH setup, where it was investigated by LEEH. Fig. 7.2 shows holograms of three molecules (a, d and g). The reconstructed holograms yield respective images of the amplitude (b, e and h), revealing different molecular configurations. Using the RCSB PDB model structure 1HRC, it is possible to find a molecular orientation of the X-ray structure that matches the observed reconstructions, as shown in Fig. 7.2 c, f and i.

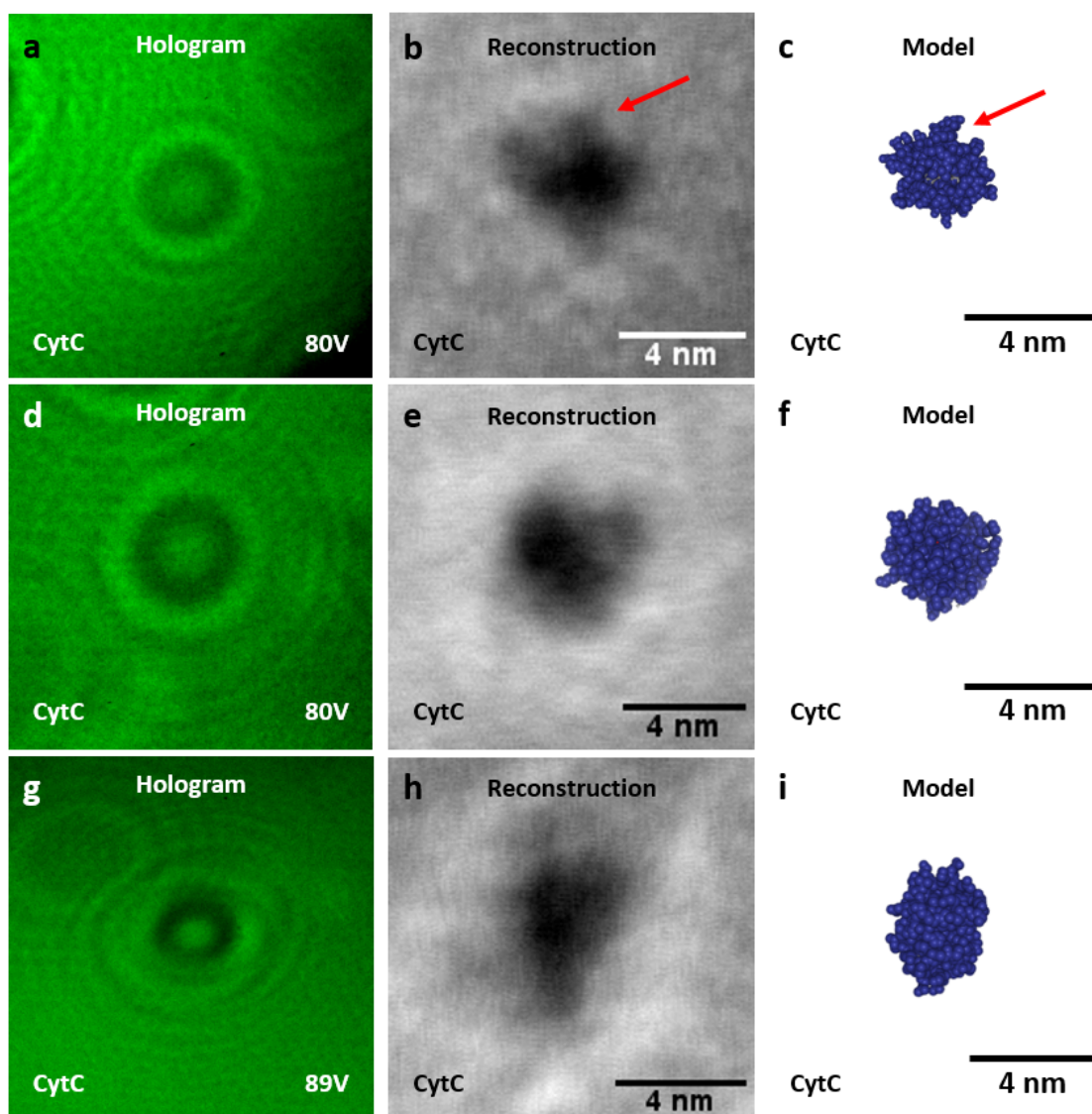


Figure 7.2: LEEH images of *native-like* cytochrome *c* (CytC) deposited on SLG showing the measured holograms (**a**, **d**, **g**) of three differently oriented example molecules. The emission voltage used for their imaging is reported in the bottom right corner. The amplitude reconstructions and model structures are displayed in **b**, **e**, **h** and **c**, **f**, **i**, respectively. The model structures are obtained from the RCSB PDB: <https://www.rcsb.org/structure/1HRC>.

The measured molecular sizes are slightly larger compared to the models, which can be due to the relatively low signal-to-noise ratio, which is especially visible at the blurred molecule edges, and does not allow for a precise identification of the molecular boundary. However, the measured signals show weak contrast differences within the amplitude reconstructions, where darker regions indicate a higher electron absorption. The side groups of the protein at the molecule edges thus appear brighter, since it presents less material, while the compact and more dense molecule center appears darker. The estimated local resolution of these images is in the range of 9 – 12 Å, where the smallest identified feature is the side group of the

cytochrome *c* molecule shown in Fig. 7.2 **b** (marked by a red arrow), which has a size of around 9 Å. Equivalent results have been reported by J.-N. Longchamp et al., where shape, size and resolution were found to be comparable [51].

7.1.2 Myoglobin

Myoglobin (Myo) is a compact, globular protein monomer consisting of 153 amino acids, which includes a heme *b* group [273]. Myoglobin can be found within the heart and skeletal muscle cells of mammals, where it is transporting oxygen from the cell membrane to the mitochondria [274][275]. Furthermore, it is responsible for the red color of the muscle tissue [276].

We investigated myoglobin from horse skeletal muscle (*Equus caballus*, 100684-32-0, Sigma); it has a molecular mass of around 17.6 kDa and its molecular size is in the range of 3 – 4 nm. The spray solution was prepared as described in Sec. 6.1.1 and typically used parameters for the native ESI process of myoglobin are:

Table 7.2: ESI parameters for a *native-like* myoglobin ion beam.

c_{Spray}	$T_{\text{capillary}}$	V_{Emitter}	$V_{\text{IonFunnel}}$	$V_{\text{QMS}}^{\text{RF}}$	U/V	Depo charge
1 mg/ml	75°C	+1350 to +1400 V	12 V	400 to 420 V	1.04	5 pAh

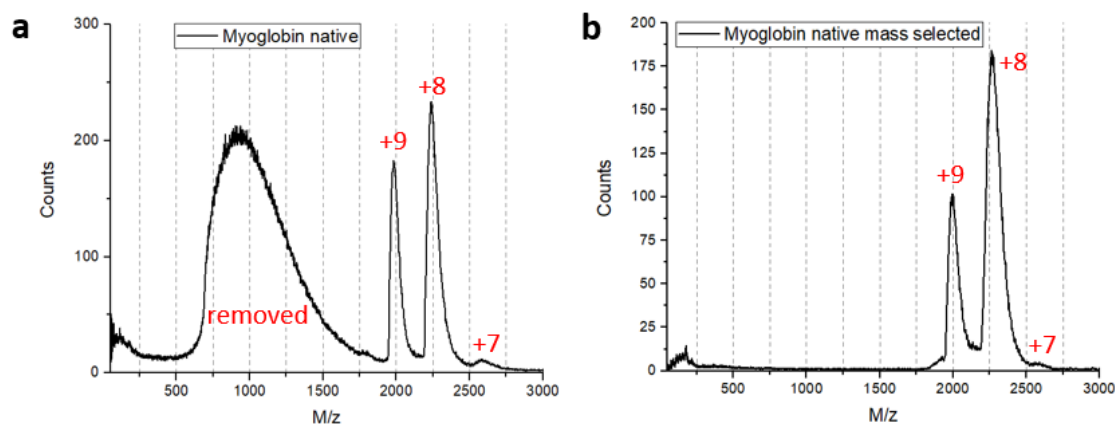


Figure 7.3: Mass spectra of *native-like* myoglobin before (a) and after mass selection (b). The peaks indicating a *native-like* species are visible at 1987 (+9), 2243 (+8) and 2558 (+7) M/z (with their respective charge states) and yield a molecule mass of 17884 ± 47 Da. The species showing a signal from around 600 to 1700 M/z was successfully filtered out by the mass selection.

The mass spectra before and after the quadrupole mass selection (QMS) are shown in Fig. 7.3 **a** and **b**, respectively. The unfiltered beam contained a large amount of unfolded or partially unfolded species in the range from 600 to 1700 M/z . After applying the QMS voltage and differential U/V value, these species were completely removed from the ion beam, only yielding *native-like* species, as indicated by the peak values.

The peaks of the filtered mass spectrum (Fig. 7.3 **b**) are located at M/z values of 1987, 2243 and 2558, which corresponds to charge states of +9, +8 and +7 for *native-like* protein ions [272][277]. The molecular mass of the sprayed protein ions was thus estimated to be 17884 ± 47 Da, which is slightly larger than the theoretical molecular mass of 17566 Da for horse skeletal muscle myoglobin given by the producer. A likely reason for the measured increased mass could be the presence of water or other solvent molecules within the protein and/or slightly shifted calibration values in the mass spectrum detector, which can lead to small shifts in the measured peak positions [278][279].

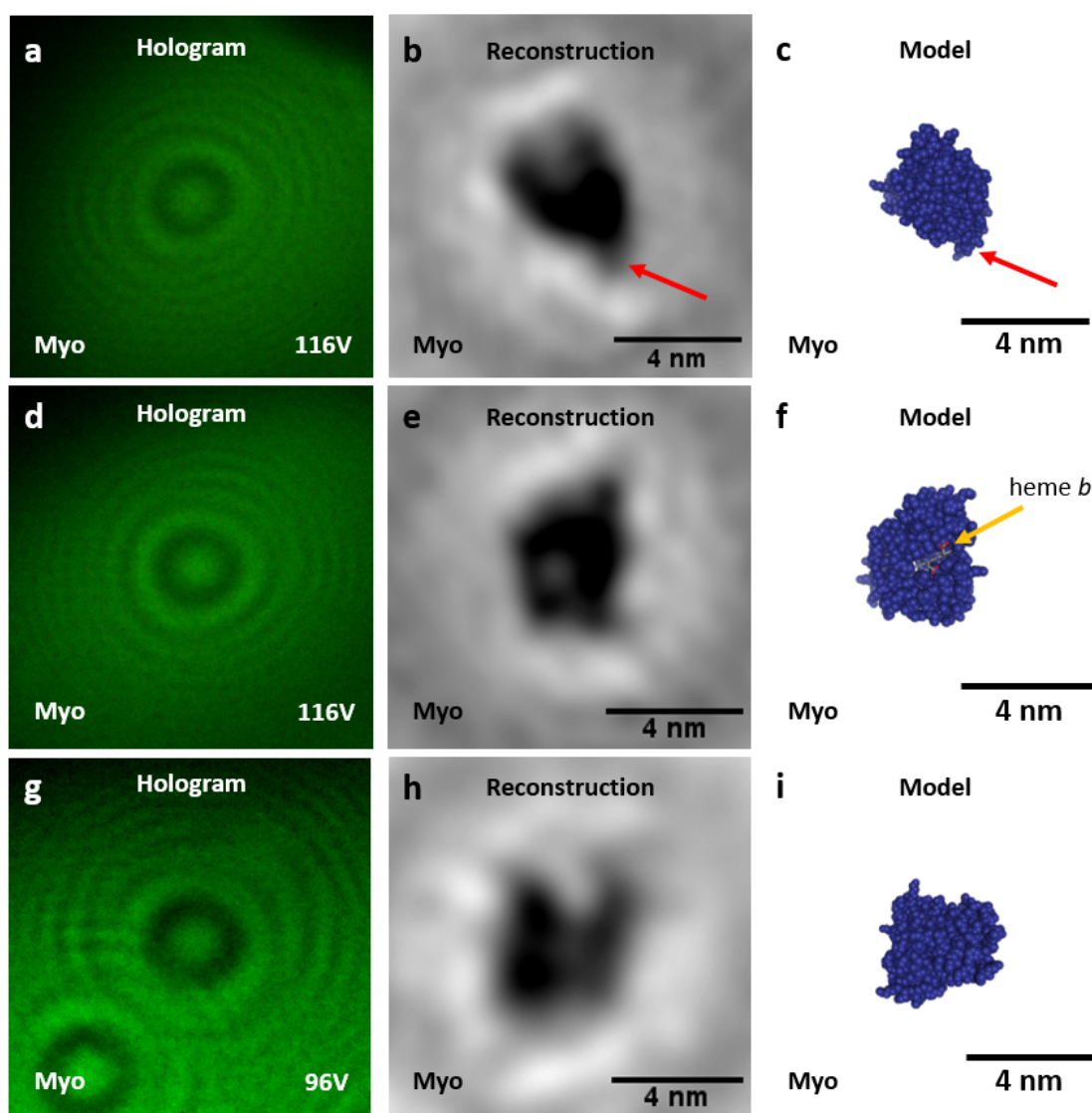


Figure 7.4: LEEH images of *native-like* myoglobin (Myo) deposited on SLG showing the measured holograms (**a**, **d**, **g**) of three differently oriented example molecules. The emission voltage used for their imaging is reported in the bottom right corner. The amplitude reconstructions and model structures are shown in **b**, **e**, **h** and **c**, **f**, **i**, respectively. The model structures are obtained from the RCSB PDB: <https://www.rcsb.org/structure/5ZZE>.

The selected myoglobin species was soft-landed onto SLG with an energy of 2 eV/charge, transferred to the LEEH setup and investigated via LEEH. In Fig. 7.4, holograms of three molecules (**a**, **d** and **g**) are displayed. The reconstructed amplitude images (**b**, **e** and **h**) show various molecular orientations. By comparing the amplitude data to the model structure 5ZZE obtained from the RCSB PDB, remarkable similarities can be found, as shown in Fig. 7.4 **c**, **f** and **i**.

The reconstructed images reveal a molecular size, which matches the sizes obtained from the model structures. Slight contrast differences within the respective molecules indicate a higher density in the molecule center, which contains the prosthetic heme *b* group, as for example visible in Fig. 7.4 **f** marked by the yellow arrow. The estimated local resolution of these images is in the range of 7 – 10 Å, with the smallest certainly identified feature being the hook-shaped side group of the myoglobin molecule shown in Fig. 7.2 **b**. The feature is marked by a red arrow in both reconstruction and model and has a size of around 7 Å.

7.1.3 Hemoglobin

Hemoglobin (Hb) is an essential protein complex, which is transporting oxygen through the blood circulatory system and is giving blood its characteristic red color. In mammals, hemoglobin is a tetramer composed of two α and two β subunits, which consist of 141 and 146 amino acids, respectively. Furthermore, each subunit contains a prosthetic heme *b* group [280][281].

We used hemoglobin from bovine blood (*Bos taurus*, 9008-02-0, Sigma); it has a molecular weight of around 64.5 kDa and a molecular size in the range of 4.5 – 6 nm. The spray solution was prepared as described in Sec. 6.1.1 and typically used parameters for the native ESI process of hemoglobin are:

Table 7.3: ESI parameters for a *native-like* hemoglobin ion beam.

c_{Spray}	$T_{\text{capillary}}$	V_{Emitter}	$V_{\text{IonFunnel}}$	$V_{\text{QMS}}^{\text{RF}}$	U/V	Depo charge
1 mg/ml	75°C	+1250 to +1300 V	10 V	580 V	1.04	6 pAh

Fig. 7.5 **a** and **b** show the mass spectra of the hemoglobin ion beam before and after mass selection, respectively. The unfiltered beam contained unfolded species (marked grey) in the range from 500 to 1800 M/z , as well as individual subunits (monomers, marked green), dimers (marked blue), tetramers (marked red) and tetramer clusters (marked yellow). For our experiment, we selected for the tetramer species by applying the respective QMS voltage and U/V value (see Tab. 7.3), which completely filtered out undesired species from the ion beam.

The filtered mass spectrum (Fig. 7.5 **b**) shows peaks at M/z values of around 3808, 4051 and 4317, which corresponds to charge states of +17, +16 and +15 for the *native-like* tetramer [282][283]. An estimation of the molecular weight yielded 64791 ± 85 Da, which is slightly

larger than the nominal molecular mass of 64453 Da for bovine blood hemoglobin. As already discussed for myoglobin, shifts in the mass spectrum calibration and additional solvent molecules within the protein complex can increase the estimated molecular weight. The hemoglobin cluster species visible at higher M/z values could not be properly cut off by the QMS and were deposited as well.

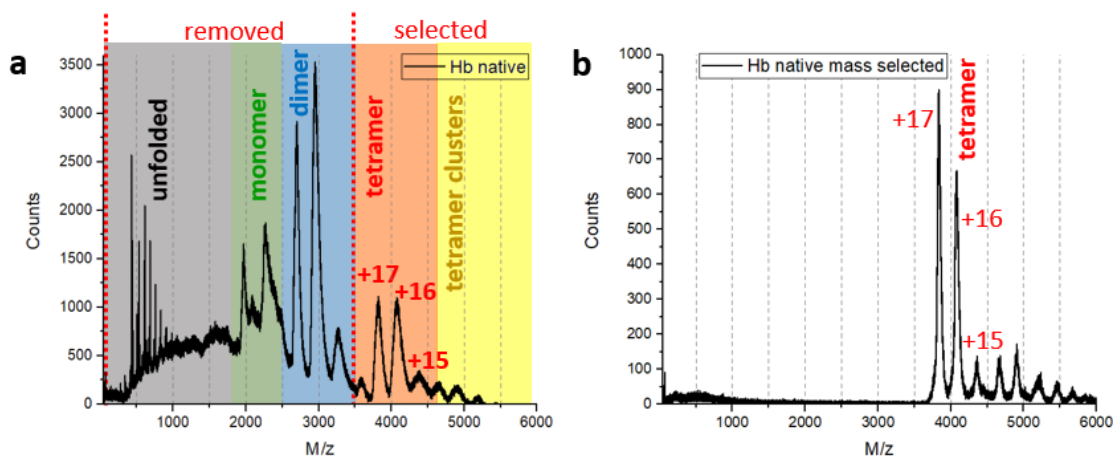


Figure 7.5: Mass spectra of *native-like* hemoglobin (Hb) before (a) and after mass selection (b). The peaks indicating *native-like* species are visible for monomers at 1968 (+8) and 2270 (+7) M/z (marked green), dimers at 2699 (+12), 2949 (+11) and 3278 (+10) M/z (marked blue), and tetramers at 3607 (+18), 3808 (+17), 4051 (+16) and 4317 (+15) M/z (marked red). Unfolded species (marked grey) are visible in the range from around 500 to 1800 M/z and tetramer clusters (marked yellow) show peaks above 4500 M/z . The mass selection was applied for the tetramer species (and its respective clusters) yielding a molecule mass of 64791 ± 85 Da, while species with lower M/z values were filtered out.

The selected hemoglobin species was soft-landed onto SLG with an energy of 2 eV/charge, the sample was transferred to the LEEH setup and measured via LEEH. The resulting holograms of three molecules (a, d and g) are displayed in Fig. 7.6. The amplitude reconstructions are shown in Fig. 7.6 b, e and h, revealing different molecule orientations. In Fig. 7.6 c, f and i, model structures with matching orientations are shown (RCSB PDB model 5ZZE).

The observed sizes in the amplitude reconstructions roughly fit or are slightly larger than the model structures. The molecules shown in Fig. 7.6 b and h seem to have partly opened substructures in contrast to the more compact structure displayed in the model. The partial flexibility of the individual subunits within the protein complex would explain the larger size of the reconstructions [51][284]. The smallest recognizable feature is the chain loop visible on the upper section of the molecule shown in Fig. 7.6 e (marked by the red arrow), which has an estimated size of 7 – 8 Å. Thus, the local resolution range for these images can be roughly estimated to be in the range of 7 – 12 Å.

In order to substantiate our findings, we conducted ambient AFM measurements on *native-like* hemoglobin proteins. While the ES-IBD process was identical in terms of deposition amount, no mass selection was applied for these experiments. Fig. 7.7 shows overview images

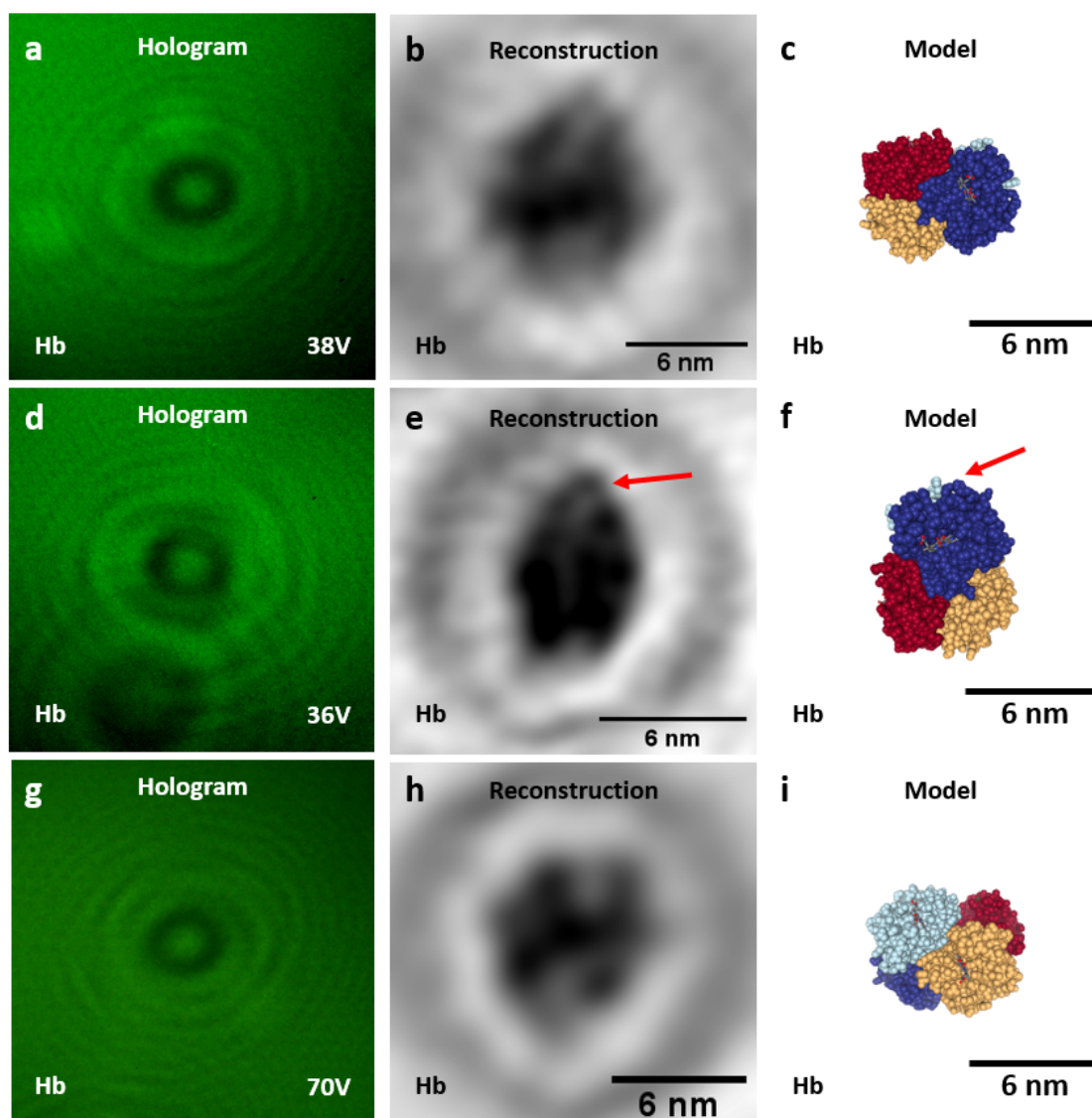


Figure 7.6: LEEH images of *native-like* hemoglobin (Hb) deposited on SLG showing the measured holograms (**a**, **d**, **g**) of three differently oriented example molecules. The emission voltage used for their imaging is reported in the bottom right corner. The amplitude reconstructions and model structures are shown in **b**, **e**, **h** and **c**, **f**, **i**, respectively. The model structures are obtained from the RCSB PDB: <https://www.rcsb.org/structure/1FSX>.

of three HOPG regions containing hemoglobin molecules (**a**, **d** and **g**), as well as the respective magnified images (**b**, **e**, **h**) and height profile plots (**c**, **f**, **i**). The height profiles reveal molecule heights of 2 – 4 nm, which is smaller than the hemoglobin sizes obtained from the model structures. Since no mass selection was used during the deposition, the sample also contains individual subunits (α and β monomers) and dimers, which are smaller in size compared to the tetramer species and have sizes of around 2 – 2.5 nm and 2.5 – 3.5 nm, respectively. Possibly matching molecules in terms of the measured heights are labeled in the AFM images depending on the species: individual subunit as M (monomer), two subunits as D (dimer),

four subunits as T (tetramer, complete protein). Similar values for AFM measurements have been reported by A. Basu et al., who measured molecular heights of around 4 nm [285]. In fact, the measured heights indicate partially unfolded molecules on the surface. Furthermore, many of the observed molecules are positioned next to HOPG step edges, which indicates protein mobility on the HOPG surface after the soft landing procedure [48].

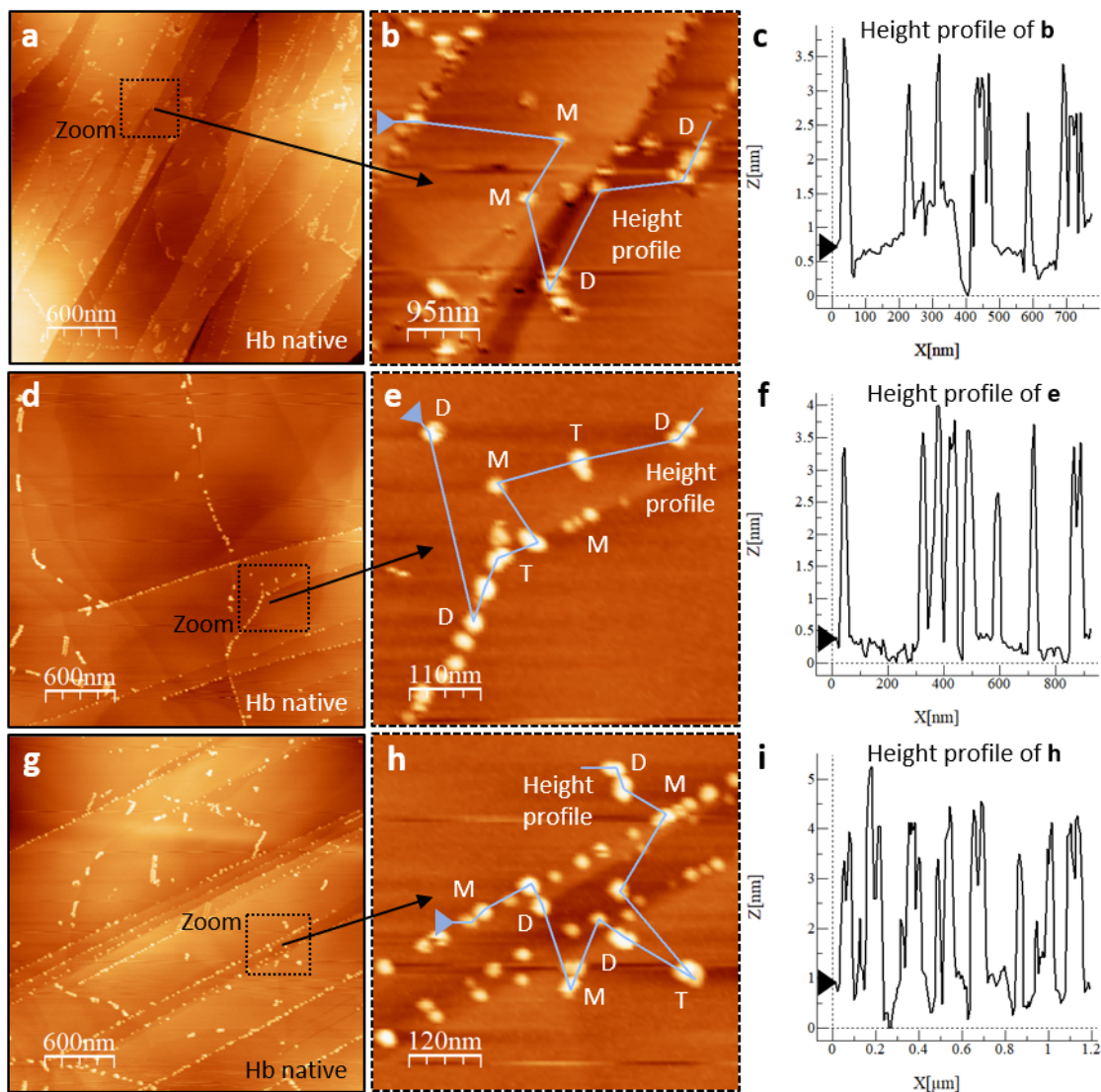


Figure 7.7: AFM images of *native-like* hemoglobin (Hb) deposited on HOPG showing overviews of the three measured areas (a, d, g), the respective magnified images containing height profiles (b, e, h) and the height profile plots (c, f, i). Different molecular heights could indicate single subunits (monomers, M), dimers (D) and/or tetramers (T).

7.1.4 Discussion on Globular Proteins

The investigation of globular protein systems yielded results that are comparable in terms of molecular size and shape to reported data from a different LEEH setup [51]. The respective

amplitude reconstructions of the measured holograms were compared to model structures and show convincing evidence of a successful ES-IBD and LEEH imaging process of *native-like* protein species with local resolutions in the range of 7 – 12 Å. This indicates that our LEEH instrument is properly calibrated. It is important to mention that the image quality of the reconstructions, and thus the obtainable resolution, strongly depends on the emitter performance, but not on the type of measured molecule. Since the investigation of these first test systems was successful, we measured large molecule complexes composed of several subunits and with different shapes, which are presented in the following Sec. 7.2.

7.2 Large Protein Complexes

This section contains the LEEH measurements on *native-like*, large protein complexes, which, as opposed to the globular proteins presented in the previous section, show very distinctive shapes. We use these systems to learn if the native ESI deposition and LEEH imaging process are applicable to large molecule species. We aim for the investigation of substructure within the complexes and try to identify subunits. Furthermore, some of the presented systems, such as beta-galactosidase and GroEL are used as reference in (Cryo-)TEM and we can compare the results obtained from LEEH to the insights provided by these techniques [286][287]. Mass spectra and LEEH images of transferrin (Tf), alcohol dehydrogenase (ADH), beta-galactosidase (β Gal) and GroEL are presented. Furthermore, AFM data of ADH and GroEL deposited on HOPG is shown for size comparison purposes.

7.2.1 Transferrin

Transferrin (Tf) is a bilobal glycoprotein monomer consisting of 679 amino acids. It is mainly produced by the liver and facilitates the iron transport through the blood plasma within the body of vertebrate species [288].

For our experiments, transferrin from human cell cultures (11096-37-0, Sigma) was used, which has a molecular weight of around 75-80 kDa and its molecular size is around 4 – 5 nm in width and 9 – 10 nm in length. The spray solution was prepared as described in Sec. 6.1.1 and typically used parameters for the native ESI process of transferrin are:

Table 7.4: ESI parameters for a *native-like* transferrin ion beam.

c_{Spray}	$T_{\text{capillary}}$	V_{Emitter}	$V_{\text{IonFunnel}}$	$V_{\text{QMS}}^{\text{RF}}$	U/V	Depo charge
1 mg/ml	75°C	+1350 to +1400 V	9.5 V	350 V	1.02	7 pAh

Fig. 7.8 shows the mass spectra of the ion beam before (a) and after (b) the quadrupole mass selection (QMS). The unfiltered ion beam was already quite pure and the mass selection did not improve the beam quality any further. However, the peak at 4006 M/z corresponding to the +19 charge state was increased after applying the filter. This effect is similar to what we

observed in the case of CytC (see Sec. 7.1.1).

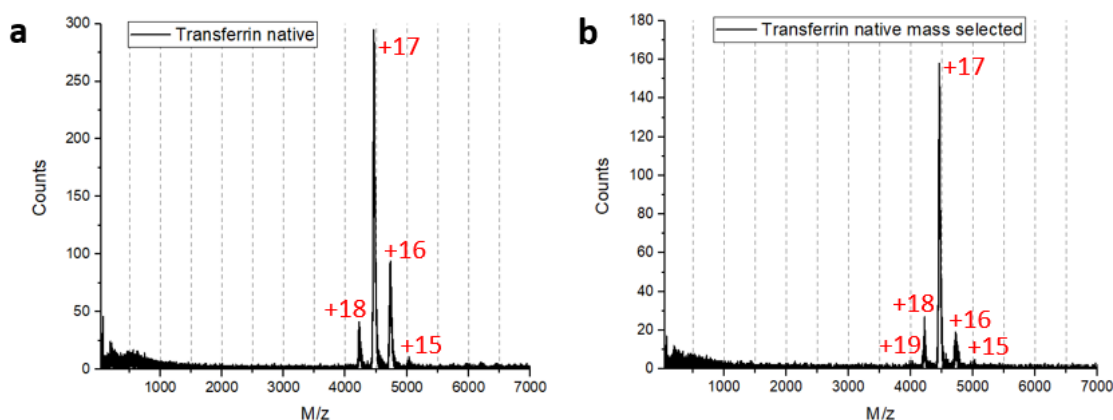


Figure 7.8: Mass spectra of *native-like* transferrin before (a) and after mass selection (b). The peaks indicating a *native-like* species are visible at 4006 (+19), 4229 (+18), 4463 (+17), 4735 (+16) and 5049 (+15) M/z (with their respective charge states) and yield a molecular mass of 75855 ± 176 Da.

The filtered mass spectrum of the transferrin ion beam (Fig. 7.8 b) shows peaks at M/z values of around 4006, 4229, 4463, 4735 and 5049, which correspond to charge states of +19, +18, +17, +16 and +15 for *native-like* protein ions [289][290]. These values are used to estimate the molecular mass of the sprayed protein yielding a mass of 75855 ± 176 Da, which is in good agreement with the nominal molecular mass of around 75.2 kDa for human transferrin. The approximated theoretical molecular weight of 75–80 kDa depends on the iron binding state, as well as the glycosylation state of the individual protein and can vary accordingly.

Mass-filtered transferrin species were soft-landed onto SLG with an energy of 2 eV/charge and directly transferred to the LEEH setup for investigation by LEEH. Fig. 7.9 shows holograms of three molecules (a, d and g). The reconstructed holograms result in amplitude images (b, e and h), revealing different molecule configurations. Via the RCSB PDB model structure 4X1B, it is possible to qualitatively reproduce the observed shapes by simple rotations of the model, as shown in Fig. 7.2 c, f and i.

The molecular sizes obtained from the amplitude reconstructions are slightly larger compared to the models with a molecule length of around 10 – 11 nm and a molecule width of around 5 – 6 nm, which could be due to the partially flexible amino acid side chains and also minor deformations upon landing. Furthermore, the measured signals show contrast differences, which indicate that exterior side groups of the protein appear brighter, while inner, more dense molecule parts appear darker. The estimated local resolution for these protein images is in the range of 8 – 12 Å. The smallest recognizable feature is the center chain connecting both transferrin lobes with each other as visible in Fig. 7.9 h, as well as a gap between the lobes, which is observable due the orientation of the molecule in Fig. 7.9 b. Both features have sizes of about 8 Å and are marked by red arrows in the respective reconstructions and models.

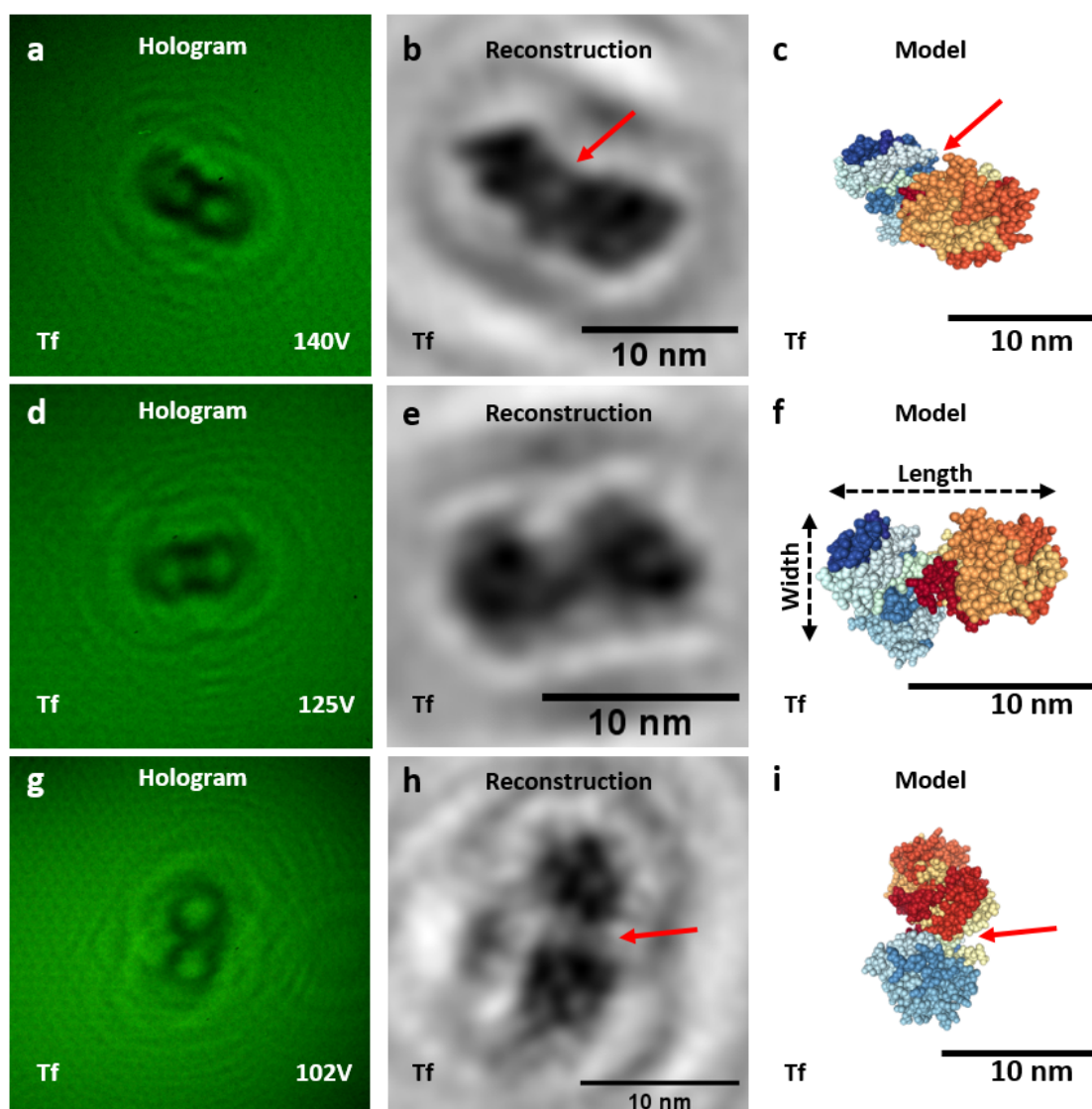


Figure 7.9: LEEH images of *native-like* transferrin (Tf) deposited on SLG showing the measured holograms (**a**, **d**, **g**) of three differently oriented example molecules. The emission voltage used for their imaging is reported in the bottom right corner. The amplitude reconstructions and model structures are displayed in **b**, **e**, **h** and **c**, **f**, **i**, respectively. The model structures are obtained from the RCSB PDB: <https://www.rcsb.org/structure/4X1B>.

7.2.2 Alcohol Dehydrogenase

Alcohol dehydrogenases (ADH) are found in various organisms, where they convert alcohols and aldehydes into each other. While breaking down alcohol in animals, ADH takes part in fermentation processes facilitated by plants, bacteria and yeast [291]. The first isolated ADH protein was obtained from yeast in 1937, is a tetramer with 347 amino acids per subunit and each subunit contains a zinc(II) ion [292][293].

Chapter 7. Measurements of Deposited Molecule Systems

We investigated yeast ADH (*Saccharomyces cerevisiae*, 9031-72-5, Sigma), which has a molecular mass of around 147.5 kDa and its width is around 5 – 6 nm, while its length is around 8 nm. The spray solution was prepared as described in Sec. 6.1.1 and typically used parameters for the native ESI process of ADH are:

Table 7.5: ESI parameters for a *native-like* alcohol dehydrogenase ion beam.

c_{Spray}	$T_{\text{capillary}}$	V_{Emitter}	$V_{\text{IonFunnel}}$	$V_{\text{QMS}}^{\text{RF}}$	U/V	Depo charge
1 mg/ml	75°C	+1300 V	10.5 V	250 V	1.02	7 pAh

Fig. 7.10 shows the mass spectra of the ADH ion beam before (a) and after (b) the quadrupole mass selection (QMS). Unknown species, probably consisting of unfolded contaminants or fragments, can be seen before mass selection in the range from 600 – 1000 M/z . These species were completely removed after applying the mass filtering (see Tab. 7.5).

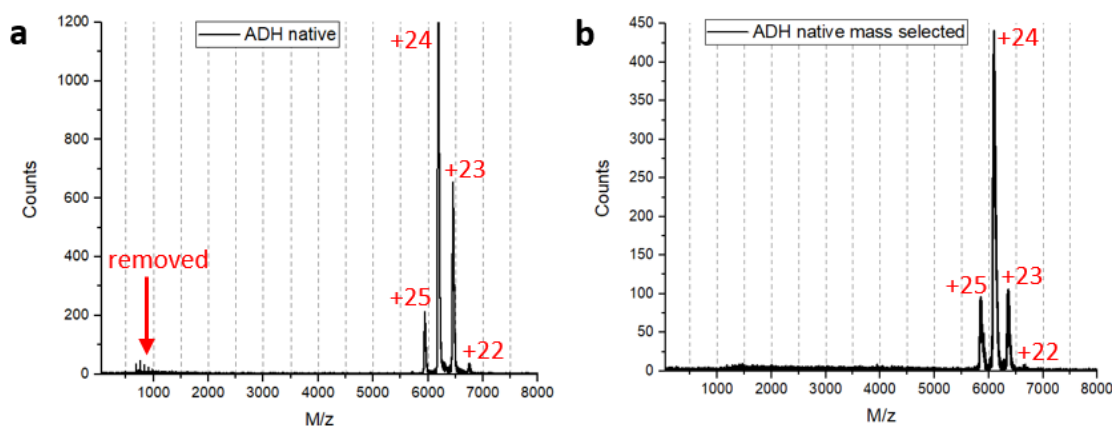


Figure 7.10: Mass spectra of *native-like* alcohol dehydrogenase (ADH) before (a) and after mass selection (b). The peaks indicating a *native-like* species are visible at 5924 (+25), 6180 (+24), 6447 (+23) and 6739 (+22) M/z (with their respective charge states) and yield a molecule mass of 148216 ± 97 Da. An unknown signal (maybe unfolded species) between 600 and 1100 M/z could be filtered out by mass selection.

The filtered mass spectrum of this ion beam (Fig. 7.10 b) shows peaks at M/z values of 5924, 6180, 6447 and 6739, which corresponds to charge states of +25, +24, +23 and +22 for *native-like* protein ions [294][295][296]. These values are used to estimate the molecular mass of the sprayed protein of 148216 ± 97 Da, which is larger than the theoretical molecular mass of 147396 Da for yeast ADH reported in literature [297] but in good agreement with the molecular weight of around 148 kDa given by the producer and again indicative of solvent and ionic adducts.

The selected ADH species was soft-landed onto SLG with an energy of 2 eV/charge. Subsequently, the sample was transferred to the LEEH setup and measured via LEEH. The resulting holograms of three molecules (a, d and g) are shown in Fig. 7.11 with the respective emission voltages of the imaging electron beam. The amplitude reconstructions are presented in Fig.

7.11 **b**, **e** and **h** revealing different molecule orientations along with the respective models obtained by rotation of the RCSB PDB structure 4W6Z, see Fig. 7.11 **c**, **f** and **i**.

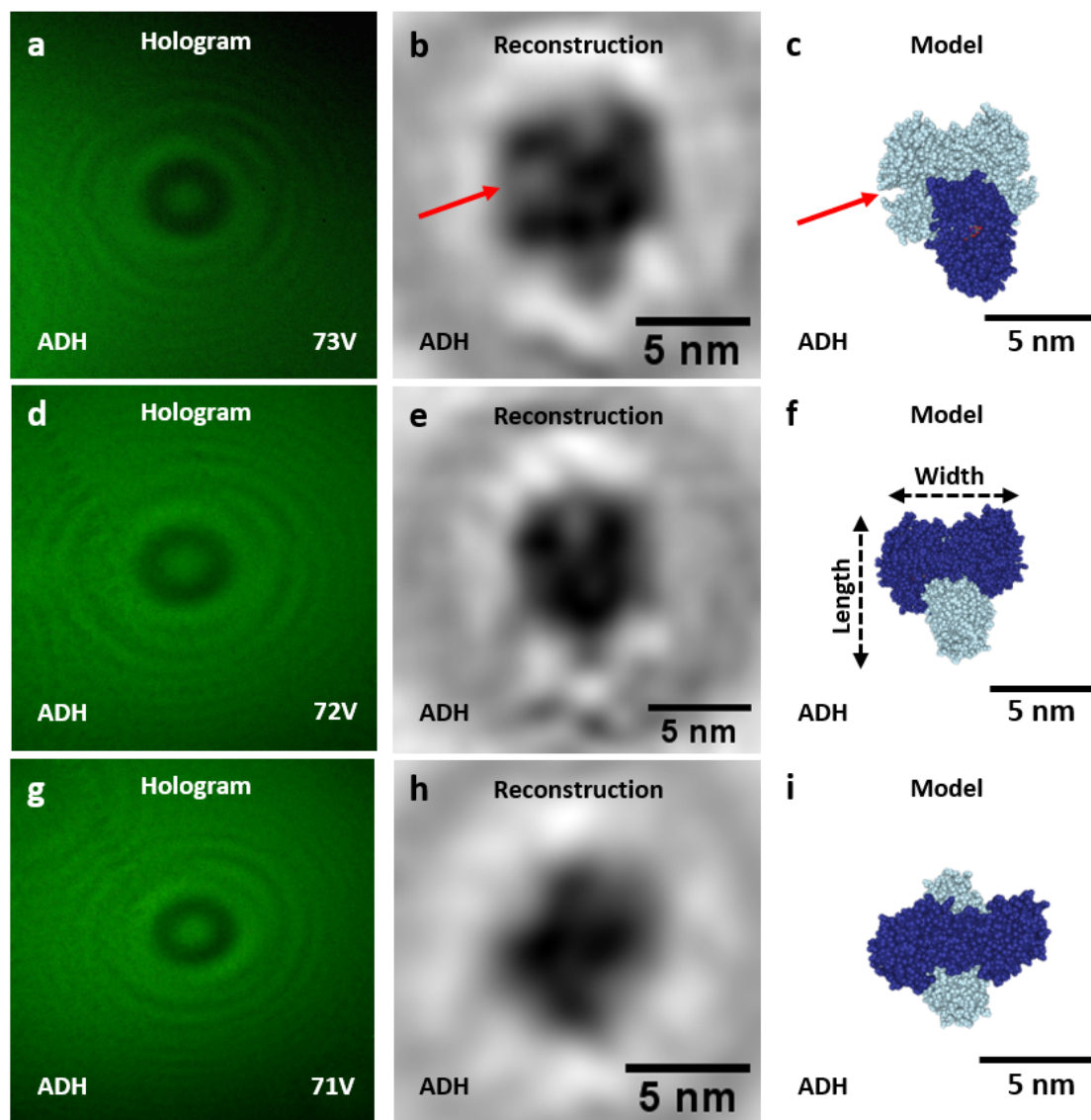


Figure 7.11: LEEH images of *native-like* alcohol dehydrogenase (ADH) deposited on SLG showing the measured holograms (**a**, **d**, **g**) of three differently oriented example molecules. The emission voltage used for their imaging is reported in the bottom right corner. The amplitude reconstructions and model structures are shown in **b**, **e**, **h** and **c**, **f**, **i**, respectively. The model structures are obtained from the RCSB PDB: <https://www.rcsb.org/structure/4W6Z>.

The measured sizes in the amplitude reconstructions fit the dimensions of the model structures and the respective orientations are easy to recognize. The smallest identifiable feature is the gap visible in the individual subgroup to the left in Fig. 7.6 **b**, which has an approximated size of 7 – 8 Å. The gap is marked by a red arrow in the reconstruction and model. As such, the local resolution range for these images is in the range of 7 – 12 Å.

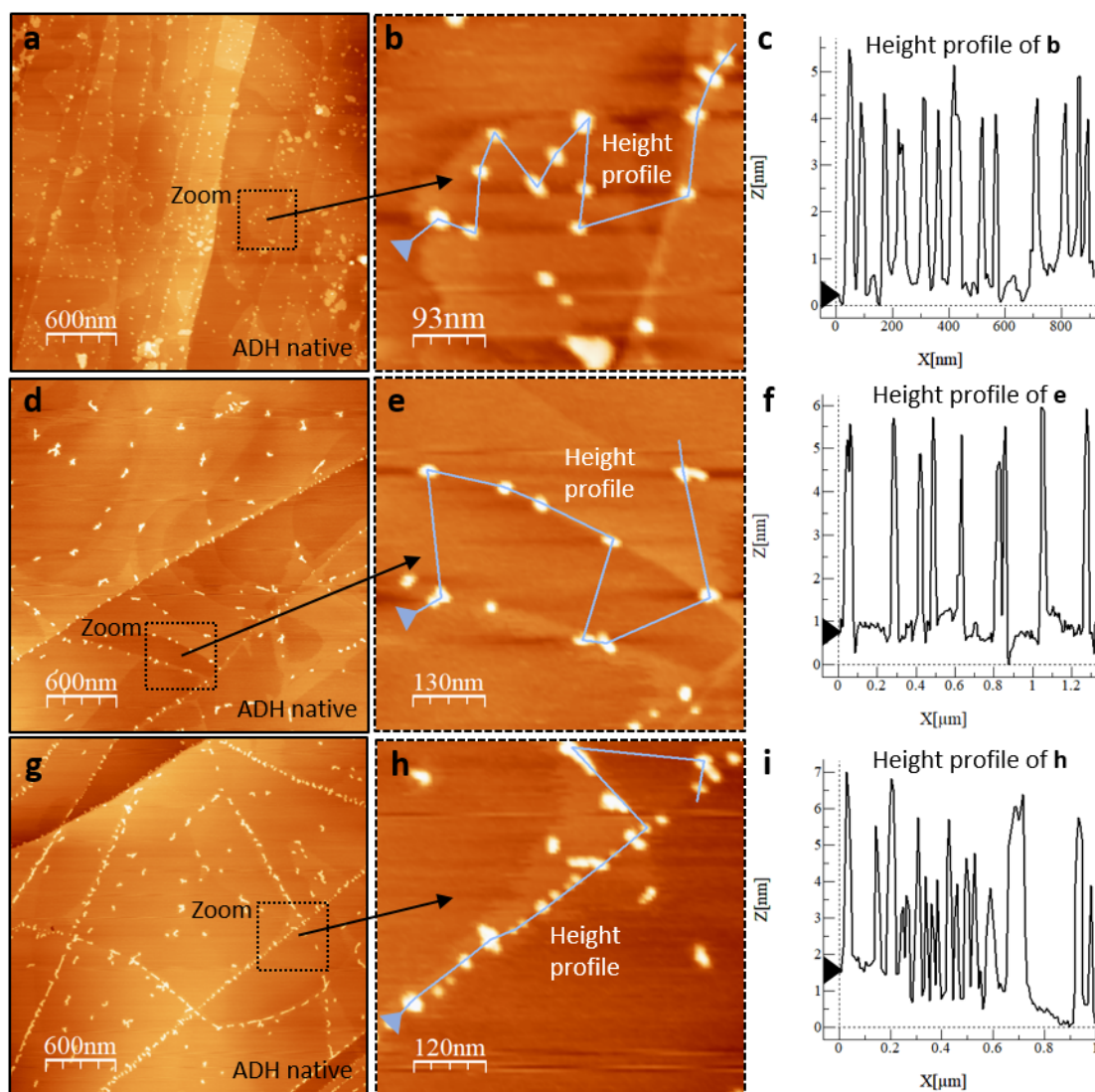


Figure 7.12: AFM images of *native-like* alcohol dehydrogenase (ADH) deposited on HOPG showing overviews of the three measured areas (**a**, **d**, **g**), the respective magnified images containing height profiles (**b**, **e**, **h**) and the height profile plots (**c**, **f**, **i**).

To confirm the sizes measured by LEEH, we also conducted ambient AFM measurements on *native-like* ADH proteins. The ES-IBD process was identical in terms of mass selection and deposition amount. In Fig. 7.12 **a**, **d** and **g**, overview images of three HOPG regions containing ADH molecules are shown. The magnified images and height profile plots are displayed in Fig. 7.12 **b**, **e**, **h** and **c**, **f**, **i**, respectively. The height profiles reveal molecule sizes ranging from 4 – 6 nm, which is smaller than the ADH sizes obtained from the model structures. However, sizes of 5 – 6 nm in principle are in good agreement for flat ADH orientations, where the width would be measured. As already mentioned for the AFM results obtained from hemoglobin, the ADH sample also shows many molecules, which are positioned next to and along HOPG step edges. This recurring effect could indicate protein mobility on the HOPG surface after

the soft landing procedure. When remeasuring the same regions after several hours or days, no further mobility of molecules was observed, i.e. their position remained unchanged in ambient conditions. In the light of this finding, the molecular adsorption on the HOPG step edges is probably related to transient mobility in the soft-landing process. The kinetic energy of the landing molecules, although unable to produce significant structural changes of the proteins, can lead to a translational motion of the molecule after impact on the surface. Similar effects for various molecule species have been reported by S. Rauschenbach et al. [48].

7.2.3 Beta-Galactosidase

Beta-galactosidase (β Gal) is an enzyme acting as a catalyst in the hydrolysis of β -galactosides yielding monosaccharides, which subsequently can be used for the energy production cycle of the respective organism. This protein complex is a tetramer, where each of its four subunits has 1023 amino acids [298][299].

We investigated beta-galactosidase from bacteria (*Escherichia coli*, 9031-11-2, Sigma), which has a molecular mass of around 465.4 kDa (116.3 kDa per subunit) and a molecular size of around 12 nm in width and 17 – 18 nm in length [286][300]. The spray solution was prepared as described in Sec. 6.1.1 and typically used parameters for the native ESI process of beta-galactosidase are:

Table 7.6: ESI parameters for a *native-like* beta-galactosidase ion beam.

c_{Spray}	$T_{\text{capillary}}$	V_{Emitter}	$V_{\text{IonFunnel}}$	$V_{\text{QMS}}^{\text{RF}}$	U/V	Depo charge
1 mg/ml	75°C	+1250 to +1350 V	10 V	250 to 350 V	1.01	5 pAh

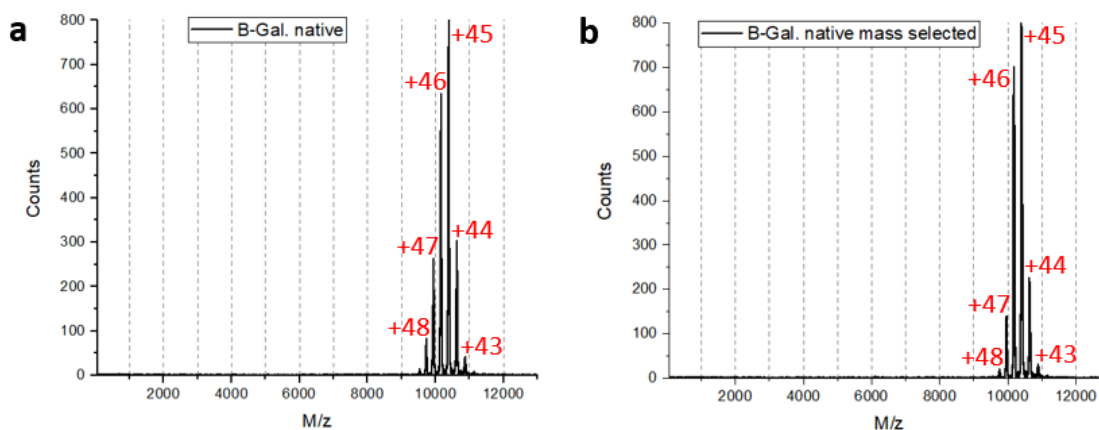


Figure 7.13: Mass spectra of *native-like* beta-galactosidase (B-Gal.) before (a) and after mass selection (b). The peaks indicating a *native-like* species are visible at 9732 (+48), 9937 (+47), 10177 (+46), 10385 (+45), 10626 (+44) and 10870 (+43) M/z (with their respective charge states) and yield a molecule mass of 467387 ± 393 Da.

In Fig. 7.13, the mass spectra of the ion beam before (a) and after (b) the quadrupole mass selection (QMS) are shown. Since the unfiltered ion beam already appeared pure, the mass

selection did not significantly impact the quality of the beam. The visible peaks at M/z values of around 9732, 9937, 10177, 10385, 10626 and 10870 correspond to charge states of +48, +47, +46, +45, +44 and +43 of *native-like* protein ions [301]. These values are used to estimate the molecular mass of the sprayed protein yielding a mass of 467387 ± 393 Da, which is higher than the theoretical molecular mass of 465412 Da for β Gal proteins obtained from literature [300]. As mentioned before, this could depend on calibration factors of our mass spectrum and/or additional solvent molecules, which can be incorporated in this large protein complex.

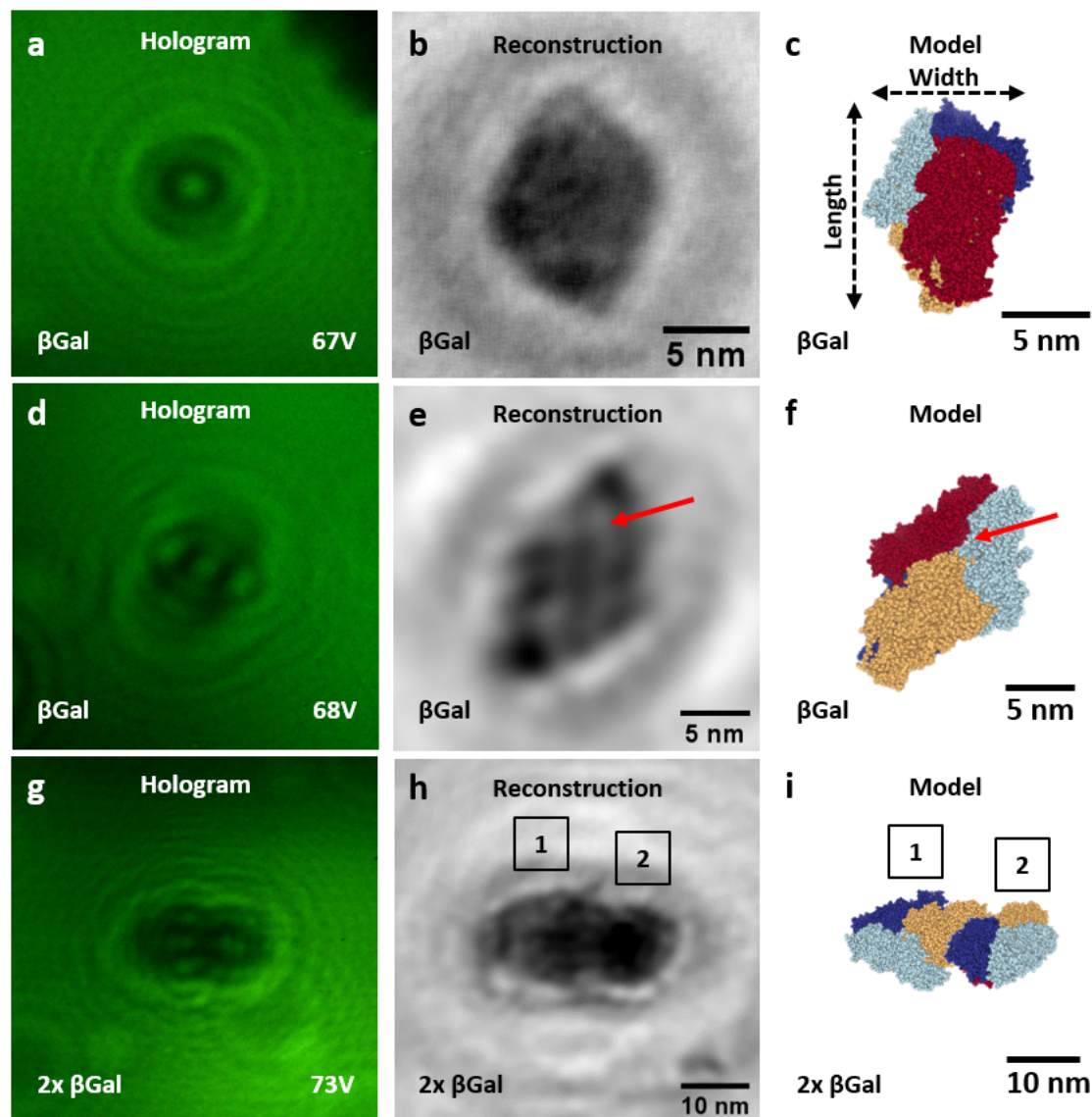


Figure 7.14: LEEH images of *native-like* beta-galactosidase (β Gal) deposited on SLG showing the measured holograms (a, d, g) of four differently oriented example molecules. The emission voltage used for their imaging is reported in the bottom right corner. The amplitude reconstructions and model structures are shown in b, e, h and c, f, i, respectively. The images in g, h and i show two molecules next to each other as indicated by 1 and 2. The model structures are obtained from the RCSB PDB: <https://www.rcsb.org/structure/6CVM>.

The *native-like* beta-galactosidase species was soft-landed onto SLG with an energy of about 2 eV/charge, subsequently transferred to the LEEH setup and investigated by LEEH. In Fig. 7.14 **a**, **d** and **g**, holograms of three molecules are displayed with the respective emission voltages of the imaging electron beam. The respective amplitude reconstructions (Fig. 7.14 **b**, **e** and **h**) show different molecule orientations and, in the case of Fig. 7.14 **h**, the presence of two β Gal proteins next to each other (labeled by **1** and **2**). The model structure 6CVM from the RCSB PDB is used to reproduce the observed reconstructions with the respectively rotated orientations, as shown in Fig. 7.14 **c**, **f** and **i**.

The presented amplitude reconstructions clearly match the oriented model structure's characteristic shape, even for the case of two β Gal molecules next to each other (Fig. 7.14 **h**). Measured sizes match the dimensions of the model structures in width and length when considering the orientations [286]. In Fig. 7.14 **e**, the contrast differences within the molecule reveal a distinguishable cavity, which can be assumed by the model (Fig. 7.14 **f**). This feature has a size of around 7 Å and is the smallest identifiable feature of the protein complex leading to an estimated local resolution in the range of 7 – 15 Å. In Sec. 7.5, I present further LEEH measurements of β Gal molecules at cryogenic temperatures, which yield similar results.

7.2.4 GroEL

GroEL is part of the chaperonin family and consists of two ring-shaped heptamers with identical subunits. Together with GroES, the barrel-like protein complex facilitates the transportation and (re-)folding of other protein species from the cytoplasm to the mitochondrial matrix, while also acting as a heat shock protein [302][303][304].

In our experiments, bacterial GroEL (*Escherichia coli* Chaperonin 60, C7688, Sigma) was used, which has a molecular weight of around 822-840 kDa and molecular dimensions of 12 – 14 nm [287]. The spray solution was prepared as described in Sec. 6.1.1 and typically used parameters for the native ESI process of GroEL are:

Table 7.7: ESI parameters for a *native-like* GroEL ion beam.

c_{Spray}	$T_{\text{capillary}}$	V_{Emitter}	$V_{\text{IonFunnel}}$	$V_{\text{QMS}}^{\text{RF}}$	U/V	Depo charge
1 mg/ml	75°C	+1300 to +1350 V	11.5 V	550 to 580 V	1.02	4 pAh

Fig. 7.15 shows the mass spectra of the ion beam before (**a**) and after (**b**) the quadrupole mass selection (QMS). The visible peaks have M/z values of 11688, 11849, 12022, 12204 and 12387, which corresponds to charge states of +71, +70, +69, +68 and +67 for *native-like* protein ions [305][306]. These values lead to an estimated molecular mass of the sprayed protein of 829650 ± 229 Da, which is in good agreement with the expected molecular weight for GroEL complexes. Furthermore, the unfiltered beam contained an unknown species (probably unfolded molecules) in the range from 100 – 3000 M/z , which was completely removed by the mass selection process.

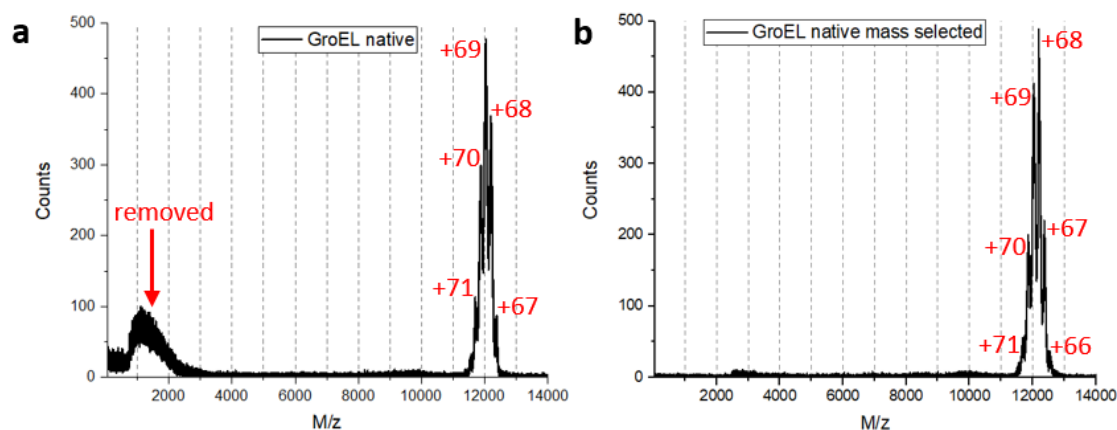


Figure 7.15: Mass spectra of *native-like* GroEL before (a) and after mass selection (b). The peaks indicating a *native-like* species are visible at 11688 (+71), 11849 (+70), 12022 (+69), 12204 (+68) and 12387 (+67) M/z (with their respective charge states) and yield a molecular mass of 829650 ± 229 Da. An unknown signal (maybe unfolded species) between 600 and 2400 M/z was filtered out by the mass selection.

The selected GroEL species was soft-landed onto the SLG sample with an energy of 2 eV/charge. Afterwards, the sample was transferred to the LEEH setup and measured via LEEH. The resulting holograms of three molecules (a, d and g) are shown in Fig. 7.16. The amplitude reconstructions are presented in Fig. 7.16 b, e and h revealing two different molecule orientations: the top view (b and e) and the side view (h). These images of the molecules in different orientations can be compared to the RCSB PDB structure 1MNF shown in Fig. 7.16 c, f and i.

The dimensions of the measured molecules are smaller than that of the model structures. Instead of the expected 12–14 nm [287], the measured sizes of the top and side view molecules are around 10–11 nm. The smallest identifiable features are the visible gaps inbetween the heptameric rings, as marked by red arrows in Fig. 7.16 h and the respective model structure 7.16 i. These gaps have an approximated size of 10–11 Å, which leads to an estimated local resolution in the range of 10–15 Å.

It is important to mention that the characteristic hole of the barrel-shaped GroEL molecule is not visible in the reconstructions. Instead, a region of high absorption is observed in the center region of the proteins, where the hole would be located. This can either be due to a tilt of the molecule relative to the imaging axis, which would lead to an eclipse of its hole, or by a partial collapse of the molecule during the ESI deposition process. Partial collapsing of the GroEL structure in the gas phase has already been reported by other authors [306] and would also account for the reduced dimensions of the proteins on the surface.

To confirm the sizes measured via LEEH, we performed ambient AFM measurements on *native-like* GroEL proteins, where the ES-IBD process was identical in terms of mass selection and deposition amount. In Fig. 7.17 a and d, two images of different HOPG regions containing GroEL molecules are shown. The respective height profile plots are displayed in Fig. 7.12 b and

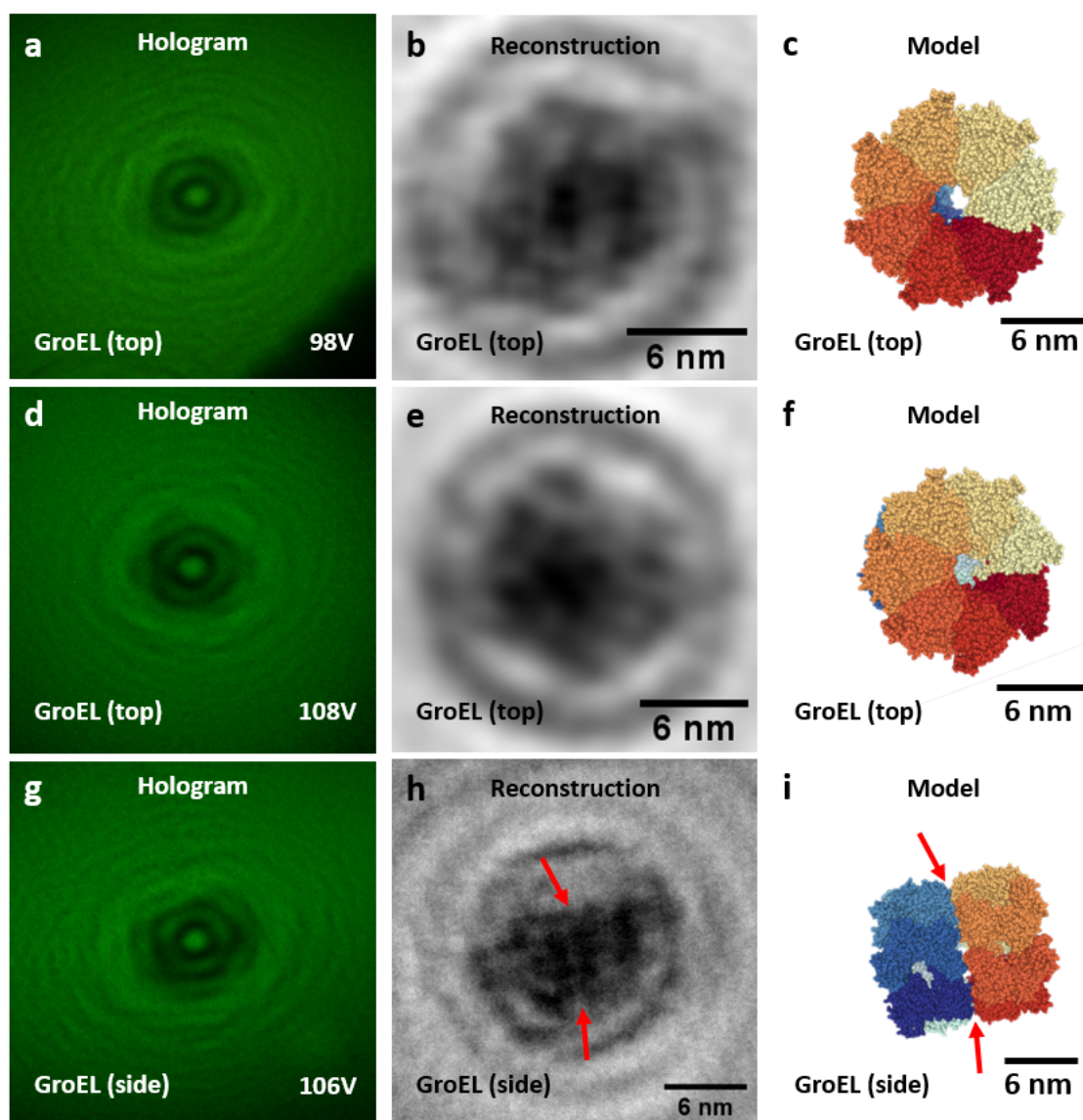


Figure 7.16: LEEH images of *native-like* GroEL deposited on SLG showing the measured holograms (a, d, g) of three differently oriented example molecules. The emission voltage used for their imaging is reported in the bottom right corner. The amplitude reconstructions and model structures are shown in b, e, h and c, f, i, respectively. While the upper two GroEL molecules are showing a top view configuration, the bottom molecule is most likely oriented in a side view configuration. The model structures are obtained from the RCSB PDB: <https://www.rcsb.org/structure/1MNF>.

c, as well as e and f. The height profiles reveal molecule sizes ranging from 6 – 10 nm, which are smaller than the expected GroEL sizes. Furthermore, no hole is visible in the obtained images. In literature, the molecular sizes of drop-casted GroEL measured via AFM are found to be in the range of 13 – 14 nm, where the hole of top view molecules can be identified [55][307][308]. However, if deposited via ES-IBD, the size of GroEL molecules measured via AFM can vary depending on the charge state of the deposited species, as indicated by J. L.

P. Benesch et al. [309]. For charge states of around +64, they report molecular diameters of around 14 nm, while for charge states around +72, molecular diameters of 11 – 12 nm were measured. In both cases, the center holes of molecules in the top view orientation were not identified, if deposited via ESI. With regard to the charge states obtained during our ESI process (+66 to +71), the larger molecules obtained from our data are in good agreement with already reported sizes [309]. The smaller molecules having sizes of around 6 nm could indicate for single heptamer units, where one half of the complex was removed. This effect could appear due to the AFM measurement process, where the scanning tip is removing the upper heptamer ring upon contact, as reported by F. Valle et al. [308] or due to the collision with the surface upon landing. In Sec. 7.5, I present further LEEH measurements of GroEL molecules at cryogenic temperatures, which show an improved signal intensity compared to the LEEH images presented in Fig. 7.16.

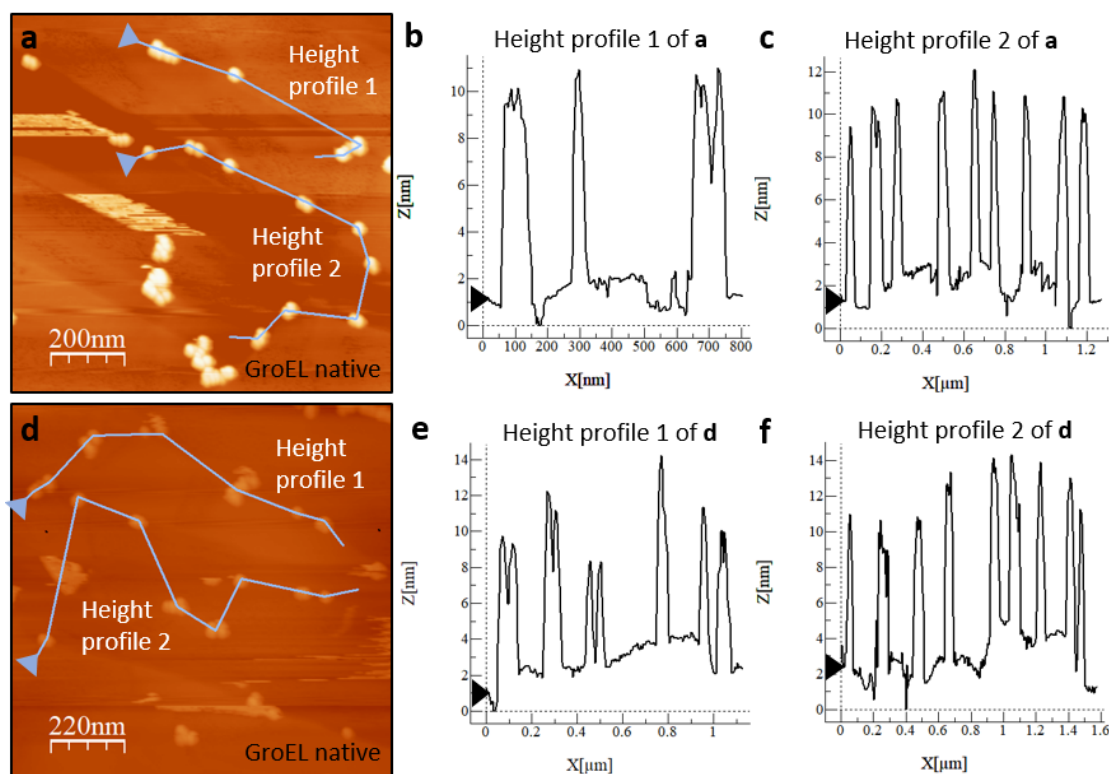


Figure 7.17: AFM images of *native-like* GroEL deposited on HOPG showing the two measured areas containing height profiles (a, d) and the respective height profile plots (b, c and e, f).

7.2.5 Discussion on Large Protein Complexes

The presented results on large protein complexes show that we are able to successfully spray and deposit these molecules via the ES-IBD process. The respective amplitude reconstructions of the measured holograms were analyzed in size and shape, yielding dimensions comparable to the respectively oriented model structures. Furthermore, the results allow the distinction

of substructures within the molecular complexes with local resolutions in the range of 7 – 15 Å. Beta-galactosidase and GroEL, which are considered as benchmark molecules in TEM techniques [286][287][310], can clearly be identified by our LEEH instrument. However, in the case of GroEL, size measurements via both LEEH and AFM suggest the deposition of collapsed species that are likely to form in the gas phase of the ESI process [306][311]. This gas-phase collapse of complex protein molecules is an interesting effect, which can also be observed for more flexible protein species, which are presented in the following Sec. 7.3.

7.3 Flexible Protein Complexes

This section contains an investigation on flexible proteins measured by LEEH. Since LEEH does not use any data averaging and allows for the imaging of individual molecules, flexible proteins are ideal systems to be investigated with our instrument and possible gas-phase species and adsorption geometries generated during the ES-IBD process can be observed directly. Mass spectra and LEEH images of the MAdCAM-Fc complex, as well as *native-like* and denatured Herceptin antibodies (AB) are presented. AFM data of *native-like* and denatured AB molecules deposited on HOPG is shown for size comparison.

7.3.1 MAdCAM-Fc Complex

The mucosal addressin cell adhesion molecule-1 (MAdCAM) is found in the membranes of mucosal endothelial cells, where it forms protein complexes with various other signaling molecules and proteins, such as integrins and selectins. Its main function is the directed trafficking of lymphocytes leading to inflammatory reactions of the affected tissue, e.g. as an overreactive immune response to certain gut microbes in the intestines, which is known as inflammatory bowel disease [312][313][314][315].

We investigated the human MAdCAM protein complexed with an Fc protein, which was obtained from the group of S. Zundler (Uni-Klinik Erlangen). The complex has an estimated molecular weight of around 90 kDa, where MAdCAM amounts to around 40 kDa and the Fc unit, which is an antibody subunit used as a marker, amounts to roughly 50 kDa. The molecular size of the complex is around 7 nm in width and up to 15 nm in length, if stained and imaged via TEM as reported by Y. Yu et al. [316]. The spray solution was prepared as described in Sec. 6.1.1 and typically used parameters for the ESI process of MAdCAM-Fc are:

Table 7.8: ESI parameters for a MAdCAM-Fc ion beam.

c_{Spray}	$T_{\text{capillary}}$	V_{Emitter}	$V_{\text{IonFunnel}}$	$V_{\text{QMS}}^{\text{RF}}$	U/V	Depo charge
1 mg/ml	75°C	+1300 to +1350 V	10 V	150 to 180 V	1.01	6 pAh

The visible peak at 9000 M/z (see Fig. 7.18) likely corresponds to a charge state of +10 considering an estimated molar mass of around 90 kDa for the MAdCAM-Fc complex [315]. The broad

peak around 7000 M/z can originate from an isolated Fc fragment, which has an estimated mass of around 49 – 50 kDa leading to an approximated charge state of +7, and/or an isolated MAdCAM unit, which has an estimated mass of around 40 – 41 kDa leading to an approximated charge state of +6. The additional signals around 800, 2200 and 3000 M/z could originate from unfolded fragment contaminants. Applying the respective QMS voltage and U/V ratio, the peaks at 2200 and 3000 M/z are significantly reduced. However, the peak around 800 M/z persisted and could not be filtered out by the mass selection due to a limited QMS window for this beam. In contrast to the mass spectra of other presented molecules, the peaks for MAdCAM-Fc are not well resolved, which could be due to the complex consisting of several substructures, which can contain additional ionic adducts and solvent.

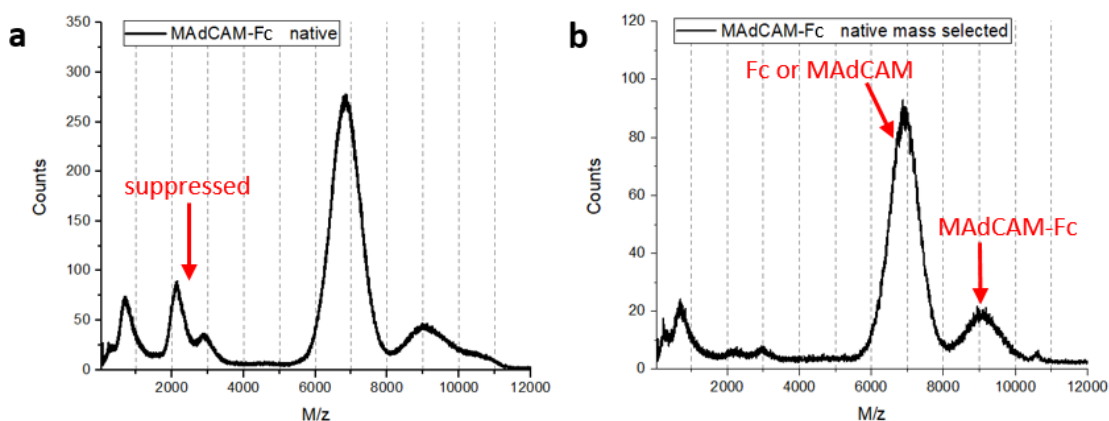


Figure 7.18: Mass spectra of *native-like* MAdCAM-Fc complex before (a) and after mass selection (b). Two broad peaks at around 7000 and 9000 M/z could indicate a folded complex species, while the signals up to 3500 M/z could correspond to unfolded species. The mass selection was applied to filter out the signal below 3500 M/z yielding a significantly reduced signal after filtering except for the peak around 800 M/z .

The selected MAdCAM-Fc species (see Fig. 7.18 b) was soft-landed onto SLG with an energy of 2 eV/charge, subsequently transferred to the LEEH setup and investigated by LEEH. In Fig. 7.19 a, d and g, holograms of three molecules are displayed. The respective amplitude reconstructions (Fig. 7.19 b, e and h) show different molecule orientations and, in the case of Fig. 7.19 h, an isolated MAdCAM molecule without the Fc unit. The 4IRZ structure from the RCSB PDB is used to model possible structures for the different acquired images, as shown in Fig. 7.19 c, f and i.

The measured sizes of the MAdCAM and Fc unit fit the expected values considering them as individual units and when considering their adduct [316]. The contrast differences within the molecule reveal cavities, which also appear for certain orientations in the model structure, see Fig. 7.19 h (marked by the red arrow). This feature has a size of around 10 Å and is the smallest reliably distinguishable feature of the protein complex leading to an approximated local resolution in the range of 10 – 15 Å. The cavities observed in the other reconstructions cannot be fitted directly to a model structure and also further features in the model are not perfectly matching the amplitude signals. This indicates the flexibility of the protein complex, where

the MADCAM and the Fc fragment can rotate and bend independently of each other leading to varying configurations. Based on these promising results of this protein complex, future steps include ES-IBD and LEEH imaging of even larger MADCAM complexes incorporating further protein species, which will be discussed in the outlook in Sec. 9.6.

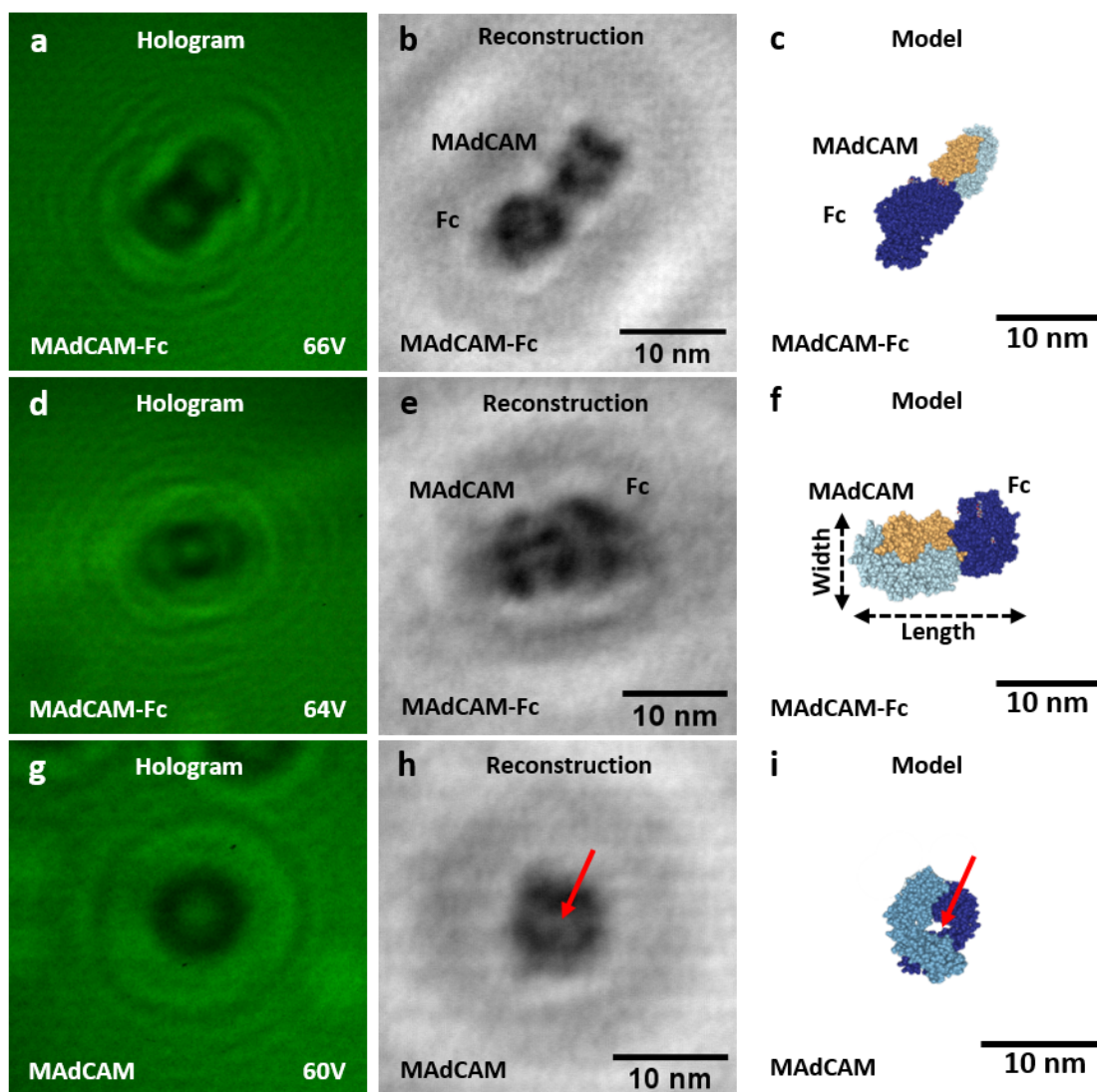


Figure 7.19: LEEH images of *native-like* MADCAM-Fc complex deposited on SLG showing the measured holograms (**a**, **d**, **g**) of three differently oriented example molecules. The emission voltage used for their imaging is reported in the bottom right corner. The respective amplitude reconstructions are shown in **b**, **e**, **h**. The reconstructions in **b** and **e** show MADCAM molecules containing a distinguishable Fc unit, while the reconstruction in **h** most probably shows a MADCAM molecule without the Fc unit. The fitted model orientations displayed in **c**, **f** and **i** are obtained from the RCSB PDB: <https://www.rcsb.org/structure/4IRZ>.

7.3.2 Native-like Herceptin Antibodies

Antibodies (AB), also referred to as immunoglobulins, are a crucial component of the immune system, which identify and neutralize molecules, viruses, bacteria and cells that are not endogenous. The most common type of antibodies in the human serum is the immunoglobulin G (IgG) consisting of two light and two heavy polypeptide chains, which are covalently bound forming the well-known Y-shaped three lobe structure [317]. IgG consists of a constant Fc region, which is the heaviest lobe within the structure, and two variable Fab regions, which can bind to the respective target molecules (antigens). The three individual lobes are connected to each other via a flexible hinge region allowing for a multitude of structural orientations, which is relevant for their biological functionality [74][318].

In our experiments, IgG Herceptin antibodies, also known as Trastuzumab, are studied. These proteins are used for the treatment of breast and stomach cancer, where they bind to the growth factor receptors (HER2) located on the cancer cells, which can inhibit their growth [319][320]. We obtained the Herceptin antibodies from the group of C. V. Robinson (University of Oxford, NHS Oxford University Hospital). The protein contains 1328 amino acids and has a molecular weight of around 148 kDa, while also containing additional polysaccharid chains on its Fc chain lobe. The molecular dimensions are 5 – 8 nm for individual lobes and up to 16 nm for the whole molecule depending on the configuration of the lobes with respect to each other. The spray solution was prepared as described in Sec. 6.1.1 and typically used parameters for the native ESI process of the AB are:

Table 7.9: ESI parameters for a *native-like* Herceptin antibody ion beam.

c_{Spray}	$T_{\text{capillary}}$	V_{Emitter}	$V_{\text{IonFunnel}}$	$V_{\text{QMS}}^{\text{RF}}$	U/V	Depo charge
1 mg/ml	75°C	+1250 to +1350 V	10 V	400 to 450 V	1.03	7 pAh

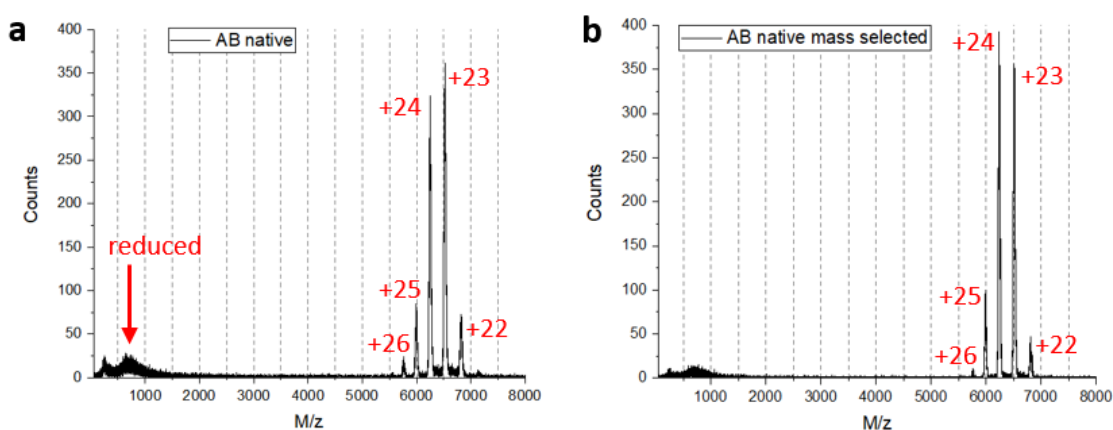


Figure 7.20: Mass spectra of *native-like* Herceptin antibodies (AB) before (a) and after mass selection (b). The peaks indicating a *native-like* species are visible at 5758 (+26), 5980 (+25), 6234 (+24), 6505 (+23) and 6816 (+22) M/z (with their respective charge states) and yield a molecular mass of 149654 ± 171 Da. The visible signal in the range of 300 – 1400 M/z was reduced by the mass selection process.

Fig. 7.20 shows the mass spectra of the ion beam before (a) and after (b) the quadrupole mass selection (QMS). An unknown, most likely unfolded species in the range of 300 – 1300 M/z was reduced by the mass selection. The visible peaks at M/z values of 5758, 5980, 6234, 6505 and 6816 correspond to charge states of +26, +25, +24, +23 and +22 for *native-like* protein ions [321][322]. These values are used to estimate the molecular mass of the sprayed protein yielding a mass of 149654 ± 171 Da, which is higher than the expected molecular weight of around 148 kDa for Trastuzumab. As mentioned before, this could depend on calibration factors of our mass spectrum and/or additional solvent molecules bound to the protein. Furthermore, the variable polysaccharide chains will contribute to the total mass of the molecule as well [320].

The selected AB species was soft-landed on SLG with an energy of 2 eV/charge. Afterwards, the sample was transferred to the LEEH setup and measured via LEEH. The resulting holograms and their reconstructions indicate the presence of different adsorption geometries of the AB molecules on SLG, as indicated by the model structures of a flat and upright adsorbed AB in Fig. 7.21 [74]. For some of the proteins, all three lobes are visible (see Fig. 7.22, 3-lobe), while other molecules show two-lobe structures (see Fig. 7.23, 2-lobe). Furthermore, compact collapsed structures are identified (see Fig. 7.24), where no distinctive lobes can be identified. Due to the high flexibility of the AB molecules, leading to several possible spatial arrangements of their three subunits, the X-ray resolved structure *IIGT* cannot directly be used as a model for our results. To account for this extra degree of freedom, different configuration of the *IIGT* structure were created by rotating the different subunits around specific peptide bonds of the hinge region, namely the Gly-236 residues of both heavy chains [74].

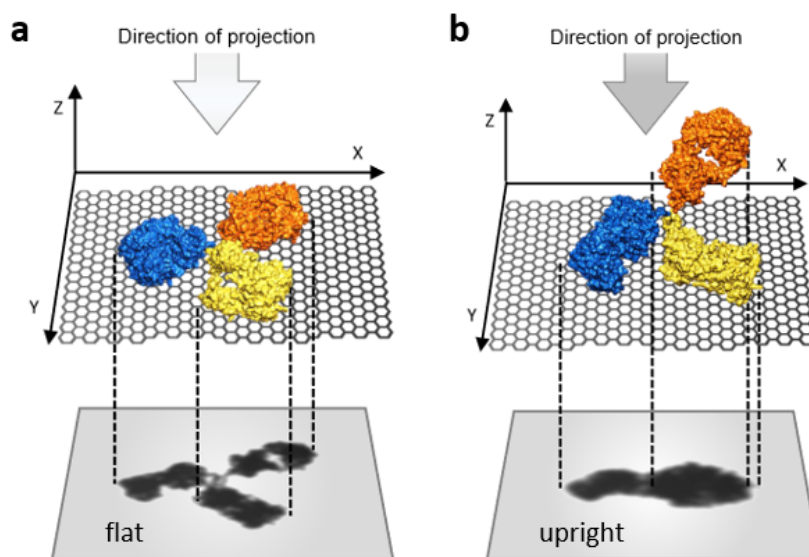


Figure 7.21: Schematic of AB model structures showing a flat (a) and an upright (b) adsorption geometry and the resulting projections as presented by H. Ochner et al. [74].

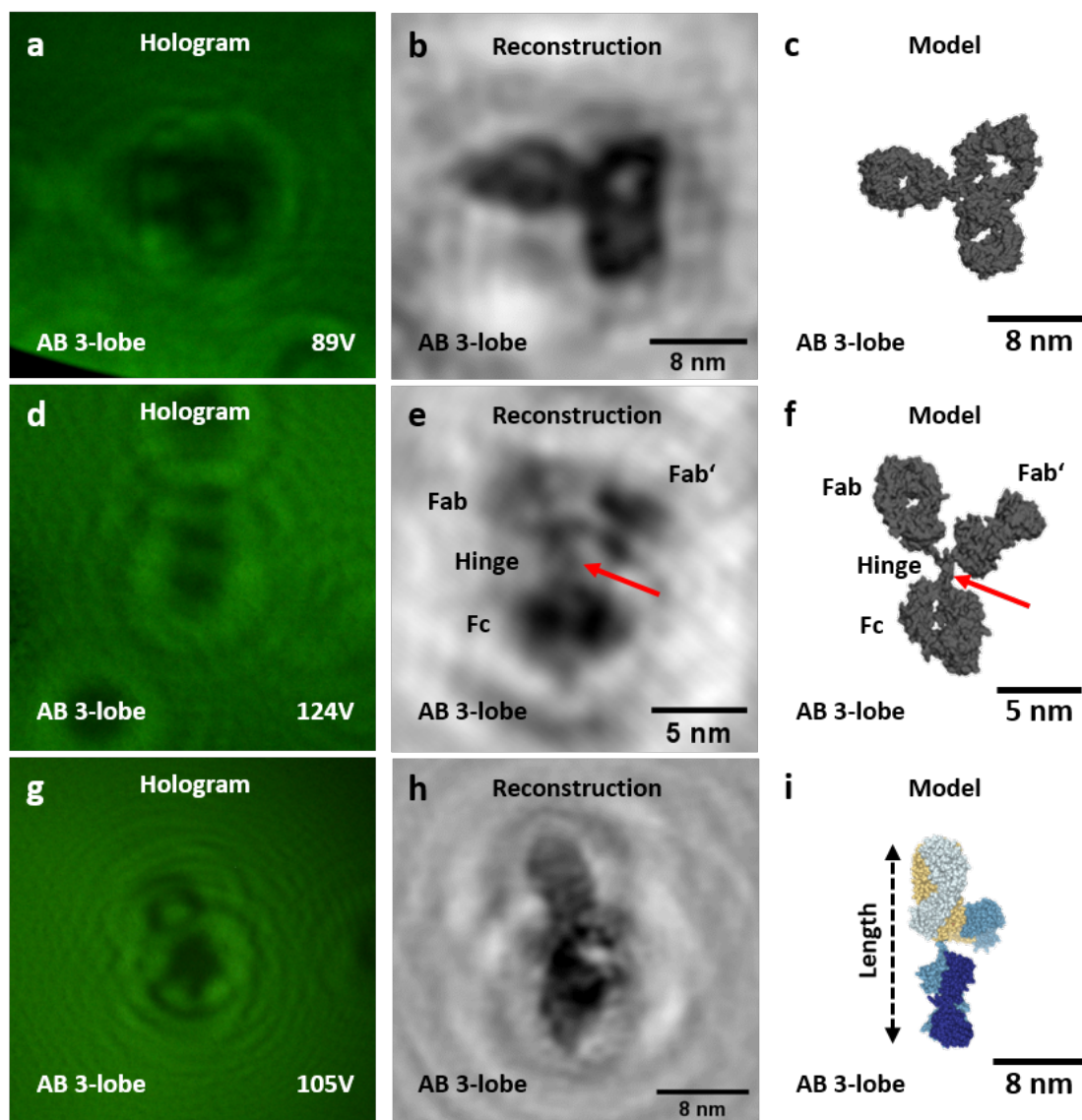


Figure 7.22: LEEH images of *native-like* Herceptin antibodies (AB) deposited on SLG showing the measured holograms (**a**, **d**, **g**) with the used emission voltages reported in the bottom right corner, the respective amplitude reconstructions (**b**, **e**, **h**) and model structures (**c**, **f**, **i**) of three example molecules, where each antibody molecule displays three lobes. The model structures are obtained from the RCSB PDB: <https://www.rcsb.org/structure/1IGT> and are reoriented by rotating the individual lobes around their flexible hinge region to properly reproduce the conformations obtained from the reconstructions.

In order to observe all three lobes constituting the IgG molecules, a flat adsorption geometry of the ABs on the (SLG) substrate is required (see Fig. 7.22) [74]. The amplitude reconstructions are presented in Fig. 7.22 **b** and **e** along with the model structures, see Fig. 7.22 **c** and **f**. A direct comparison between the acquired images and models shows striking similarities both in overall shape and dimensions. In Fig. 7.22 **e**, the individual peptide chains constituting the hinge region are visible, allowing the identification of the different subunits, as labeled in Fig. 7.22 **f**. This fine detail suggests a local resolution of about 5 Å. Three lobes are sometimes also

recognizable in images of upright molecules where one of the lobes is only partially visible, as shown in Fig. 7.22 **g**, which also contains a charge.

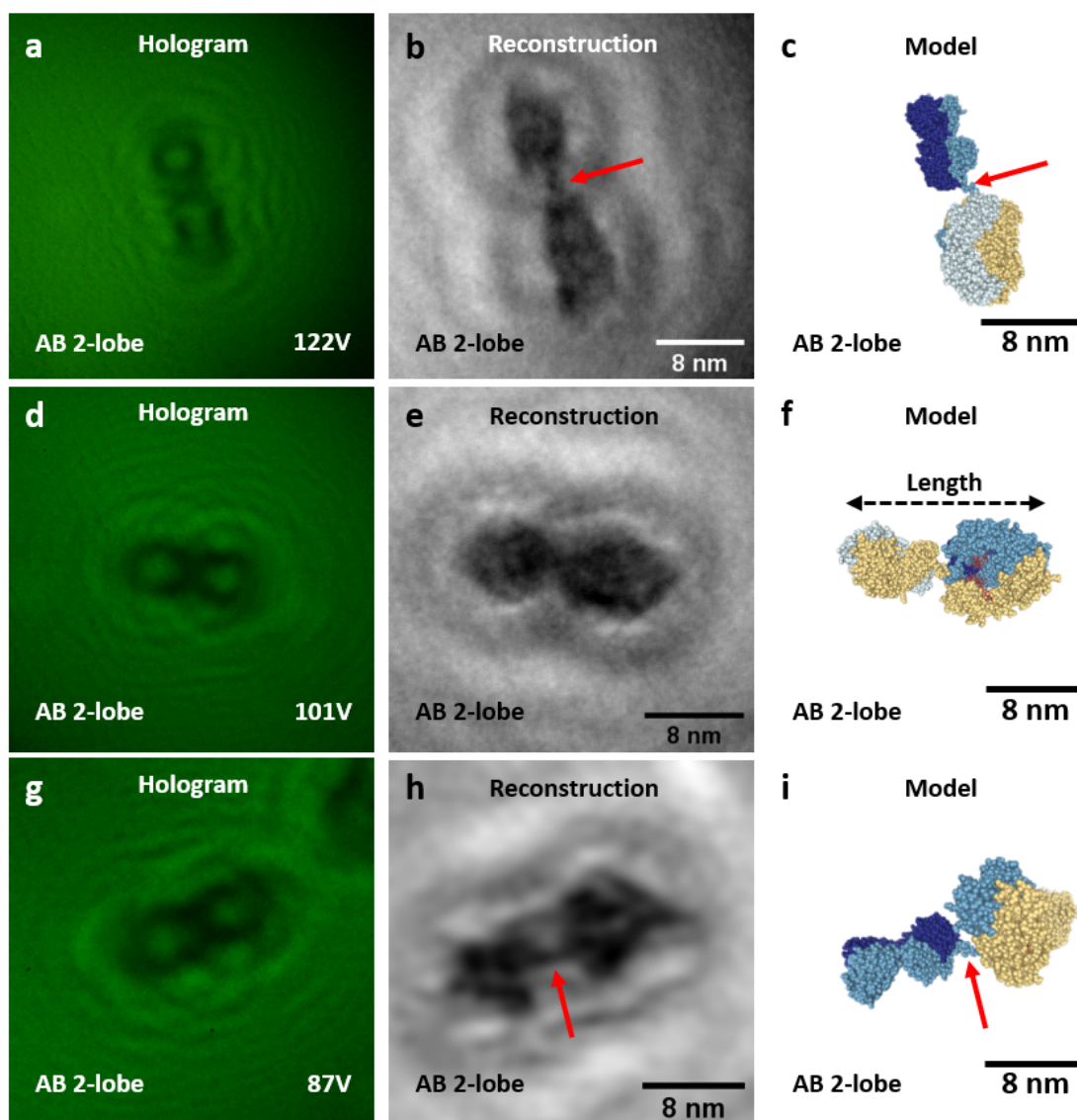


Figure 7.23: LEEH images of *native-like* Herceptin antibodies (AB) deposited on SLG showing the measured holograms (**a**, **d**, **g**) with the used emission voltages reported in the bottom right corner, the respective amplitude reconstructions (**b**, **e**, **h**) and model structures (**c**, **f**, **i**) of three differently oriented example molecules, where each antibody molecule displays two lobes. The model structures are obtained from the RCSB PDB: <https://www.rcsb.org/structure/1IGT>.

However, in the majority of cases, molecules adsorbed in an upright geometry only show two distinguishable subunits while the third one remains eclipsed behind the others as presented in Fig. 7.23. All three of the presented upright molecules show a detailed hinge region, which is especially resolved for the proteins shown in Fig. 7.23 **b** and **h** (marked by red arrows). According to this, the analysis of the images 7.23 **b** and **h** lead to an estimated local resolution of about 6 Å. However, the distinction between Fab and Fc units is debatable for this configuration,

since the third lobe facing upwards from the substrate can influence the contrast of the two adsorbed lobes. In order to avoid any speculation, the subunits are thus not labeled.

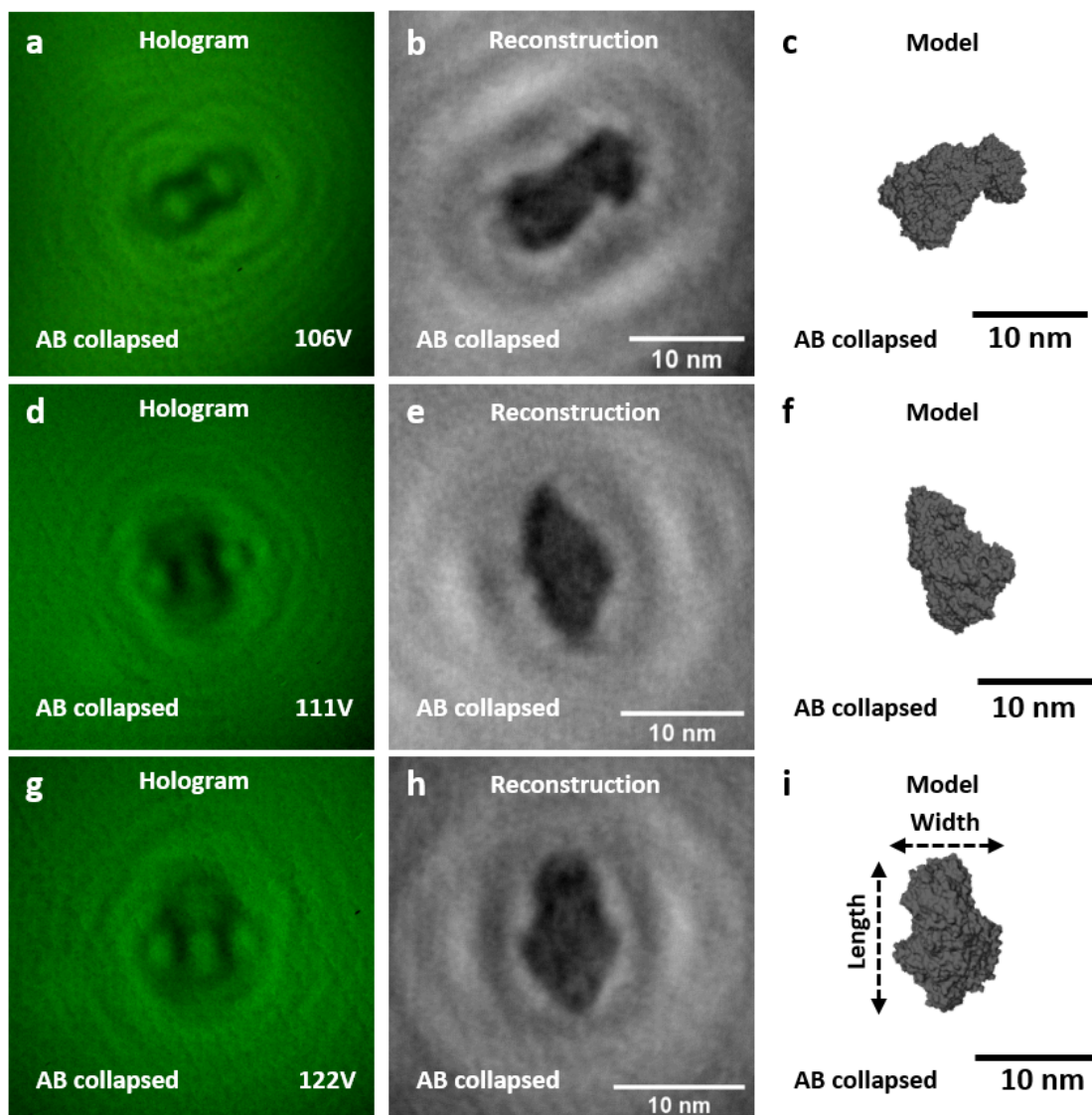


Figure 7.24: LEEH images of *native-like* Herceptin antibodies (AB) deposited on SLG showing the measured holograms (**a**, **d**, **g**) with the used emission voltages reported in the bottom right corner, the respective amplitude reconstructions (**b**, **e**, **h**) and model structures (**c**, **f**, **i**) of three differently oriented example molecules, where each antibody molecule displays a collapsed structure. Individual lobes are not recognizable for the imaged molecules. The model structures are obtained from measurements and simulations conducted by K. Hansen et al. [323].

The different adsorption geometries of antibodies on SLG have been also reported by J. G. Vilhena et al. [58], who showed that two-lobe (upright) structures appear more often than three-lobe (flat) structures using a combined AFM and molecular dynamics approach for AB molecules on HOPG. In our studies, the measured statistics (around 1300 molecules in 8 separate experiments) yield a relative amount of 2% for molecules revealing three lobes

and around 20% for molecules showing two lobes, while the remaining 78% of measured molecules are collapsed structures, see Fig. 7.24 [74].

The images of the three compact shaped molecules, reported here as examples, do not show any identifiable subunits. To clarify their origin, a statistical evaluation of the molecular dimensions was carried out for all the different species, i.e. three-lobe, two-lobe and compact structures. While the evaluation of the total dimensions of three- and two-lobe molecules does not provide useful hints regarding the IgG flexibility, the dimensions of the more rigid subunits confirm the retention of their *native-like* structure after deposition. The measured subunit widths are in the range of 3 – 6 nm, the subunit lengths are in the range of 4 – 7 nm. Both sizes are in good agreement with the expected subunit dimensions obtained from crystallographic model structures. The dimensions of the compact structures are 4–7 nm in width and 6–10 nm in length and are larger than the individual subunits but smaller compared to the extended antibody [74]. These species can originate from the collapsing of AB molecules in the gas phase during the ES-IBD process, as also suggested by gas-phase molecular dynamic investigations of K. Hansen et al. [323]. In particular, comparing their collapsed AB models to our images reveals large similarities in both shape and dimensions, see Fig. 7.24.

We performed ambient AFM measurements on *native-like* AB proteins soft-landed onto HOPG to confirm the presence of these compact structures. In Fig. 7.25 **a, d** and **g**, overview images of three HOPG regions containing AB molecules are shown. The magnified images and height profile plots are displayed in Fig. 7.25 **b, e, h** and **c, f, i**, respectively. The height profiles reveal molecule sizes ranging from 4 – 6 nm, which fits the sizes of single lobes and collapsed structures. While J. G. Vilhena et al. report measured heights of around 3 nm for flat AB species [58], our results are more comparable with the data presented by X. Wang et al., who measured molecular heights of around 5 nm [324]. Regarding the shapes of some individual ABs, it could be possible to identify two-lobe configurations (encircled in white) and probably even three-lobe configurations (encircled in blue). However, the vast majority of the objects resemble individual compact structures as also observed by LEEH imaging.

The adjusted landing energy of the molecular ion beam can affect the amount of compact and extended (two- and three-lobe) AB structures adsorbed on the surface. While only about $11 \pm 2\%$ of the molecules are extended for a landing energy of 0.5 eV/charge, the amount increases to about $22 \pm 4\%$ for an energy of 5 eV/charge and about $33 \pm 3.5\%$ for an energy of 25 eV/charge [74]. This further indicates that the majority of gas-phase conformations are collapsed [323] and that the kinetic energy of the molecules is mostly converted into soft vibrational modes within the molecules, which can lead to conformational changes upon landing, yielding an increased amount of extended structures for higher landing energies [325]. This confirms the assumption that the observed compact AB structures are indeed collapsed molecules.

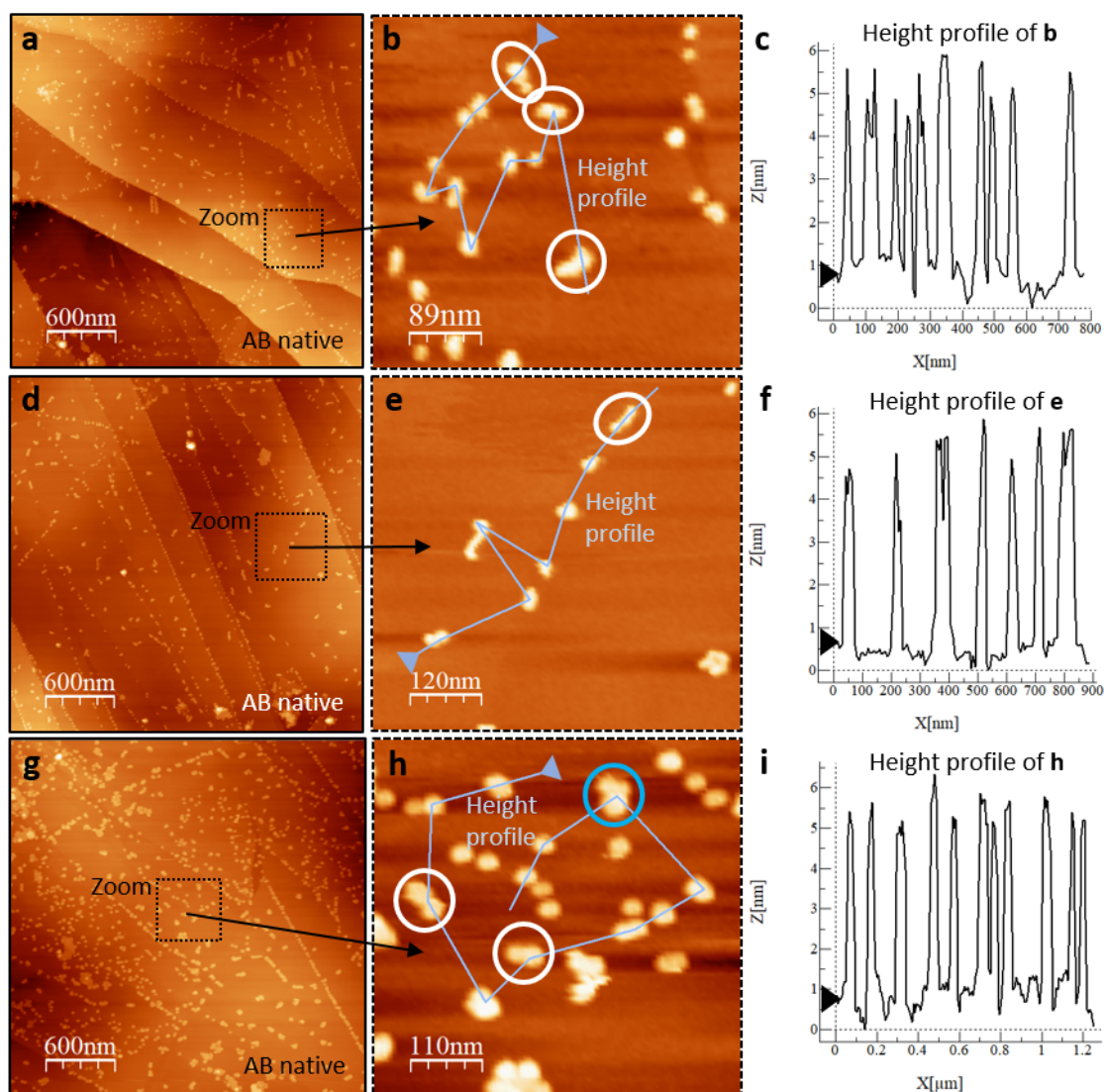


Figure 7.25: AFM images of *native-like* Herceptin antibodies (AB) deposited on HOPG showing overviews of three different sample regions (**a**, **d**, **g**), the respective magnified images containing height profiles (**b**, **e**, **h**) and the height profile plots (**c**, **f**, **i**). Possible two-lobe orientations are marked by a white circle, while the blue encircled molecule in **h** could indicate a three-lobe orientation. Other molecules are most likely collapsed AB structures.

7.3.3 Denatured Herceptin Antibodies

Complementary to *native-like* Herceptin, we investigated denatured AB proteins via LEEH and AFM to gain information about the unfolded structure of these flexible molecules and further underpin the possibilities offered by our experimental methodology to follow the effects induced by the deposition method. In these experiments, the IgG Herceptin antibodies discussed in Sec. 7.3.2 are prepared as described in Sec. 6.1.1 with a final concentration of 1 mg/ml *native-like* AB in 200 mM AmAc. Afterwards, the spray solution is diluted in a 1:1 ratio with ethanol and an amount of 0.3% vol. of formic acid are added subsequently to initiate the

denaturation process [241][242][326]. Typically used parameters for the ESI process of the denatured AB are:

Table 7.10: ESI parameters for a denatured Herceptin antibody ion beam.

c_{Spray}	$T_{\text{capillary}}$	V_{Emitter}	$V_{\text{IonFunnel}}$	$V_{\text{QMS}}^{\text{RF}}$	U/V	Depo charge
1 mg/ml	130°C	+2650 to +2700 V	9 V	150 to 200 V	1.02	7 pAh

Fig. 7.26 shows the mass spectra of the ion beam before (a) and after (b) the quadrupole mass selection (QMS). Before mass selection, broad peaks are visible around 550, 1900, 2200, 2700 (+55), 3300 (+45), 4100 (+36), 4450 (+33), 5150 (+29), 5400 (+28), 6100 (+24) and 6350 (+23) M/z (with the respective estimated charge states). After applying the QMS voltage and U/V value, only broad peaks around 600, 1600, 1950, 2800 (+53) and 4450 (+33) M/z remain. The respective charge states were approximated for an estimated molecular weight of around 149 kDa, which was determined for the *native-like* AB species in Sec. 7.3.2. The mass spectrum of the filtered ion beam suggests a denatured and/or partially folded species [327][328].

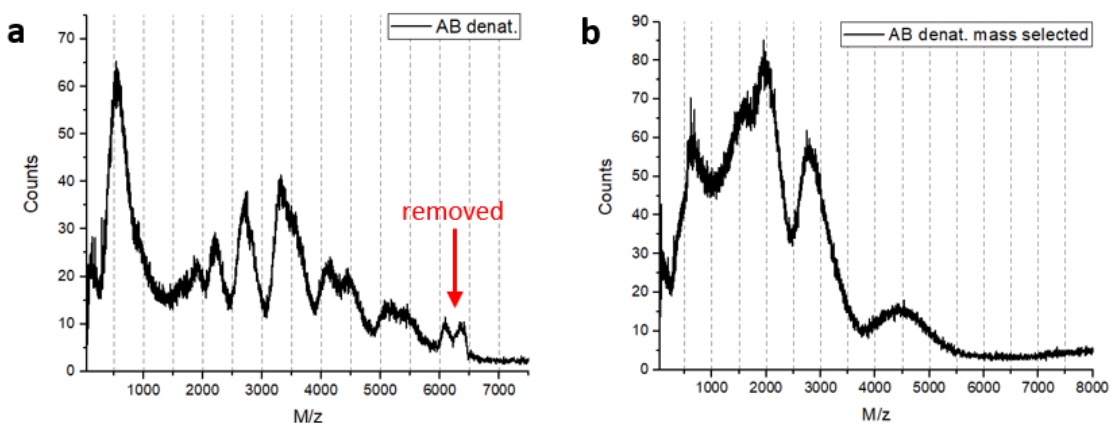


Figure 7.26: Mass spectra of denatured Herceptin antibodies (AB) before (a) and after mass selection (b). Several broad peaks are visible around 547, 1917, 2207, 2710, 3312, 3556, 4115, 4462, 5131, 5399, 6074 and 6354 M/z . The applied mass selection filtered out possibly *native-like* species at M/z values above 5500 and increased the signal amount of unfolded species (below 3000 M/z) significantly.

The selected AB species was soft-landed onto SLG with an energy of 2 eV/charge, subsequently transferred to the LEEH setup and measured via LEEH. In Fig. 7.27 a, b and c, holograms of three molecules are shown. The respective reconstructed amplitude images in Fig. 7.27 d, e and f suggest non-native molecule species. Neither individual lobes, nor compact collapsed structures are visible for the presented examples, which appear relatively elongated and slender. The measured sizes range from widths of around 1.5 – 2 nm to lengths of up to almost 20 nm. The obtained dimensions, shapes and contrast variations within the molecules indicate partially unfolded proteins instead of completely unfolded polypeptide chains. This observation is supported by the structural composition of IgG antibodies, where the respective light and heavy chains are covalently bound via disulfide bridges, which are not affected by the used denaturation method [318]. The estimated local resolution for these samples

is difficult to determine due to the lack of significantly identifiable features. Regarding the displayed images, the smallest visible feature is around $10 - 15 \text{ \AA}$ in size, which in this case can be assumed as an approximation for the imaging resolution range.

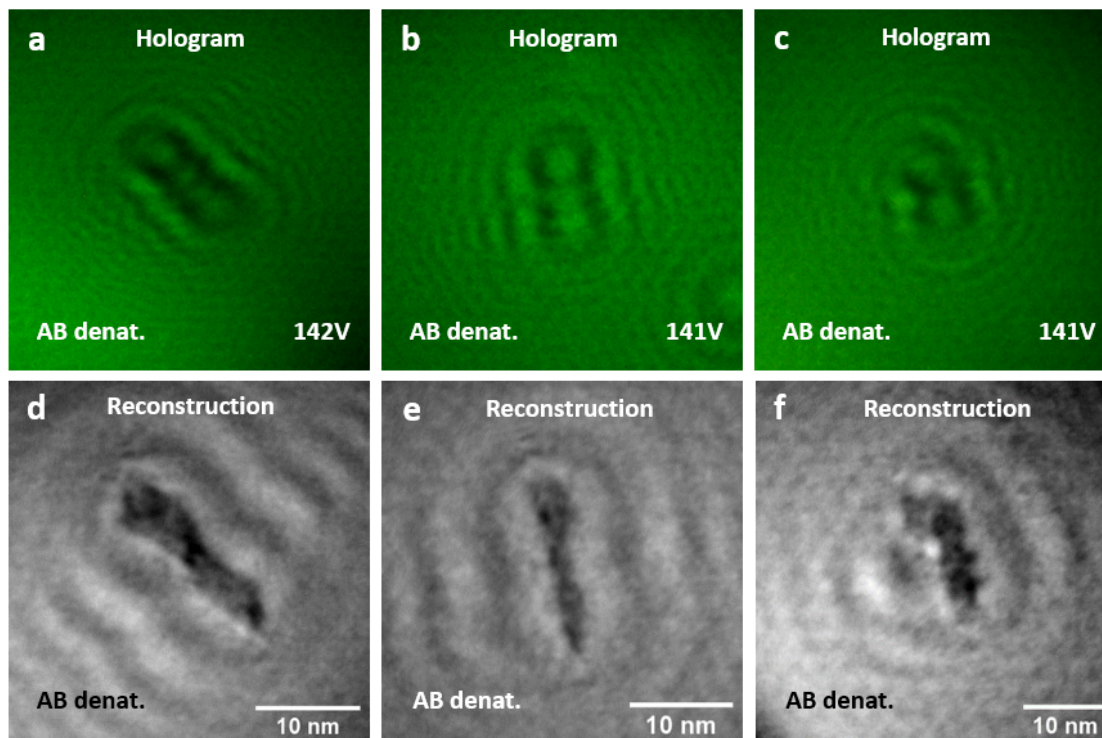


Figure 7.27: LEEH images of denatured Herceptin antibodies (AB) deposited on SLG showing the measured holograms (**a**, **b**, **c**) of three different molecules. The emission voltage used for their imaging is reported in the bottom right corner. The respective amplitude reconstructions are shown in **d**, **e**, **f**. No individual lobes are recognizable and the reconstructed molecules differ from collapsed structures in terms of size and shape.

As for the *native-like* AB proteins, we also performed ambient AFM measurements on the denatured species to compare the dimensions obtained from LEEH to the sizes measured via AFM. Furthermore, these experiments can reveal size differences between *native-like* and denatured Herceptin molecules. The same mass selection was used for the ES-IBD process, however, the deposition amount was reduced to 3 pAh to avoid clusters of the partially unfolded proteins on the used HOPG substrate, since the formation of clusters would alter the measurable heights of the deposited molecules. Fig. 7.28 **a**, **d** and **g** displays overview images of three HOPG regions containing AB molecules. The respective magnified images and height profile plots are shown in Fig. 7.28 **b**, **e**, **h** and **c**, **f**, **i**. The measured height profiles reveal molecular heights ranging from 1.5 – 3.5 nm, which matches the molecular widths obtained from LEEH measurements. When comparing the heights to the AFM data of *native-like* AB proteins (see Fig. 7.25), the resulting size difference of around 0.5 – 4.5 nm shows a significant reduction in the measured heights of the denatured species, which indicates that the deposited molecules are indeed unfolded.

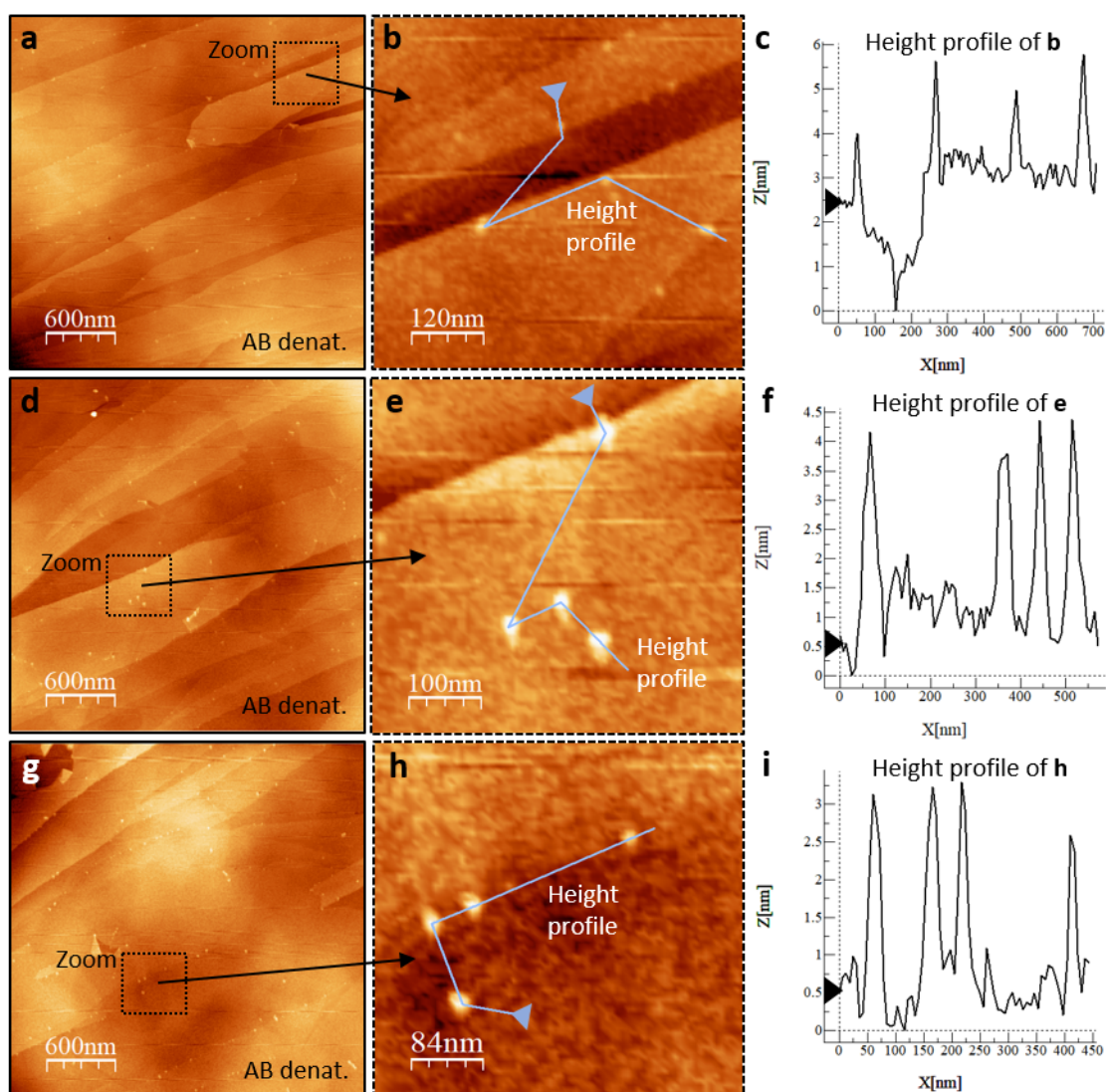


Figure 7.28: AFM images of denatured Herceptin antibodies (AB) deposited on HOPG showing overviews of the three measured areas (**a**, **d**, **g**), the respective magnified images containing height profiles (**b**, **e**, **h**) and the height profile plots (**c**, **f**, **i**).

7.3.4 Discussion on Flexible Protein Complexes

The investigation of flexible protein systems showed that our LEEH instrument is capable of resolving differences in structure and adsorption geometry, which is difficult to determine for individual molecules using other techniques with the obtained resolution. The displayed data indicates a successful ES-IBD and LEEH imaging process of the flexible *native-like* and denatured protein species with local resolutions in the range of 5 – 15 Å. First test measurements of the MAdCAM-Fc complex yielded structures fitting the expected models and reveal subunits of the protein complex, which have to be further investigated (see Sec. 9.6). For the *native-like* AB species, the analyzed results reveal several different adsorption geometries

including three-lobe, two-lobe and compact structures. We found that the compact structures, which constitute the main species observed on the substrate, are collapsed gas-phase configurations of AB molecules [323]. In general, our method allows for the observation of ES-IBD effects on protein structure and can reveal information about their gas-phase conformation. Furthermore, the amount of compact and extended adsorbed ABs can be influenced by the chosen landing energy of the molecular ion beam during the ES-IBD process [74]. Additionally, we are able to clearly distinguish *native-like* and denatured AB proteins in terms of their dimensions and shapes.

7.4 Compact Molecules of Reduced Dimensions

In this section, LEEH data of three different non-protein molecules is shown, which form clusters on the SLG substrate. Sub-monolayers of hemin, phosphotungstic acid (PTA) and platinum phthalocyanine (PtPc) were deposited on individual SLG samples via ES-IBD (hemin, PTA) and thermal evaporation (PtPc), and subsequently imaged in our LEEH microscope showing molecular self-assembly into various structures [329]. The molecular structures of the three systems are shown in Fig. 7.29. These molecules are small compared to the presented proteins and were investigated to test if our LEEH instrument is able to resolve individual units and substructure within the molecules.

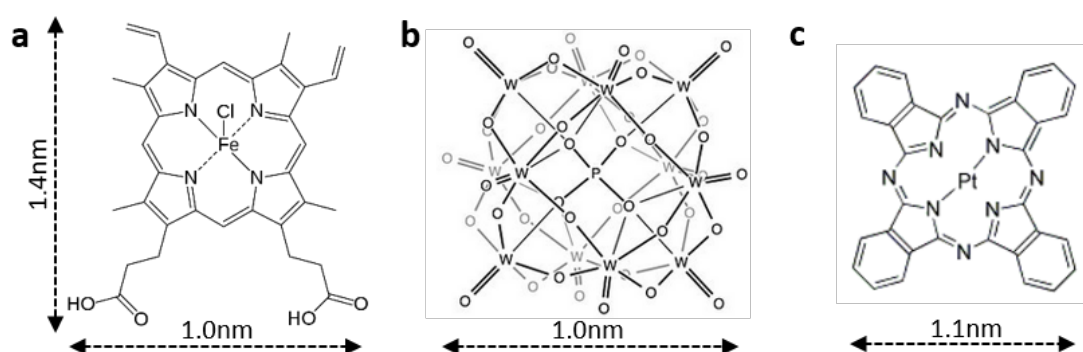


Figure 7.29: Molecular structures of hemin (a), PTA (b) and PtPc (c).

7.4.1 Hemin

Hemin is a protoporphyrin molecule, which binds a ferric ion (Fe^{3+}) and a coordinated chloride as ligands (see Fig. 7.29 a). The chemical formula is $\text{C}_{34}\text{H}_{32}\text{N}_4\text{O}_4\text{FeCl}$ with a molar mass of 652 Da and a molecular size of around 1.0 – 1.4 nm [330]. We used the ES-IBD process for the deposition of this molecule where the spray solution contained 1 mg/ml hemin (16009-13-5, TCI) in acetonitril and 0.3% vol. formic acid. Typically used ESI parameters are shown in Tab. 7.11.

Table 7.11: ESI parameters for a hemin ion beam.

C_{Spray}	$T_{\text{capillary}}$	V_{Emitter}	$V_{\text{IonFunnel}}$	$V_{\text{QMS}}^{\text{RF}}$	U/V	Depo charge
1 mg/ml	70°C	+3400 V	6.2 V	380 V	1.02	10 pAh

In Fig. 7.30, the mass spectra of the ion beam before (a) and after (b) the quadrupole mass selection (QMS) are presented. Before mass selection, peaks at 317, 451, 616.5, 955 and 1270 M/z are visible. While the signal at 616.5 M/z corresponds to a charge state of +1 for hemin without the chloride and the signal at 1270 M/z most likely corresponds to a charge state of +1 for a hemin dimer, where only one chloride is missing [331][332], it is unclear which species are represented by the peaks at 317, 451 and 955 M/z . After applying the QMS voltage and U/V value, the signal at 317 M/z was removed and the signals at 451 and 955 M/z were reduced yielding an ion beam mainly composed of individual hemin molecules without the chloride ligand.

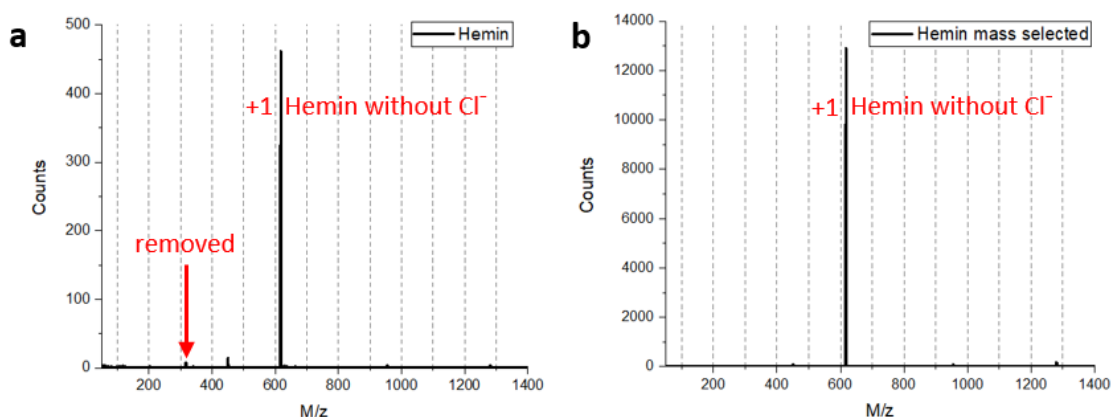


Figure 7.30: Mass spectra of hemin before (a) and after mass selection (b). The peak at 616.5 M/z indicates a hemin species without the chlorine ion with a charge state of +1. The peak at 1270 indicates a hemin cluster, which most likely consists of two heme groups, where one chlorine ion is removed from the complex leading to a charge state of +1. Small peaks at 317, 451 and 955 were either removed or reduced by the mass selection process.

The selected hemin species was deposited onto SLG with an energy of 2 eV/charge and subsequently transferred to the LEEH setup, where it was measured via LEEH. In Fig. 7.31 a, b and c, holograms of example molecules are shown. In Fig. 7.31 d, e and f the respective amplitude reconstructions are displayed, revealing that the measured signals appear to be clusters, where round features with a dark contrast can be distinguished in all three images.

In Fig. 7.31 d and e, five and four molecules are identifiable, respectively, while for panel f it is difficult to determine, if three or four objects are present within the cluster. The measured sizes of the individual features range from around 1.2 – 1.8 nm, which is larger than the expected size for a hemin molecule. Thus, the resolution can only be obtained from the molecular sizes, since no porphyrin substructures are identified, yielding a local resolution of around 12 Å.

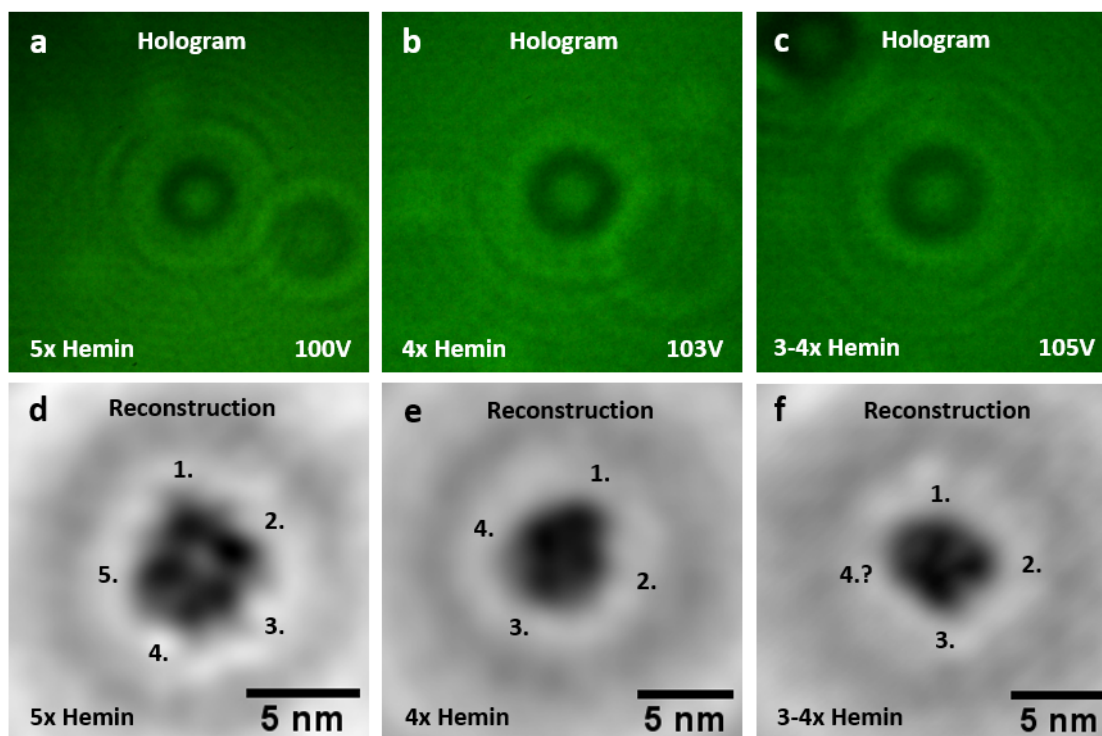


Figure 7.31: LEEH images of hemin clusters deposited on SLG showing the measured holograms (**a**, **b**, **c**) with the used emission voltages reported in the bottom right corner, and the respective amplitude reconstructions (**d**, **e**, **f**) of three example clusters consisting of five (**d**), four (**e**) and three to four individual molecules (**f**).

7.4.2 Phosphotungstic Acid

Phosphotungstic acid (PTA) belongs to the group of polyoxometalates, which are anionic, closed 3D frameworks consisting of several transition metal oxyanions (see Fig. 7.29 **b**) [333]. Its chemical formula is $\text{H}_3\text{PW}_{12}\text{O}_{40}$ and it has a molar mass of 2880 Da with a molecular size of around 1.0 nm [334][335]. Solid PTA (12501-23-4, Sigma) was diluted in acetonitril with a final concentration around 10^{-4} M and subsequently sprayed via ESI using a negative emitter voltage. Typically used ESI parameters are:

Table 7.12: ESI parameters for a phosphotungstic acid ion beam.

c_{Spray}	$T_{\text{capillary}}$	V_{Emitter}	$V_{\text{IonFunnel}}$	$V_{\text{QMS}}^{\text{RF}}$	U/V	Depo charge
1 mg/ml	100°C	-2600 V	9 V	260 V	1.04	10 pAh

The recorded mass spectrum of a PTA ion beam before and after mass selection is shown in Fig. 7.32 **a** and **b**, respectively. The ion beam shows a pure PTA species at 956 M/z , which corresponds to a charge state of -3 [336]. The visible signal did not change during the application of the QMS voltage and U/V ratio (see Tab. 7.12).

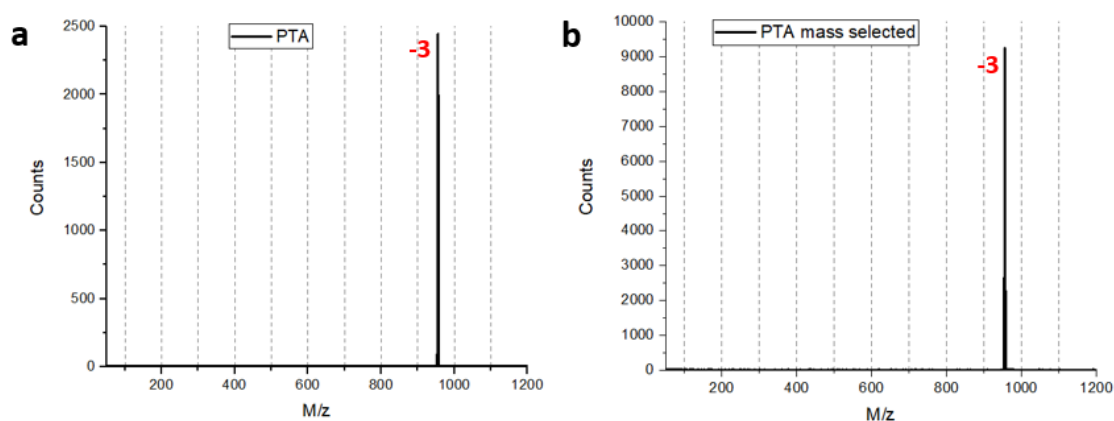


Figure 7.32: Mass spectra of phosphotungstic acid (PTA) before (a) and after mass selection (b). The peak at 956 M/z indicates a PTA species with a charge state of -3.

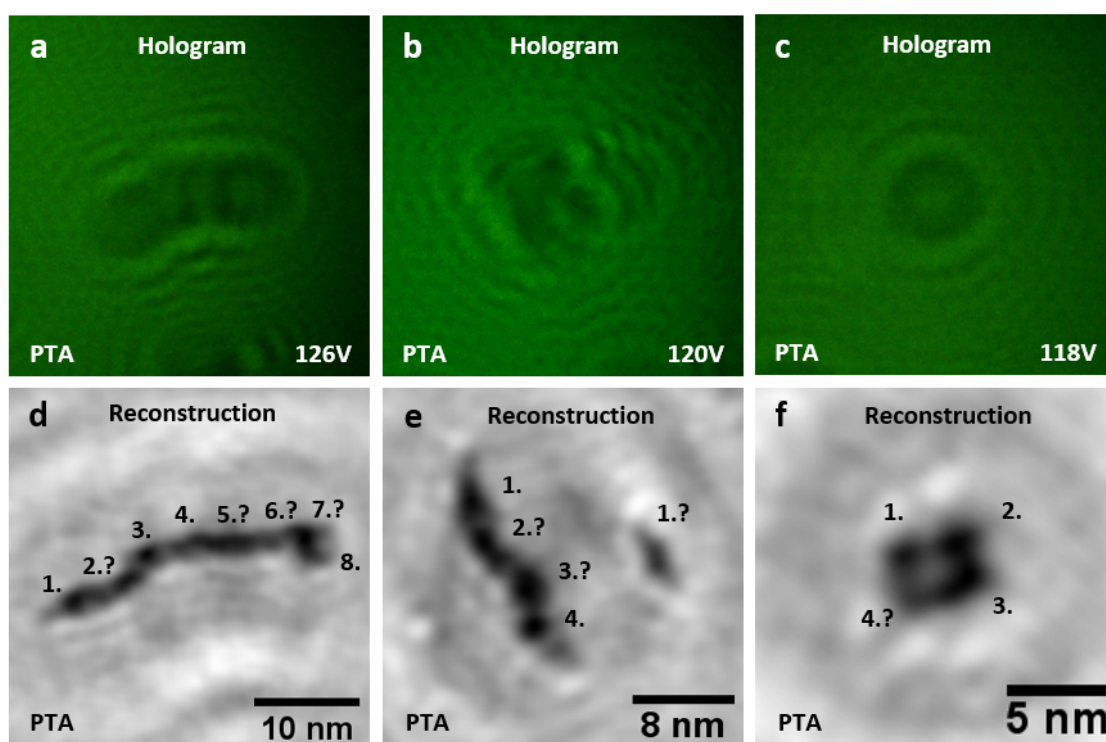


Figure 7.33: LEEH images of phosphotungstic acid (PTA) clusters deposited on SLG showing the measured holograms (a, b, c) with the used emission voltages reported in the bottom right corner, and the respective amplitude reconstructions (d, e, f) of three example clusters consisting of several individual units forming chain-like clusters (d, e) and a small cluster, which is most probably consisting of four individual units (f).

Around 10 pAh of PTA was deposited onto SLG with an energy of 2 eV/charge, transferred to the LEEH setup and measured via LEEH. Three holograms are shown in Fig. 7.33 a, b and c along with their respective amplitude reconstructions (Fig. 7.33 d, e and f), where clusters consisting of several objects are visible. Distinguishing individual molecules within the clusters

is difficult and only darker regions, which are too large to be single molecules, are identifiable. In particular, the dark areas within the clusters have sizes in the range of 1.5 – 2.5 nm, which is around twice the expected size for PTA molecules obtained from the molecular structure.

The smallest recognizable features in the presented images have sizes around 15 Å, which can be assumed as the obtained local resolution limit for the presented data. In **d** and **e**, chain-like clusters with lengths of around 30 nm (**d**) and 14 nm (**e**) can be seen, whereas **f** shows a roughly 5 nm large, rectangular cluster consisting of four subunits. The formation of PTA clusters on SLG has been investigated by TEM measurements yielding clusters of varying size [337], which are partially comparable to our observations by LEEH.

7.4.3 Platinum Phthalocyanine

Platinum phthalocyanine (PtPc, see Fig. 7.29 **c**) is a 2D metal complex containing 18 delocalized π -electrons, which is used in catalysis, photoreactive processes and acts as a pigment with its purple color [338][339]. Its chemical formula is $C_{32}H_{16}N_8Pt$ and it has a molar mass of 707.6 Da with a molecular size of about 1.1 – 1.3 nm.

We deposit PtPc (LT-N219 Lumtec) via thermal evaporation onto our SLG samples (see Sec. 6.2). For this procedure, the OMBE source containing PtPc is first heated to 375°C and kept at this temperature for 36 h to remove contaminants, such as hydrocarbons, which might have adsorbed on the evaporator. The second step is the pre-heating of the source to 435°C for 20 min to stabilize the evaporation temperature. Finally, the thermal evaporation onto the sample takes place at 435°C for around 90 min. After the procedure, the sample is transferred to the LEEH system, where it is imaged via LEEH.

In Fig. 7.34 **a**, **b** and **c**, images of three holograms are displayed. The respective amplitude reconstructions are shown in Fig. 7.34 **d**, **e** and **f**, revealing four clusters, which presumably consist of two to five molecules per cluster. Comparable to the hemin and PTA reconstructions, blob-like objects are visible in the presented images, which have a strong absorption. While in **d** two separated clusters can be seen, **e** and **f** show one cluster.

In general, the shapes of the reconstructed PtPc clusters are similar to the results obtained for hemin. The individual dark objects within the clusters have sizes in the range of 1.6 – 2.8 nm, thus being larger than the expected molecule size of around 1.3 nm for PtPc. The obtainable local resolution for the presented molecules within the clusters is around 16 Å, which is twice as high as the standard local resolution obtained for most protein samples presented in this work.

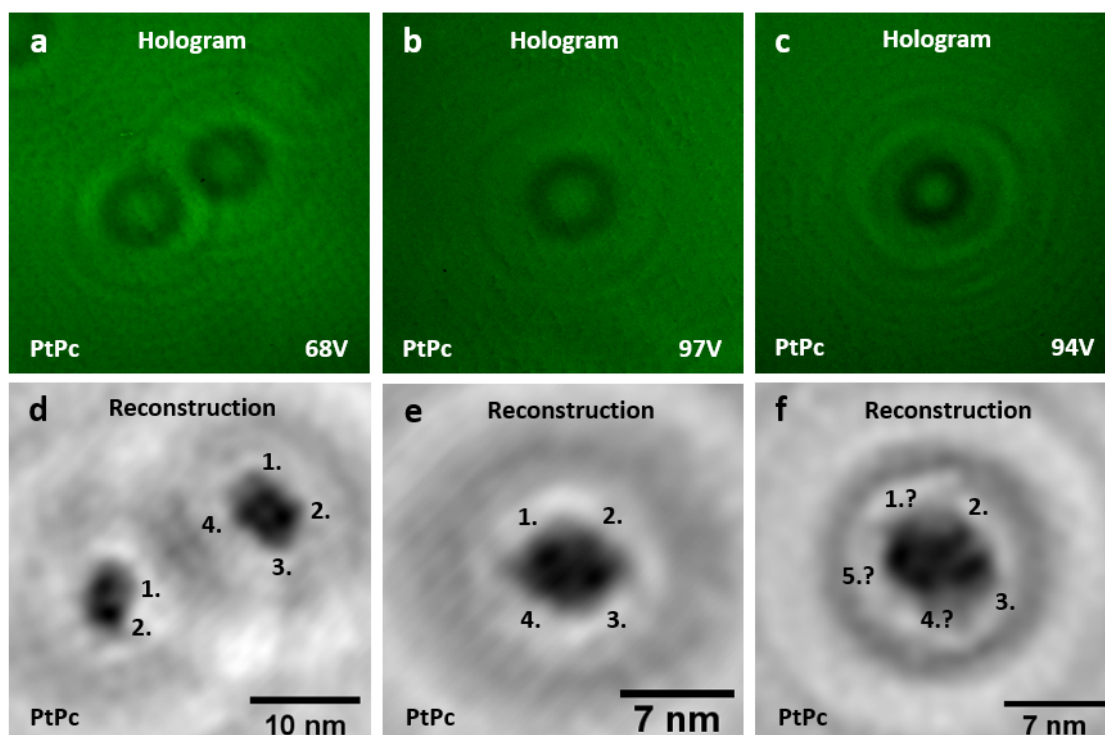


Figure 7.34: LEEH images of platinum phthalocyanine (PtPc) clusters deposited on SLG showing the measured holograms (**a**, **b**, **c**) with the used emission voltages reported in the bottom right corner, and the respective amplitude reconstructions (**d**, **e**, **f**) of three example images. **d** shows two clusters consisting of two and four objects. **e** and **f** show a single cluster each, which consists of four and presumably five molecules, respectively.

7.4.4 Discussion on Compact Molecule Systems

The presented first steps towards the investigation of different small molecular systems via LEEH showed the formation of nanometer sized molecule clusters on the SLG substrate, which exhibit a high imaging contrast. The cluster formation could originate from the landing process during deposition, when the kinetic energy of the individual molecules is converted to translational movement on the substrate and/or intrinsic molecular diffusion on the surface at room temperature [48]. In both cases, individually deposited molecules move on the surface and get in contact with other moving molecules or they get immobilized on a charge, defect and/or step edge (e.g. at an SLG-BLG interface). During measurements, neither individual molecules, nor molecular movement were observed, indicating that the clustering happens upon deposition and that the clusters are stable. The cluster formation makes the investigation of individual molecules challenging, as shown in the presented results. The amplitude reconstructions of recognizable subunits within these clusters are larger in size compared to the expected model structure dimensions and the estimated local resolutions obtained from LEEH measurements of these relatively small objects are within the range of 12 – 16 Å, which is larger than the typically achieved local resolutions of measured protein systems. A possibility to reduce the clustering can be the molecule deposition on a cold sample, including

a low temperature sample transfer and measurement, which could improve the obtainable resolution for acquired images of these molecular systems.

7.5 Proteins Measured at Cryogenic Temperatures

As shown in Sec. 4.2.2.2 and 4.2.6.2, the emitter performance in terms of emission stability improved when measuring at low temperature [72]. Additionally, a cold sample reduces the number of excited modes of the substrate [70] and deposited molecules [71], which can compromise the formation of fine fringes in the hologram. Thus, we used the novel Cryo-LEEH microscope head (Sec. 3.2) to conduct preliminary test measurements on two large protein systems, namely beta-galactosidase (β Gal) and GroEL.

Both protein systems were prepared and soft-landed onto SLG via the native ES-IBD method using the already mentioned mass selection and deposition parameters (β Gal: Tab. 7.6; GroEL: Tab. 7.7). While the deposition procedure took place at room temperature, the samples, as well as the emitters, were cooled down to a stable temperature of about 50 K before starting the LEEH measurements.

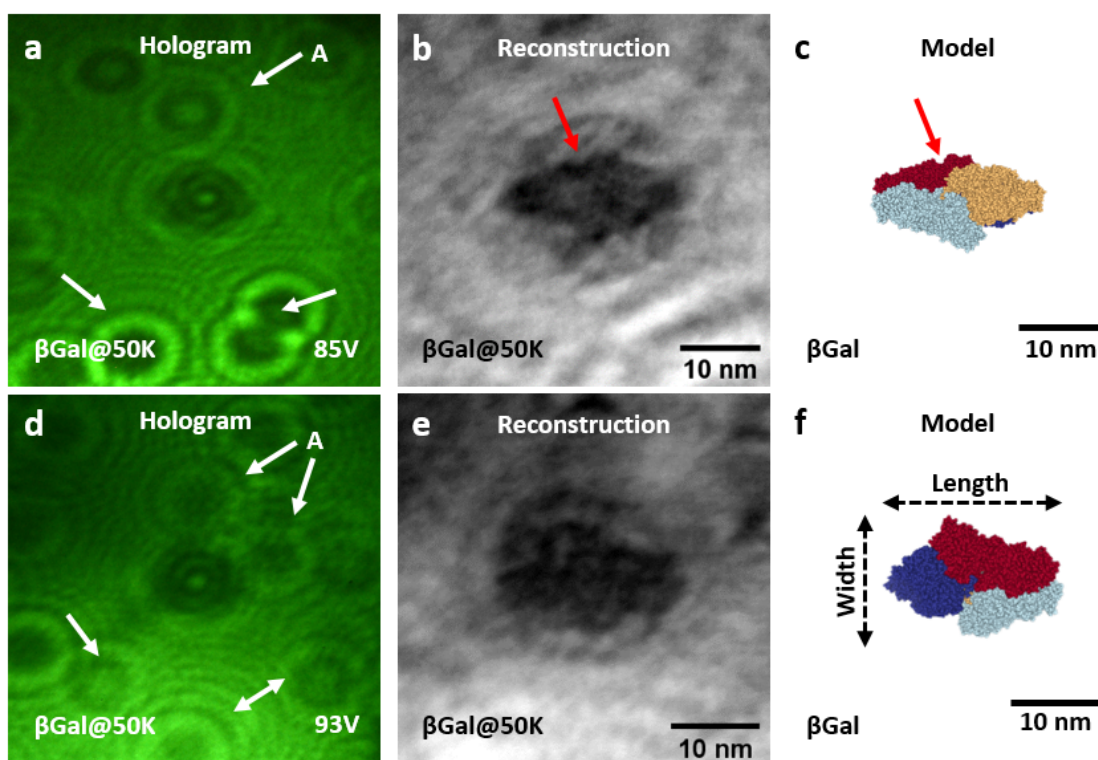


Figure 7.35: LEEH images of *native-like* beta-galactosidase (β Gal) deposited on SLG and measured at 50 K showing the measured holograms (**a**, **d**) with the used emission voltages reported in the bottom right corner, the respective amplitude reconstructions (**b**, **e**) and model structures (**c**, **f**) of two differently oriented example molecules. Contaminating adsorbates (A) are marked by white arrows. The model structures are obtained from the RCSB PDB: <https://www.rcsb.org/structure/6CVM>.

In Fig. 7.35, the measured holograms (**a**, **d**) and amplitude reconstructions (**b**, **e**) of two β Gal molecules are presented. The holograms show a large number of fringes around the molecules, however, the adsorbates nearby (*A*, marked by white arrows) cover them partially. Using the structure 6CVM from the RCSB PDB, the observed reconstructions can be reproduced, as shown in Fig. 7.35 **c** and **f**. Width and length of the reconstructed proteins match the expected dimensions from the model. Furthermore, the contrast differences in Fig. 7.35 **b** convincingly show distinguishable subunits when compared to the model structure. Both reconstructions show ring-shaped signals around the molecules, which originate from the twin-image (see Sec. 2.1). The smallest recognizable feature is the 8 Å sized cavity visible in Fig. 7.35 **b** (marked by the red arrow) yielding an estimated local resolution of about 8 Å for this image, which is comparable to the local resolution obtained from images at room temperature (see Sec. 7.2.3).

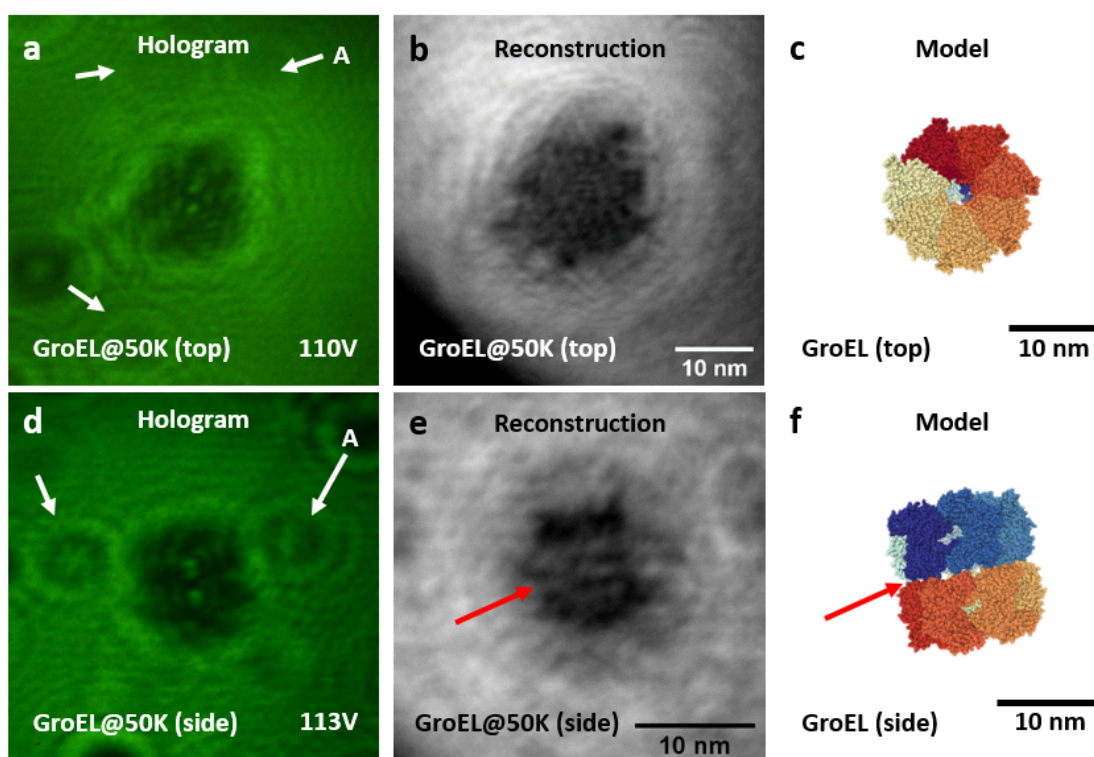


Figure 7.36: LEEH images of *native-like* GroEL deposited on SLG and measured at 50 K showing the measured holograms (**a**, **d**) with the used emission voltages reported in the bottom right corner, the respective amplitude reconstructions (**b**, **e**) and model structures (**c**, **f**) of two differently oriented example molecules. While the GroEL molecule is showing a top view configuration, the bottom molecule is oriented in a side view configuration. Contaminating adsorbates (*A*) are marked by white arrows. The model structures are obtained from the RCSB PDB: <https://www.rcsb.org/structure/1MNF>.

Measured holograms of two GroEL molecules are shown in Fig. 7.36 **a** and **d** with the respective amplitude reconstructions **b** and **e**. The holograms show a large amount of fringes, which are partially covered by adsorbates (*A*, marked by white arrows). The reconstructions reveal different adsorption geometries for the presented proteins, where the molecule in Fig. 7.36 **b** resembles a top view and the molecule in Fig. 7.36 **e** resembles a side view configuration. Both

reconstructions can be reproduced with respectively oriented models of the structure *1MNF* from the RCSB PDB, as shown in Fig. 7.36 **c** and **f**.

The dimensions of the top view GroEL molecule shown in Fig. 7.36 **b** are about 14 nm in diameter, which matches the expected size obtained from the model structure. However, no hole is visible in the protein center and the molecule shape is difficult to interpret, which indicates a tilted and/or slightly collapsed configuration. The side view molecule presented in Fig. 7.36 **e** only has a width of about 10 nm, which is smaller than the expected size for GroEL and most likely due to a collapsed structure as discussed for the measurements conducted at room temperature (Sec. 7.2.4). The smallest identifiable feature is the gap between the two heptameric rings, which has a size of about 10 – 11 Å and is visible in Fig. 7.36 **e** (marked by the red arrow). Thus, the obtained local resolution for this image can be estimated to about 10 Å, which matches the local resolution obtained from the GroEL images measured at room temperature (see Sec. 7.2.4). Furthermore, it is important to mention that the obtained contrast for these reconstructions is improved, leading to better defined shapes when compared to the reconstructions measured at room temperature. This could be due to the improved emission quality of the emitter at low temperatures, which can yield a higher coherence of the electron beam and thus better resolvable fringes in the hologram.

In general, the Cryo-LEEH setup performs well and yields promising data. A direct comparison of molecules measured at RT and LT is difficult, since the emitter performance changes upon cooling. The holograms of both beta-galactosidase and GroEL measured at 50 K result in amplitude reconstructions, which yield comparable local resolutions as the measurements at room temperature, even for a higher emission stability and a large amount of fine hologram fringes obtained at low temperatures. As visible in the hologram images, this could be due to the increased amount of contaminations around the measured molecules, which compromise the visibility of fringes in certain positions and thus, also negatively impact the achievable resolution of the reconstructions. For this reason, we will soon add cooling shields to the Cryo-LEEH system, which act as an additional cryotrap and should reduce the adsorption of contaminants on the sample. A drawing of the shields, which are currently under construction, is presented in Sec. 9.1. Nevertheless, these first test experiments suggest that LEEH measurements at low temperatures can in principle improve the hologram quality and lead to resolutions which are closer to the theoretically achievable limit.

8 Conclusion

The goal of this work was to build a high-performance LEEH microscope with an optimized measurement routine, which is capable of measuring various complex molecule systems at resolutions close to the experimentally achievable imaging limits of the technique.

Starting from an empty measurement box within the precision laboratory at the beginning of this project, I presented a newly constructed and vibration-isolated LEEH microscope, which is operating at magnifications up to 10^6 in UHV conditions. The setup is a completely unique and highly flexible system, which offers the necessary emitter characterization and preparation possibilities and has various storage units, as well as an efficient emitter and sample transfer via its load locks and the UHV suitcase. The efficient detection system and self-programmed remote control software complete the setup. The recent installation of the Cryo-LEEH microscope enables us to conduct LEEH measurements at cryogenic temperatures, which is a novel development yielding promising results.

I established optimized preparation and characterization protocols yielding ultra-clean free-standing SLG substrate and sharp tungsten tips, which enable the emission of coherent low-energy electrons. Furthermore, I explored a novel emitter functionalization method, which involves the controlled uptake of SLG by the emitter apex to improve its emission quality. The native ES-IBD procedure is a reliable, controlled and contamination-free deposition method capable of soft-landing various complex molecule systems onto our substrate. These techniques, combined with the presented measurement process, hologram detection, image reconstruction and data analysis, result in a unique, reliable and efficient experimental workflow, which allows our setup to go beyond what has already been reported by different LEEH experiments.

The presented data shows that our microscope setup is indeed capable of answering scientific questions by measuring a variety of molecular systems on the single-molecule level at local resolutions of up to 5\AA , which surpasses the capabilities of other LEEH instruments reported in the literature. This allows for the investigation of individual, highly complex and flexible

Chapter 8. Conclusion

proteins like Herceptin antibodies, where our measurements revealed different adsorption geometries upon deposition and confirmed the presence of collapsed structures originating from the gas phase of the ES-IBD process. The high-resolution imaging of these gas-phase structures is of high relevance for the investigation and understanding of the gas-phase conformation of molecules. By collecting a plethora of individual antibody structures in many experiments, we gained novel insights into the statistical distribution of the deposited species and how they are affected by changes in the landing energy.

The preliminary measurements of beta-galactosidase and GroEL at cryogenic temperatures show that the imaging performance of our setup can be further improved beyond the so far obtained resolution limit, although the initial goal of a resolution below 3 Å, i.e. atomic resolution, has yet to be achieved. Therefore, in the following Chap. 9, I present several possible improvements for our technique, which could eventually enable our instrument to resolve structural details on the atomic scale.

9 Outlook

This chapter contains information about upcoming developments for our experimental setup, as well as for our reconstruction method and analysis. As pointed out during the thesis and summarized in the conclusion, a few aspects of our experimental setup can be improved in order to achieve the ultimate resolution possible with our LEEH microscope. In the following, I thus report the design of the cooling shields for the Cryo-LEEH microscope head and the planned implementation of Helmholtz coils for an increased control over the illumination area of the electron beam and to remove possible effects originating from stray magnetic fields. I briefly report on a novel ESI source capable of delivering a high molecular ion beam flux after applying a mass and ion mobility filtering, which is specifically designed to be directly connected to our LEEH system and thus allows for a direct deposition on a low temperature substrate. Preliminary data obtained from a phase reconstruction algorithm are also presented, and the possibility for tomographic LEEH measurements via the installed rotation stage is discussed. Additionally, I suggest further interesting molecular systems measurable via LEEH.

9.1 Cryoholography

So far, the installation of the Cryo-LEEH setup (see Sec. 3.2) enables measurements at temperatures as low as 50 K at both the sample and tip position if helium is used as cooling agent. The cooling of the electron emitter improves its emission performance in terms of stability, as shown in Sec. 4.2.2.2 (Fig. 4.9 and 4.10), and amount of obtainable fringes in the hologram, see Sec. 4.2.6.2 (Fig. 4.22). However, we observed sample contamination during the cooling and imaging procedure at low temperatures (see Sec. 5.2.2.8 Fig. 5.10 and Sec. 7.5) due to the cold parts acting as a cryotrap.

To circumvent these issues, we are going to install additional cooling shields, which cover the microscope head as shown in Fig. 9.1 **b**. These shields are an additional isolation for heat radiation, thus allowing for lower measurement temperatures at the tip and sample holder positions. Furthermore, their large surface area can trap a large amount of possible

contaminants within the UHV chamber and decrease the amount of particles adsorbing on the sample while cooling. The first parts are already under construction and the installation and testing of the shields is planned for the upcoming months.

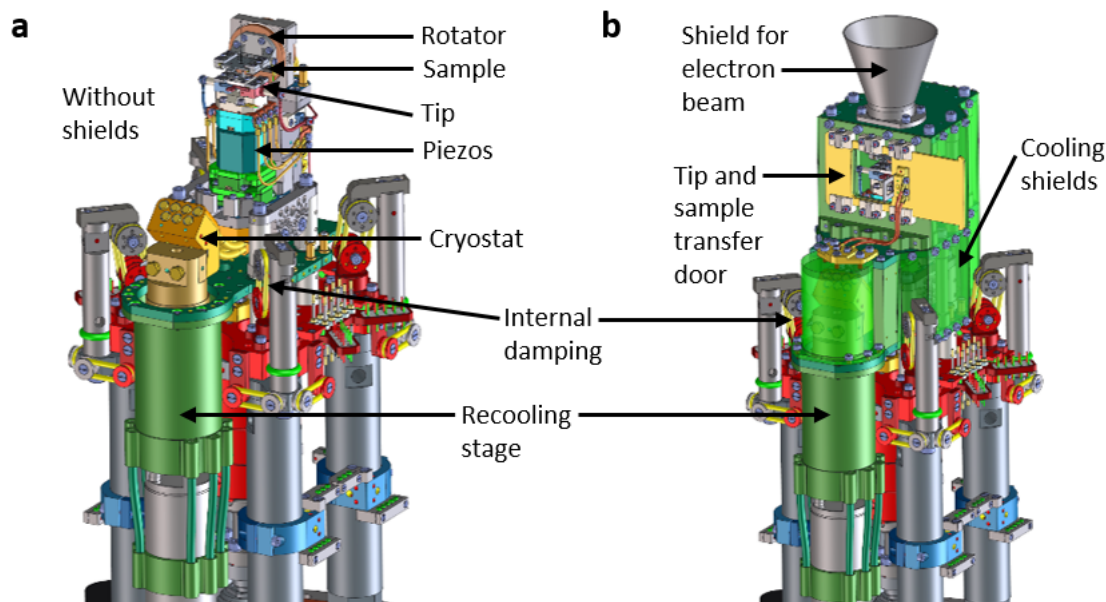


Figure 9.1: Schematic showing the Cryo-LEEH system without **a** and with cooling shields **b** (colored in light green). The installation also includes a shielding door for the tip and sample transfer (colored in yellow) and an extra shield for the electron beam (colored in gray).

9.2 Compensation of Stray Magnetic Fields

Due to their low energies, the emitted electrons used for imaging in LEEH are susceptible to stray magnetic fields, which can cause distortions in the resulting holograms. These stray fields can originate from magnetized setup parts, which are positioned in close proximity to the microscope head. Although great care was taken in terms of used materials while constructing the assembly, it is very difficult to completely avoid any sort of magnetization of certain parts. For example, the cold cathode pressure sensors contain a strong magnet, which can influence the electron beam directly and also magnetize other metallic parts in their proximity over time.

A possibility to protect the electron beam from stray magnetic fields is the use of μ -metal shields, which could screen the expanding beam along the axis towards the detector, which is a distance of about 11 cm [340][341]. Since all parts of the microscope head itself are non-magnetic with the exception of the currently used thermocouple sensors, these shields could be added to the system by attaching thin μ -metal plates or foils on top of the cooling shields. This could prevent the influence of stray magnetic fields originating from magnetized chamber parts, which would act on the electron beam upon leaving the microscope head. The slightly magnetized thermocouples, which are currently attached to the microscope head to track

its temperatures while cooling, will be removed in the upcoming design and replaced by non-magnetic diode sensors.

Another issue is the exact trajectory and width of the beam opening angle, which is formed when electrons are emitted from the source. While usually being directed towards the detector, the beam trajectories vary depending on the tip apex and can also be tilted, as discussed in Sec. 4.2.6.3, resulting in an illumination area, which is partly or even completely outside the detector area. This leads to a cut off hologram signal and thus less resolvable fringes around the object, which compromises the quality of the reconstructed images.

This issue can be tackled using Helmholtz coils, which consist of two independent, parallel positioned and usually circular coils with an identical radius and number of windings in a certain distance to each other. When passing a current through the wire coils, a magnetic field is generated, which is tunable and homogenous within a finite volume between both coils and can compensate other stray fields and/or influence an electron beam within the affected volume [104][106]. Depending on the applied current I , the amount of windings N , the coil radius R and the adjusted distance d between the coils, the magnetic flux density $\vec{B}(z)$ at a position z between the coils can be calculated via [105][342]:

$$\vec{B}(z) = \frac{\mu_0 N I}{2} \left(\frac{R^2}{\left(R^2 + \left(z - \frac{d}{2}\right)^2\right)^{\frac{3}{2}}} + \frac{R^2}{\left(R^2 + \left(z + \frac{d}{2}\right)^2\right)^{\frac{3}{2}}} \right) \vec{e}_z \xrightarrow[z=0]{d=R} \vec{B}(0) = \frac{8\mu_0 N I}{\sqrt{125}R} \vec{e}_z \quad (9.1)$$

We are currently constructing a pair of Helmholtz coils, which will be positioned in one direction along the chamber axis with the LEEH microscope in between the coils, as shown in Fig. 9.2. After installation, the influence of the coils on the electron beam, which will be possible in one direction so far, has to be investigated and the used parameters, which include the number of windings N and the used current I , have to be calibrated. With well-adjusted settings, the coils should be able to steer a tilted electron beam towards the detector center, which could improve the quality of the recorded holograms.

Furthermore, the homogeneous field generated by the Helmholtz coils can be used to compensate inhomogeneous stray magnetic fields affecting the electron beam within a small volume in close proximity to the emission source. Combined with the μ -metal shields, these installations can improve the electron beam quality and its incident position on the detector, ultimately increasing the quality of the observed holograms.

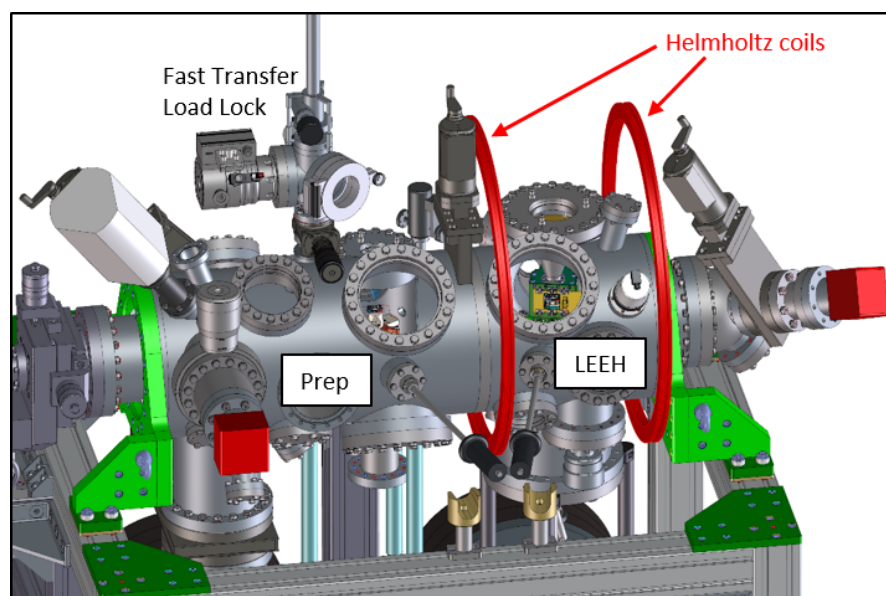


Figure 9.2: Schematic showing the planned positioning of a Helmholtz coil pair (colored in red) surrounding the LEEH microscope, which will allow to steer the electron beam in one direction.

9.3 Novel ESI Source

Our experimental workflow includes sample transfer steps to other setups for the deposition of molecules onto the SLG substrate. While the sample is kept in UHV conditions throughout the procedure, the possibility to directly deposit molecules within our LEEH setup is appealing for two reasons: First, the venting and consequent pumping of the respective transfer load locks usually takes at least 8 hours to reach an acceptable pressure range for the transfer through each load lock. A direct deposition within the LEEH setup would save time and allow for sample imaging shortly after the deposition took place. Second, the deposition on a cold sample would be much more convenient without the need for a low-temperature suitcase transfer. This way, the molecules could be directly landed onto a cooled SLG substrate, which could lead to less diffusion and/or conformational changes upon impact. This can be useful for the investigation of small molecules, which tend to form clusters on the surface (see Sec. 7.4) and/or flexible molecules, which show conformational changes depending on their landing energy (see Sec. 7.3.2).

We are currently constructing a novel ESI source, which can be directly connected to the preparation chamber (Prep) of our LEEH setup (see Fig. 9.3 a). We would use our manipulator, which can be cooled and modified to measure the current flow of landing molecule ions, as sample holder for the deposition process. This new ESI setup consists of an ESI part (colored in purple in Fig. 9.3) containing ion optics, quadrupole mass filters, an ion mobility filter, a supporting frame, and a connection chamber (colored in yellow in Fig. 9.3), which guides the ion beam towards the LEEH Prep chamber. The design and construction of this compact setup has been a complex task carried in a joint effort with Paul Fremdling (Oxford University).

This new source is designed for being capable of delivering a high flux of *native-like* proteins within the ion beam and will improve the flexibility and capabilities of our LEEH technique.

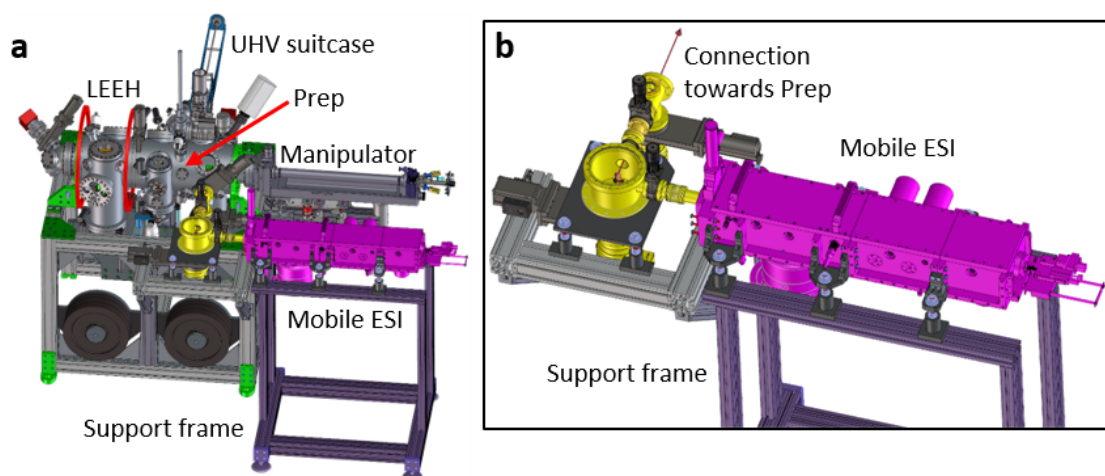


Figure 9.3: **a** Schematic showing the planned mobile ESI (colored in purple) connected to the LEEH setup. **b** Zoom in of the mobile ESI (colored in purple) and connection part (colored in yellow) towards the preparation chamber (Prep) of the LEEH setup.

9.4 Phase Retrieval

In general, the holograms contain amplitude and phase information [20]. In this work, I have presented amplitude reconstructions for our data analysis, since the phase information is lost during the reconstruction process due to the ambiguity of its sign, as discussed in Sec. 2.1. However, by using an iterative phase reconstruction algorithm, the phase information can be retrieved, as shown by T. Latychevskaia et al. [228][343].

We employed an iterative phase reconstruction algorithm for our holograms, which yields phase signals within the respectively reconstructed molecules, as shown for three example hemoglobin (Hb) molecules in Fig. 9.4. As shown in the thesis of Hannah Ochner [79], we examined and analyzed the phase reconstruction data of several different molecules. However, the interpretation of this data is far from trivial and additional efforts on the experimental and theoretical level are required. Nevertheless, the identification of the phase signal could open novel opportunities for the characterization of complex molecule systems.

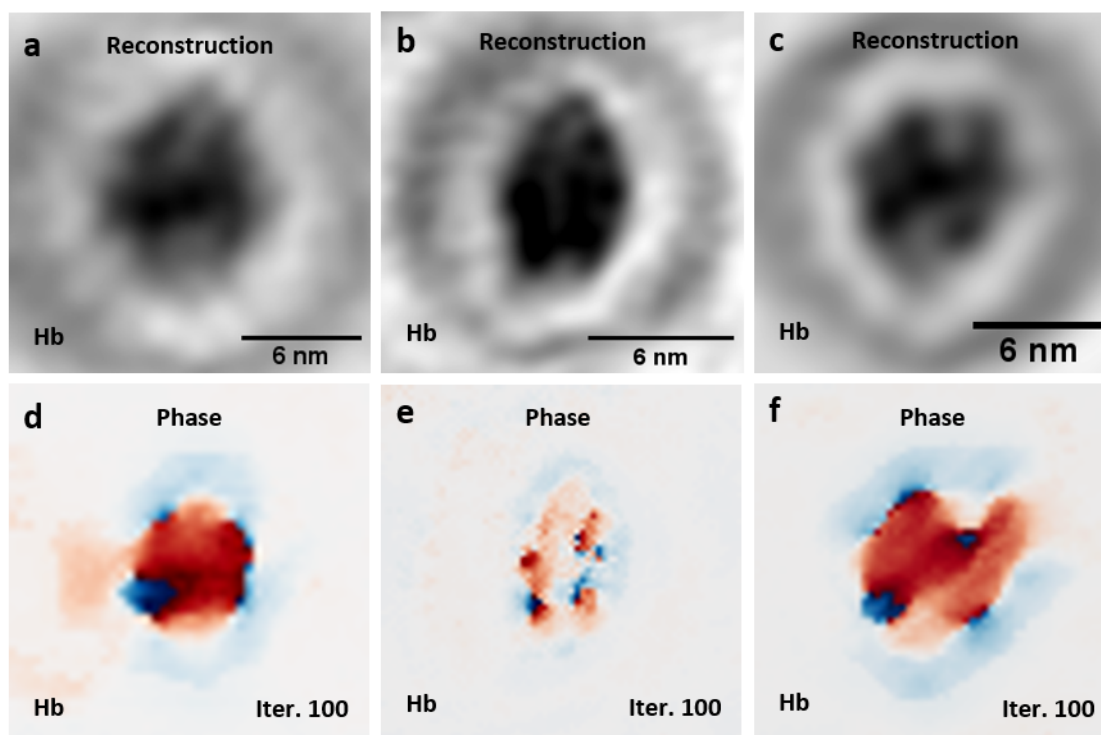


Figure 9.4: Phase reconstructions of *native-like* hemoglobin (Hb) imaged via LEEH showing the amplitude reconstructions (**a**, **b**, **c**) and the respective iterated phase reconstructions (**d**, **e**, **f**) after 100 iteration steps of the three example molecules from Fig. 7.6. Each molecule shows four separate spots (colored in dark blue) indicating phase shifts within the molecule.

9.5 3D Imaging

A multitude of interesting molecular systems, such as folded proteins, possess a 3D structure. Thus, 3D information of the imaged molecule is necessary to fully understand its structural and functional details. This is usually achieved by imaging many different molecules, which are oriented in various geometries on the sample. Fitting the different measured conformations to respective orientation angles and combining these results can lead to a 3D image of the averaged molecular species [344]. However, this method does not work properly for molecular systems, which have inherent conformational differences, such as flexible proteins. While this approach can be used in LEEH, holography in principle already yields 3D information by preserving amplitude and phase information within each individually imaged hologram [108][345], whereby the 3D information has to be reconstructed, e.g. by using deconvolution algorithms [107]. However, these reconstruction methods are computationally demanding and their efficiency for 3D objects remain to be explored.

Another technical possibility to gain 3D information about a single imaged object is tomography, which is widely applied in high-resolution microscopy techniques, such as Cryo-TEM [346][347][348]. We recently implemented a piezo-rotation stage in our Cryo-LEEH microscope head, as shown in Fig. 9.5, which enables tomography of individual molecule systems

via rotation of the sample in one direction. The stage has still to be properly calibrated and tested, but allows for rotation angles of more than 20° per side. We are indeed planning a measurement routine, where the target molecule can be imaged from various sample angles. This will be the first step towards tomographic LEEH measurements allowing us to gain direct information about the three-dimensional structure of the deposited molecules on the single-molecule level.

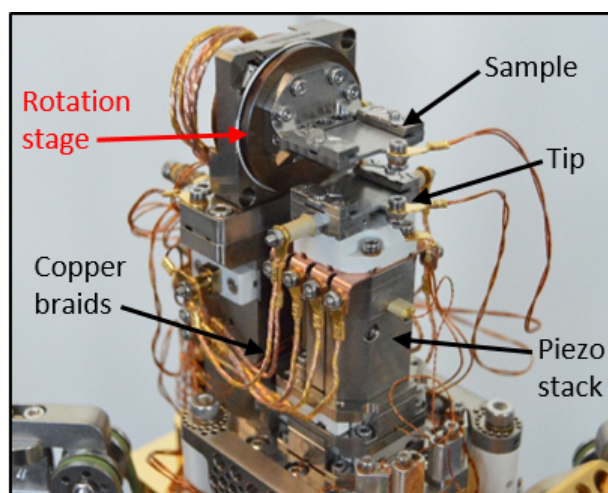


Figure 9.5: Photo of the Cryo-LEEHead including the rotational stage (marked by the red arrow), which can be used for tomographic-like experiments by tilting the sample.

9.6 Measurable systems

In the previous sections, I have shown that our LEEH microscope is capable of investigating a multitude of molecular systems. However, the results obtained from the small, non-protein molecules are still inconclusive regarding the measured sizes and undefined structures (see Sec. 7.4). For this reason, we want to further investigate these and similar systems, such as other porphyrin-based molecules [349], with our improved Cryo-LEEHead microscope head by measuring the molecules at low temperatures. We also consider to deposit these systems on a cold sample with the aim of reducing their clustering behaviour. Furthermore, we are planning to use 3D DNA origami structures with defined sizes [350] as test systems for our setup, which can be used for calibration experiments in 2D and probably even 3D, when using our rotation stage for tomographic experiments. Regarding flexible proteins, we want to continue the investigation of different MAdCAM complexes (see Sec. 7.3.1), for example MAdCAM-integrin ($\alpha_4\beta_7$) or MAdCAM-L-selectin [316], which is of medical relevance for the identification of molecular mechanisms leading to the development of inflammatory bowel disease [315]. Finally, we will remeasure some of the presented protein systems at cryogenic temperatures after installing the cooling shields to prevent sample contaminations, which could lead to an improved image quality of the measured holograms and thus increase the experimentally obtainable resolution.

A Appendix

High-quality CNT images of the emitter comparison analysis presented in Sec. 4.2.6.1:

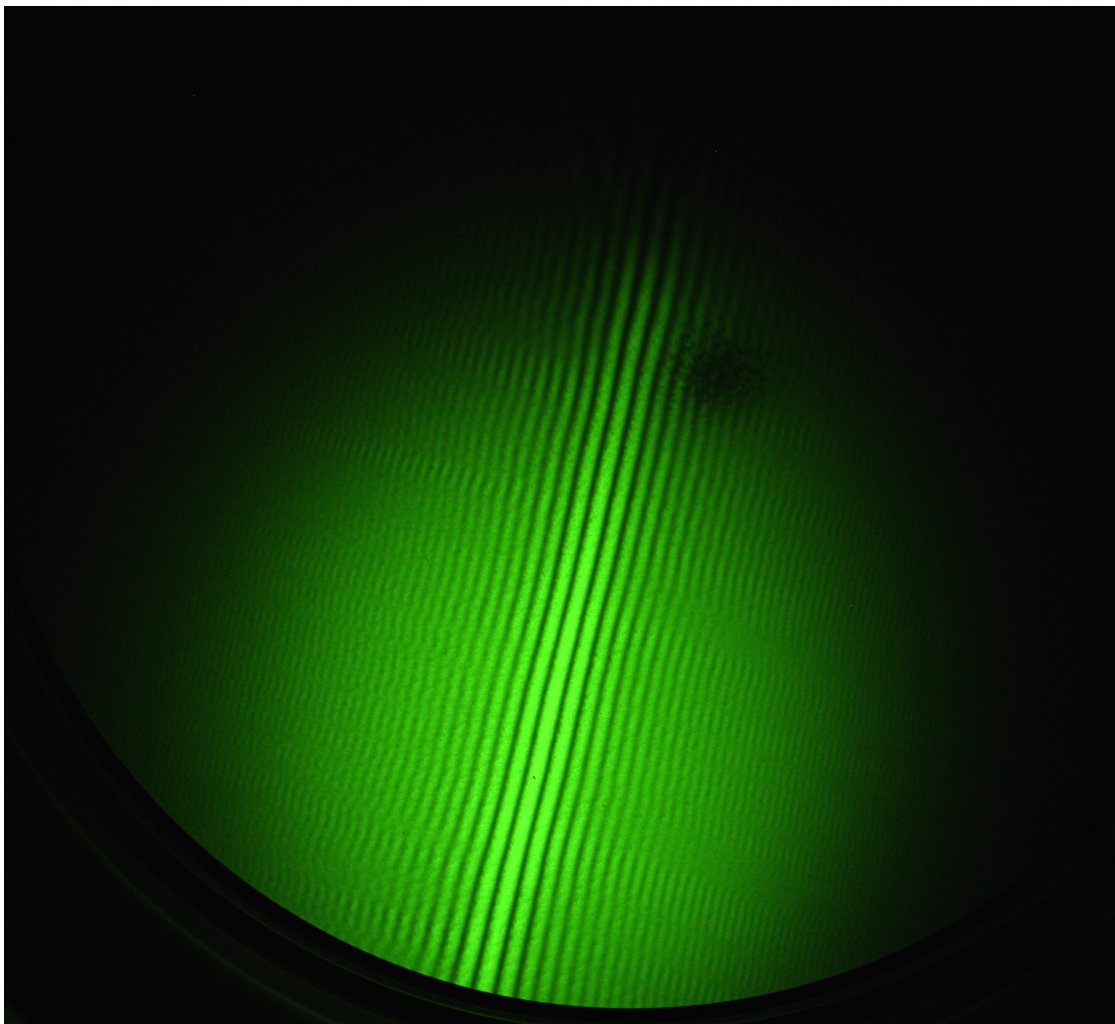


Figure A.1: Non-compressed image of the CNT measured via *scI*. The field emission voltage was 72 V.

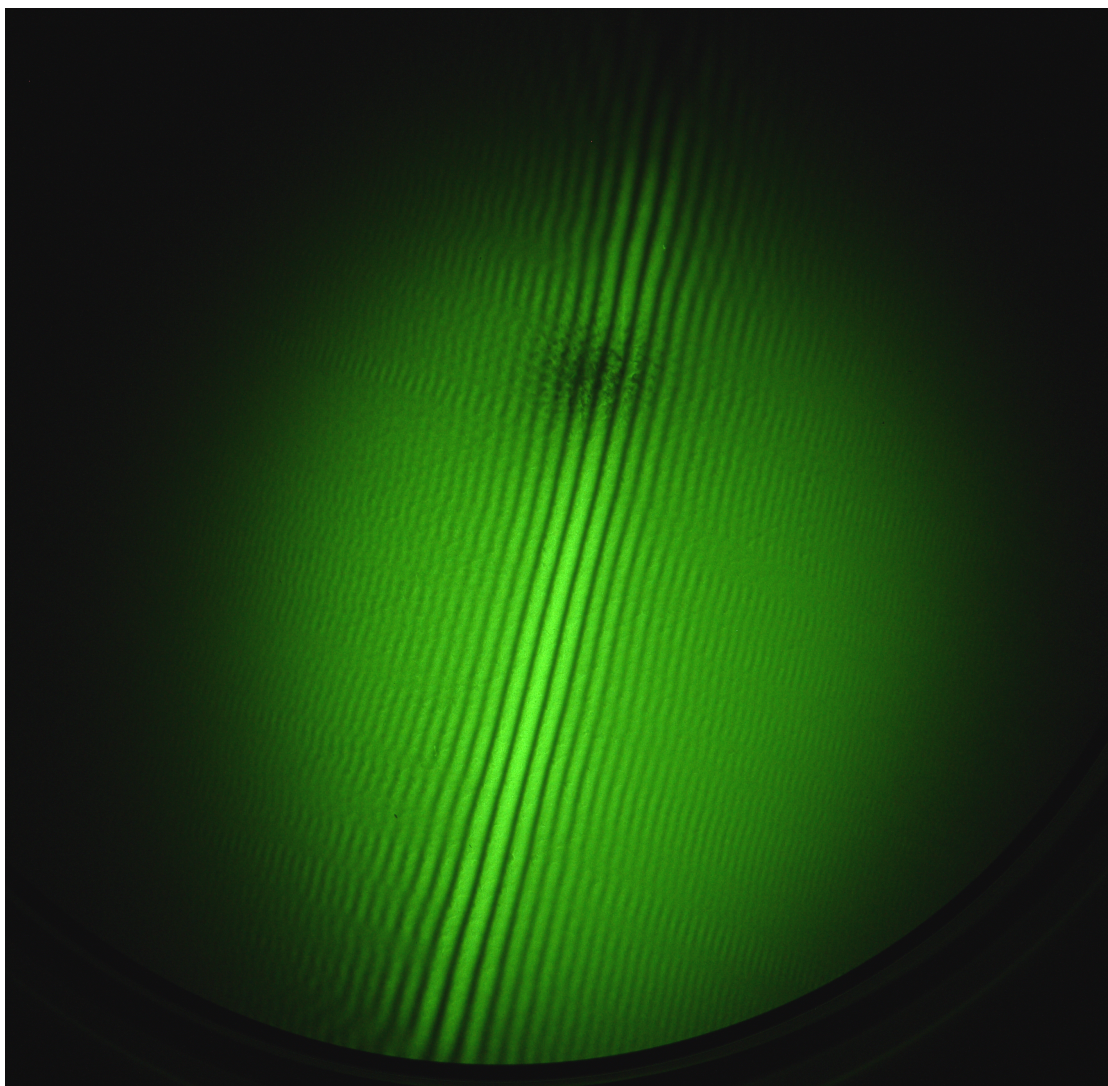


Figure A.2: Non-compressed image of the CNT measured via *sc2*. The field emission voltage was 77 V.

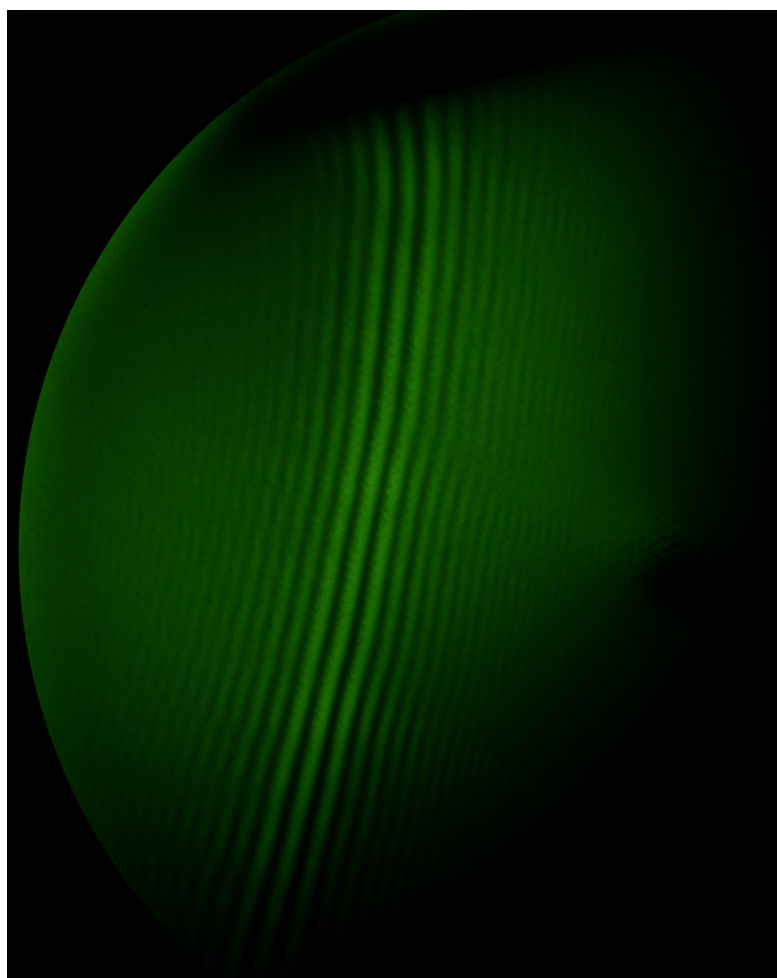


Figure A.3: Non-compressed image of the CNT measured via *sc3*. The field emission voltage was 54 V.

High-quality CNT images of the emitter comparison analysis at RT and LT presented in Sec. 4.2.6.2:

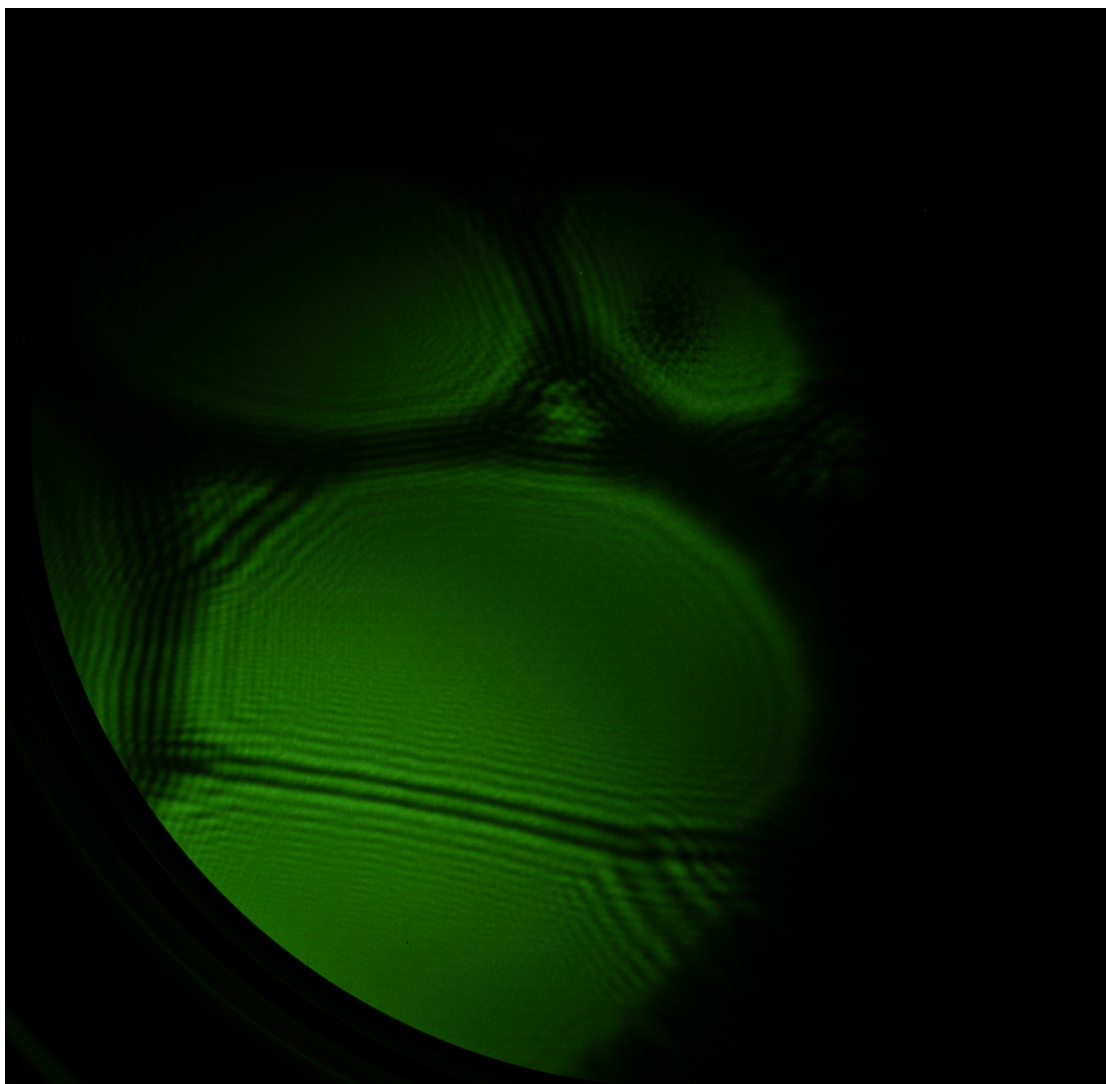


Figure A.4: Non-compressed image of the CNT measured at RT. The field emission voltage was 92 V.

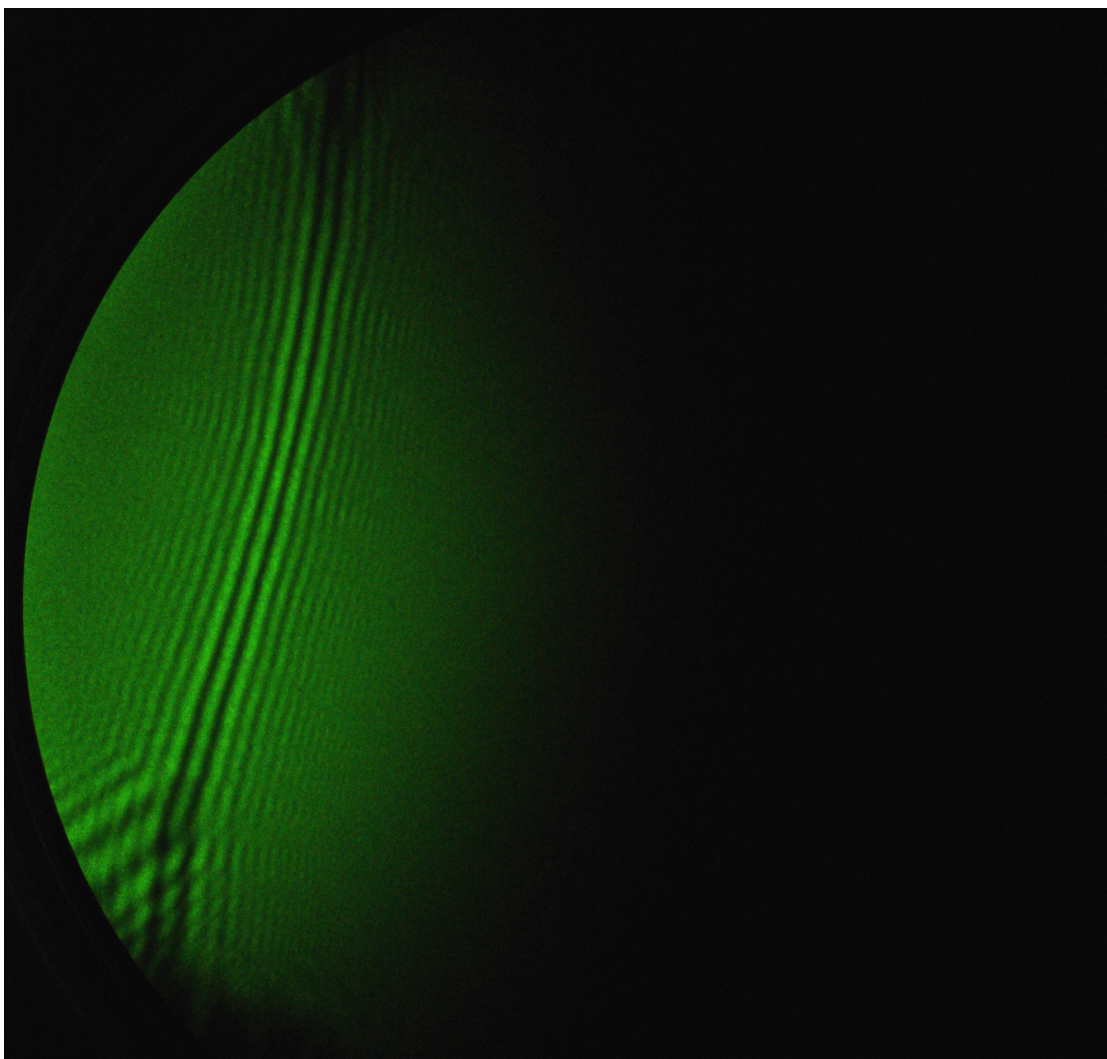


Figure A.5: Non-compressed image of the CNT measured at LT. The field emission voltage was 73 V.

Bibliography

- [1] Peter W Hawkes and John CH Spence. *Science of microscopy*, volume 1. Springer, 2007.
- [2] Florian Schueder, Juanita Lara-Gutiérrez, Brian J Beliveau, Sinem K Saka, Hiroshi M Sasaki, Johannes B Woehrstein, Maximilian T Strauss, Heinrich Grabmayr, Peng Yin, and Ralf Jungmann. Multiplexed 3d super-resolution imaging of whole cells using spinning disk confocal microscopy and dna-paint. *Nature communications*, 8(1):1–9, 2017.
- [3] Anna-Karin Gustavsson, Petar N Petrov, and WE Moerner. Light sheet approaches for improved precision in 3d localization-based super-resolution imaging in mammalian cells. *Optics express*, 26(10):13122–13147, 2018.
- [4] Yicong Wu, Xiaofei Han, Yijun Su, Melissa Glidewell, Jonathan S Daniels, Jiamin Liu, Titas Sengupta, Ivan Rey-Suarez, Robert Fischer, Akshay Patel, et al. Multiview confocal super-resolution microscopy. *Nature*, pages 1–6, 2021.
- [5] Eva Rittweger, Kyu Young Han, Scott E Irvine, Christian Eggeling, and Stefan W Hell. Sted microscopy reveals crystal colour centres with nanometric resolution. *Nature Photonics*, 3(3):144–147, 2009.
- [6] Alexey N Butkevich, Gyuzel Yu Mitronova, Sven C Sidenstein, Jessica L Klocke, Dirk Kamin, Dirk NH Meineke, Elisa D’Este, Philip-Tobias Kraemer, Johann G Danzl, Vladimir N Belov, et al. Fluorescent rhodamines and fluorogenic carbopyronines for super-resolution sted microscopy in living cells. *Angewandte Chemie International Edition*, 55(10):3290–3294, 2016.
- [7] Paolo Bianchini, Chiara Peres, Michele Oneto, Silvia Galiani, Giuseppe Vicidomini, and Alberto Diaspro. Sted nanoscopy: a glimpse into the future. *Cell and tissue research*, 360(1):143–150, 2015.
- [8] Eric Betzig, Stefan W Hell, and William E Moerner. The nobel prize in chemistry 2014. *Nobel Media AB*, 2014.
- [9] Gerd Binnig, Heinrich Rohrer, Ch Gerber, and Edmund Weibel. Surface studies by scanning tunneling microscopy. *Physical review letters*, 49(1):57, 1982.
- [10] Friedrich Lenz. Towards atomic resolution. In *Advances in Imaging and Electron Physics*, volume 96, pages 791–803. Elsevier, 1996.
- [11] Gerd Binnig and Heinrich Rohrer. In touch with atoms. *More Things in Heaven and Earth*, pages 543–554, 1999.
- [12] Gerd Binnig and Heinrich Rohrer. Scanning tunneling microscopy. *IBM Journal of research and development*, 44(1/2):279, 2000.

Bibliography

- [13] Ernst Ruska. The development of the electron microscope and of electron microscopy. *Bioscience reports*, 7(8):607–629, 1987.
- [14] Ewen Callaway. The revolution will not be crystallized: a new method sweeps through structural biology. *Nature News*, 525(7568):172, 2015.
- [15] Stefan Raunser. Cryo-em revolutionizes the structure determination of biomolecules. *Angewandte Chemie International Edition*, 56(52):16450–16452, 2017.
- [16] Ewen Callaway. Revolutionary cryo-em is taking over structural biology. *Nature*, 578(7794):201–202, 2020.
- [17] GA Morton and EG Ramberg. Point projector electron microscope. *Physical Review*, 56(7):705, 1939.
- [18] Veronica Granata. The davisson–germer experiment. *Modern Physics*, pages 15–1, 2020.
- [19] Dennis Gabor. A new microscopic principle. *nature*, 161:777–778, 1948.
- [20] Dennis Gabor. Microscopy by reconstructed wave-fronts. *Proceedings of the Royal Society of London. Series A. Mathematical and Physical Sciences*, 197(1051):454–487, 1949.
- [21] Edgar Völkl, Lawrence F Allard, and David C Joy. *Introduction to electron holography*. Springer Science & Business Media, 1999.
- [22] A Götzhäuser, B Völkel, B Jäger, M Zharnikov, HJ Kreuzer, and M Grunze. Holographic imaging of macromolecules. *Journal of Vacuum Science & Technology A: Vacuum, Surfaces, and Films*, 16(5):3025–3028, 1998.
- [23] Erwin W Muller. Field ion microscopy. *Principles and Applications*, 1969.
- [24] AJ Melmed and J Smit. Field-ion transmission microscopy. *Journal of Physics E: Scientific Instruments*, 12(5):355, 1979.
- [25] Werner Stocker, Hans-Werner Fink, and Roger Morin. Low-energy electron and ion projection microscopy. *Ultramicroscopy*, 31(4):379–384, 1989.
- [26] Hans-Werner Fink. Coherent point source electron beams. *Journal of Vacuum Science & Technology B: Microelectronics and Nanometer Structures*, 8(6):1323, nov 1990. doi: 10.1116/1.584911.
- [27] Gerd Binnig, Heinrich Rohrer, Ch Gerber, and Eddie Weibel. Tunneling through a controllable vacuum gap. *Applied Physics Letters*, 40(2):178–180, 1982.
- [28] Hans-Werner Fink, Werner Stocker, and Heinz Schmid. Holography with low-energy electrons. *Physical review letters*, 65(10):1204, 1990.
- [29] HJ Kreuzer, K Nakamura, A Wierzbicki, H-W Fink, and H Schmid. Theory of the point source electron microscope. *ultramicroscopy*, 45(3-4):381–403, 1992.
- [30] JCH Spence, W Qian, and MP Silverman. Electron source brightness and degeneracy from fresnel fringes in field emission point projection microscopy. *Journal of Vacuum Science & Technology A: Vacuum, Surfaces, and Films*, 12(2):542–547, 1994.
- [31] MP Silverman, Wayne Strange, and JCH Spence. The brightest beam in science: new directions in electron microscopy and interferometry. *American Journal of Physics*, 63(9):800–813, 1995.
- [32] A Götzhäuser, B Völkel, M Grunze, and HJ Kreuzer. Optimization of the low energy

- electron point source microscope: imaging of macromolecules. *Micron*, 33(3):241–255, 2002.
- [33] Hans-Werner Fink, Heinz Schmid, Eugen Ermantraut, and Torsten Schulz. Electron holography of individual dna molecules. *JOSA A*, 14(9):2168–2172, 1997.
- [34] Andreas Eisele, Berthold Völkel, Michael Grunze, and Armin Götzhäuser. Nanometer resolution holography with the low energy electron point source microscope. *Zeitschrift für Physikalische Chemie*, 222(5-6):779–787, 2008.
- [35] Matthias Germann, Tatiana Latychevskaia, Conrad Escher, and Hans-Werner Fink. Nondestructive imaging of individual biomolecules. *Physical Review Letters*, 104(9):095501, 2010.
- [36] Jean-Nicolas Longchamp, Tatiana Latychevskaia, Conrad Escher, and Hans-Werner Fink. Low-energy electron transmission imaging of clusters on free-standing graphene. *Applied Physics Letters*, 101(11):113117, 2012.
- [37] M Prigent and P Morin. Charge effect in point projection images of carbon fibres. *Journal of microscopy*, 199(3):197–207, 2000.
- [38] Shouh Hwang, Che-Cheng Chang, Chien-Hung Lu, Shih-Chin Liu, Yuan-Chih Chang, Ting-Kuo Lee, Horng-Tay Jeng, Hong-Shi Kuo, Chun-Yueh Lin, Chia-Seng Chang, et al. Investigation of single-walled carbon nanotubes with a low-energy electron point projection microscope. *New Journal of Physics*, 15(4):043015, 2013.
- [39] Josh Y Mutus, Lucian Livadaru, Radovan Urban, Jason Pitters, A Peter Legg, Mark H Salomons, Martin Cloutier, and Robert A Wolkow. Nanoscale structuring of tungsten tip yields most coherent electron point-source. *New Journal of Physics*, 15(7):073038, 2013.
- [40] Konstantin S Novoselov and AK Geim. The rise of graphene. *Nat. Mater*, 6(3):183–191, 2007.
- [41] JY Mutus, L Livadaru, JT Robinson, R Urban, MH Salomons, M Cloutier, and RA Wolkow. Low-energy electron point projection microscopy of suspended graphene, the ultimate ‘microscope slide’. *New Journal of Physics*, 13(6):063011, 2011.
- [42] Tim J. Booth, Peter Blake, Rahul R. Nair, Da Jiang, Ernie W. Hill, Ursel Bangert, Andrew Bleloch, Mhairsi Gass, Kostya S. Novoselov, M. I. Katsnelson, and A. K. Geim. Macroscopic graphene membranes and their extraordinary stiffness. *Nano Letters*, 8(8):2442–2446, jul 2008. doi: 10.1021/nl801412y.
- [43] Deji Akinwande, Christopher J. Brennan, J. Scott Bunch, Philip Egberts, Jonathan R. Felts, Huajian Gao, Rui Huang, Joon-Seok Kim, Teng Li, Yao Li, Kenneth M. Liechti, Nanshu Lu, Harold S. Park, Evan J. Reed, Peng Wang, Boris I. Yakobson, Teng Zhang, Yong-Wei Zhang, Yao Zhou, and Yong Zhu. A review on mechanics and mechanical properties of 2d materials—graphene and beyond. *Extreme Mechanics Letters*, 13:42–77, may 2017. doi: 10.1016/j.eml.2017.01.008.
- [44] RR Nair, P Blake, JR Blake, R Zan, S Anissimova, U Bangert, AP Golovanov, SV Morozov, AK Geim, KS Novoselov, et al. Graphene as a transparent conductive support for studying biological molecules by transmission electron microscopy. *Applied Physics Letters*, 97(15):153102, 2010.

- [45] Jean-Nicolas Longchamp, Tatiana Latychevskaia, Conrad Escher, and Hans-Werner Fink. Low-energy electron holographic imaging of individual tobacco mosaic virions. *Applied Physics Letters*, 107(13):133101, 2015.
- [46] Tatiana Latychevskaia, Flavio Wicki, Jean-Nicolas Longchamp, Conrad Escher, and Hans-Werner Fink. Direct observation of individual charges and their dynamics on graphene by low-energy electron holography. *Nano letters*, 16(9):5469–5474, 2016.
- [47] Jean-Nicolas Longchamp, Conrad Escher, Tatiana Latychevskaia, and Hans-Werner Fink. Low-energy electron holographic imaging of gold nanorods supported by ultraclean graphene. *Ultramicroscopy*, 145:80–84, 2014.
- [48] Stephan Rauschenbach, Frank L Stadler, Eugenio Lunedei, Nicola Malinowski, Sergej Koltsov, Giovanni Costantini, and Klaus Kern. Electrospray ion beam deposition of clusters and biomolecules. *small*, 2(4):540–547, 2006.
- [49] Gordon Rinke, Stephan Rauschenbach, Ludger Harnau, Alyazan Albarghash, Matthias Pauly, and Klaus Kern. Active conformation control of unfolded proteins by hyperthermal collision with a metal surface. *Nano letters*, 14(10):5609–5615, 2014.
- [50] Victor A. Mikhailov, Todd H. Mize, Justin L. P. Benesch, and Carol V. Robinson. Mass-selective soft-landing of protein assemblies with controlled landing energies. *American Chemical Society (ACS)*, 86(16):8321–8328, jul 2014. doi: 10.1021/ac5018327.
- [51] Jean-Nicolas Longchamp, Stephan Rauschenbach, Sabine Abb, Conrad Escher, Tatiana Latychevskaia, Klaus Kern, and Hans-Werner Fink. Imaging proteins at the single-molecule level. *Proc. Natl. Acad. Sci.*, 114(7):1474–1479, jan 2017. doi: 10.1073/pnas.1614519114.
- [52] Z Nawaz, TRI Cataldi, J Knall, R Somekh, and JB Pethica. Stm imaging of molecules: factors affecting their reliable imaging. *Surface science*, 265(1-3):139–155, 1992.
- [53] Atsushi Ikai. Stm and afm of bio/organic molecules and structures. *Surface Science Reports*, 26(8):261–332, 1996.
- [54] Esben P Friis, Jens Enevold Thaulov Andersen, LL Madsen, P Møller, and Jens Ulstrup. In situ stm and afm of the copper protein pseudomonas aeruginosa azurin. *Journal of Electroanalytical Chemistry*, 431(1):35–38, 1997.
- [55] F Valle, JA Derosé, G Dietler, M Kawe, A Plückthun, and G Semenza. Imaging the native structure of the chaperone protein groel without fixation using atomic force microscopy. *Journal of Microscopy*, 203(2):195–198, 2001.
- [56] Daniel J Müller, Harald Janovjak, Tiina Lehto, Lars Kuerschner, and Kurt Anderson. Observing structure, function and assembly of single proteins by afm. *Progress in biophysics and molecular biology*, 79(1-3):1–43, 2002.
- [57] Claire S. Goldsbury, Simon Scheuring, and Laurent Kreplak. Introduction to atomic force microscopy (AFM) in biology. *Current Protocols in Protein Science*, 58(1), nov 2009. doi: 10.1002/0471140864.ps1707s58.
- [58] J. G. Vilhena, A. C. Dumitru, Elena T. Herruzo, Jesús I. Mendieta-Moreno, Ricardo Garcia, P. A. Serena, and Rubén Pérez. Adsorption orientations and immunological recognition of antibodies on graphene. *Nanoscale*, 8(27):13463–13475, 2016. doi: 10.1039/c5nr07612a.

- [59] Francesco Simone Ruggeri, Johnny Habchi, Andrea Cerreta, and Giovanni Dietler. Afm-based single molecule techniques: unraveling the amyloid pathogenic species. *Current pharmaceutical design*, 22(26):3950–3970, 2016.
- [60] Eva Nogales and Sjors H.W. Scheres. Cryo-em: A unique tool for the visualization of macromolecular complexity. *Molecular Cell*, 58(4):677–689, may 2015. doi: 10.1016/j.molcel.2015.02.019.
- [61] Yuxi Liu, Shane Gonen, Tamir Gonen, and Todd O Yeates. Near-atomic cryo-em imaging of a small protein displayed on a designed scaffolding system. *Proceedings of the National Academy of Sciences*, 115(13):3362–3367, 2018.
- [62] Kazuyoshi Murata and Matthias Wolf. Cryo-electron microscopy for structural analysis of dynamic biological macromolecules. *Biochimica et Biophysica Acta (BBA) - General Subjects*, 1862(2):324–334, feb 2018. doi: 10.1016/j.bbagen.2017.07.020.
- [63] Andrea Ilari and Carmelinda Savino. Protein structure determination by x-ray crystallography. *Bioinformatics*, pages 63–87, 2008.
- [64] Alexander Wlodawer, Zbigniew Dauter, and Mariusz Jaskolski. *Protein crystallography*. Springer, 2017.
- [65] Dominique P. Frueh, Andrew C. Goodrich, Subrata H. Mishra, and Scott R. Nichols. Nmr methods for structural studies of large monomeric and multimeric proteins. *Current Opinion in Structural Biology*, 23(5):734–739, oct 2013. doi: 10.1016/j.sbi.2013.06.016.
- [66] Stanley J. Opella. Structure determination of membrane proteins by nuclear magnetic resonance spectroscopy. *Annual Review of Analytical Chemistry*, 6:305–328, 2013.
- [67] Lindsay A Baker and John L Rubinstein. Radiation damage in electron cryomicroscopy. *Methods in enzymology*, 481:371–388, 2010.
- [68] Oliviero Carugo and Kristina Djinović Carugo. When x-rays modify the protein structure: radiation damage at work. *Trends in Biochemical Sciences*, 30(4):213–219, apr 2005. doi: 10.1016/j.tibs.2005.02.009.
- [69] Karol Nass. Radiation damage in protein crystallography at x-ray free-electron lasers. *Acta Crystallographica Section D Structural Biology*, 75(2):211–218, jan 2019. doi: 10.1107/s2059798319000317.
- [70] F Ma, HB Zheng, YJ Sun, D Yang, KW Xu, and Paul K Chu. Strain effect on lattice vibration, heat capacity, and thermal conductivity of graphene. *Applied Physics Letters*, 101(11):111904, 2012.
- [71] Kei Moritsugu, Osamu Miyashita, and Akinori Kidera. Temperature dependence of vibrational energy transfer in a protein molecule. *The Journal of Physical Chemistry B*, 107(14):3309–3317, 2003.
- [72] B Cho, T Ichimura, R Shimizu, and C Oshima. Quantitative evaluation of spatial coherence of the electron beam from low temperature field emitters. *Physical review letters*, 92(24):246103, 2004.
- [73] Tatiana Latychevskaia and Hans-Werner Fink. Practical algorithms for simulation and reconstruction of digital in-line holograms. *Applied optics*, 54(9):2424–2434, 2015.
- [74] Hannah Ochner, Sven Szilagyi, Sabine Abb, Joseph Gault, Carol V. Robinson, Luigi Malavolti, Stephan Rauschenbach, and Klaus Kern. Low-energy electron holography

- imaging of conformational variability of single-antibody molecules from electrospray ion beam deposition. *Proceedings of the National Academy of Sciences*, 118(51), 2021. doi: 10.1073/pnas.2112651118.
- [75] Tatiana Latychevskaia and Hans-Werner Fink. Practical algorithms for simulation and reconstruction of digital in-line holograms. *Applied optics*, 54(9):2424–2434, 2015.
 - [76] Tatiana Latychevskaia and Hans-Werner Fink. Simultaneous reconstruction of phase and amplitude contrast from a single holographic record. *Optics express*, 17(13):10697–10705, 2009.
 - [77] Tatiana Latychevskaia and Hans-Werner Fink. Solution to the twin image problem in holography. *Physical review letters*, 98(23):233901, 2007.
 - [78] Karen M Molony, Bryan M Hennelly, Damien P Kelly, and Thomas J Naughton. Reconstruction algorithms applied to in-line gabor digital holographic microscopy. *Optics Communications*, 283(6):903–909, 2010.
 - [79] Hannah Ochner. *Amplitude and phase reconstruction for Low Energy Electron Holography of individual proteins*. PhD thesis, École polytechnique fédéral de Lausanne, 2021.
 - [80] Joseph W Goodman. *Statistical optics*. John Wiley & Sons, 2015.
 - [81] Bahaa EA Saleh and Malvin Carl Teich. *Fundamentals of photonics*. John Wiley & sons, 2019.
 - [82] Eugene Hecht. Literatur. In *Optik*, pages 1337–1344. De Gruyter, 2018.
 - [83] Hannes Lichte and Michael Lehmann. Electron holography—basics and applications. *Reports on Progress in Physics*, 71(1):016102, 2007.
 - [84] Joseph W Goodman. *Statistical optics (wiley classics library)*. 2000.
 - [85] Vu Thien Binh and V Semet. Interactions of low-energy coherent electron beams with nano-scale objects: a study by fresnel projection microscopy. *Ultramicroscopy*, 73(1-4): 107–117, 1998.
 - [86] Friso Van der Veen and Franz Pfeiffer. Coherent x-ray scattering. *Journal of Physics: Condensed Matter*, 16(28):5003, 2004.
 - [87] Tatiana Latychevskaia. Spatial coherence of electron beams from field emitters and its effect on the resolution of imaged objects. *Ultramicroscopy*, 175:121–129, 2017.
 - [88] Dominik Ehberger, Jakob Hammer, Max Eisele, Michael Krüger, Jonathan Noe, Alexander Högele, and Peter Hommelhoff. Highly coherent electron beam from a laser-triggered tungsten needle tip. *Physical review letters*, 114(22):227601, 2015.
 - [89] Soichiro Matsunaga and Yasunari Sohda. Reducing virtual source size by using facetless electron source for high brightness. *AIP Advances*, 9(6):065001, jun 2019. doi: 10.1063/1.5098528.
 - [90] Che-Cheng Chang, Hong-Shi Kuo, Shouh Hwang, and Tien T Tsong. A fully coherent electron beam from a noble-metal covered w (111) single-atom emitter. *Nanotechnology*, 20(11):115401, 2009.
 - [91] GF Missiroli, G Pozzi, and U Valdre. Electron interferometry and interference electron microscopy. *Journal of Physics E: Scientific Instruments*, 14(6):649, 1981.

-
- [92] Jo Verbeeck, Giovanni Bertoni, and Peter Schattschneider. The fresnel effect of a defocused biprism on the fringes in inelastic holography. *Ultramicroscopy*, 108(3):263–269, 2008.
- [93] Tatiana Latychevskaia, Jean-Nicolas Longchamp, Conrad Escher, and Hans-Werner Fink. On artefact-free reconstruction of low-energy (30–250 ev) electron holograms. *Ultramicroscopy*, 145:22–27, 2014.
- [94] Andrew Zangwill. *Physics at surfaces*. Cambridge university press, 1988.
- [95] Ernst Abbe. Xv.—the relation of aperture and power in the microscope (continued). *Journal of the royal microscopical society*, 3(6):790–812, 1883.
- [96] U Schnars and W Jueptner. Digital holography,|| springer, 2005.
- [97] JCH Spence and JM Cowley. Electron holography at low energy. In *Introduction to Electron Holography*, pages 311–331. Springer, 1999.
- [98] Tatiana Latychevskaia. Lateral and axial resolution criteria in incoherent and coherent optics and holography, near-and far-field regimes. *Applied optics*, 58(13):3597–3603, 2019.
- [99] Lord Rayleigh. Xxi. investigations in optics, with special reference to the spectroscop. *The London, Edinburgh, and Dublin Philosophical Magazine and Journal of Science*, 8(49):261–274, 1879.
- [100] Hui Meng and Fazle Hussain. In-line recording and off-axis viewing technique for holographic particle velocimetry. *Applied optics*, 34(11):1827–1840, 1995.
- [101] Claude Elwood Shannon. Communication in the presence of noise. *Proceedings of the IRE*, 37(1):10–21, 1949.
- [102] Tatiana Latychevskaia and Hans-Werner Fink. Resolution enhancement in in-line holography by numerical compensation of vibrations. *Optics express*, 25(17):20109–20124, 2017.
- [103] Matthias Germann, Tatiana Latychevskaia, Conrad Escher, and Hans-Werner Fink. Pulsed electron holography. *Applied Physics Letters*, 102(20):203115, 2013.
- [104] Edwin L Bronaugh. Helmholtz coils for calibration of probes and sensors: limits of magnetic field accuracy and uniformity. In *Proceedings of International Symposium on Electromagnetic Compatibility*, pages 72–76. IEEE, 1995.
- [105] MS Crosser, Steven Scott, Adam Clark, and PM Wilt. On the magnetic field near the center of helmholtz coils. *Review of Scientific Instruments*, 81(8):084701, 2010.
- [106] Andres F Restrepo Alvarez, Edinson Franco-Mejia, and Carlos R Pinedo-Jaramillo. Study and analysis of magnetic field homogeneity of square and circular helmholtz coil pairs: A taylor series approximation. In *2012 VI Andean Region International Conference*, pages 77–80. IEEE, IEEE, 2012.
- [107] Tatiana Latychevskaia, Fabian Gehri, and Hans-Werner Fink. Depth-resolved holographic reconstructions by three-dimensional deconvolution. *Optics express*, 18(21):22527–22544, 2010.
- [108] Tatiana Latychevskaia. Three-dimensional structure from single two-dimensional diffraction intensity measurement. *Physical Review Letters*, 127(6):063601, 2021.

Bibliography

- [109] Precision laboratory. https://www.fkf.mpg.de/2489208/01_Precision_Laboratory, last accessed on 17.12.2021.
- [110] BF Miessner. Hum in all-electric radio receivers. *Proceedings of the Institute of Radio Engineers*, 18(1):137–166, 1930.
- [111] Erlend Kristiansen and Olav Egeland. Frequency-dependent added mass in models for controller design for wave motion damping. *IFAC Proceedings Volumes*, 36(21):67–72, 2003.
- [112] TL Ibbs, KE Grew, and AA Hirst. Thermal diffusion at low temperatures. *Proceedings of the Physical Society (1926-1948)*, 41(1):456, 1928.
- [113] Gert Ehrlich. Direct observations of the surface diffusion of atoms and clusters. *Surface science*, 246(1-3):1–12, 1991.
- [114] AR Faruqi, R Henderson, M Pryddetch, P Allport, and A Evans. Direct single electron detection with a cmos detector for electron microscopy. *Nuclear Instruments and Methods in Physics Research Section A: Accelerators, Spectrometers, Detectors and Associated Equipment*, 546(1-2):170–175, 2005.
- [115] G McMullan, AR Faruqi, and R Henderson. Direct electron detectors. *Methods in enzymology*, 579:1–17, 2016.
- [116] Shouleh Nikzad, Aimee Smith, Tom S Elliott, Todd J Jones, TA Tombrello, and Qiuming Yu. Low-energy electron detection with delta-doped ccds. In *Solid State Sensor Arrays: Development and Applications*, volume 3019, pages 241–248. International Society for Optics and Photonics, 1997.
- [117] Blake C Jacquot, Michael E Hoenk, Todd J Jones, TJ Cunningham, and Shouleh Nikzad. Direct detection of 100–5000 ev electrons with delta-doped silicon cmos and electron-multiplying ccd imagers. *IEEE transactions on electron devices*, 59(7):1988–1992, 2012.
- [118] Joseph Ladislav Wiza et al. Microchannel plate detectors. *Nucl. Instrum. Methods*, 162(1-3):587–601, 1979.
- [119] Dominic J Ruggieri. Microchannel plate imaging detectors. Technical report, Varian Associates, Palo Alto, CA, 1972.
- [120] J Oberheide, P Wilhelms, and M Zimmer. New results on the absolute ion detection efficiencies of a microchannel plate. *Measurement Science and Technology*, 8(4):351, 1997.
- [121] David Nečas and Petr Klapetek. Gwyddion: an open-source software for SPM data analysis. *Central European Journal of Physics*, 10:181–188, 2012. ISSN 1895-1082. doi: 10.2478/s11534-011-0096-2.
- [122] Helen M. Berman, John Westbrook, Zukang Feng, Gary Gilliland, T. N. Bhat, Helge Weissig, Ilya N. Shindyalov, and Philip E. Bourne. The Protein Data Bank. *Nucleic Acids Research*, 28(1):235–242, 01 2000. ISSN 0305-1048. doi: 10.1093/nar/28.1.235. URL <https://doi.org/10.1093/nar/28.1.235>.
- [123] Michael Drechsler. Erwin müller and the early development of field emission microscopy. *Surface Science*, 70(1):1–18, 1978.
- [124] Robert Gomer. *Field emission and field ionization*. Number 9. Harvard University Press, 1961.

- [125] Toshio Sakurai, Akira Sakai, and Howard W Pickering. Atome-probe field ion microscopy and its applications. *Advances in Electronics and Electron Physics Suppl*, 1989.
- [126] Arthur T Hubbard. *The Handbook of surface imaging and visualization*. CRC press, 1995.
- [127] Erwin W Müller. Work function of tungsten single crystal planes measured by the field emission microscope. *Journal of Applied Physics*, 26(6):732–737, 1955.
- [128] Erwin W Müller. Das feldionenmikroskop. *Zeitschrift für Physik*, 131(1):136–142, 1951.
- [129] JA Panitz. Field-ion microscopy-a review of basic principles and selected applications. *Journal of Physics E: Scientific Instruments*, 15(12):1281, 1982.
- [130] Michael Kenneth Miller, Alfred Cerezo, MG Hetherington, and George DW Smith. Atom probe field ion microscopy. 1996.
- [131] Anne-Sophie Lucier. *Preparation and characterization of tungsten tips suitable for molecular electronics studies*. PhD thesis, McGill University, 2004.
- [132] William Paul and Peter Grütter. Field ion microscopy for the characterization of scanning probes. In *Surface Science Tools for Nanomaterials Characterization*, pages 159–198. Springer Berlin Heidelberg, 2015. doi: 10.1007/978-3-662-44551-8_5.
- [133] TT Tsong. Atom-probe field ion microscopy cambridge university, cambridge, england, 1990; gl kellogg. *Surf. Sci. Rep*, 21(1), 1994.
- [134] Stefan Ernst. Optimisation of the preparation process for tips used in scanning tunneling microscopy. *Physics, Technische Universität Dresden*, 2006.
- [135] Inger Ekvall, Erik Wahlström, Dan Claesson, Håkan Olin, and Eva Olsson. Preparation and characterization of electrochemically etched w tips for stm. *Measurement Science and Technology*, 10(1):11, 1999.
- [136] O Girit, Jannik C Meyer, Rolf Erni, Marta D Rossell, C Kisielowski, Li Yang, Cheol-Hwan Park, MF Crommie, Marvin L Cohen, Steven G Louie, et al. Graphene at the edge: stability and dynamics. *science*, 323(5922):1705–1708, 2009.
- [137] Edward Arthur Davis and Isabel Falconer. *JJ Thompson and the Discovery of the Electron*. CRC Press, 2002.
- [138] Shigehiko Yamamoto. Fundamental physics of vacuum electron sources. *Reports on Progress in Physics*, 69(1):181, 2005.
- [139] Conyers Herring and MH Nichols. Thermionic emission. *Reviews of modern physics*, 21(2):185, 1949.
- [140] JB Pendry. Theory of photoemission. *Surface Science*, 57(2):679–705, 1976.
- [141] David J Smith. The realization of atomic resolution with the electron microscope. *Reports on Progress in Physics*, 60(12):1513, 1997.
- [142] Azad Mohammed and Avin Abdullah. Scanning electron microscopy (sem): A review. In *Proceedings of the 2018 International Conference on Hydraulics and Pneumatics—HERVEX, Băile Govora, Romania*, pages 7–9, 2018.
- [143] Tatiana Latychevskaia, Jean-Nicolas Longchamp, Conrad Escher, and Hans-Werner Fink. Holography and coherent diffraction with low-energy electrons: A route towards structural biology at the single molecule level. *Ultramicroscopy*, 159:395–402, dec 2015. doi: 10.1016/j.ultramic.2014.11.024.

Bibliography

- [144] William E Packard, Young Liang, Ning Dai, John D Dow, Ruth Nicolaides, Robert C Jaklevic, and William J Kaiser. Nano-machining of gold and semiconductor surfaces. *Journal of Microscopy*, 152(3):715–725, 1988.
- [145] Gerd Binnig, Heinrich Rohrer, Ch Gerber, and Edmund Weibel. Surface studies by scanning tunneling microscopy. *Physical review letters*, 49(1):57, 1982.
- [146] D. K. Biegelsen, F. A. Ponce, and J. C. Tramontana. Simple ion milling preparation of (111) tungsten tips. *Applied Physics Letters*, 54(13):1223–1225, mar 1989. doi: 10.1063/1.100722.
- [147] Allan J. Melmed. The art and science and other aspects of making sharp tips. *Journal of Vacuum Science & Technology B: Microelectronics and Nanometer Structures*, 9(2):601, mar 1991. doi: 10.1116/1.585467.
- [148] B Hübner, HWP Koops, H Pagnia, N Sotnik, J Urban, and M Weber. Tips for scanning tunneling microscopy produced by electron-beam-induced deposition. *Ultramicroscopy*, 42:1519–1525, 1992.
- [149] R. Zhang. Preparation of sharp polycrystalline tungsten tips for scanning tunneling microscopy imaging. *Journal of Vacuum Science & Technology B: Microelectronics and Nanometer Structures*, 14(1):1, jan 1996. doi: 10.1116/1.589029.
- [150] Wei-Tse Chang, Ing-Shouh Hwang, Mu-Tung Chang, Chung-Yueh Lin, Wei-Hao Hsu, and Jin-Long Hou. Method of electrochemical etching of tungsten tips with controllable profiles. *Review of Scientific Instruments*, 83(8):083704, aug 2012. doi: 10.1063/1.4745394.
- [151] M. Kulakov, I. Luzinov, and K. G. Kornev. Capillary and surface effects in the formation of nanosharp tungsten tips by electropolishing. *Langmuir*, 25(8):4462–4468, mar 2009. doi: 10.1021/la802489b.
- [152] Bing-Feng Ju, Yuan-Liu Chen, and Yaozheng Ge. The art of electrochemical etching for preparing tungsten probes with controllable tip profile and characteristic parameters. *Review of Scientific Instruments*, 82(1):013707, jan 2011. doi: 10.1063/1.3529880.
- [153] Yeong-Cheol Kim and David N Seidman. An electrochemical etching procedure for fabricating scanning tunneling microscopy and atom-probe field-ion microscopy tips. *Metals and Materials International*, 9(4):399–404, 2003.
- [154] L. Ottaviano, L. Lozzi, and S. Santucci. Scanning auger microscopy study of w tips for scanning tunneling microscopy. *Review of Scientific Instruments*, 74(7):3368–3378, jul 2003. doi: 10.1063/1.1581392.
- [155] Till Hagedorn, Mehdi El Ouali, William Paul, David Oliver, Yoichi Miyahara, and Peter Grütter. Refined tip preparation by electrochemical etching and ultrahigh vacuum treatment to obtain atomically sharp tips for scanning tunneling microscope and atomic force microscope. *Review of Scientific Instruments*, 82(11):113903, 2011.
- [156] Alain Stalder. *Mechanics and electronics on the atomic scale: a study using scanning probe methods*. 1995.
- [157] Vu Thien Binh. In situ fabrication and regeneration of microtips for scanning tunnelling microscopy. *Journal of Microscopy*, 152(2):355–361, 1988.

- [158] AP Janssen and JP Jones. The sharpening of field emitter tips by ion sputtering. *Journal of Physics D: Applied Physics*, 4(1):118, 1971.
- [159] LW Nordhiem. The effect of the image force on the emission and reflexion of electrons by metals. *Proceedings of the Royal Society of London. Series A, Containing Papers of a Mathematical and Physical Character*, 121(788):626–639, 1928.
- [160] Ralph Howard Fowler and Lothar Nordheim. Electron emission in intense electric fields. *Proceedings of the Royal Society of London. Series A, Containing Papers of a Mathematical and Physical Character*, 119(781):173–181, 1928.
- [161] Wayne B Nottingham, RH Good, Erwin W Müller, R Kollath, GL Weissler, WP Allis, LB Loeb, A von Engel, and PF Little. Electron-emission gas discharges i/elektronen-emission gasentladungen i. *Encyclopedia of Physics/Handbuch der Physik*. <https://doi.org/10.1007/978-3-642-45844-6>, 1956.
- [162] A Schirmeisen. *Metallic Adhesion and Tunneling at the Atomic Scale*. PhD thesis, McGill University, 1999.
- [163] Claudia Lenk, Steve Lenk, Mathias Holz, Elshad Guliyev, Martin Hofmann, Tzvetan Ivanov, Ivo W. Rangelow, Mahmoud Behzadrad, Ashwin K. Rishinaramangalam, Daniel Feezell, and Tito Busani. Experimental study of field emission from ultrasharp silicon, diamond, GaN, and tungsten tips in close proximity to the counter electrode. *Journal of Vacuum Science & Technology B*, 36(6):06JL03, nov 2018. doi: 10.1116/1.5048518.
- [164] Kuo-chin Li, Guoqin Li, Chongyou Wang, et al. *Tungsten: its history, geology, ore-dressing, metallurgy, chemistry, analysis, applications, and economics*. Number 94. Reinhold publishing corporation, 1955.
- [165] D Atlan, G Gardet, Vu Thien Binh, N Garcia, and JJ Saenz. 3d calculations at atomic scale of the electrostatic potential and field created by a teton tip. *Ultramicroscopy*, 42: 154–162, 1992.
- [166] O. Albrechtsen. Reliable tip preparation for high-resolution scanning tunneling microscopy. *Journal of Vacuum Science & Technology B: Microelectronics and Nanometer Structures*, 12(6):3187, nov 1994. doi: 10.1116/1.587497.
- [167] Christoph Schiller, Arie A Koomans, Theo L van Rooy, Christian Schönenberger, and Herman B Elswijk. Decapitation of tungsten field emitter tips during sputter sharpening. *Surface science*, 339(3):L925–L930, 1995.
- [168] JY Cavaille and M Drechsler. Ion impact on field emitter crystals. *Revue De Physique Appliquee*, 12(10):1631–1639, 1977.
- [169] G. J. de Raad, P. M. Koenraad, and J. H. Wolter. Use of the schiller decapitation process for the manufacture of high quality tungsten scanning tunneling microscopy tips. *Journal of Vacuum Science & Technology B: Microelectronics and Nanometer Structures*, 17(5): 1946, 1999. doi: 10.1116/1.590854.
- [170] Anne-Sophie Lucier, Henrik Mortensen, Yan Sun, and Peter Grütter. Determination of the atomic structure of scanning probe microscopy tungsten tips by field ion microscopy. *Physical Review B*, 72(23):235420, dec 2005. doi: 10.1103/physrevb.72.235420.
- [171] Moh'd Rezeq, Jason Pitters, and Robert Wolkow. Tungsten nanotip fabrication by spa-

- tially controlled field-assisted reaction with nitrogen. *The Journal of Chemical Physics*, 124(20):204716, may 2006. doi: 10.1063/1.2198536.
- [172] Radovan Urban, Robert A. Wolkow, and Jason L. Pitters. Single atom gas field ion sources for scanning ion microscopy. In *Helium Ion Microscopy*, pages 31–61. Springer International Publishing, 2016. doi: 10.1007/978-3-319-41990-9_2.
- [173] William Paul, Yoichi Miyahara, and Peter Grütter. Implementation of atomically defined field ion microscopy tips in scanning probe microscopy. *Nanotechnology*, 23(33):335702, 2012.
- [174] Michael T Postek. An approach to the reduction of hydrocarbon contamination in the scanning electron microscope. *Scanning: The Journal of Scanning Microscopies*, 18(4): 269–274, 1996.
- [175] MR Scheinfein, W Qian, and JCH Spence. Aberrations of emission cathodes: Nanometer diameter field-emission electron sources. *Journal of applied physics*, 73(5):2057–2068, 1993.
- [176] Vu Thien Binh, V Semet, and N Garcia. Low-energy-electron diffraction by nano-objects in projection microscopy without magnetic shielding. *Applied physics letters*, 65(19): 2493–2495, 1994.
- [177] Hans-Werner Fink. Mono-atomic tips for scanning tunneling microscopy. *IBM journal of research and development*, 30(5):460–465, 1986.
- [178] Hans-Werner Fink. Point source for ions and electrons. *Physica Scripta*, 38(2):260, 1988.
- [179] Hong-Shi Kuo, Ing-Shouh Hwang, Tsu-Yi Fu, Jun-Yi Wu, Che-Cheng Chang, and Tien T Tsong. Preparation and characterization of single-atom tips. *nano letters*, 4(12):2379–2382, 2004.
- [180] Tsu-Yi Fu, Lung-Chieh Cheng, C.-H. Nien, and Tien T. Tsong. Method of creating a pd-covered single-atom sharp w pyramidal tip: Mechanism and energetics of its formation. *Physical Review B*, 64(11):113401, aug 2001. doi: 10.1103/physrevb.64.113401.
- [181] Hong-Shi Kuo, Shouh Hwang, Tsu-Yi Fu, Yu-Chun Lin, Che-Cheng Chang, and Tien T Tsong. Noble metal/w (111) single-atom tips and their field electron and ion emission characteristics. *Japanese journal of applied physics*, 45(11R):8972, 2006.
- [182] Gert Ehrlich and FG Hudda. Direct observation of individual adatoms: nitrogen on tungsten. *The Journal of Chemical Physics*, 36(12):3233–3247, 1962.
- [183] Klaus D Rendulic and Zlatko Knor. Chemisorption and gas-promoted field evaporation. *Surface Science*, 7(2):205–214, 1967.
- [184] Heinz Schmid and Hans-Werner Fink. Carbon nanotubes are coherent electron sources. *Applied physics letters*, 70(20):2679–2680, 1997.
- [185] Jean-Marc Bonard, Frederic Maier, Thomas Stöckli, André Châtelain, Walt A de Heer, Jean-Paul Salvetat, and Laszlo Forro. Field emission properties of multiwalled carbon nanotubes. *Ultramicroscopy*, 73(1-4):7–15, 1998.
- [186] J-M Bonard, J-P Salvetat, T Stöckli, L Forro, and A Chatelain. Field emission from carbon nanotubes: perspectives for applications and clues to the emission mechanism. *Applied Physics A*, 69(3):245–254, 1999.

-
- [187] N De Jonge and NJ Van Druten. Field emission from individual multiwalled carbon nanotubes prepared in an electron microscope. *Ultramicroscopy*, 95:85–91, 2003.
- [188] Niels De Jonge, Yann Lamy, Koen Schoots, and Tjerk H Oosterkamp. High brightness electron beam from a multi-walled carbon nanotube. *Nature*, 420(6914):393–395, 2002.
- [189] Niels de Jonge. Brightness of carbon nanotube electron sources. *Journal of Applied Physics*, 95(2):673–681, jan 2004. doi: 10.1063/1.1632551.
- [190] Kenneth A Dean and Babu R Chalamala. The environmental stability of field emission from single-walled carbon nanotubes. *Applied physics letters*, 75(19):3017–3019, 1999.
- [191] D Ferrer, T Tanii, I Matsuya, G Zhong, S Okamoto, H Kawarada, T Shinada, and I Ohdomari. Enhancement of field emission characteristics of tungsten emitters by single-walled carbon nanotube modification. *Applied physics letters*, 88(3):033116, 2006.
- [192] RB Sharma, VN Tondare, DS Joag, A Govindaraj, and CNR Rao. Field emission from carbon nanotubes grown on a tungsten tip. *Chemical physics letters*, 344(3-4):283–286, 2001.
- [193] Jun Jiao, Lifeng Dong, David W Tuggle, Catherine L Mosher, Sean Foxley, and Jaswant Tawdekar. Fabrication and characterization of carbon nanotube field emitters. *MRS Online Proceedings Library (OPL)*, 706, 2001.
- [194] Niels de Jonge, Yann Lamy, and Monja Kaiser. Controlled mounting of individual multiwalled carbon nanotubes on support tips. *Nano Letters*, 3(12):1621–1624, 2003.
- [195] Xin Bai, Mingsheng Wang, Gengmin Zhang, Jie Yu, Zhaoxiang Zhang, Dengzhu Guo, Xingyu Zhao, and Zengquan Xue. Field emission of individual carbon nanotubes on tungsten tips. *Journal of Vacuum Science & Technology B: Microelectronics and Nanometer Structures*, 25(2):561, 2007. doi: 10.1116/1.2709902.
- [196] Yahachi Saito, Koichi Hata, Akihiro Takakura, Junko Yotani, and Sashiro Uemura. Field emission of carbon nanotubes and its application as electron sources of ultra-high luminance light-source devices. *Physica B: Condensed Matter*, 323(1-4):30–37, 2002.
- [197] Zhong-Shuai Wu, Songfeng Pei, Wencai Ren, Daiming Tang, Libo Gao, Bilu Liu, Feng Li, Chang Liu, and Hui-Ming Cheng. Field emission of single-layer graphene films prepared by electrophoretic deposition. *Advanced Materials*, 21(17):1756–1760, may 2009. doi: 10.1002/adma.200802560.
- [198] Indranil Lahiri, Ved Prakash Verma, and Wonbong Choi. An all-graphene based transparent and flexible field emission device. *Carbon*, 49(5):1614–1619, apr 2011. doi: 10.1016/j.carbon.2010.12.044.
- [199] Xiuyuan Shao, Avinash Srinivasan, Wei Kean Ang, and Anjam Khursheed. A high-brightness large-diameter graphene coated point cathode field emission electron source. *Nature Communications*, 9(1), mar 2018. doi: 10.1038/s41467-018-03721-y.
- [200] Cédric Barroo and Thierry Visart de Bocarmé. Imaging graphene by field ion microscopy. *Microscopy and Microanalysis*, 22(S3):1542–1543, jul 2016. doi: 10.1017/s1431927616008552.
- [201] Yahachi Saito, Yuhdai Watanabe, Tohru Hoshino, Hitoshi Nakahara, Kazuya Kunoh, Shigekazu Nagai, and Koichi Hata. Fem and fim of graphene: Possible observation of

- electronic states at edges. In *2018 31st International Vacuum Nanoelectronics Conference (IVNC)*, pages 1–2. IEEE, 2018.
- [202] Rahul Raveendran Nair, Peter Blake, Alexander N Grigorenko, Konstantin S Novoselov, Tim J Booth, Tobias Stauber, Nuno MR Peres, and Andre K Geim. Fine structure constant defines visual transparency of graphene. *Science*, 320(5881):1308–1308, 2008.
- [203] Min-Ho Park, Tae-Hoon Kim, and Cheol-Woong Yang. Thickness contrast of few-layered graphene in sem. *Surface and interface analysis*, 44(11-12):1538–1541, 2012.
- [204] Kurt W Kolasinski. *Surface science: foundations of catalysis and nanoscience*. John Wiley & Sons, 2012.
- [205] Ruben Mas-Balleste, Cristina Gomez-Navarro, Julio Gomez-Herrero, and Felix Zamora. 2d materials: to graphene and beyond. *Nanoscale*, 3(1):20–30, 2011.
- [206] Phaedon Avouris, Tony F Heinz, and Tony Low. *2D Materials*. Cambridge University Press, 2017.
- [207] A. H. Castro Neto, F. Guinea, N. M. R. Peres, K. S. Novoselov, and A. K. Geim. The electronic properties of graphene. *Reviews of Modern Physics*, 81(1):109–162, jan 2009. doi: 10.1103/revmodphys.81.109.
- [208] Teng Li. Extrinsic morphology of graphene. *Modelling and Simulation in Materials Science and Engineering*, 19(5):054005, 2011.
- [209] Daniel R Cooper, Benjamin D’Anjou, Nageswara Ghattamaneni, Benjamin Harack, Michael Hilke, Alexandre Horth, Norberto Majlis, Mathieu Massicotte, Leron Vandsburger, Eric Whiteway, et al. Experimental review of graphene. *International Scholarly Research Notices*, 2012, 2012.
- [210] Matthew J. Allen, Vincent C. Tung, and Richard B. Kaner. Honeycomb carbon: A review of graphene. *Chemical Reviews*, 110(1):132–145, jul 2009. doi: 10.1021/cr900070d.
- [211] Xuesong Li, Weiwei Cai, Jinho An, Seyoung Kim, Junghyo Nah, Dongxing Yang, Richard Piner, Aruna Velamakanni, Inhwa Jung, Emanuel Tutuc, et al. Large-area synthesis of high-quality and uniform graphene films on copper foils. *science*, 324(5932):1312–1314, 2009.
- [212] Zonghoon Lee, Ki-Joon Jeon, Albert Dato, Rolf Erni, Thomas J Richardson, Michael Frenklach, and Velimir Radmilovic. Direct imaging of soft- hard interfaces enabled by graphene. *Nano letters*, 9(9):3365–3369, 2009.
- [213] Andre K Geim and Konstantin S Novoselov. The rise of graphene. In *Nanoscience and technology: a collection of reviews from nature journals*, pages 11–19. World Scientific, 2010.
- [214] Jannik C Meyer, C O Girit, MF Crommie, and A Zettl. Imaging and dynamics of light atoms and molecules on graphene. *Nature*, 454(7202):319–322, 2008.
- [215] Sumedh P. Surwade, Zhiting Li, and Haitao Liu. Thermal oxidation and unwrinkling of chemical vapor deposition-grown graphene. *The Journal of Physical Chemistry C*, 116(38):20600–20606, sep 2012. doi: 10.1021/jp306537y.
- [216] Fu Liu, Mingjie Wang, Yao Chen, and Jianmin Gao. Thermal stability of graphene in inert atmosphere at high temperature. *Journal of Solid State Chemistry*, 276:100–103, 2019.

-
- [217] Jean-Nicolas Longchamp, Conrad Escher, and Hans-Werner Fink. Ultraclean freestanding graphene by platinum-metal catalysis. *Journal of Vacuum Science & Technology B, Nanotechnology and Microelectronics: Materials, Processing, Measurement, and Phenomena*, 31(2):020605, mar 2013. doi: 10.1116/1.4793746.
- [218] MK Nizam, D Sebastian, MI Kairi, M Khavarian, and AR Mohamed. Synthesis of graphene flakes over recovered copper etched in ammonium persulfate solution. *Sains Malays*, 46(7):1039–1045, 2017.
- [219] Xuesong Li, Yanwu Zhu, Weiwei Cai, Mark Borysiak, Boyang Han, David Chen, Richard D. Piner, Luigi Colombo, and Rodney S. Ruoff. Transfer of large-area graphene films for high-performance transparent conductive electrodes. *Nano Letters*, 9(12):4359–4363, oct 2009. doi: 10.1021/nl902623y.
- [220] Craig L Beyler and Marcelo M Hirschler. Thermal decomposition of polymers. *SFPE handbook of fire protection engineering*, 2, 2002.
- [221] André Beyer and Armin Götzhäuser. Low energy electron point source microscopy: beyond imaging. *Journal of physics: Condensed matter*, 22(34):343001, 2010.
- [222] I. Horcas, R. Fernández, J. M. Gómez-Rodríguez, J. Colchero, J. Gómez-Herrero, and A. M. Baro. WSXM: A software for scanning probe microscopy and a tool for nanotechnology. 78(1):013705, jan 2007. doi: 10.1063/1.2432410.
- [223] Prasad Govindrao Jamkhande, Namrata W Ghule, Abdul Haque Bamer, and Mohan G Kalaskar. Metal nanoparticles synthesis: An overview on methods of preparation, advantages and disadvantages, and applications. *Journal of Drug Delivery Science and Technology*, 53:101174, 2019.
- [224] Charles Martin, ET Arakawa, TA Callcott, and JC Ashley. Low energy electron attenuation length studies in thin amorphous carbon films. *Journal of electron spectroscopy and related phenomena*, 35(2):307–317, 1985.
- [225] Jacek B Jasinski, Santoshrupa Dumpala, GU Sumanasekera, Mahendra K Sunkara, and PJ Ouseph. Observation and interpretation of adjacent moire patterns of different shapes in bilayer graphene. *Applied Physics Letters*, 99(7):073104, 2011.
- [226] Rikson Siburian and Junji Nakamura. Formation process of pt subnano-clusters on graphene nanosheets. *The Journal of Physical Chemistry C*, 116(43):22947–22953, oct 2012. doi: 10.1021/jp307327e.
- [227] Mohammad Zarshenas, Victor Gervilla, Davide G. Sangiovanni, and Kostas Sarakinos. Room-temperature diffusion of metal clusters on graphene. *Physical Chemistry Chemical Physics*, 23(23):13087–13094, 2021. doi: 10.1039/d1cp00522g.
- [228] Tatiana Latychevskaia, Flavio Wicki, Conrad Escher, and Hans-Werner Fink. Imaging the potential distribution of individual charged impurities on graphene by low-energy electron holography. *Ultramicroscopy*, 182:276–282, 2017.
- [229] John B Fenn, Matthias Mann, Chin Kai Meng, Shek Fu Wong, and Craig M Whitehouse. Electrospray ionization for mass spectrometry of large biomolecules. *Science*, 246(4926): 64–71, 1989.
- [230] John B Fenn, Matthias Mann, Chin Kai Meng, Shek Fu Wong, and Craige M Whitehouse.

- Electrospray ionization—principles and practice. *Mass Spectrometry Reviews*, 9(1):37–70, 1990.
- [231] Julian P. Whitelegge, Cameron B. Gundersen, and Kym F. Faull. Electrospray-ionization mass spectrometry of intact intrinsic membrane proteins. In *Protein Science*, pages 1423–1430, 1998.
- [232] Leonhard H Urner, Ildir Liko, Hsin-Yung Yen, Kin-Kuan Hoi, Jani Reddy Bolla, Joseph Gault, Fernando Gonçalves Almeida, Marc-Philip Schweder, Denis Shutin, Svenja Ehrmann, et al. Modular detergents tailor the purification and structural analysis of membrane proteins including g-protein coupled receptors. *Nature communications*, 11(1):1–10, 2020.
- [233] Joost Snijder, Rebecca J Rose, David Veessler, John E Johnson, and Albert JR Heck. Studying 18 mda virus assemblies with native mass spectrometry. *Angewandte Chemie International Edition*, 52(14):4020–4023, 2013.
- [234] Albert JR Heck. Native mass spectrometry: a bridge between interactomics and structural biology. *Nature methods*, 5(11):927–933, 2008.
- [235] Matthias Wilm. Principles of electrospray ionization. *Molecular and cellular proteomics*, 10(7):M111.009407, jul 2011. doi: 10.1074/mcp.m111.009407.
- [236] Aneika C Leney and Albert JR Heck. Native mass spectrometry: what is in the name? *Journal of the American Society for Mass Spectrometry*, 28(1):5–13, 2016.
- [237] Ildir Liko, Timothy M Allison, Jonathan TS Hopper, and Carol V Robinson. Mass spectrometry guided structural biology. *Elsevier BV*, 40:136–144, oct 2016. doi: 10.1016/j.sbi.2016.09.008.
- [238] Helena Hernandez and Carol V Robinson. Determining the stoichiometry and interactions of macromolecular assemblies from mass spectrometry. *Nature protocols*, 2(3):715–726, 2007.
- [239] Howard G Barth, Christian Jackson, and Barry E Boyes. Size exclusion chromatography. *Analytical chemistry*, 66(12):595–620, 1994.
- [240] Richard R. Burgess. A brief practical review of size exclusion chromatography: Rules of thumb, limitations, and troubleshooting. *Protein Expression and Purification*, 150:81–85, oct 2018. doi: 10.1016/j.pep.2018.05.007.
- [241] Jong Wha Lee and Hugh I. Kim. Investigating acid-induced structural transitions of lysozyme in an electrospray ionization source. *Royal Society of Chemistry (RSC)*, 140(2):661–669, 2015. doi: 10.1039/c4an01794c.
- [242] Liyun Zhang, Lisa A Vasicek, SuChun Hsieh, Shuli Zhang, Kevin P Bateman, and Jack Henion. Top-down LC–MS quantitation of intact denatured and native monoclonal antibodies in biological samples. *Bioanalysis*, 10(13):1039–1054, jul 2018. doi: 10.4155/bio-2017-0282.
- [243] Zheng Ouyang, Zoltán Takáts, Thomas A Blake, Bogdan Gologan, Andy J Guymon, Justin M Wiseman, Justin C Oliver, V Jo Davisson, and R Graham Cooks. Preparing protein microarrays by soft-landing of mass-selected ions. *Science*, 301(5638):1351–1354, 2003.

- [244] Stephan Rauschenbach, Ralf Vogelgesang, N. Malinowski, Jürgen W. Gerlach, Mohamed Benyoucef, Giovanni Costantini, Zhitao Deng, Nicha Thontasen, and Klaus Kern. Electrospray ion beam deposition: Soft-landing and fragmentation of functional molecules at solid surfaces. *American Chemical Society (ACS)*, 3(10):2901–2910, sep 2009. doi: 10.1021/nn900022p.
- [245] Matthias Wilm and Matthias Mann. Analytical properties of the nanoelectrospray ion source. In *Analytical chemistry*, 1996.
- [246] Geoffrey Ingram Taylor. Disintegration of water drops in an electric field. *Proceedings of the Royal Society of London. Series A. Mathematical and Physical Sciences*, 280(1382): 383–397, 1964.
- [247] Lord. Rayleigh. Xx. on the equilibrium of liquid conducting masses charged with electricity. *The London, Edinburgh, and Dublin Philosophical Magazine and Journal of Science*, 1882.
- [248] Richard B. Cole. Electrospray ionization mass spectrometry: fundamentals, instrumentation, and applications. *Wiley-Interscience*, 1997.
- [249] Richard B. Cole. Some tenets pertaining to electrospray ionization mass spectrometry. *Journal of Mass Spectrometry*, 2000.
- [250] Paul Kebarle and Michael Peschke. On the mechanisms by which the charged droplets produced by electrospray lead to gas phase ions. *Analytica Chimica Acta*, 406(1):11–35, 2000.
- [251] P Kebarle. A brief overview of the present status of the mechanisms involved in electrospray mass spectrometry. *Journal of mass spectrometry*, 35(7):804–817, 2000.
- [252] Lars Konermann, Elias Ahadi, Antony D Rodriguez, and Siavash Vahidi. Unraveling the mechanism of electrospray ionization, 2013.
- [253] Elias Ahadi and Lars Konermann. Modeling the behavior of coarse-grained polymer chains in charged water droplets: Implications for the mechanism of electrospray ionization. *American Chemical Society (ACS)*, 116(1):104–112, dec 2011. doi: 10.1021/jp209344z.
- [254] Christopher J Hogan Jr, James A Carroll, Henry W Rohrs, Pratim Biswas, and Michael L Gross. Combined charged residue-field emission model of macromolecular electrospray ionization. *Analytical chemistry*, 81(1):369–377, 2009.
- [255] JV Iribarne and BA Thomson. On the evaporation of small ions from charged droplets. *The Journal of chemical physics*, 64(6):2287–2294, 1976.
- [256] BA Thomson and JV Iribarne. Field induced ion evaporation from liquid surfaces at atmospheric pressure. *The Journal of Chemical Physics*, 71(11):4451–4463, 1979.
- [257] Kathrin Breuker and Fred W McLafferty. Stepwise evolution of protein native structure with electrospray into the gas phase, 10- 12 to 102 s. *Proceedings of the National Academy of Sciences*, 105(47):18145–18152, 2008.
- [258] Philip E. Miller and M. Bonner Denton. The quadrupole mass filter: basic operating concepts. In *Journal of chemical education*, page 617, 1986.
- [259] DJ Douglas. Linear quadrupoles in mass spectrometry. *Mass spectrometry reviews*, 28(6):937–960, 2009.

Bibliography

- [260] Grant E Johnson, Don Gunaratne, and Julia Laskin. Soft-and reactive landing of ions onto surfaces: Concepts and applications. *Mass spectrometry reviews*, 35(3):439–479, 2016.
- [261] Lukas Krumbein, Kelvin Anggara, Martina Stella, Tomasz Michnowicz, Hannah Ochner, Sabine Abb, Gordon Rinke, André Portz, Michael Dürr, Uta Schlickum, et al. Fast molecular compression by a hyperthermal collision gives bond-selective mechanochemistry. *Physical Review Letters*, 126(5):056001, 2021.
- [262] KG Günther. Aufdampfschichten aus halbleitenden iii-v-verbindungen. *Zeitschrift für Naturforschung A*, 13(12):1081–1089, 1958.
- [263] John E Davey and Titus Pankey. Epitaxial gas films deposited by vacuum evaporation. *Journal of Applied Physics*, 39(4):1941–1948, 1968.
- [264] WL Winterbottom and JP Hirth. Diffusional contribution to the total flow from a knudsen cell. *The Journal of Chemical Physics*, 37(4):784–793, 1962.
- [265] S Kowarik, A Gerlach, and F Schreiber. Organic molecular beam deposition: fundamentals, growth dynamics, and in situ studies. *Journal of Physics: Condensed Matter*, 20(18):184005, 2008.
- [266] Aftab Farrukh, Xiao-jun Tian, Fan-fang Kong, Yun-jie Yu, Shi-hao Jing, Gong Chen, Yao Zhang, Yuan Liao, Yang Zhang, and Zhen-chao Dong. Bias-polarity dependent electroluminescence from a single platinum phthalocyanine molecule. *Chinese Journal of Chemical Physics*, 34(1):87–94, 2021.
- [267] André Beyer, Dirk H. Weber, Berthold Völkel, and Armin Gölzhäuser. Characterization of nanowires with the low energy electron point source (LEEPS) microscope. *physica status solidi (b)*, 247(10):2550–2556, sep 2010. doi: 10.1002/pssb.201046260.
- [268] Sarah E. J. Bowman and Kara L. Bren. The chemistry and biochemistry of heme c: functional bases for covalent attachment. *Natural Product Reports*, 25(6):1118, 2008. doi: 10.1039/b717196j.
- [269] John C Reed. Cytochrome c: can't live with it—can't live without it. *Cell*, 91(5):559–562, 1997.
- [270] Xuejun Jiang and Xiaodong Wang. Cytochrome c-mediated apoptosis. *Annual review of biochemistry*, 73(1):87–106, 2004.
- [271] Yong-Ling P Ow, Douglas R Green, Zhenyue Hao, and Tak W Mak. Cytochrome c: functions beyond respiration. *Nature reviews Molecular cell biology*, 9(7):532–542, 2008.
- [272] Y-T Li, Y-L Hsieh, JD Henion, and B Ganem. Studies on heme binding in myoglobin, hemoglobin, and cytochrome c by ion spray mass spectrometry. *Journal of the American Society for Mass Spectrometry*, 4(8):631–637, 1993.
- [273] Mark S Hargrove, Szymon Krzywda, Anthony J Wilkinson, Yi Dou, Masao Ikeda-Saito, and John S Olson. Stability of myoglobin: a model for the folding of heme proteins. *Biochemistry*, 33(39):11767–11775, 1994.
- [274] Marc W Merx, Ulrich Flögel, Thomas Stumpe, Axel Gödecke, Ulrich KM Decking, and Jürgen Schrader. Myoglobin facilitates oxygen diffusion. *The FASEB Journal*, 15(6):1077–1079, 2001.

- [275] Jonathan B Wittenberg and Beatrice A Wittenberg. Myoglobin function reassessed. *Journal of experimental biology*, 206(12):2011–2020, 2003.
- [276] DJ Livingston and WD Brown. The chemistry of myoglobin and its reactions. *Food Technology*, (RESEARCH), 1981.
- [277] Ya wen Li, Quan Chi, Tao Feng, Huaming Xiao, Linghe Li, and Xian Wang. Interactions of indole alkaloids with myoglobin: A mass spectrometry based spectrometric and computational method. *Rapid Communications in Mass Spectrometry*, 34(7), feb 2020. doi: 10.1002/rcm.8656.
- [278] Catherine A. Cassou and Evan R. Williams. Desalting protein ions in native mass spectrometry using supercharging reagents. *The Analyst*, 139(19):4810–4819, 2014. doi: 10.1039/c4an01085j.
- [279] Amber D. Rolland and James S. Prell. Approaches to heterogeneity in native mass spectrometry. *Chemical Reviews*, sep 2021. doi: 10.1021/acs.chemrev.1c00696.
- [280] Roman Aranda IV, He Cai, Chad E Worley, Elena J Levin, Rong Li, John S Olson, George N Phillips Jr, and Mark P Richards. Structural analysis of fish versus mammalian hemoglobins: effect of the heme pocket environment on autooxidation and heme loss. *Proteins: Structure, Function, and Bioinformatics*, 75(1):217–230, 2009.
- [281] Mostafa H Ahmed, Mohini S Ghatge, and Martin K Safo. Hemoglobin: structure, function and allostery. *Sub-cellular biochemistry*, 94:345, 2020.
- [282] Charlotte A. Scarff, Vibhuti J. Patel, Konstantinos Thalassinou, and James H. Scrivens. Probing hemoglobin structure by means of traveling-wave ion mobility mass spectrometry. *Journal of the American Society for Mass Spectrometry*, 20(4):625–631, dec 2008. doi: 10.1016/j.jasms.2008.11.023.
- [283] Brian L Boys, Mark C Kuprowski, and Lars Konermann. Symmetric behavior of hemoglobin α - and β -subunits during acid-induced denaturation observed by electrospray mass spectrometry. *Biochemistry*, 46(37):10675–10684, 2007.
- [284] Gusztáv Schay, András D Kaposi, László Smeller, Krisztián Szigeti, Judit Fidy, and Levente Herenyi. Dissimilar flexibility of α and β subunits of human adult hemoglobin influences the protein dynamics and its alteration induced by allosteric effectors. *Plos one*, 13(3):e0194994, 2018.
- [285] Anirban Basu and Gopinatha Suresh Kumar. A biophysical investigation on the binding of proflavine with human hemoglobin: Insights from spectroscopy, thermodynamics and AFM studies. *Journal of Photochemistry and Photobiology B: Biology*, 165:42–50, dec 2016. doi: 10.1016/j.jphotobiol.2016.10.010.
- [286] A. Bartesaghi, D. Matthies, S. Banerjee, A. Merk, and S. Subramaniam. Structure of -galactosidase at 3.2-Å resolution obtained by cryo-electron microscopy. *Proceedings of the National Academy of Sciences*, 111(32):11709–11714, jul 2014. doi: 10.1073/pnas.1402809111.
- [287] Noriyuki Ishii. Groel and the groel-groes complex. *Macromolecular Protein Complexes*, pages 483–504, 2017.
- [288] Peter T Gomme, Karl B McCann, and Joseph Bertolini. Transferrin: structure, function and potential therapeutic actions. *Drug discovery today*, 10(4):267–273, 2005.

Bibliography

- [289] Jake W. Pawlowski, Noelle Kellicker, Cedric E. Bobst, and Igor A. Kaltashov. Assessing the iron delivery efficacy of transferrin in clinical samples by native electrospray ionization mass spectrometry. *The Analyst*, 141(3):853–861, 2016. doi: 10.1039/c5an02159f.
- [290] Dorothee B Ott, Andrea Hartwig, and Martin J Stillman. Competition between al^{3+} and fe^{3+} binding to human transferrin and toxicological implications: Structural investigations using ultra-high resolution esi ms and cd spectroscopy. *Metallomics*, 11(5): 968–981, 2019.
- [291] Olga De Smidt, James C Du Preez, and Jacobus Albertyn. The alcohol dehydrogenases of *saccharomyces cerevisiae*: a comprehensive review. *FEMS yeast research*, 8(7):967–978, 2008.
- [292] E Negelein and HJ Wulff. Diphosphopyridinproteid, alkohol, acetaldehyd. *Biochem. Z*, 293:351, 1937.
- [293] Vladimir Leskovac, Svetlana Trivić, and Draginja Peričin. The three zinc-containing alcohol dehydrogenases from baker’s yeast, *saccharomyces cerevisiae*. *FEMS yeast research*, 2(4):481–494, 2002.
- [294] Hao Zhang, Weidong Cui, Jianzhong Wen, Robert E. Blankenship, and Michael L. Gross. Native electrospray and electron-capture dissociation in FTICR mass spectrometry provide top-down sequencing of a protein component in an intact protein assembly. *Journal of the American Society for Mass Spectrometry*, 21(12):1966–1968, dec 2010. doi: 10.1016/j.jasms.2010.08.006.
- [295] Hao Zhang, Weidong Cui, Jianzhong Wen, Robert E. Blankenship, and Michael L. Gross. Native electrospray and electron-capture dissociation FTICR mass spectrometry for top-down studies of protein assemblies. *Analytical Chemistry*, 83(14):5598–5606, jun 2011. doi: 10.1021/ac200695d.
- [296] Luis F. Schachner, Ashley N. Ives, John P. McGee, Rafael D. Melani, Jared O. Kafader, Philip D. Compton, Steven M. Patrie, and Neil L. Kelleher. Standard proteoforms and their complexes for native mass spectrometry. *Journal of the American Society for Mass Spectrometry*, 30(7):1190–1198, apr 2019. doi: 10.1007/s13361-019-02191-w.
- [297] Savarimuthu Baskar Raj, S. Ramaswamy, and Bryce V. Plapp. Yeast alcohol dehydrogenase structure and catalysis. *Biochemistry*, 53(36):5791–5803, sep 2014. doi: 10.1021/bi5006442.
- [298] Audree V Fowler and Irving Zabin. The amino acid sequence of beta-galactosidase of *escherichia coli*. *Proceedings of the National Academy of Sciences*, 74(4):1507–1510, 1977.
- [299] Brian W. Matthews. The structure of *e. coli* beta-galactosidase. *Comptes Rendus Biologies*, 328(6):549–556, jun 2005. doi: 10.1016/j.crvi.2005.03.006.
- [300] RH Jacobson, X-J Zhang, RF DuBose, and BW Matthews. Three-dimensional structure of beta-galactosidase from *e. coli*. *Nature*, 369(6483):761–766, 1994.
- [301] Huilin Li. An integrated native mass spectrometry and top-down proteomics method that connects sequence to structure and function of macromolecular complexes. *Nature Chemistry*, 10, 02 2018. doi: 10.1038/nchem.2908.
- [302] Wayne A Fenton and Arthur L Horwich. Groel-mediated protein folding. *Protein science: a publication of the Protein Society*, 6(4):743, 1997.

- [303] Paul B Sigler, Zhaohui Xu, Hays S Rye, Steven G Burston, Wayne A Fenton, and Arthur L Horwich. Structure and function in groel-mediated protein folding. *Annual review of biochemistry*, 67(1):581–608, 1998.
- [304] Zong Lin and Hays S. Rye. GroEL-mediated protein folding: Making the impossible, possible. *Critical Reviews in Biochemistry and Molecular Biology*, 41(4):211–239, jan 2006. doi: 10.1080/10409230600760382.
- [305] Esther van Duijn, Patrick J Bakkes, Ron MA Heeren, Robert HH van den Heuvel, Harm van Heerikhuizen, Saskia M van der Vies, and Albert JR Heck. Monitoring macromolecular complexes involved in the chaperonin-assisted protein folding cycle by mass spectrometry. *Nature Methods*, 2(5):371–376, 2005.
- [306] Christopher J. Hogan, Brandon T. Ruotolo, Carol V. Robinson, and Juan Fernandez de la Mora. Tandem differential mobility analysis-mass spectrometry reveals partial gas-phase collapse of the GroEL complex. *The Journal of Physical Chemistry B*, 115(13): 3614–3621, apr 2011. doi: 10.1021/jp109172k.
- [307] Jianxun Mou, S Sheng, Rouya Ho, and Zhifeng Shao. Chaperonins groel and groes: views from atomic force microscopy. *Biophysical journal*, 71(4):2213–2221, 1996.
- [308] F Valle, JA DeRose, G Dietler, M Kawe, A Plückthun, and G Semenza. Afm structural study of the molecular chaperone groel and its two-dimensional crystals: an ideal “living” calibration sample. *Ultramicroscopy*, 93(1):83–89, 2002.
- [309] Justin L.P. Benesch, Brandon T. Ruotolo, Douglas A. Simmons, Nelson P. Barrera, Nina Morgner, Luchun Wang, Helen R. Saibil, and Carol V. Robinson. Separating and visualising protein assemblies by means of preparative mass spectrometry and microscopy. *Journal of Structural Biology*, 172(2):161–168, nov 2010. doi: 10.1016/j.jsb.2010.03.004.
- [310] Alan Merk, Alberto Bartesaghi, Soojay Banerjee, Veronica Falconieri, Prashant Rao, Mindy I Davis, Rajan Pragani, Matthew B Boxer, Lesley A Earl, Jacqueline LS Milne, et al. Breaking cryo-em resolution barriers to facilitate drug discovery. *Cell*, 165(7):1698–1707, 2016.
- [311] Esther van Duijn, Arjan Barendregt, Silvia Synowsky, Cees Versluis, and Albert J. R. Heck. Chaperonin complexes monitored by ion mobility mass spectrometry. *Journal of the American Chemical Society*, 131(4):1452–1459, jan 2009. doi: 10.1021/ja8055134.
- [312] SO Sampaio, X Li, M Takeuchi, C Mei, U Francke, EC Butcher, and MJ Briskin. Organization, regulatory sequences, and alternatively spliced transcripts of the mucosal addressin cell adhesion molecule-1 (madcam-1) gene. *The Journal of Immunology*, 155(5):2477–2486, 1995.
- [313] Dominic Picarella, Peter Hurlbut, James Rottman, Xiaojie Shi, Eugene Butcher, and Douglas J Ringler. Monoclonal antibodies specific for beta 7 integrin and mucosal addressin cell adhesion molecule-1 (madcam-1) reduce inflammation in the colon of scid mice reconstituted with cd45rbhigh cd4+ t cells. *The Journal of Immunology*, 158(5):2099–2106, 1997.
- [314] Satoshi Tanida, Tsutomu Mizoshita, Takashi Mizushima, Makoto Sasaki, Takaya Shimura, Takeshi Kamiya, Hiromi Kataoka, and Takashi Joh. Involvement of oxidative

- stress and mucosal addressin cell adhesion molecule-1 (madcam-1) in inflammatory bowel disease. *Journal of clinical biochemistry and nutrition*, 48(2):112–116, 2011.
- [315] Sebastian Zundler, Emily Becker, Lisa Lou Schulze, and Markus F Neurath. Immune cell trafficking and retention in inflammatory bowel disease: mechanistic insights and therapeutic advances. *Gut*, 68(9):1688–1700, 2019.
- [316] Yamei Yu, Jianghai Zhu, Li-Zhi Mi, Thomas Walz, Hao Sun, JianFeng Chen, and Timothy A. Springer. Structural specializations of alpha4beta7, an integrin that mediates rolling adhesion. *Journal of Cell Biology*, 196(1):131–146, jan 2012. doi: 10.1083/jcb.201110023.
- [317] Puregmaa Khongorzul, Cai Jia Ling, Farhan Ullah Khan, Awais Ullah Ihsan, and Juan Zhang. Antibody–drug conjugates: a comprehensive review. *Molecular Cancer Research*, 18(1):3–19, 2020.
- [318] Peter H Schur. Igg subclasses—a review. *Annals of allergy*, 58(2):89–96, 1987.
- [319] Steven Shak. Overview of the trastuzumab (herceptin) anti-her2 monoclonal antibody clinical program in her2-overexpressing metastatic breast cancer. herceptin multinational investigator study group. In *Seminars in oncology*, volume 26, pages 71–77, 1999.
- [320] HM Shepard, P Jin, DJ Slamon, Z Pirot, and DC Maneval. Herceptin. *Therapeutic Antibodies*, pages 183–219, 2008.
- [321] Julien Marcoux, Thierry Champion, Olivier Colas, Elsa Wagner-Rousset, Nathalie Corvaia, Alain Van Dorsselaer, Alain Beck, and Sarah Cianférani. Native mass spectrometry and ion mobility characterization of trastuzumab emtansine, a lysine-linked antibody drug conjugate. *Protein Science*, 24(8):1210–1223, mar 2015. doi: 10.1002/pro.2666.
- [322] Hae-Min Park, Valerie J. Winton, Jared J. Drader, Sheri Manalili Wheeler, Greg A. Lazar, Neil L. Kelleher, Yichin Liu, John C. Tran, and Philip D. Compton. Novel interface for high-throughput analysis of biotherapeutics by electrospray mass spectrometry. *Analytical Chemistry*, 92(2):2186–2193, dec 2019. doi: 10.1021/acs.analchem.9b04826.
- [323] Kjetil Hansen, Andy M Lau, Kevin Giles, James M McDonnell, Weston B Struwe, Brian J Sutton, and Argyris Politis. A mass-spectrometry-based modelling workflow for accurate prediction of igg antibody conformations in the gas phase. *Angewandte Chemie*, 130(52):17440–17445, 2018.
- [324] Xiaoqiang Wang, Yuming Wang, Hai Xu, Honghong Shan, and Jian R Lu. Dynamic adsorption of monoclonal antibody layers on hydrophilic silica surface: A combined study by spectroscopic ellipsometry and afm. *Journal of colloid and interface science*, 323(1):18–25, 2008.
- [325] Kelvin Anggara, Yuntao Zhu, Martina Delbianco, Stephan Rauschenbach, Sabine Abb, Peter H Seeberger, and Klaus Kern. Exploring the molecular conformation space by soft molecule–surface collision. *Journal of the American Chemical Society*, 142(51):21420–21427, 2020.
- [326] Victor Le-Minh, N Thuy Tran, Ali Makky, Veronique Rosilio, Myriam Taverna, and Claire Smadja. Capillary zone electrophoresis-native mass spectrometry for the quality control of intact therapeutic monoclonal antibodies. *Journal of Chromatography A*, 1601:375–384, 2019.

- [327] Alain Beck, François Debaene, Hélène Diemer, Elsa Wagner-Rousset, Olivier Colas, Alain Van Dorsselaer, and Sarah Cianférani. Cutting-edge mass spectrometry characterization of originator, biosimilar and biobetter antibodies. *Journal of Mass Spectrometry*, 50(2):285–297, 2015.
- [328] Kai Scheffler and Eugen Damoc. Full characterization of heterogeneous antibody samples under denaturing and native conditions on the q exactive biopharma mass spectrometer. *Appl Note*, 72348, 2017.
- [329] JM MacLeod and Federico Rosei. Molecular self-assembly on graphene. *Small*, 10(6):1038–1049, 2014.
- [330] Hans Fischer. Hemin. *Organic syntheses*, 21:53–53, 2003.
- [331] Anna Rita Bilia, Diamanto Lazari, Luigi Messori, Vania Taglioli, Claudia Temperini, and Franco Francesco Vincieri. Simple and rapid physico-chemical methods to examine action of antimalarial drugs with hemin: its application to artemisia annua constituents. *Life sciences*, 70(7):769–778, 2002.
- [332] Zhibin Yin, Binwen Sun, Xiaohua Wang, Xiaoling Cheng, Wei Hang, and Benli Huang. Comprehensive analysis of metalloporphyrins via high irradiance laser ionization time-of-flight mass spectrometry. *Journal of Analytical Atomic Spectrometry*, 29(9):1714–1719, 2014.
- [333] De-Liang Long, Eric Burkholder, and Leroy Cronin. Polyoxometalate clusters, nanostructures and materials: From self assembly to designer materials and devices. *Chemical Society Reviews*, 36(1):105–121, 2007.
- [334] WU Hsein. Molybdc acids, phosphotungstic acids. *The Journal of Biological Chemistry*, 43:189, 1920.
- [335] José Alves Dias, Sílvia Cláudia Loureiro Dias, Ednéia Caliman, Judit Bartis, and Lynn Francesconi. Keggin structure polyoxometalates. *Inorganic Syntheses: Volume 36*, pages 210–217, 2014.
- [336] YanXuan Fan, Yan Zhang, QiaoDi Jia, Jie Cao, and WenJie Wu. The stabilizing role of cyclodextrins on keggins phosphotungstic acid by complexation unveiled by electrospray mass spectrometry. *Mass Spectrometry Letters*, 6(1):13–16, 2015.
- [337] N. Vats, S. Rauschenbach, W. Sigle, S. Sen, S. Abb, A. Portz, M. Duerr, M. Burghard, P. A. van Aken, and K. Kern. Electron microscopy of polyoxometalate ions on graphene by electrospray ion beam deposition. *Nanoscale*, 10(10):4952–4961, 2018. doi: 10.1039/c8nr00402a.
- [338] Hans J Wagner, Rafik O Loutfy, and Cheng-Kuo Hsiao. Purification and characterization of phthalocyanines. *Journal of materials science*, 17(10):2781–2791, 1982.
- [339] Keiichi Sakamoto and Eiko Ohno-Okumura. Syntheses and functional properties of phthalocyanines. *Materials*, 2(3):1127–1179, 2009.
- [340] D Dubbers. Simple formula for multiple mu-metal shields. *Nuclear Instruments and Methods in Physics Research Section A: Accelerators, Spectrometers, Detectors and Associated Equipment*, 243(2-3):511–517, 1986.
- [341] Rudolf M Tromp, M Mankos, MC Reuter, AW Ellis, and M Copel. A new low energy electron microscope. *Surface Review and Letters*, 5(06):1189–1197, 1998.

Bibliography

- [342] Jian Wang, Shouxian She, and Sijiong Zhang. An improved helmholtz coil and analysis of its magnetic field homogeneity. *Review of scientific instruments*, 73(5):2175–2179, 2002.
- [343] Tatiana Latychevskaia, Petr Formanek, Christoph T Koch, and Axel Lubk. Off-axis and inline electron holography: Experimental comparison. *Ultramicroscopy*, 110(5):472–482, 2010.
- [344] A. Bartesaghi, P. Sprechmann, J. Liu, G. Randall, G. Sapiro, and S. Subramaniam. Classification and 3d averaging with missing wedge correction in biological electron tomography. *Journal of Structural Biology*, 162(3):436–450, jun 2008. doi: 10.1016/j.jsb.2008.02.008.
- [345] Paul A. Midgley and Rafal E. Dunin-Borkowski. Electron tomography and holography in materials science. *Nature Materials*, 8(4):271–280, apr 2009. doi: 10.1038/nmat2406.
- [346] Tanmay AM Bharat, Norman E Davey, Pavel Ulbrich, James D Riches, Alex De Marco, Michaela Rumlova, Carsten Sachse, Tomas Ruml, and John AG Briggs. Structure of the immature retroviral capsid at 8 Å resolution by cryo-electron microscopy. *Nature*, 487(7407):385–389, 2012.
- [347] Alberto Bartesaghi, Federico Lecumberry, Guillermo Sapiro, and Sriram Subramaniam. Protein secondary structure determination by constrained single-particle cryo-electron tomography. *Structure*, 20(12):2003–2013, dec 2012. doi: 10.1016/j.str.2012.10.016.
- [348] Jana Ognjenovic, Reinhard Grischammer, and Sriram Subramaniam. Frontiers in cryo electron microscopy of complex macromolecular assemblies. *Annual review of biomedical engineering*, 21:395–415, 2019.
- [349] Patrick Zwick, Diana Dulić, Herre S. J. van der Zant, and Marcel Mayor. Porphyrins as building blocks for single-molecule devices. *Nanoscale*, 13(37):15500–15525, 2021. doi: 10.1039/d1nr04523g.
- [350] Swarup Dey, Chunhai Fan, Kurt V Gothelf, Jiang Li, Chenxiang Lin, Longfei Liu, Na Liu, Minke AD Nijenhuis, Barbara Saccà, Friedrich C Simmel, et al. Dna origami. *Nature Reviews Methods Primers*, 1(1):1–24, 2021.

Acknowledgements

This PhD project took more than 4 years and the collaboration of two PhD students to get this far. During this time, many people supported me and I am very grateful to each of them!

First of all, I want to thank Prof. Klaus Kern, who gave me this incredible chance to construct and establish our LEEH microscope. The precision laboratory, which was founded by Prof. Kern, provided a state-of-the-art working environment and allowed our setup to perform beyond the so far known limits of low-energy electron holography. I really enjoyed each step of this truly interdisciplinary work from the microscope construction to the sample preparation and measurements and could not have thought of a better PhD project for me. Thank you for letting me freely explore, learn and improve my scientific skills in this wonderful environment!

I want to thank my thesis jury committee including Frédéric Courbin, Giovanni Dietler, Stephan Rauschenbach, and Federico Forneris for taking the time and patience to evaluate my work.

My gratitude goes to my laboratory supervisors: Sabine Abb and Luigi Malavolti. Thanks to Sabine for teaching me everything I needed to know about the ES-IBD setup and process and helping us with the initial work on the LEEH setup. Also thanks to Luigi, who not only supported us in the lab but also proof-read this thesis several times, which helped me a lot!

Next we have the Holo and ESI group members. First, I want to thank my PhD colleague Hannah Ochner, who started this project together with me. Without her theoretical know-how and skills we would not have advanced that quickly in hologram reconstruction. Our joined effort in this work yielded the countless beautiful molecule images and she knows exactly how difficult LEEH can be, especially regarding our dear emitters. It was a real pleasure to work with you and thank you for always being patient, objective and a good team player! I also want to thank Moritz Edte, our new PhD who will take on the LEEH legacy, for being a great and curious student. Even though he wants to be the very best, he still has a lot to learn, but I am very confident that he will manage to surpass us eventually. Finally, I want to thank Kelvin Anggara, who took great care of the ESI setup when we were not around and was always helpful in various scientific discussions.

Acknowledgements

Without information exchange and collaborations, science in general would be much less efficient and would most probably generate fewer breakthroughs. With this, I want to thank our collaborators during the course of this work. I am very grateful for all the help and insight about LEEH we received from Jean-Nicolas Longchamp, who was one of the few people actually working on this type of microscope. Our substrate and emitter preparation protocols were based on his expertise in the field, which allowed us to swiftly progress with our project. Regarding ESI and ES-IBD, I want to thank the group of Carol Robinson (University of Oxford), including Joseph Gault, Tim Esser, Paul Fremdling, and especially Stephan Rauschenbach, who gave us valuable information about handling the native ESI process and to be expected mass spectra for our various protein samples. We also received Herceptin antibody and GroEL samples from them, which yielded intriguing samples for our LEEH setup. Furthermore, the construction of the novel ESI source is a joined effort of our groups. I also want to thank the group of Sebastian Zundler (Uniklinikum Erlangen) and especially Lisa Lou Schulze, who provided us with the MAdCAM complexes, which are an interesting molecule system for our microscope. Finally, I want to thank Nilesh Vats for introducing me to the SLG preparation technique and providing us with the possibility to do TEM measurements. Helping you to spray the various alkali-iodide salts via ESI was a fresh and relaxing alternation when compared to our usually more difficult protein samples.

Even the best experimentalist is only as good as his workshop. Thankfully, our competent technicians Wolfgang Stiepany, Peter Andler, Marko Memmler and Isabel Wolf set the bar very high, so that we never had to worry about a wrong setup part or flawed electric connection. Especially Wolfgang helped us so much with the planning, construction and all of the improvement steps of our LEEH microscope and I learned so many valuable things from him! He is definitely a genius with regards to everything related to UHV and usually knows how to solve setup-related problems. Outside the labs, Sabine Birtel was our almost omniscient contact point for all the non-scientific matters and issues. Thank you so much for all the management and the thousand answered questions regarding everything about the bureaucratic processes.

Concerning further group members, I want to thank Christian Ast, Manish Garg, Klaus Kuhnke and Aparajita Singha for the interesting scientific discussions and input. Furthermore, I am grateful for the countless Nalewka, party and game evenings together with Tomasz Michnowicz, Anna Roslawska, Alessio Scavuzzo, Piotr Kot, Tobias Wollandt, Katharina Polyudov, Dinesh Pinto, Domenico Paone and Janis Siebrecht. I also thank Marko Burghard and Rico Gutzler for the occasional table tennis and jogging rounds. Furthermore, I want to thank Abhishek Grewal and Lukas Powalla for all the nice training sessions and relaxed dinner and game evenings. I am also grateful for meeting Markus Joos, Hrag Karakachian and Eric Reutter via the IMPRS, who started their PhD at the same time as me. Our coffee and da Franco meetings were always refreshing and fun!

Next, I want to thank my old study colleagues, the Nanos. It is fascinating how that many completely different people can have such a strong friendship and I am glad that we all are still in frequent contact and support each other even after scattering all over the world. The

future belongs to Nano! I also want to thank my friends here in Stuttgart, which always help me to relax after long working days by joining me for our trainings, going out or simply having exciting game evenings.

Finally, I want to thank my parents, siblings and other family members for their constant support and help in all life situations. And last, but not least, I am grateful to my girlfriend Melanie 'Melo' Handrich, who is always there for me and encourages me to keep going and strive for the best. Without her, I might not have come to Stuttgart in the first place. Thank you for being such a great, caring and loving partner and let us see what the future holds for us next!

Stuttgart, March 29, 2022

Sven Szilagyi

Sven Alexander Szilagyi



Personal Data

Born on 21st of May 1992 in Pforzheim, Germany
 German nationality
 Address: Emiliestraße 35, 70563 Stuttgart, Germany
 Tel. (mobile): +49-1577-4027642
 E-Mail: sven.szilagyi@web.de

Academic Education

- Since 09/2017 **PhD Candidate at EDPY (EPFL, Switzerland)**
 Max Planck Institute for Solid State Research (MPI-FKF) Stuttgart
 Department: Nanoscale Science; Director: Prof. Dr. Klaus Kern
 PhD project: construction of a Low Energy Electron Holography microscope with the aim of imaging native proteins on a single molecule level
- 10/2014 – 04/2017 **Master student in Nano-Science (M.Sc.) - final grade: 1.20 (very good)**
 Eberhard Karls University Tuebingen
 Master Thesis (at ZMBP): 'A reflected light sheet microscope for single cell imaging'
 Grading: 1.00 (very good)
- 10/2011 - 09/2014 **Bachelor student in Nano-Science (B.Sc.) - final grade: 1.46 (very good)**
 Eberhard Karls University Tuebingen
 Bachelor Thesis (at IFIB): 'Aufnahme und Wirkung von Fe₂O₃PVADTAF-Nanopartikeln in *Trypanosoma brucei brucei*' - Grading: 1.00 (very good)
 ('Uptake and effect of Fe₂O₃PVADTAF nanoparticles in *Trypanosoma brucei brucei*')
- 07/2011 **Abitur - final grade: 1.9 (good)**
 Otto-Hahn-Gymnasium Ludwigsburg

Practical Experience

- 09/2016 - 07/2017 **Cellular Nanoscience (ZMBP, University of Tuebingen)**
 Research assistant, group leader: Prof. Dr. Erik Schaeffer
 Projects: setup and adjustment of a reflected light sheet microscope
- 04/2016 - 07/2016 **Laboratory for Cell Mimicry (iNANO, Aarhus University, Denmark)**
 Practical internship guest student, group leader: Assoc. Prof. Dr. Brigitte Staedler
 Project: synthesis, characterization and cell uptake kinetics of block-copolymer-liposome hybrids (capsosomes) as well as their degradation behavior in cells
- 10/2014 - 03/2016 **Cellular Nanoscience (ZMBP, University of Tuebingen)**
 Research assistant, group leader: Prof. Dr. Erik Schaeffer
 Projects: silica coating and functionalization of nano-diamonds (NDs);
 installation of a heating laser for molecular thermophoresis experiments;
 low-frequency table damping setup for optical tweezers measurements;
 synthesis and fluorescent labelling of giant unilamellar vesicles (GUVs);
 hardware-to-software interface setup for stage control in microscopes;
 protein linked coupling of surface attached GUVs and NDs

CURRICULUM VITAE

- 08/2014 - 09/2014 **Hofmeister GmbH & Co. KG (warehouse in Bietigheim)**
Summer jobber
Task: stock picking and customer service
- 09/2013 - 02/2014 **Plant Physiology (ZMBP, University of Tuebingen)**
Research assistant, group leader: Dr. Gabriel Schaaf
Project: molecular plant nutrition - iron homeostasis:
iron uptake in genetically modified *Arabidopsis thaliana*
- 08/2013 **Soft Matter Physics (IfAP, University of Tuebingen)**
Research assistant, group leader: Prof. Dr. Frank Schreiber
Project: adjustment of a surface-sensitive X-ray laser
- 08/2011 - 09/2011 **Daimler AG (factory in Esslingen-Mettingen)**
Summer jobber
Task: automatic gearbox fabrication

Publications (Author and Co-Author)

Ochner, Hannah and **Szilagyi, Sven A.** and Abb, Sabine and Malavolti, Luigi and Rauschenbach, Stephan and Kern, Klaus. "Phase reconstruction of low-energy electron holography holograms of proteins." (2022): in preparation.

Szilagyi, Sven A. and Ochner, Hannah and Edte, Moritz and Abb, Sabine and Longchamp, Jean-Nicolas and Malavolti, Luigi and Rauschenbach, Stephan and Kern, Klaus. "A novel low temperature low-energy electron holography microscope with in situ electrospray ion beam deposition sample preparation." (2022): in preparation.

Jannasch, Anita and **Szilagyi, Sven A.** and Burmeister, Moritz and Davis, Q. Tyrell and Hermsdorf, Gero L. and De, Suman and Schäffer, Erik. "Fast 3D imaging of giant unilamellar vesicles using reflected light-sheet microscopy with single molecule sensitivity." *Journal of Microscopy* 285.1 (2022): 40-51.

Ochner, Hannah and **Szilagyi, Sven A.** and Abb, Sabine and Gault, Joseph and Robinson, Carol V. and Malavolti, Luigi and Rauschenbach, Stephan and Kern, Klaus. "Low-energy electron holography imaging of conformational variability of single-antibody molecules from electrospray ion beam deposition" *PNAS* 118.51 (2021).

Vats, Nilesh and Negi, Devendra S. and Singh, Deobrat and Sigle, Wilfried and Abb, Sabine and Sen, Suman and **Szilagyi, Sven A.** and Ochner, Hannah and Ahuja, Rajeev and Kern, Klaus. "Catalyzing Bond-Dissociation in Graphene via Alkali-Iodide Molecules" *Small* 17.42 (2021): 2102037.

Vats, Nilesh and Wang, Yi and Sen, Suman and **Szilagyi, Sven A.** and Ochner, Hannah and Abb, Sabine and Burghard, Marko and Sigle, Wilfried and Kern, Klaus and van Aken, Peter. "Substrate-Selective Morphology of Cesium Iodide Clusters on Graphene." *ACS nano* 14.4 (2020): 4626-4635.

Brodzskij, Edit and Hviid, Martin J. and Ade, Carina and Schattling, Philipp S. and Burmeister, Moritz and **Szilagyi, Sven A.** and Gal, Noga and Zhu, Chuntao and Han, Xiaojun and Städler, Brigitte. "Interaction of pH-responsive polyanions with phospholipid membranes." *Polymer Chemistry* 10.44 (2019): 5992-5997.

Hermsdorf, Gero L. and **Szilagyi, Sven A.** and Rösch, Sebastian and Schäffer, Erik. "High performance passive vibration isolation system for optical tables using six-degree-of-freedom viscous damping combined with steel springs." *Review of Scientific Instruments* 90.1 (2019): 015113.

CURRICULUM VITAE

Languages and IT

German (native); English (fluent)

Leadership training at MPI FKF (Organisation and Participation)

IT: Microsoft Office; LaTeX; Matlab; Origin; LabView; Python; ImageJ; SolidWorks; Adobe Illustrator

Driving licence class B

Social Engagement

PhD representative at MPI FKF (duration: year 2018)

Private coaching for students in biology, chemistry, physics, mathematics (since 2009)

Leading an out-door workout and calisthenics group for students (since 2013)

Regular blood donations at Deutsches Rotes Kreuz (German Red Cross)

Stuttgart, 12.01.2022

A handwritten signature in black ink, reading 'S. Szilagyi' in a cursive script.

Sven Szilagyi